



2009

APPLICATIONS OF COMPUTATIONAL FLUID DYNAMICS TO PLANETARY ATMOSPHERES

Xiaolong Deng

University of Kentucky, xdeng0@engr.uky.edu

[Click here to let us know how access to this document benefits you.](#)

Recommended Citation

Deng, Xiaolong, "APPLICATIONS OF COMPUTATIONAL FLUID DYNAMICS TO PLANETARY ATMOSPHERES" (2009).
University of Kentucky Doctoral Dissertations. 711.
https://uknowledge.uky.edu/gradschool_diss/711

This Dissertation is brought to you for free and open access by the Graduate School at UKnowledge. It has been accepted for inclusion in University of Kentucky Doctoral Dissertations by an authorized administrator of UKnowledge. For more information, please contact UKnowledge@lsv.uky.edu.

ABSTRACT OF DISSERTATION

Xiaolong Deng

The Graduate School
University of Kentucky
2009

APPLICATIONS OF COMPUTATIONAL FLUID DYNAMICS TO
PLANETARY ATMOSPHERES

ABSTRACT OF DISSERTATION

A dissertation submitted in partial fulfillment of the
requirements for the degree of Doctor of Philosophy in the
College of Engineering
at the University of Kentucky

By
Xiaolong Deng

Lexington, Kentucky

Co-Director: Dr. Raymond P. LeBeau, Assistant Professor of Mechanical
Engineering
and Dr. Vincent R. Capece, Professor of Mechanical Engineering

Lexington, Kentucky

2009

Copyright © Xiaolong Deng 2009

ABSTRACT OF DISSERTATION

APPLICATIONS OF COMPUTATIONAL FLUID DYNAMICS TO PLANETARY ATMOSPHERES

Computational Fluid Dynamics (CFD) has been applied to many areas. As one of the most important fluids, the atmosphere is closely related to people's life. Studying the atmospheres on other planets can help people understand the Earth's atmosphere and the climate and weather phenomena in it. Because of the complexity of a planetary atmosphere and the limitation of observations, applying CFD to the study of planetary atmospheres is becoming more and more popular. This kind of CFD simulations will also help people design the mission to the extra planets.

In this dissertation, through CFD simulations, we studied the three important phenomena in a planetary atmosphere: vortices, zonal winds and clouds. The CFD model Explicit Planetary Isentropic Coordinate (EPIC) Global Circulation Model (GCM) was applied in these simulations. Dynamic simulations of the Great Dark Spots (GDS) on Neptune and the Uranian Dark Spot (UDS) were performed. In this work, constructed zonal wind profiles and vertical pressure-temperature profile were constructed based on the observational data. Then, we imported a two-flux radiation model with two-band absorption coefficients into EPIC to study the seasonal changes on Uranus. Finally, a methane cloud model was imported to study the cloud formation around a great vortex and its effects on the vortex.

In the process of the dynamic simulations of Neptune's atmosphere and its vortices in it, the parameters about the background and the vortex itself were investigated to try to fit the observational results. We found that a small gradient of background absolute vorticity near a GDS is needed to sustain a great vortex in the atmosphere. The drift rate and oscillations of a GDS are closely related to the zonal wind profile and the vortex characteristics. The dynamic simulations of the UDS suggested why it is hard to observe a great vortex on Uranus and indicated that a region of near constant absolute vorticity appearing at $\sim 28^\circ\text{N}$ in the zonal wind profile is possibly recommended to the sustainability of the UDS. With the two-flux radiation model, we simulated the seasonal change of the zonal wind profile on Uranus. The observational temperature distribution and global convection were also achieved. With the methane cloud model, we simulated the poleward cloud above great vortices on both Neptune

and Uranus. The results suggested that the cloud model can help the GDS on Neptune to keep its shape and moderate its oscillations. Similarly, it can also help the UDS to keep its form.

KEYWORDS: Computational Fluid Dynamics, planetary atmosphere, great vortex, radiation, cloud

Xiaolong Deng

Student's Signature

May 07, 2009

Date

APPLICATIONS OF COMPUTATIONAL FLUID DYNAMICS TO PLANETARY
ATMOSPHERES

By

Xiaolong Deng

Dr. Raymond P. LeBeau

Director of Dissertation

Dr. L. Scott Stephens

Director of Graduate Studies

May 07, 2009

Date

DISSERTATION

Xiaolong Deng

The Graduate School
University of Kentucky
2009

APPLICATIONS OF COMPUTATIONAL FLUID DYNAMICS TO
PLANETARY ATMOSPHERES

DISSERTATION

A dissertation submitted in partial fulfillment of the
requirements for the degree of Doctor of Philosophy in the
College of Engineering
at the University of Kentucky

By
Xiaolong Deng

Lexington, Kentucky

Co-Director: Dr. Raymond P. LeBeau, Assistant Professor of Mechanical
Engineering
and Dr. Vincent Capece, Professor of Mechanical Engineering

Lexington, Kentucky

2009

Copyright © Xiaolong Deng 2009

I dedicate my dissertation to my loving parents,
Yingchang Deng and Zhengrong Wu,
and my dearest wife, Yuqian Zhang.

Your love and encouragement are the greatest impetus for me to go ahead.

ACKNOWLEDGEMENTS

I would first like to thank my mentor Dr. Raymond P. LeBeau, who has given me a lot of directions during my graduate study. I feel grateful and lucky to have had the opportunity to work with you. Without your help, this dissertation cannot be finished.

I would like to thank my co-advisor Dr. Vincent R. Capece and my committee member Dr. James M. McDonough from the Department of Mechanical Engineering. During these years in the University of Kentucky, I learned a lot from you. I would like to thank Dr. Zhongwei Shen from the Department of Mathematics, who provided a lot of help in both my qualify exam and my final exam. I would like to thank Dr. M. Pinar Mengüç from the Department of Mechanical Engineering for being on my committee during the qualify exam. And I would like to thank Dr. Terrence Draper from the Department of Physics and Astronomy for being my outside examiner. I would like to thank all of you for your time and advice during the defense process.

I would like to thank Dr. Mohamed Hassan Ali for helping me a lot of when I was a teaching assistant. I took many classes in the Department of Mechanical Engineering, Department of Mathematics and Department of Computer Science. I would like to thank all the faculties who taught these classes. Also, I would like to thank all the staffs in these departments who gave me help on many things.

I would like to thank the former head, Dr. George P. G. Huang, and my former labmates in the UK CFD lab, Mr. Daniel A. Reasor Jr., Mr. Narendra Beliganur Kotragouda, Mr. Anand Palki, Ms. Sri Swetha Pangul uri, Mr. Saurabh Gupta, Mr. Nelson Kudzo Akafuah, Mr. V V Sunil Kumar Vytla, Mr. Ahmad A. Salaimah, Mr. Chaitanya P.S.K. Penugonda, Mr. Pavan Kristipati, Mr. Shih-Che Huang and Dr. Chih-Hao Chang, for your all kinds of help and discussions with me.

Finally, I would like to thank my parents Yingchang Deng and Zhengrong wu, and my dear wife Yuqian Zhang, for your unconditional love, patience and care.

TABLE OF CONTENTS

Acknowledgement	iii
List of Tables	vii
List of Figures	viii
Chapter 1 Introduction	1
1.1 Great Vortices in Planetary Atmospheres	3
1.2 Characteristics and Atmospheres of Neptune and Uranus	14
1.3 Fluid Dynamics in Planetary Atmosphere	27
1.4 EPIC GCM	35
1.5 Computer Resource	41
Chapter 2 Experimental Methodology	44
2.1 Constructed Zonal Wind Profiles	44
2.2 Constructed Pressure-Temperature Profiles	49
2.3 Vortex Generation	52
2.4 Fitting GDS with Least Squares Method	58
2.5 Power Spectrum Calculation	60
Chapter 3 Dynamic Simulations of Great Dark Spots on Neptune	64
3.1 Basic Parameters	67
3.2 Quarter Globe Simulations	69
3.3 Comparison to Whole Globe Simulations	81
3.4 Whole Globe Domain Simulations	82
3.5 Simulations with $Q_y = 1/12$ and Reference Latitude 18°S	107

3.6	Simulations with Smooth Q_y Change	114
3.7	Discussion	124
Chapter 4 Dynamic Simulations on Uranian Dark Spot		130
4.1	Model Setup	132
4.2	Coarse Grid Simulations	136
4.3	Finer Grid Simulations	146
4.4	Discussion	154
Chapter 5 Radiation Model and Seasonal Change of Zonal Wind Profile on Uranus		161
5.1	Heat Term in EPIC Model	161
5.2	Two-Flux Model	162
5.3	Basic Considerations	164
5.4	Geometry	165
5.5	Absorption Coefficient	167
5.6	Realizing the Radiation Model in the EPIC GCM	173
5.7	Grid Setup and Time Step	174
5.8	Simulation Results	174
5.9	Discussion	181
Chapter 6 Cloud Model and Bright Companion		196
6.1	Initial Methane Distribution	199
6.2	Microphysics	201
6.3	Realizing the Cloud Model in the EPIC GCM	201
6.4	Zonal Wind Profile	202
6.5	Other Parameters	202
6.6	Simulation Results	203
6.7	Discussion	216

Chapter 7 Discussion	220
Bibliography	225
Vita	236

LIST OF TABLES

1.1	Clusters used in this work	42
3.1	The default 10-layer setup on Neptune in the dynamic simulations	68
3.2	Selected simulation results for GDS-89 on Neptune. The Q_y values marked with an * are pole-to-pole simulations. Others are quarter globe simulations with latitude region from south pole to equator and longitude region from -90° to 90°	80
3.3	Selected simulation results for GDS-89 on Neptune in whole globe region.	127
3.3	Selected simulation results for GDS-89 on Neptune in whole globe region. - Continued	128
3.3	Selected simulation results for GDS-89 on Neptune in whole globe region. - Continued2	129
4.1	Uranus Vortex Simulations on the Coarse Grid	159
4.2	Uranus Vortex Simulations on the Finer Grid	160
5.1	The 10 layers setup on Uranus for the one-band test simulation case of the radiation model	175
5.2	The 10 layers setup on Uranus for the two-band simulation cases of the radiation model	184
6.1	The 10 layers setup on Neptune in the cloud model simulations	204
6.2	Comparison between the simulation cases with cloud model and without cloud model.	211

LIST OF FIGURES

1.1	NASA image of Hurricane Katrina on 29 August 2005[71].	4
1.2	Great Red Spot and Oval BA on Jupiter. This photo is from NASA published on The New York Times website in 2006[72].	5
1.3	Major cloud and vortex features on Neptune, visible when Voyager II passed by on 14 August 1989 (a) and 20 August 1989(b). In both panels, we can see GDS (at 18.2°S at this time) and its bright companion on its south edge. The cloud feature scooter (at 40°S) can also be seen in these two panels. In panel (a), near the south pole, the cloud feature SPF (South Pole Feature) can be observed at 73°S. In panel (b), the second dark spot DS2 was at 53.3°S when the image was made. This figure is from Sromovsky 1993[91].	6
1.4	The observations of GDS-89. In this figure, we can see the GDS and its companion. And the oscillations of the shape and orientation of GDS and the "tail" can also be seen. The numbers on the subplots are the days from the first image. This figure is from Stratman et al. 2001[98].	8
1.5	Latitudinal and longitudinal size change of the GDS-89. The points and error bars on them are from observational results. The solid lines are empirical fit to the data with equations 1.1 and parameters shown in Figure 1.6. This figure is from Sromovsky et al 1993[91].	9
1.6	The parameters for the empirical fit to the observational GDS-89 size oscillation data. This figure is from Table 1 in Sromovsky et al 1993[91].	9

1.7	The three-wavelength composite image of dark spot on Uranus observed on August 23, 2006. The elongated feature measures 1,100 miles by 1,900 miles (1,700 kilometers by 3,000 kilometers). This figure is from the website http://hubblesite.org/newscenter/archive/releases/2006/47	10
1.8	The bright companion clouds of Uranian Dark Spot. This photo is taken on 30 July 2006. It is from Hammel et al. 2009[38].	11
1.9	Data about the UDS (left) and its bright companion (right). This is from Hammel et al 2009[38].	12
1.10	Views of Uranus from Voyager II. In panel (A), the color balance was adjusted to simulate the view of human’s eyes. In panel (B), blue is from ultraviolet images, green is from violet and blue images, red is from green and orange images. This figure is from Smith et al. 1986[86].	17
1.11	Fitting parameters to the zonal wind profile on Neptune. This figure is from Sromovsky 1993[91] Table AI.	20
1.12	Observations of wind speed from Limaye and Sromovsky 1991[53] and Lindal et al. 1990[55], and fitted curves for Neptune. The points at the latitudes $\pm 60^\circ$ are from Lindal et al. 1990. The solid curve is a fourth-order fit, excluding the near polar point; the dashed curve is a sixth-order fit, including all the data. This figure is from Sromovsky 1993[91].	21
1.13	Observations of drift rate from Limaye and Sromovsky 1991[53] and Lindal et al. 1990[55], and fitted curves for Neptune. The points and the solid curve are same as Figure 1.12. The dashed curve is the fit to long-term GDS and DS2 motions, for comparison. This figure is from Sromovsky 1993[91].	22

1.14	Voyager II Measured rotation periods, corresponding zonal velocities and fitted curves for the southern hemisphere of Uranus. The points connected by the solid curve are about the rotation period; the points connected by the dashed curve are about corresponding zonal velocities, relative to the 17.24-hour rotation period of the magnetic field. This figure is from Smith et al. 1986[86].	23
1.15	HST observational results of 10 Uranian clouds in 1997. This table is from Karkoschka 1998[42].	24
1.16	Observational results (70 points) from Keck imaging and three zonal wind profiles. These observations were done in August 2003 and July and August 2004. The solid line is the symmetric fitted curve Smith 1986; the dashed line is the asymmetric fitted curve Karkoschka 1998; the dash-dot line is the asymmetric fitted curve Sromovsky 2005. This figure is from Sromovsky 2005[95].	25
1.17	Horizontal Discretization of EPIC - distribution of u, v, h and q in the staggered C-grid. This figure is from Dowling et al. 1998.	37
1.18	Vertical Discretization of EPIC. This figure is from Dowling et al. 1998.	38
1.19	C-grid geometry at the north pole in EPIC model. $\pi r_{large}^2 = 2 \times \pi r_{small}^2$; $r_{small} = \frac{1}{2}R \Delta \lambda + \sqrt{\frac{1}{2}R \Delta \lambda} \approx 1.21R \Delta \lambda$. This figure is from Dowling et al. 1998.	39
2.1	Left: Zonal wind profiles used in the Neptune study. Middle: Corresponding absolute-vorticity profiles. Right: Corresponding relative-vorticity profiles. Default $Q_y = 0$, default $\lambda_0 = -24^\circ$, if not mentioned. The wind profiles for the northern hemisphere are symmetric to the southern ones. This figure is from LeBeau and Deng 2007[47].	45

2.2	Left: Zonal wind profiles used in the Uranus study. Right: Corresponding absolute-vorticity profiles. "Smith (1986)" is a symmetric profile, while the other two are asymmetric. The equations for these profiles are from Sromovsky 2005[95].	48
2.3	Left: Constructed zonal wind profiles used in the Uranus study, from the equator to 70°N. Observational data points [35][95] and Sromovsky and Fry 2005 profile are plotted to compare. Right: Corresponding absolute-vorticity profiles.	49
2.4	Left: Constructed zonal wind profiles used in the Uranus study, from 10°N to 40°N. In the modified region, averaged data points are calculated from the observational results[35][95]. Right: Corresponding absolute-vorticity profiles.	50
2.5	Left: Vertical P-T profiles for Neptune, $N^2 = 0.64 \times 10^{-4} s^{-2}$ profile is the one used in the current simulations. Right: Corresponding N^2 values in EPIC for different layers. Here 10-layer setup and 13-layer setup are shown on the right plot.	52
2.6	Left: Vertical P-T profiles for Uranus, $N^2 = 0.09 \times 10^{-4} s^{-2}$ profile is the one used in the current simulations. Right: Corresponding N^2 values in EPIC for different layers.	53
2.7	The three vortex shapes used in the simulations. The one from LeBeau and Dowling 1998 [45] is called L&D; the Gaussian one is from Stratman et al. 2001[98]; the last one is calculated from stream functions. These figures are from LeBeau and Deng[46].	56
2.8	The vortex velocity distributions from the three vortex generation methods. The one from LeBeau and Dowling 1998 [45] is called L&D; the Gaussian one is from Stratman et al. 2001[98]; the last one is calculated from stream function. These figures are from LeBeau and Deng[46].	57

3.1	Sromovsky et al. 1993 fitted zonal wind profile and three constructed zonal wind profiles, comparing with the full set of cloud tracking data for Neptune. The $Q_y = 1$ curve is the fitted curve using the Limaye and Sromovsky 1991 data[53] (crosses) and the Lindal et al. 1990 data[55] (points). Lighter squares are pre-Voyager ground-based observations; darker squares are Voyager cloud-tracking data from Hammel et al. 1989[29]; circles and diamonds are post-Voyager HST observations from Hammel et al. 1995[32], Sromovsky et al. 1996[93], and Hammel and Lockwood 1997[33]. The lighter dashed line is the GDS-DS2 fit of Sromovsky et al. 1993[91]. Constructed profiles staying in the error range of the observational data points show that a range of possible change on the profile is permitted. This figure is from LeBeau and Dowling 1998[45].	65
3.2	Fitted ($Q_y = 1$ (fit)) and constructed ($Q_y = 0$, $Q_y = 1/6$, $Q_y = 1/3$, $Q_y = 2/3$ and $Q_y = 1$ (exact)) Neptune's zonal wind profiles. Left plot shows the zonal wind profiles in the southern hemisphere; right plot shows the absolute vorticity profiles corresponding to these zonal wind profiles.	70
3.3	Drift curves of simulation results with different zonal wind profiles for LeBeau_Dowling spots. Other parameters used here are: reference strength 1, reference size 1, initial AR 1.5, and starting latitude S32°.	71
3.4	Drift curves of simulation results with different zonal wind profiles for Gaussian Spots at different altitudes. These cases all start from 26°S at 200 mbar, 500 mbar or 1000 mbar. The initial maximum velocity of these cases is 50 m/s.	72
3.5	Oscillation and tail formation of GDS with $Q_y = 0$, reference size 1, reference strength 1 and starting latitude 28°. Solid curve is the ellipse fit. This plot is on layer 7 (868 mbar).	73

3.6	Oscillations of GDS at different layers with $Q_y = 0$, reference size 1, reference strength 1 and starting latitude 28° . Dotted contour is in layer 7 (868 mbar); solid contour is in layer 8 (1636 mbar); dashed contour is in layer 9 (3044 mbar).	74
3.7	Oscillation and tail formation of GDS with $Q_y = 0.214$, reference size 1, reference strength 0.7 and starting latitude 32° . Solid curve is the ellipse fit. This plot is on layer 7 (868 mbar).	75
3.8	Oscillations of GDS at different layers with $Q_y = 0.214$, reference size 1, reference strength 0.7 and starting latitude 32° . Dotted contour is in layer 7 (868 mbar); solid contour is in layer 8 (1636 mbar); dashed contour is in layer 9 (3044 mbar).	76
3.9	Oscillations of simulated GDS starting with different parameters. The top subplot is for the inverse aspect ratio (b/a); the middle one is for the orientation angle (radians); the bottom subplot shows the power spectrum calculated from the orientation angle oscillation data. The S26 and S28 cases are in $Q_y = 0$ background zonal wind profile and with reference strength 1, reference size 1 and initial AR 1.5. The S31 case is in $Q_y = 0.214$ profile and with reference strength 0.5. The S32 case is in $Q_y = 0.286$ profile and with reference strength 0.7.	77
3.10	Phase plot for six LeBeau-Dowling vortices, having different initial conditions, starting from different latitudes and in the constructed zonal wind profiles with different Q_y . Top left plot is from Voyager-II observational results of GDS-89; top right plot is from Kida theory; others are as the parameters shown on them. All these cases are in quarter globe domain and the initial aspect ratios of the spots are all 1.5.	78

3.11	Simulation to NGDS-32, comparing with the symmetric case in the southern hemisphere. Basic parameters are: $Q_y = 0$, reference strength 1, reference size 1, initial AR 1.5 and starting latitude 32°	79
3.12	Comparison of simulations with different simulation domains. Simulation parameters are: $Q_y = 0$, reference strength 1, reference size 1, initial AR 1.5, starting latitude $S28^\circ$. The top subplot is the drift curves; the middle subplot is the oscillation of the orientation angle (notice here the quarter globe case is shifted $+0.2$ radians and the longitudinal half globe case is shifted -0.2 radians, for clarity); the bottom subplot is the oscillation of the inverse aspect ratio (b/a).	82
3.13	The contour plots of the whole globe simulation with $Q_y = 0$, reference strength 1, reference size 1 and initial AR 1.5. The top plot is from 71.2 days to 80.1 days; the bottom plot is from 182 days to 191 days. The contour plot of potential vorticity is on layer 7 (867.9 mbar).	83
3.14	Drift rate of great dark spot in the zonal wind profiles with different Q_y : 0, $1/12$, $1/6$, $1/3$, and $2/3$ with reference latitude $24^\circ S$. Except Q_y , all other parameters are default: starting from $28^\circ S$, relative strength 1, relative size 1, and layer 5 to 9.	85
3.15	Drift rate (top panel), oscillation of inverse aspect ratio (middle panel) and oscillation of orientation angle (bottom panel) of great dark spot with different initial spot size. Except relative spot size, all these spots have the default parameters: starting from $28^\circ S$; relative strength 1; layer 5 to 9; $Q_y = 0$ with reference latitude $24^\circ S$. All plots start from 30 days, after the initial adjustment. In the "Relative size = 0.6" case, when the spot passes 23° (~ 100 days), the spot becomes not regular so that the inverse aspect ratio and the orientation angle are not defined well.	86

3.16	Oscillation and tail formation of GDS with $Q_y = 0$, relative size 0.5, relative strength 1 and starting latitude 28°S. Solid curve is the ellipse fit. The contour plot of potential vorticity is on layer 7 (867.9 mbar). The levels for the contour are 0.2, 0.6 and 0.8 times of the peak value of the potential vorticity.	87
3.17	Drift rate (top panel), oscillation of inverse aspect ratio (middle panel) and oscillation of orientation angle (bottom panel) of great dark spot with different initial spot strength. Except relative spot strength, all these spots have the default parameters: starting from 28°S; relative size 1; layer 5 to 9; $Q_y = 0$ with reference latitude 24°S. All plots start from 30 days, after the initial adjustment.	88
3.18	Drift rate (top panel), oscillation of inverse aspect ratio (middle panel) and oscillation of orientation angle (bottom panel) of great dark spot with different initial spot strength. The relative size for these cases are all 0.8. Except relative size and relative spot strength, all these spots have the default parameters: starting from 28°S, layer 5 to 9, and $Q_y = 0$ with reference latitude 24°S. All plots start from 30 days, after the initial adjustment.	89
3.19	Drift rate (top panel), oscillation of inverse aspect ratio (middle panel) and oscillation of orientation angle (bottom panel) of great dark spot with different P-T profiles. The $N^2 = 0.64 \times 10^{-4} s^{-2}$ and $N^2 = 0.36 \times 10^{-4} s^{-2}$ cases are constructed P-T profiles with constant Brunt-Väisälä frequency. The nominal one is from Conrath 1991[13]. Except the P-T profile, all these spots have the default parameters: relative size 1, relative strength 1, starting from 28°S; layer 5 to 9; $Q_y = 0$ with reference latitude 24°S. All plots start from 0 days to show the effect of the P-T profile from the beginning.	91

3.20	The structure scheme used to modify the vertical shear. Above p_1 , $m_1 = 0.0$ case (gray) and $m_1 = 0.2$ case (solid) are shown here. Below P_1 , different m_2 cases are shown. $P_0 = 500$ mbar is the level where $u_v(P_0) = 1$. This figure is from García-Melendo et al. 2007[25].	92
3.21	Drift rate (top panel), oscillation of inverse aspect ratio (middle panel) and oscillation of orientation angle (bottom panel) of great dark spot with different vertical shear. These cases include $m_2 = 0, 0.1$ and -0.1 . Except the vertical shear, all these spots have the default parameters: relative size 1, relative strength 1, starting from 28°S , layer 5 to 9, and $Q_y = 0$ with reference latitude 24°S . These plots start from 0, because the sheared winds cannot sustain the spots for a long enough time.	93
3.22	Drift rate (top panel), oscillation of inverse aspect ratio (middle panel) and oscillation of orientation angle (bottom panel) of great dark spot with different vertical shear. These cases include $m_2 = 0, 0.01$ and -0.01 . Except the vertical shear, all these spots have the default parameters: relative size 1, relative strength 1, starting from 28°S , layer 5 to 9, and $Q_y = 0$ with reference latitude 24°S	94
3.23	Drift rate (top panel), oscillation of inverse aspect ratio (middle panel) and oscillation of orientation angle (bottom panel) of great dark spot with different vertical shear. These cases include $m_2 = 0, 0.03$ and -0.03 . Except the vertical shear, all these spots have the default parameters: relative size 1, relative strength 1, starting from 28°S , main layer 7, and $Q_y = 0$ with reference latitude 24°S	95

3.24	Drift rate (top panel), oscillation of inverse aspect ratio (middle panel) and oscillation of orientation angle (bottom panel) of great dark spot with different initial aspect ratios. The initial aspect ratios are 1.5, 1.2 and 1.0, respectively. In each figure, except the initial aspect ratio, all these spots have the default parameters: relative size 1, relative strength 1, layer 5 to 9, starting from 28°N, and $Q_y = 0$	96
3.25	Drift rate (top panel), oscillation of inverse aspect ratio (middle panel) and oscillation of orientation angle (bottom panel) of great dark spot with different central spot layers. In these cases, the spots are at layer 6, 7 and 8, respectively. In each figure, except the spot layer, all these spots have the default parameters: relative size 1, relative strength 1, AR 1.5, starting from 28°N, and $Q_y = 0$	97
3.26	Zonal wind profiles (left panel) and their corresponding absolute vorticity profiles (middle panel) and relative vorticity profiles (right panel) for different reference latitude. All the constructed profiles are $Q_y = 0$ ones so that their absolute vorticities are all constant above $\sim 45^\circ\text{S}$. When the reference latitude is closer to the equator, the constant absolute vorticity is higher and the crossing-zero point of the relative vorticity profile is closer to the equator.	98
3.27	Drift rate (top panel), oscillation of inverse aspect ratio (middle panel) and oscillation of orientation angle (bottom panel) of great dark spot in the zonal wind profiles with different reference latitude. These cases include reference latitude = 24°S (default), 21°S, 20°S, 19°S, 18°S and 16°S. Except the reference latitude, all these spots have the default parameters: relative size 1, relative strength 1, starting from 28°S, layer 5 to 9 and $Q_y = 0$	99

- 3.28 Drift rate (top panel), oscillation of inverse aspect ratio (middle panel) and oscillation of orientation angle (bottom panel) of great dark spot starting from different latitudes. The top figure is in the constructed zonal wind profile with reference latitude 24°S and the spots start from 28°S, 26°S and 24°S, respectively. The lower one is in the constructed zonal wind profile with reference latitude 21°S and the spots also start from 28°S, 26°S and 24°S, respectively. In each figure, except the starting latitude, all these spots have the default parameters: relative size 1, relative strength 1, layer 5 to 9, and $Q_y = 0$ 101
- 3.29 Drift rate (top panel), oscillation of inverse aspect ratio (middle panel) and oscillation of orientation angle (bottom panel) of great dark spot starting from different latitudes. The top figure is in the constructed zonal wind profile with reference latitude 19°S and the spots start from 28°S, 26°S and 24°S, respectively. The lower one is in the constructed zonal wind profile with reference latitude 17°S and the spots also start from 28°S, 24°S and 22°S, respectively. In each figure, except the starting latitude, all these spots have the default parameters: relative size 1, relative strength 1, layer 5 to 9, and $Q_y = 0$ 102
- 3.30 Drift rate (top panel), oscillation of inverse aspect ratio (middle panel) and oscillation of orientation angle (bottom panel) of great dark spot starting from different latitudes. This plot is in the constructed zonal wind profile with reference latitude 24°S and the spots also start from 28°S, 30°S and 32°S, respectively. Except the starting latitude, all these spots have the default parameters: relative size 1, relative strength 1, layer 5 to 9, and $Q_y = 1/12$. Starting time is from 0 so that we can see the evolution of the 28°S case and 30°S case more clearly. 103

3.31	Zonal wind profiles (left panel) and their corresponding absolute vorticity profiles (middle panel) and relative vorticity profiles (right panel) for different reference latitudes and different transition methods. The bottom figure shows the detail plots from the equator to 30°S of the top figure.	105
3.32	Zonal wind profiles (left panel) and their corresponding absolute vorticity profiles (middle panel) and relative vorticity profiles (right panel) for $Q_y = 1/12$, reference latitude 18°S and transition between 5°S and the equator, with and without peak.	107
3.33	Drift rate (top panel), oscillation of inverse aspect ratio (middle panel) and oscillation of orientation angle (bottom panel) of great dark spot in different zonal wind profiles. In these cases, the spots are at layer 7, with relative size 0.8, relative strength 0.5 and initial aspect ratio 1.5, and start from 28°S. The zonal wind profiles all have reference latitude 18°S.	108
3.34	Drift rate (top panel), oscillation of inverse aspect ratio (middle panel) and oscillation of orientation angle (bottom panel) of great dark spots starting from different latitudes. In these cases, the spots are at layer 7, with relative size 0.8, relative strength 0.5 and initial aspect ratio 1.5. The zonal wind profile has a reference latitude 18°S and $Q_y = 1/12$ with peak near 45°S.	109
3.35	Drift rate (top panel), oscillation of inverse aspect ratio (middle panel) and oscillation of orientation angle (bottom panel) of great dark spots in different simulation domains. In these cases, the spots are at layer 7, with relative size 0.8, relative strength 0.5 and initial aspect ratio 1.5, and start from 28°S. The zonal wind profile has a reference latitude 18°S and $Q_y = 1/12$ with peak near 45°S.	110

3.36	Drift rate (top panel), oscillation of inverse aspect ratio (middle panel) and oscillation of orientation angle (bottom panel) of great dark spots with different initial aspect ratios. In these cases, the spots are at layer 7, with relative size 0.8, relative strength 0.5 and initial aspect ratio 1.5, and start from 28°S. The zonal wind profile has a reference latitude 18°S and $Q_y = 1/12$ with peak near 45°S.	111
3.37	Drift rate (top panel), oscillation of inverse aspect ratio (middle panel) and oscillation of orientation angle (bottom panel) of great dark spots at different layers. In these cases, the spots are at layer 8, 7 and 6, respectively. Other parameters are: relative size 0.8, relative strength 0.5 and initial aspect ratio 1.5. All these spots start from 28°S. The zonal wind profile has a reference latitude 18°S and $Q_y = 1/12$ with peak near 45°S.	112
3.38	Drift rate (top panel), oscillation of inverse aspect ratio (middle panel) and oscillation of orientation angle (bottom panel) of great dark spots with different P-T profiles. In these cases, the spots are at layer 7 with relative size 0.8, relative strength 0.5 and initial aspect ratio 1.5. All these spots start from 28°S. The zonal wind profile has a reference latitude 18°S and $Q_y = 1/12$ with peak near 45°S.	113
3.39	Drift rate (top panel), oscillation of inverse aspect ratio (middle panel) and oscillation of orientation angle (bottom panel) of great dark spots with different initial relative strength. In these cases, the spots are at layer 7 with relative size 0.8 and initial aspect ratio 1.5. All these spots start from 28°S. The zonal wind profile has a reference latitude 18°S and $Q_y = 1/12$ with peak near 45°S.	114

3.40	Zonal wind profiles (left panel) and their corresponding absolute vorticity profiles (middle panel) and relative vorticity profiles (right panel) for different Q_y with transition on both ends. The constant Q_y region is 28°S to 38°S.	115
3.41	Drift rate (top panel), oscillation of inverse aspect ratio (middle panel) and oscillation of orientation angle (bottom panel) of great dark spots with different Q_y . In these cases, the spots are at layer 7 with relative size 0.8, relative strength 0.5 and initial aspect ratio 1.5. All these spots start from 29°S. The zonal wind profile has a reference latitude 24°S.	116
3.42	Drift rate (top panel), oscillation of inverse aspect ratio (middle panel) and oscillation of orientation angle (bottom panel) of great dark spots with different Q_y . In these cases, the spots are at layer 8 with relative size 0.8, relative strength 0.5 and initial aspect ratio 1.5. All these spots start from 29°S. The zonal wind profile has a reference latitude 24°S.	117
3.43	Oscillations of three simulation cases. The top panel shows oscillation of inverse aspect ratio, the middle panel shows oscillation of orientation angle and the bottom panel shows the power spectrum calculating from the angle oscillations. In the middle panel, the dotted line is shifted 0.2 above and the dashed line is shifted 0.2 below to make their curves clearer in the plot. R24 means reference latitude 24°S and R18 means reference latitude 18°S. The three numbers separated by slash are initial relative size/relative strength/aspect ratio. The notation trans1 means transition from 5°S to the equator; the notation trans2 means transition from 28°S to the equator and 38°S to 66°S. The notation "peak" means there is a small jump on the constructed zonal wind profile near 45°S. The last numbers are starting latitudes.	118

- 3.44 The contour plots of the whole globe simulation with $Q_y = 1/12$, reference latitude 18°S , relative size 0.8, relative strength 0.5 and initial AR 1.5. The zonal wind profile transit from 5°S to the equator and has a peak near 45°S . The spot is generated at main layer 8 and starts from 28°S . The top plot is from 23.7 days to 32.6 days; the bottom plot is from 84.8 days to 93.7 days. The contour plot of potential vorticity is on layer 8 (1636 mbar).120
- 3.45 The contour plots of the whole globe simulation with $Q_y = 0$ between 28°S and 38° , reference latitude 24°S , relative size 0.8, relative strength 0.5 and initial AR 1.5. The zonal wind profile transit smoothly to both the equator and the high latitudes. The spot is generated at main layer 8 and starts from 29°S . The contour plot of potential vorticity is on layer 8 (1636 mbar). 121
- 3.46 Oscillations of three simulation cases with different initial aspect ratio. The top panel shows oscillation of inverse aspect ratio, the middle panel shows oscillation of orientation angle and the bottom panel shows the power spectrum calculating from the angle oscillations. In the middle panel, the dotted line is shifted 0.2 above and the dashed line is shifted 0.2 below to make their curves clearer in the plot. R24 means reference latitude 24°S . The three numbers separated by slash are initial relative size/relative strength/aspect ratio. The last numbers are starting latitudes.122
- 3.47 Oscillations of nine simulation cases. The top panel and the middle panel show the effects of simulation domain. The character "Q" means quarter globe; "H" means southern hemisphere; "P" means pole to pole half globe. The bottom panel shows the effect of different layer and the effect of modifying a constructed zonal wind profile with method 2. The notation "trans1" and "trans2" mean transition method 1 and transition method 2 as discussed above. 123

3.48 Phase plot for six LeBeau_Dowling vortices, having different initial conditions, starting from different latitudes and in different constructed zonal wind profiles. Top left plot is from Voyager-II observational results of GDS-89; top right plot is from Kida theory; others are as the parameters shown on them. All these cases are in whole globe domain. The explanation of the parameters used here are same as Figure 3.43. 126

4.1 Uranus vorticity-model input parameters. (a) Vertical temperature-pressure profiles are shown for Uranus. The $N^2 = 0.09 \times 10^{-4} s^{-2}$ profile corresponds to that used in the current simulations: the Lindal et al. (1987) profile above 630 mbars, and the constant N^2 profile below 630 mbars. (b) The values for the square of the Brunt-Väisälä (buoyancy) frequency N - computed with EPIC for the two profiles in panel (a) - are overlaid by the locations of the layer boundaries (dashed lines) in the simulation grid. The triangles represent the the location of the layer midpoints for the constant N^2 profile. 133

4.2 Uranus zonal wind profiles and initial constructed profiles. (a) We show zonal wind profiles, including fitted and constructed profiles, compared with the cloud-tracking data (open symbols) from Hammel et al. 2005[35] and Sromovsky and Fry 2005[95]. (b) This panel shows the correlating profiles in absolute vorticity based on the profiles in the left panel. 135

4.3	Coarse-grid sensitivity of vortex lifetime to zonal wind profiles. For these simulations, a 70 m/s vortex was initially placed in five different zonal wind profiles using a whole-globe domain. The number indicates the initial latitude of the vortex, all of which are between 28°N and 31°N. The dimensions of each frame are 47° by 30°. The vortices placed in the profiles of Karkoschka 1998[42] and Smith et al. 1986[86] are clearly shearing by 20 days. The Sromovsky and Fry 2005[95] vortices remain more compact, while the $Q_y = 0$ vortex evidences the least amount of shearing.	137
4.4	Longitudinal size change with time for different fit zonal wind profiles and $Q_y = 0$ constructed zonal wind profile. These four cases all drift roughly to the same latitude, 28°N, although they start from different initial latitudes.	138
4.5	Sensitivity of vortex lifetime to maximum vortex wind velocity. We examined the evolution of different strength vortices initially placed at 28°N in the profile of Sromovsky and Fry 2005. This plot presents the evolution of the vortex major axis measured in degrees of longitude with the time to a 20° length being defined as the vortex lifespan. There are considerable gains in lifespan from 30 m/s to 90 m/s, but after this the increases in lifespan are muted.	139
4.6	Sensitivity of vortex drift rate to maximum vortex wind velocity. This plot has the same cases as Figure 4.5. Similar results can be achieved as Figure 4.5: from 30 m/s to 90 m/s, drift rate increases significantly; after 90 m/s, the change in drift rate is muted.	140
4.7	Contour plot of the simulated UDS in the Sromovsky zonal wind profile with different initial maximum wind velocities. These simulations all start from 28°N. The same runs are plotted in Figure 4.6 about their lifetime.	141

4.8	Drift of Uranian Dark Spot. Two groups of cases are shown in this figure. One is about those cases drift to 28° with different zonal wind profiles; another is about those cases drift from 28° . All these spots have a 70 m/s initial maximum velocity.	142
4.9	Longitudinal size change of spot vs. initial latitude of spot center, with Sromovsky and Fry 2005 zonal wind profile and maximum wind velocity 70 m/s.	144
4.10	Drift of spot vs. initial latitude of spot center, with Sromovsky and Fry 2005 zonal wind profile and maximum wind velocity 70 m/s.	145
4.11	Sensitivity of vortex lifetime to zonal wind profiles in the finer grid. For these simulations, a 70 m/s vortex was initially placed in five different zonal wind profiles using a whole-globe domain. To compare with the coarse grid simulations, in these finer grid simulations, the starting latitudes of the vortices are same as the cases shown in Figure 4.3.	147
4.12	Sensitivity of vortex lifetime to zonal wind profiles in the finer grid. This plot is similar to Figure 4.11, just starting from different latitudes. The first four simulation cases all drift to 28°N , comparing with the last case, which starts from 28°N	148
4.13	Contour plots of the simulated UDS on $Q_y = 0$ constructed zonal wind profile. In this simulation, a vortex with initial maximum velocity 70 m/s was placed in a whole-globe domain, starting from 28°N . The upper panel is for the whole life of the simulation; the lower panel is about the last stage of the simulation to show the effect of the vortex on the boundary of the $Q_y = 0$ area. The scale of the plot in the lower panel is doubled than that of the upper panel to show a wider area. The numbers in the subplots are the times of the simulations, in unit days.	149

4.14	Finer-grid drift of spots with different zonal wind profiles, initial latitudes and layers. p is the pressure of the central vortex layer, so $p1000$ is 1000 mbar pressure and $p4000$ is 4000 mbar pressure.	150
4.15	Longitudinal size change of spots in finer grid with different zonal wind profiles, initial latitudes and layers.	151
4.16	Upper panel: sensitivity of vortex lifetime to maximum vortex wind velocity. Lower panel: sensitivity of vortex drift rate to maximum vortex wind velocity. These plots are about finer grid simulations. We examined the evolution of different strength vortices initially placed at 29.8°N in the profile of Sromovsky and Fry 2005. This plot presents the evolution of the vortex major axis measured in degrees of longitude with the time to a 10° length being defined as the vortex lifespan. There were considerable gains in lifespan from 30 m/s to 90 m/s, but after this the increases in lifespan are muted. The lifespan of the 110 m/s case is even shorter than that of the 90 m/s case. After 50 days, the 90 m/s case and the 110 m/s case show fluctuations with ~ 3 days periods.	152
4.17	Contour plot of the simulated UDS on Sromovsky zonal wind profile with different initial maximum wind velocity. This plot is about finer grid simulations. These simulations all start from 29.8°N	153
4.18	Contour plot of the simulated UDS on Sromovsky zonal wind profile with initial maximum wind velocity 90 m/s and 110 m/s. This plot is about finer grid simulations. These simulations all start from 29.8°N . The final stages of these two simulations are shown. We can see the fluctuations near the end of their lives (10° longitudinal extent). The numbers in the subplots are the times of the simulations, in unit days.	157

4.19	Change of longitudinal size vs. initial latitude of spot center. The zonal wind profile is Sromovsky and Fry 2005 and the maximum wind velocity is 70 m/s.	158
4.20	Drift of spot vs. initial latitude of spot center. The zonal wind profile is Sromovsky and Fry 2005 and the maximum wind velocity is 70 m/s. . . .	158
5.1	The scheme of the two-flux method used in this project.	164
5.2	H ₂ -H ₂ absorption calculated using the formalism of Bachet <i>et al.</i> 1983[4], from Weisstein 1996[104].	169
5.3	H ₂ -He absorption calculated using the formalism of Cohen <i>et al.</i> 1982[11], from Weisstein 1996[104].	169
5.4	H ₂ -CH ₄ absorption calculated using the formalism of Orton <i>et al.</i> 1983[73], from Weisstein 1996[104].	170
5.5	CH ₄ absorption around 6190Å at 290 and 100 K. This figure is from Lunine 1993[58].	171
5.6	Table of the absorption coefficients for CH ₄ around 6190Å between 100 and 290K. This figure is from Lunine 1993[58].	172
5.7	Evolution of the zonal wind profile starting from Smith 1986 symmetric fitting profile. This figure is about the one-band test case with absorption coefficient $0.01 \text{ m}^{-1}(\text{kg}/\text{m}^3)^{-1}$	176
5.8	Comparison of simulation result with observational results. The upper panel compares the results to the Karkoschka observational result in 1997 and fitted curve in 1998[42]. The dashed straight lines are at the latitudes of observations. The lower panel compares the results to the observational (2003) points and fitted profile by Sromovsky and Fry in 2005[95].	177

5.9	Comparison of the simulated zonal wind profiles in layer 5, layer 6 and layer 7 in 1997 (upper panel) and 2003 (lower panel). This figure is about the two-band simulation case with absorption coefficients in solar radiation waveband $(\alpha/\rho)_{CH_4} = 6.0 \times 10^{-4} \text{m}^{-1} \text{am}^{-1}$, and in infrared waveband $(\alpha/\rho^2)_{H_2-H_2} = 4.0 \times 10^{-5} \text{m}^{-1} \text{am}^{-1}$, $(\alpha/\rho^2)_{H_2-He} = 5.0 \times 10^{-5} \text{m}^{-1} \text{am}^{-1}$ and $(\alpha/\rho^2)_{H_2-CH_4} = 3.0 \times 10^{-3} \text{m}^{-1} \text{am}^{-1}$. The layer setup is the one in Table 5.2 and the initial methane relative humidity is 0.6.	183
5.10	Evolution of the zonal wind profile starting from Smith 1986 symmetric fitted profile. This figure is about the two-band simulation case with absorption coefficients in solar radiation waveband $(\alpha/\rho)_{CH_4} = 6.0 \times 10^{-4} \text{m}^{-1} \text{am}^{-1}$, and in infrared waveband $(\alpha/\rho^2)_{H_2-H_2} = 4.0 \times 10^{-5} \text{m}^{-1} \text{am}^{-1}$, $(\alpha/\rho^2)_{H_2-He} = 5.0 \times 10^{-5} \text{m}^{-1} \text{am}^{-1}$ and $(\alpha/\rho^2)_{H_2-CH_4} = 3.0 \times 10^{-3} \text{m}^{-1} \text{am}^{-1}$. The layer setup is the one in Table 5.2 and the initial methane relative humidity is 0.6.	185
5.11	Comparison of simulation result with observational results. The upper panel compares the results to the Karkoschka observational result in 1997 and fitted curve in 1998[42]. The dashed straight lines are at the latitudes of observations. The lower panel compares the results to the observational (2003) points and fitted profile by Sromovsky and Fry in 2005[95]. This figure is about the same case as in Figure 5.10.	186
5.12	Evolution of the zonal wind profile starting from Smith 1986 symmetric fitted profile. This figure is about the two-band simulation case with absorption coefficients in solar radiation waveband $(\alpha/\rho)_{CH_4} = 6.0 \times 10^{-4} \text{m}^{-1} \text{am}^{-1}$, and in infrared waveband $(\alpha/\rho^2)_{H_2-H_2} = 4.0 \times 10^{-5} \text{m}^{-1} \text{am}^{-1}$, $(\alpha/\rho^2)_{H_2-He} = 5.0 \times 10^{-5} \text{m}^{-1} \text{am}^{-1}$ and $(\alpha/\rho^2)_{H_2-CH_4} = 3.0 \times 10^{-3} \text{m}^{-1} \text{am}^{-1}$. The layer setup is the one in Table 5.2 and the initial methane relative humidity is 0.8.	187

5.13	Comparison of simulation result with observational results. The upper panel compares the results to the Karkoschka observational result in 1997 and fitted curve in 1998[42]. The dashed straight lines are at the latitudes of observations. The lower panel compares the results to the observational (2003) points and fitted profile by Sromovsky and Fry in 2005[95]. This figure is about the same case as in Figure 5.12.	188
5.14	Evolution of the zonal wind profile starting from Smith 1986 symmetric fitted profile. This figure is about the two-band simulation case with absorption coefficients in solar radiation waveband $(\alpha/\rho)_{CH_4} = 4.0 \times 10^{-4} \text{m}^{-1} \text{am}^{-1}$, and in infrared waveband $(\alpha/\rho^2)_{H_2-H_2} = 4.0 \times 10^{-5} \text{m}^{-1} \text{am}^{-1}$, $(\alpha/\rho^2)_{H_2-He} = 5.0 \times 10^{-5} \text{m}^{-1} \text{am}^{-1}$ and $(\alpha/\rho^2)_{H_2-CH_4} = 3.0 \times 10^{-3} \text{m}^{-1} \text{am}^{-1}$. The layer setup is the one in Table 5.2 and the initial methane relative humidity is 0.6.	189
5.15	Comparison of simulation result with observational results. The upper panel compares the results to the Karkoschka observational result in 1997 and fitted curve in 1998[42]. The dashed straight lines are at the latitudes of observations. The lower panel compares the results to the observational (2003) points and fitted profile by Sromovsky and Fry in 2005[95]. This figure is about the same case as in Figure 5.14.	190
5.16	The S34 cloud feature (upper panel) and its oscillation (lower panel) plots from Sromovsky and Fry 2005[95].	191

5.17 Heat distribution in the simulation with radiation model on Uranus. Upper panel is at 5.56 days (1986), middle panel is at 1997 and the bottom panel is at 2003. This figure is about the two-band simulation case with absorption coefficients in solar radiation waveband $(\alpha/\rho)_{CH_4} = 6.0 \times 10^{-4} \text{m}^{-1} \text{am}^{-1}$, and in infrared waveband $(\alpha/\rho^2)_{H_2-H_2} = 4.0 \times 10^{-5} \text{m}^{-1} \text{am}^{-1}$, $(\alpha/\rho^2)_{H_2-He} = 5.0 \times 10^{-5} \text{m}^{-1} \text{am}^{-1}$ and $(\alpha/\rho^2)_{H_2-CH_4} = 3.0 \times 10^{-3} \text{m}^{-1} \text{am}^{-1}$. The layer setup is the one in Table 5.2 and the initial methane relative humidity is 0.6. 192

5.18 Uranus with Keck and VLA at different waveband and different time. The far left picture is taken in 2004 at H-band ($1.6\text{-}\mu\text{m}$); the other three are in 2005 at 0.7cm, 2005 at 1.3cm and 2003 at 2.0cm, respectively. This figure is from Hammel 2006[36]. 193

5.19 Temperature distribution of Uranian atmosphere at layer 6 (2088 mbars) from the simulation with radiation model. Upper panel is at 5.56 days (1986), middle panel is at 1997 and the bottom panel is at 2005. This figure is about the two-band simulation case with absorption coefficients in solar radiation waveband $(\alpha/\rho)_{CH_4} = 6.0 \times 10^{-4} \text{m}^{-1} \text{am}^{-1}$, and in infrared waveband $(\alpha/\rho^2)_{H_2-H_2} = 4.0 \times 10^{-5} \text{m}^{-1} \text{am}^{-1}$, $(\alpha/\rho^2)_{H_2-He} = 5.0 \times 10^{-5} \text{m}^{-1} \text{am}^{-1}$ and $(\alpha/\rho^2)_{H_2-CH_4} = 3.0 \times 10^{-3} \text{m}^{-1} \text{am}^{-1}$. The layer setup is the one in Table 5.2 and the initial methane relative humidity is 0.6. 193

5.20	Convection in the simulation case with radiation model on Uranus in 1997. The upper panel shows the contour plot of vertical velocity in the unit K (potential temperature). The bottom panel shows the convection velocities. This figure is about the two-band simulation case with absorption coefficients in solar radiation waveband $(\alpha/\rho)_{CH_4} = 6.0 \times 10^{-4} \text{m}^{-1} \text{am}^{-1}$, and in infrared waveband $(\alpha/\rho^2)_{H_2-H_2} = 4.0 \times 10^{-5} \text{m}^{-1} \text{am}^{-1}$, $(\alpha/\rho^2)_{H_2-He} = 5.0 \times 10^{-5} \text{m}^{-1} \text{am}^{-1}$ and $(\alpha/\rho^2)_{H_2-CH_4} = 3.0 \times 10^{-3} \text{m}^{-1} \text{am}^{-1}$. The layer setup is the one in Table 5.2 and the initial methane relative humidity is 0.6.	194
5.21	Convection in the simulation case with radiation model on Uranus in 2005. The upper panel shows the contour plot of vertical velocity in the unit K (potential temperature). The bottom panel shows the convection velocities. This figure is about the two-band simulation case with absorption coefficients in solar radiation waveband $(\alpha/\rho)_{CH_4} = 6.0 \times 10^{-4} \text{m}^{-1} \text{am}^{-1}$, and in infrared waveband $(\alpha/\rho^2)_{H_2-H_2} = 4.0 \times 10^{-5} \text{m}^{-1} \text{am}^{-1}$, $(\alpha/\rho^2)_{H_2-He} = 5.0 \times 10^{-5} \text{m}^{-1} \text{am}^{-1}$ and $(\alpha/\rho^2)_{H_2-CH_4} = 3.0 \times 10^{-3} \text{m}^{-1} \text{am}^{-1}$. The layer setup is the one in Table 5.2 and the initial methane relative humidity is 0.6.	195
6.1	Observed bright companions to Neptune's Great Dark Spots. The left four panels are NGDS32 and its bright companion in 1994 and 1996. The rightmost panel is about GDS-89 and its bright companion, inverted across the equator, for comparison. This figure is from Stratman et al. 2001[98].	197
6.2	Stratman's simulated bright companions to great dark spots. C, D, E, F are cases with different vortex heights at different vortex center layers. This figure is from Stratman et al. 2001[98].	198

6.3 The scheme of the five phases and related eleven phase-change processes in the EPIC microphysics model. The processes are: P_{COND} : condensation of vapor to cloud liquid and evaporation of liquid cloud, P_{INIT} : initiation of ice crystals, P_{DEPI} : deposition of vapor onto ice crystals and sublimation of cloud ice to vapor, P_{SMITI} : melting of cloud ice to form cloud liquid, P_{RACW} : collection of cloud liquid droplets by rain, P_{RAUT} : auto-conversion of cloud liquid droplets to rain, P_{REVP} : evaporation of rain, P_{SEVP} : sublimation and depositional growth of snow, P_{SMITS} : melting of snow to form rain, P_{SACI} : collection of cloud ice crystals by snow, and P_{SAUT} : autoconversion of cloud ice crystals to snow. This figure and its explanation are from Palotai and Dowling 2008[75]. 199

6.4 Three zonal wind profiles on Neptune. The left panel shows the zonal wind profile; the middle panel shows the related absolute vorticity, and the right one shows the relative vorticity. The solid curve is the fitted zonal wind profile from Sromovsky et al. 1993[91]. The dashed curve is the artificial $Q_y = 0$ case, which has a constant absolute vorticity from 0° to 48°S in the middle panel. The dash dotted curve is the artificial zonal wind profile used in this work. It has near constant absolute vorticity $Q_y = 1/12$ from 28°S to 38°S , with reference latitude 24°S . At the southern end, it merges smoothly to the $Q_y = 0$ case; at the northern end, it merges smoothly to the equator. The zonal wind profile has zero potential vorticity at the equator and the poles. 203

6.5	Simulated great dark spot and the cloud features around it, with initial relative humidity 80%. Spot is at layer 7 and the cloud is at layer 5. The dotted, dashed and dash-dotted curves near the center are the contour plots of the potential vorticity. The solid ellipse curve is the fitting ellipse to the contour shape, which is used to calculate the aspect ratio and the orientation angle. The orange dash-dotted curves around are the methane relative humidity contour at saturation level - 1.0.	205
6.6	Simulated great dark spot and the cloud features around it, with initial relative humidity 60%. Spot is at layer 7 and the cloud is at layer 5. The meaning of the curves is same as that in Figure 6.5.	206
6.7	Simulated great dark spot and the cloud features around it, with initial relative humidity 60%. Spot is at layer 8 and the cloud is at layer 5. The meaning of the curves is same as that in Figure 6.5.	207
6.8	Evolution of the methane cloud near a great vortex. This plot shows the contour of the relative humidity. The solid curve is the cloud boundary - relative humidity ≥ 1 . After initial adjustment, a stable cloud is formed on the south top of the great dark spot. This plot is from 0.28 days to 79.44 days.	208
6.9	Drifts of great dark spots with time. To compare more clearly, the dashed line is shifted 2° downwards; the dash-dot line is shifted 4° downwards; the dash-dot-dot-dot line is shifted 6° downwards.	209
6.10	Oscillation of inverse aspect ratio (upper panel) and orientation angle (lower panel) of the fitting ellipse to the great dark spot, with or without cloud model, in the deeper layer - layer 8.	210
6.11	Oscillation of inverse aspect ratio (upper panel) and orientation angle (lower panel) of the fitting ellipse to the great dark spot, with or without cloud model, in the upper layer - layer 7.	210

6.12	Comparison of the pressure changes. The two cases included here are the deeper spot cases with or without cloud. This comparison is at the time 48 days and 14.7 hours. These curves show the pressures at the latitude of the centers of the great dark spots. The solid curves are about the cases with the cloud model; the dotted curves are about the cases without the cloud model. Pressures in layer 5 (upper), layer 6 (middle) and layer 7 (lower) are shown here.	212
6.13	Comparison of the conservation of potential vorticity. The two cases included here are the deeper spot cases with or without cloud.	214
6.14	Comparison of the conservation of potential vorticity. The two cases included here are the upper spot cases with or without cloud.	214
6.15	Formation of cloud above the simulated UDS. The dark curves are the contours of potential vorticity of the simulated UDS at layer 7 (868 mbar). The grey solid curves are the contours of methane relative humidity at layer 5 (247 mbar). The horizontal axis is longitude (deg) and the vertical axis is latitude (deg). The numbers in each subplot is the time in unit days.	215
6.16	Comparison of longitudinal size change of spots in finer grid with and without cloud. These two cases are all in Sromovsky and Fry 2005 fit zonal wind profile and start from 32°N. Other parameters are same as those standard parameters of finer grid simulation cases in Chapter 4. . .	217
6.17	Comparison of drift rate in finer grid with and without cloud. These two cases are same as those in Figure 6.16.	217
6.18	Contour plot of the simulated UDS on Sromovsky and Fry 2005 fit zonal wind profile with (upper panel) and without (lower panel) cloud model. These two cases are same as those in Figure 6.16. The numbers in the subplots are the times of the simulations, in unit days.	218

Chapter 1 Introduction

In recent years, together with the development of high performance computers and algorithms, Computational Fluid Dynamics (CFD) has been developed rapidly and has now been applied in many areas. Its application in meteorological study is historically one of the most active areas and has pushed the development of CFD itself. The atmosphere of Earth is closely related to people's life. At small scales, both animals and plants need to breathe atmosphere. In large scale, it transfer water and energy globally. There are many phenomena in the atmosphere, like vortices, winds and clouds. Sometimes, they benefit people and other living things. Sometimes, they can also bring disasters. It is important to understand the atmosphere.

Since atmospheres are basically large fluid systems, we need to apply fluid dynamics to study them. Because these systems are huge and complex, we need to apply CFD methods to study many phenomena in atmospheres.

In recent years, our knowledge of other planets has increased. Many satellites, detectors and landers have been launched to observe them closely. In the planning of these missions, CFD simulations of the atmospheres can provide good information and predictions about seasonal changes, suitable orbits and landing location.

Different from the terrestrial planets (Earth, Mercury, Venus and Mars), the gas-giant planets (Jupiter, Saturn, Uranus and Neptune) do not have solid surface and so their topographies are relatively simple. Also, because of their long distance to the Sun, the solar radiation energy to Neptune and Uranus is not as strong as that to Earth. This reduces the energy available to drive atmospheric motions. This is one reason why studying the atmospheres of Uranus and Neptune is in some ways simpler than that of Earth. For example, a great vortex on the Earth will be influenced not only by the atmosphere and the sea, but also by the coast and the continent.

Moreover, stronger solar insolation on Earth generates more convection and changes the flow motion in the vortex. Therefore, large vortices on Earth can only last for weeks. But on Neptune, a great vortex can exist for several months or even several years with a stable status. The Great Red Spot on Jupiter has been there for more than three hundred years. Certainly, they all have sufficiently dense and continuous atmospheres and the movement of the atmosphere obeys fluid dynamics with meteorological laws. Therefore, studying the great vortices on Neptune and Uranus can be a good starting point for understanding the great vortices in planetary atmospheres, including those on Earth.

In the last few decades, people have observed some distinct phenomena on Uranus and Neptune. Several Great Dark Spots (GDS) were observed on Neptune. The first, GDS-89, showed strong oscillations and steady drift to the equator, along with other measurable characteristics. Later, NGDS-32 held relatively stable latitude and lasted for several years. The first Uranian Dark Spot (UDS) appeared recently. The dynamics of these phenomena and the sustainability of the background atmospheres need more study. Furthermore, the formation of bright companions (methane clouds) of GDS and UDS and their effects on the vortices also need more research. Because of its unique obliquity, the seasonal changes on Uranus are different from other planets in the solar system. Its zonal wind profile and some other special related phenomena need to be explained. All these stimulate us to apply the modern CFD tools to the study of planetary atmospheres.

My dissertation work is about applying Computational Fluid Dynamics to study the atmospheres on Neptune and Uranus. Our primary goals are to explain the observational results of Neptune's Great Dark Spots (Chapter 3) and their bright companions (Chapter 6), the Uranian Dark Spot (Chapter 4) and its bright companion (Chapter 6), and the changing zonal wind profiles on Uranus (Chapter 5). To study the seasonal changes of Uranian atmosphere, a two-flux radiation model is

imported in the Explicit Planetary Isentropic Coordinate (EPIC) Global Circulation Model (GCM). To study the bright companions of GDSs and UDS, a methane cloud model is included. In this chapter, we first talk about some related observational results in planetary atmospheres. Then we will discuss some basic fluid dynamics theories applied in our research. Finally, we will discuss EPIC, which is the CFD model we will use in our simulations.

1.1 Great Vortices in Planetary Atmospheres

On the Earth, every year, people can observe large atmospheric vortices. Figure 1.1 shows the famous Hurricane Katrina, which hit New Orleans in August 2005. Hurricanes are the most visible vortices on Earth, but all high pressure and low pressure areas exhibit vortex-like behavior.

CFD simulation is one of the most promising methods to solve this kind of problems. As I mentioned before, our CFD simulations are on gas-giant planets. Observation is an important means to detect facts, especially for the outer planetary atmospheres. Just like the relationship between experiments and CFD simulations, observations are important to verify the results of our CFD studies. Also, CFD studies may provide guidance to direct later observations.

GRS on Jupiter

On Jupiter, there have been several long-lived great vortices. The most famous is the Great Red Spot (GRS), located at 22° latitude in the southern hemisphere. GRS was possibly first observed in 1665 and has apparently persisted for more than 340 years. Some other vortices, like the white ovals and Oval BA (also called "Red Junior", from the merge of white ovals), also exist on Jupiter, but with lifetimes of decades rather than centuries. In Figure 1.2 we can see the Great Red Spot and the smaller Oval BA to the left.



Figure 1.1: NASA image of Hurricane Katrina on 29 August 2005[71].

Farther out and smaller than Jupiter, Neptune and Uranus are the less observed gas-giant planets in the outer solar system. However, like the better known GRS on Jupiter, both atmospheres have exhibited large vortex features, known as Great Dark Spots (GDS) on Neptune and the Uranian Dark Spot (UDS) on Uranus. Dark spots are roughly elliptical regions in the planetary atmosphere identified by their darker

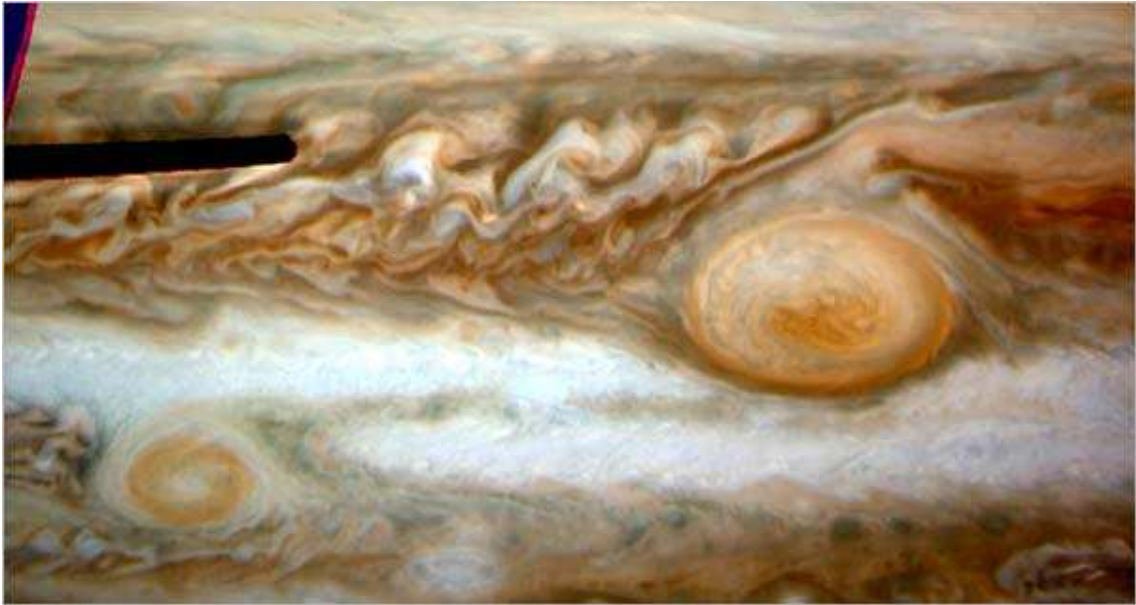


Figure 1.2: Great Red Spot and Oval BA on Jupiter. This photo is from NASA published on The New York Times website in 2006[72].

albedo. Different from the GRS, in which the local velocities can be measured by tracking small clouds within the feature, the GDSs did not have such small clouds so it is something of a presumption that they are, in fact, vortices.

Great Dark Spots on Neptune

Before the encounter of Voyager II with Neptune in 1989, it was believed that the atmosphere of Neptune would prove uninteresting since it receives relatively little solar radiation to drive atmospheric motions and since Uranus was quite uneventful. To the contrary, the encounter showed that the atmosphere of Neptune was quite dynamic. Figure 1.3 shows the major features observed by Voyager II in 1989. GDS-89 and DS2 were revealed; prominent cloud features, like the Bright Companion, the northern streaks, the Near Equatorial Feature, Scooter, and South Polar Features were also discovered.[41]

As seen in Figure 1.3, GDS-89 was a roughly elliptical region that was a darker blue (about a 10% change in albedo) compared to the surrounding region. Its shape

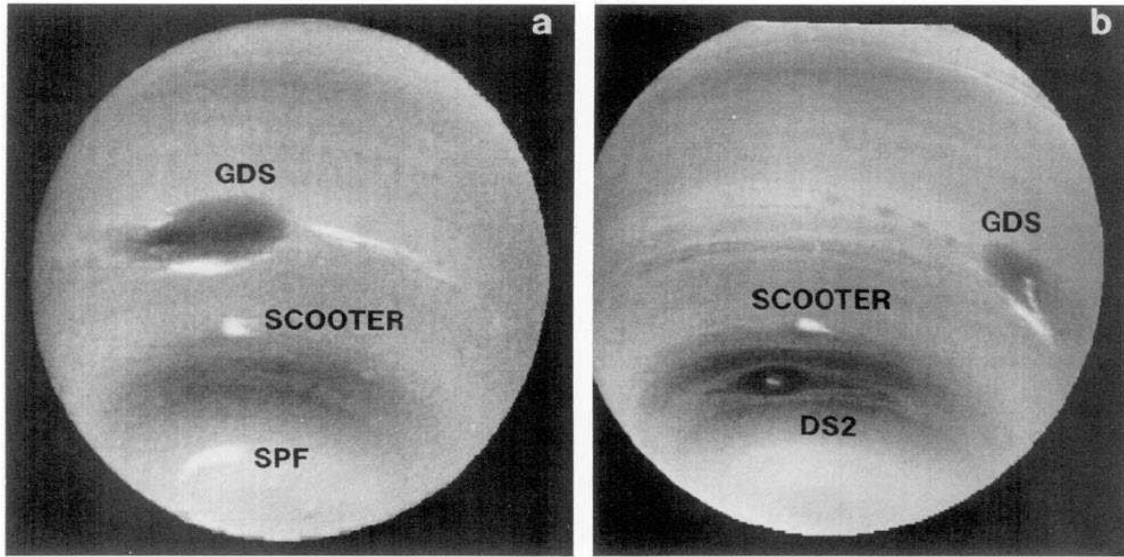


Figure 1.3: Major cloud and vortex features on Neptune, visible when Voyager II passed by on 14 August 1989 (a) and 20 August 1989(b). In both panels, we can see GDS (at 18.2°S at this time) and its bright companion on its south edge. The cloud feature scooter (at 40°S) can also be seen in these two panels. In panel (a), near the south pole, the cloud feature SPF (South Pole Feature) can be observed at 73°S . In panel (b), the second dark spot DS2 was at 53.3°S when the image was made. This figure is from Sromovsky 1993[91].

was partially obscured by a bright methane cloud (the Bright Companion). GDS-89 is arguably the most dynamic vortex feature in the outer solar system. It is also one of the largest known long-lived vortex features. Unlike the GRS of Jupiter, which has existed at a fixed latitude for hundreds of years, GDS-89 showed an equatorward drift and disappeared within a few years after it was first observed. Also, GDS-89 oscillated continuously in both aspect ratio and angle of orientation during the Voyager II encounter (Figure 1.4).

As summarized in Ingersoll et al,[41] GDS-89 drifted northward in latitude between 27 and 17°S at an average rate of 0.00170 degrees/hour or about 1.2 degrees/month. In longitude, the motion appeared to correlate well with simple advection by the zonal winds. The 8-day (193 hour) oscillation is defined by changes in ellipse orientation (with a total amplitude of about 14° of the semimajoraxis about the

horizontal) and aspect ratio (0.35 to 0.55, defined as semiminoraxis/semimajoraxis) corresponding to a longitudinal extent of 30 to 45 degrees and 12 to 17 degrees in latitude in the time frame best observed by Voyager II. Longer-term, GDS-89 also appeared to increase in area due to the growth of the average latitudinal extent from 8 to 15 degrees over a span of 225 days (see Figure 1.5), creating an increasingly circular spot. The fitted equations to these data are[91]

$$\begin{aligned} w_\lambda &= a_1 + a_2(t - t_0) + a_3 \sin(2\pi(t - t_0)/T); \\ h_\phi &= b_1 + b_2(t - t_1) + b_3 \sin(2\pi(t - t_1)/T), \end{aligned} \tag{1.1}$$

where parameters are shown in Figure 1.6. This size increase is believed to be the result of the GDS-89 conserving its mass and angular momentum.

Other notable features of GDS-89 like the tadpole-like "tails" are not so easily characterized quantitatively, but are critical qualitative aspects of the morphology. Notably, unlike the Great Red Spot and White Ovals of Jupiter, there were no apparent small features within the vortex that allowed for direct measurement of the vorticity within the Great Dark Spot.

After the Voyager II era, and after the apparent disappearance of GDS-89 in the southern hemisphere[92], new large vortex features on Neptune were observed with the post-repair Hubble Space Telescope. The first revealed a possible GDS-like vortex in the northern hemisphere in the fall of 1994[32], later designated Northern Great Dark Spot (NGDS)-32. This vortex came with its own Bright Companion cloud and was located in the northern mid-latitude region (originally at 32°N). Observations show that NGDS-32 may have existed throughout 1994-1996, and the motions of its companion cloud feature suggest that this vortex may have experienced a variable latitudinal drift, although no general equatorward drift like GDS-89 was found. In the same frame, another Great Dark Spot in the northern hemisphere NGDS-15 was

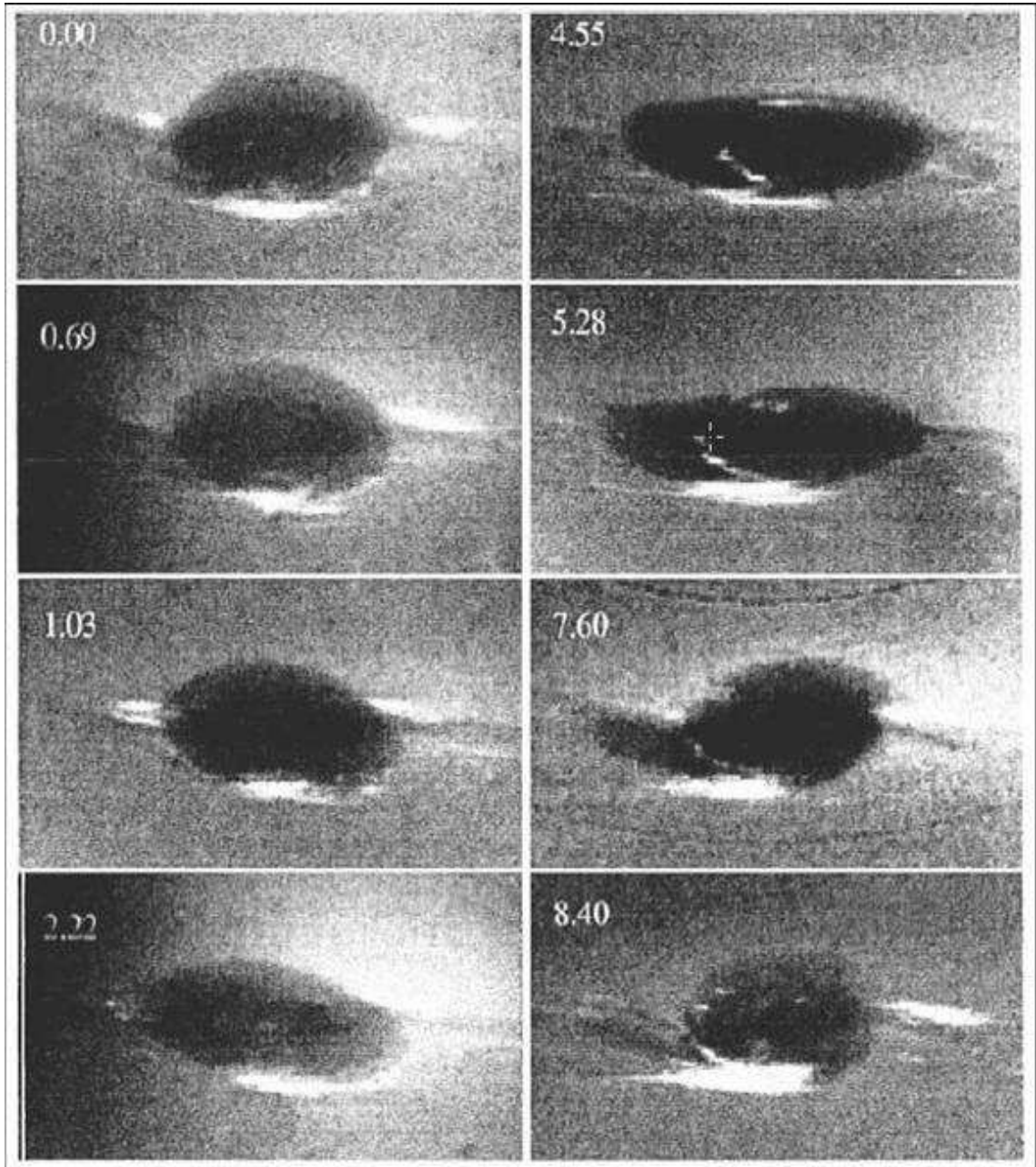


Figure 1.4: The observations of GDS-89. In this figure, we can see the GDS and its companion. And the oscillations of the shape and orientation of GDS and the "tail" can also be seen. The numbers on the subplots are the days from the first image. This figure is from Stratman et al. 2001[98].

also revealed at about 15°N . NGDS-15 was smaller than GDS-89 and NGDS32. It appeared only in the 1996 observations and no bright companion was observed.

Though NGDS-32 as a dark spot disappeared in the direct observations by July

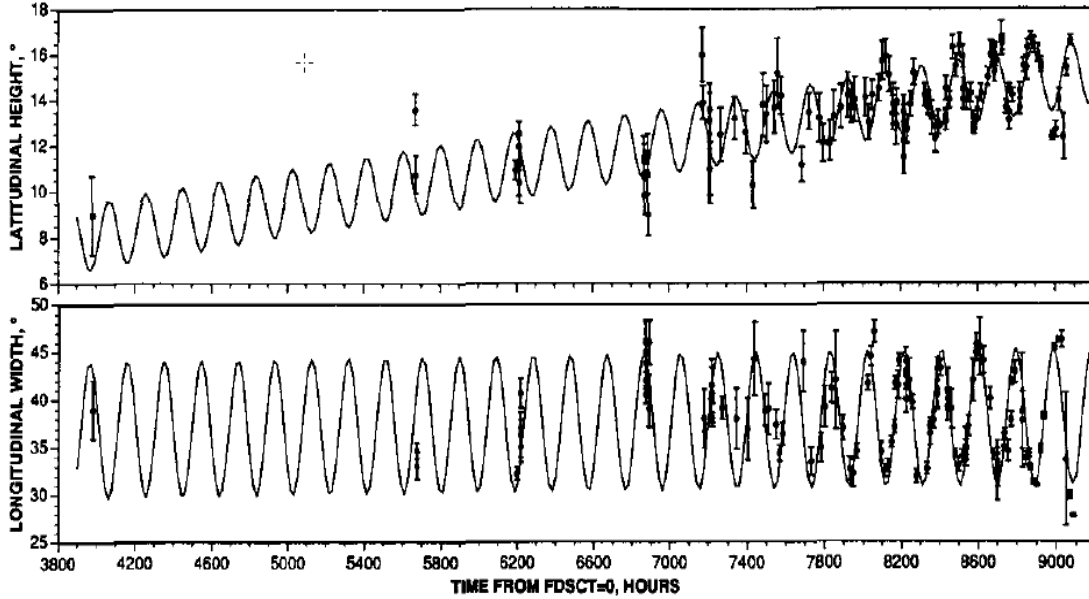


Figure 1.5: Latitudinal and longitudinal size change of the GDS-89. The points and error bars on them are from observational results. The solid lines are empirical fit to the data with equations 1.1 and parameters shown in Figure 1.6. This figure is from Sromovsky et al 1993[91].

Empirical Model Fits to GDS Shape Oscillations Using χ^2 Minimization

Description	Name	All data (Value \pm SE)	$t > 7000$ hr (Value \pm SE)	Units
Fit parameters				
Oscillation period	T	192.6 ± 0.7	193.2 ± 0.8	hr
Time phase for longitudinal oscillation	t_0	8363 ± 2	8362.5 ± 2.5	hr
Longitude width offset	a_1	38.3 ± 0.4	38.0 ± 0.3	$^{\circ}$ Long.
Longitudinal width drift rate	a_2	-0.00037 ± 0.0007	0.00027 ± 0.0005	$^{\circ}$ /hr
Longitudinal width oscillation amplitude	a_3	7.38 ± 0.35	7.2 ± 0.3	$^{\circ}$ Long.
Phase of latitudinal size oscillation	t_1	8365.8 ± 5	8365 ± 5	hr
Latitude size offset	b_1	14.1 ± 0.2	14.1 ± 0.16	$^{\circ}$ Lat.
Latitude size drift rate	b_2	0.00132 ± 0.0006	0.00137 ± 0.00024	$^{\circ}$ /hr
Amplitude of latitudinal size oscillation	b_3	-1.50 ± 0.2	-1.46 ± 0.2	$^{\circ}$ Lat.
Fit quality				
RMS deviation	χ^2_{min}/N	12.2	13.2	
	σ	2.45	1.98	$^{\circ}$ Lat.

Figure 1.6: The parameters for the empirical fit to the observational GDS-89 size oscillation data. This figure is from Table 1 in Sromovsky et al 1993[91].

1997, the cloud patterns implied that it may have persisted in some form into the year 2000[94]. NGDS-32 did not exhibit general meridional drift, but it might have oscillated in latitude slightly on the order of a few tenths of a degree with a period of several hundred days, as inferred from changes in the longitudinal drift rate. It is possible that NGDS-15 had drifted equatorward by a degree or two between

March 1996 and July 1997, but the limited number of observations available makes this somewhat speculative. All these post-Voyager HST (Hubble Space Telescope) observations and ground-based observations are at a much lower resolution than the Voyager observations, so detailed motions of NGDS features like morphology changes are not detectable.

Dark Spot on Uranus

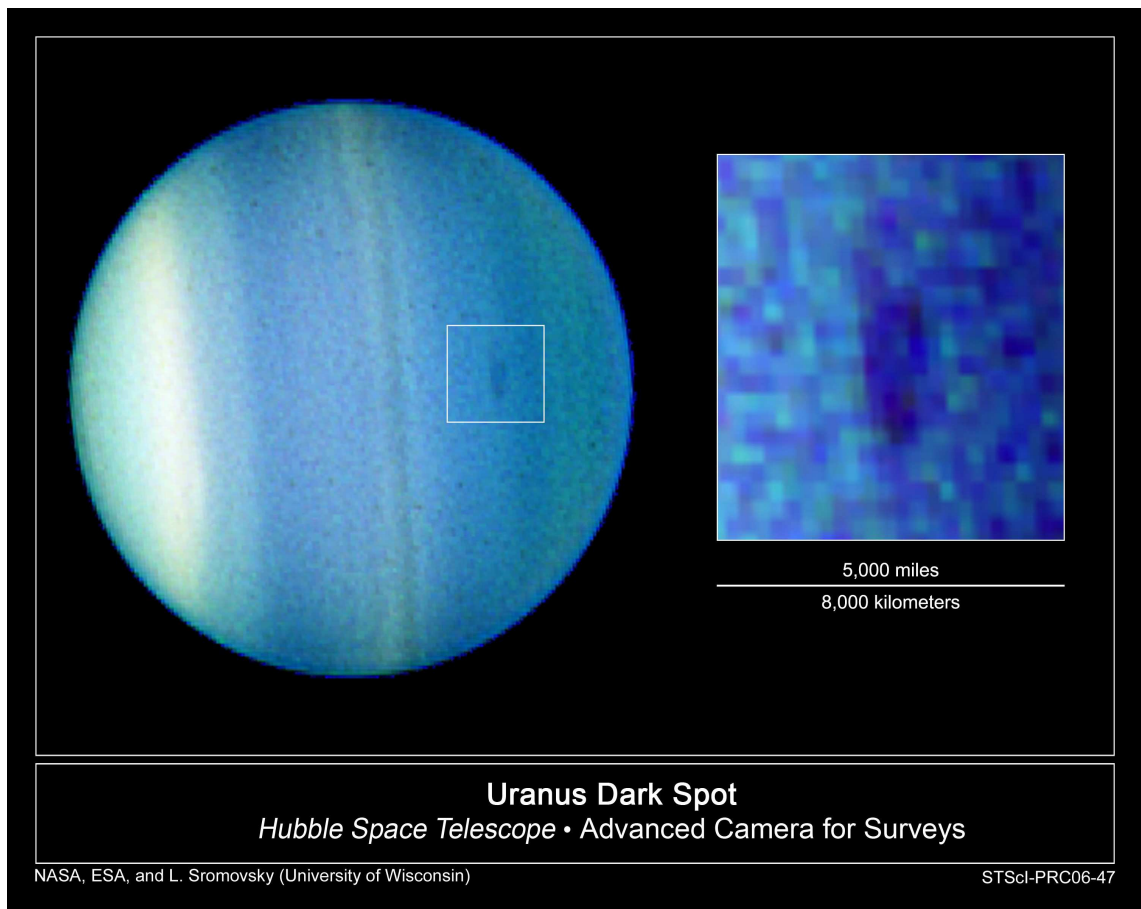


Figure 1.7: The three-wavelength composite image of dark spot on Uranus observed on August 23, 2006. The elongated feature measures 1,100 miles by 1,900 miles (1,700 kilometers by 3,000 kilometers). This figure is from the website <http://hubblesite.org/newscenter/archive/releases/2006/47>.

Though the atmosphere of Uranus has become increasingly dynamic in recent years, no GDS-like features were observed on Uranus until August 23, 2006, when

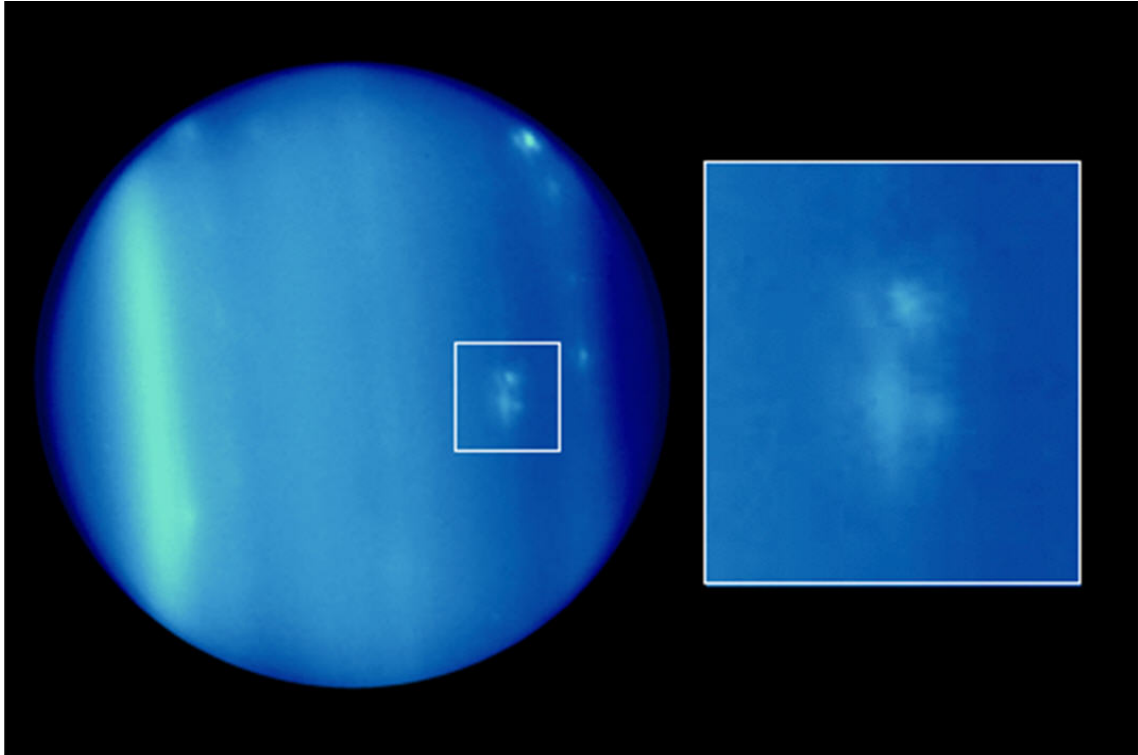


Figure 1.8: The bright companion clouds of Uranian Dark Spot. This photo is taken on 30 July 2006. It is from Hammel et al. 2009[38].

astronomers at the University of Wisconsin-Madison took the first definitive UDS images in their HST observations[96]. In this observation, astronomers found the first definitive dark spot at a latitude of 28°N on Uranus[96] (Figure 1.7). The size of this elongated dark spot was roughly 2° (1300 km) in latitude and 5° (2700 km) in longitude[38]. On August 24, 2006, this UDS was again spotted. About 52 days later, the UDS might be observed by Sromovsky using the Keck observatory at Mauna Kea, Hawaii. This suggests that the lifetime of this UDS is at least more than 50 days and there was not obvious drift. The bright companion clouds of the UDS can be seen in Figure 1.8; these clouds were observed even before the UDS was defined. The latitude and longitude locations of the UDS and its bright companion can be seen in Figure 1.9.

This dark spot may be related to Uranus approaching its equinox in 2007, when

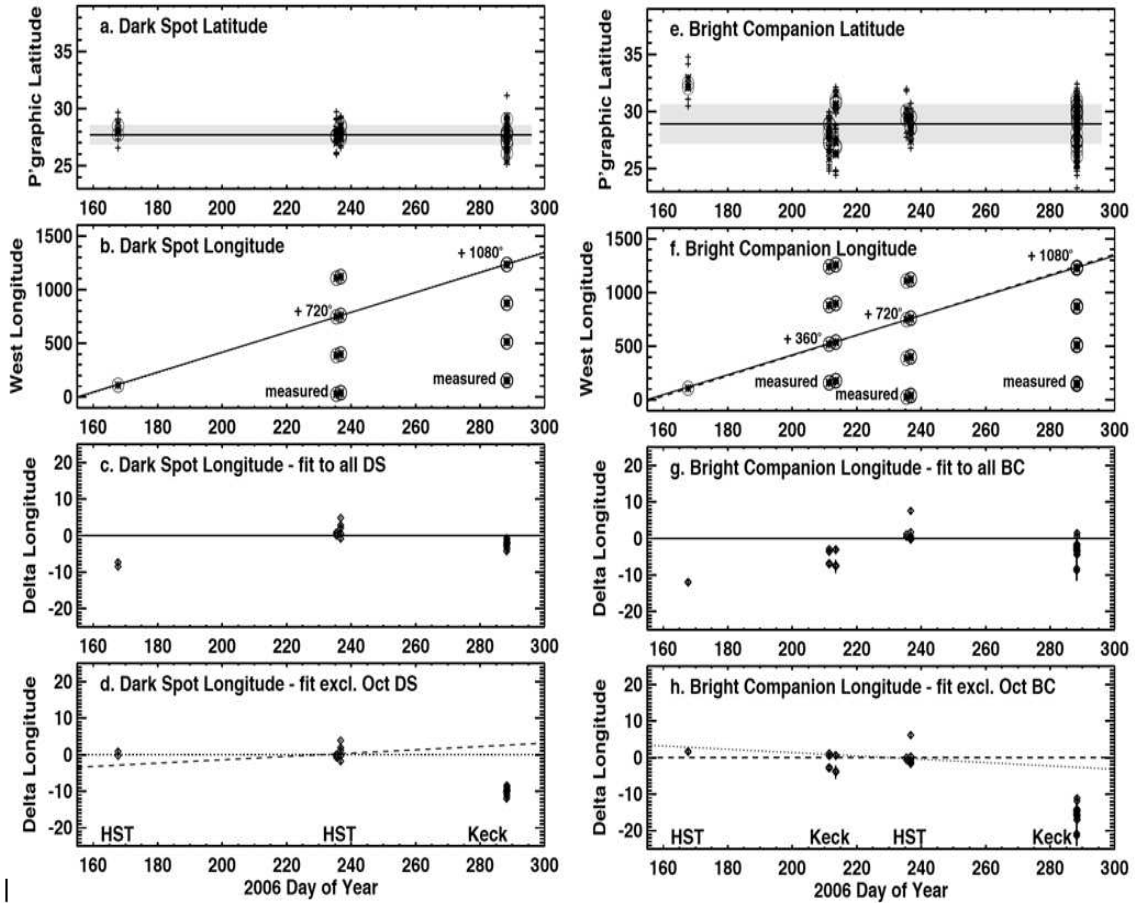


Figure 1.9: Data about the UDS (left) and its bright companion (right). This is from Hammel et al 2009[38].

both the northern and the southern hemispheres received sunshine equally. During this process, the northern hemisphere was approaching its spring and received more and more solar radiation. Of interest is how strongly and quickly the atmosphere of Uranus can respond to the seasonal changes[96], since the latitude of this dark spot was just fully exposed to sunlight after a long shadow period.

The obvious comparison between Neptune’s GDSs and the Uranian dark spot comes from the frequency of observed dark spots on Neptune and Uranus. In contrast to the somewhat frequent observations of GDSs in the Neptune’s atmosphere, in Uranus’ atmosphere, dark spots was not observed before August 23, 2006. This leads to a sustainability question for the Uranian Dark Spot and dark spots on Uranus

generally. Our simulations of the UDS, including the investigation of different zonal wind profiles, aim to study the sustainability problem in the Uranian atmosphere.

GDS-89 and the later appearance of the NGDS features in the Neptune's atmosphere, together with the recently-discovered UDS on Uranus, also present a unique opportunity to validate computational fluid dynamics in atmospheric models. Computational models can fill the gaps between observations, improving our understanding of the time-varying morphology of these features. Matching observed features can also constrain unobservable or poorly known aspects of the atmospheric physics. Also, comparing the simulation results in the both planets provides a chance to engage in comparative planetology, determining what aspects of the atmospheres and the vortices are critical for their origins, appearance, and sustainability. This prospect is especially interesting for Uranus and Neptune, since in many ways they are the two most similar planets in the solar system, yet Neptune has had a history of large vortex features while Uranus has for nearly two decades lacked any such observed features (until recently).

Cyclone and Anticyclone

A cyclone is a concept in meteorology, which refers to a closed area with circular fluid motion rotating in the same direction as the planet. On the Earth, in the northern hemisphere, it rotates counter clockwise; in the southern hemisphere, it rotates clockwise. On the contrary, anticyclone refers to a closed area with circular fluid motion rotating in the contrary direction of the planet. It rotates clockwise in the northern hemisphere and counter clockwise in the southern hemisphere.

Here we need to talk about the definition of the north pole, which is related to cyclone and anticyclone. According to the standard of the International Astronomical Union (IAU), north is defined as the pole above the orbital plane. From the dynamical definition, a north pole is defined so that the planet rotates counter clockwise. For

Earth and most other planets, these two definitions are consistent with each other. But for Uranus, because of its unique axial tilt angle (will be discussed in the next section), the north pole from the IAU definition is the south pole from the dynamical definition. We follow the IAU definition in this work.

Therefore, on Uranus, a cyclone rotates clockwise in the northern hemisphere and counter clockwise in the southern hemisphere; a anticyclone rotates counter clockwise in the northern hemisphere and clockwise in the southern hemisphere.

Related to pressure, a cyclone is a low pressure area so that the winds move inward spirally; a anticyclone is a high pressure area and the winds move outward spirally.

The great vortices talked above can be classified into these two classes. Hurricane Katrina was a cyclone - a low-pressure area; Great Red Spot is a anticyclone - a high-pressure area; Great Dark Spots on Neptune were anticyclones; Uranian Dark Spot was also a anticyclone.

When a cyclone or a anticyclone is in a balanced state and the winds move parallel to isobars, a concept called geostrophic flow can be applied to it. Geostrophic balance means that the Coriolis force and the pressure gradient force are in exact balance so that the velocity of the fluid parcels $V = V_g$, where the geostrophic wind V_g is defined by

$$fV_g = -\partial\Phi/\partial n. \quad (1.2)$$

1.2 Characteristics and Atmospheres of Neptune and Uranus

To construct the simulations to the features and phenomena on Neptune and Uranus, we need to get some basic ideas about their characteristics and their atmospheres.

As sister planets, Neptune and Uranus are quite similar in some aspects. They are both gas-giant planets. Their locations in the solar system are next to each other: Uranus is the seventh planet and Neptune is the eighth (although the distance between their orbits is more than 1.5 billion kilometers, about half of the distance of

the Uranus to the Sun). They have similar sizes: the equatorial radius and the polar radius of Uranus are 25560 km and 24972 km, respectively; those of Neptune are 24764 km and 24343 km. They have similar bluish appearances in the visible light band, a consequence of their similar atmosphere components: the main components of Uranus include H_2 ($83.3\pm 3\%$), He ($15\pm 3\%$) and CH_4 ($\sim 2.3\%$); those of Neptune are H_2 ($80\pm 3.2\%$), He ($19\pm 3.2\%$) and CH_4 ($1.5\pm 0.5\%$).

Also, as gas-giant planets, Neptune and Uranus have similar internal structures and atmospheric structures. From the bottom of the atmosphere to the core, the mass becomes denser and hotter and forms a superheated liquid mantle, relatively rich in water, ammonia and methane. The temperature can be as high as 5000 K. These mantle materials are called ice, although they are not like the solid ice on the Earth. Since this kind of ice is dominant in both Neptune and Uranus, different from Jupiter and Saturn, Neptune and Uranus are also called ice giants. The cores of Neptune and Uranus are composed of iron, nickel and silicates. To the outside, both Neptune and Uranus has atmospheric layers troposphere, stratosphere, thermosphere and then the exosphere. On each planet, the boundary between the troposphere and the stratosphere is called tropopause, which is located at about 0.1 bar. The troposphere is the main weather layer in the atmosphere and the temperature decreases with altitude. It also includes most of the mass in the atmosphere above the convection driven mantle. In the stratosphere, the temperature increases with altitude because of the absorption of solar radiation by some atmospheric components. In the troposphere, above 2 bars, clouds are mainly composed of methane. Below this, clouds of water, ammonia and hydrogen sulfide are believed to form. In our work, the bright companions are other cloud features are believed to be methane clouds and the great vortices are believed to be between about 1 bar to 4 bars. Therefore, our simulations are mainly in the troposphere and the methane cloud model is imported in Chapter 6 to study the bright companions. The vertical setup for both the

Neptune and Uranus are similar, because of their similar vertical structures.

However, historically they have shown considerable differences in dynamics. As discussed previously, in the past few decades there have been observed several Great Dark Spots and many cloud features observed on Neptune (see Figure 1.3), while on Uranus, little major atmosphere activity has been observed (see Figure 1.10) until recently. This has always been a point of curiosity, as Uranus receives more solar radiation than Neptune and would therefore be expected to have greater solar radiation energy in the atmosphere. A possible explanation for the difference is that internal heat has proven to be the main heat source for the upper atmosphere of Neptune. Although Neptune is much farther than Uranus to the Sun and receives only 40% of sunlight received by Uranus, both planets have similar surface temperature. The radiation energy from Neptune to space is about 2.61 times that it receives. For Uranus, internal heat is not strong and solar radiation is still the main energy source. The radiation energy from Uranus to space is about 1.1 times of the radiation energy it receives - nearly balanced.

Another key difference between Uranus and Neptune is their axial tilt. For the tilt angle of the pole direction to the orbital plane, Neptune has 28.32° tilt, similar to Earth and relatively normal in the solar system. Uranus is most well known for its extreme obliquity. The unique fact about Uranus in our solar system is that its rotational axis is inclined 97.77° relative to its orbital plane, giving rise to extreme seasonal insolation changes. Because of this obliquity, the poles absorb more energy from the sun, especially near solstices; however, the equatorial area radiates more energy to space than it is expected. Also, when the solar radiation is mainly on one hemisphere, the area near the other pole is also warm. These are explained as an effect of convection. Convection in the Uranian atmosphere takes heat from the poles to lower latitudes so that the temperature difference between them is much smaller than the result expected directly from simple solar absorption.

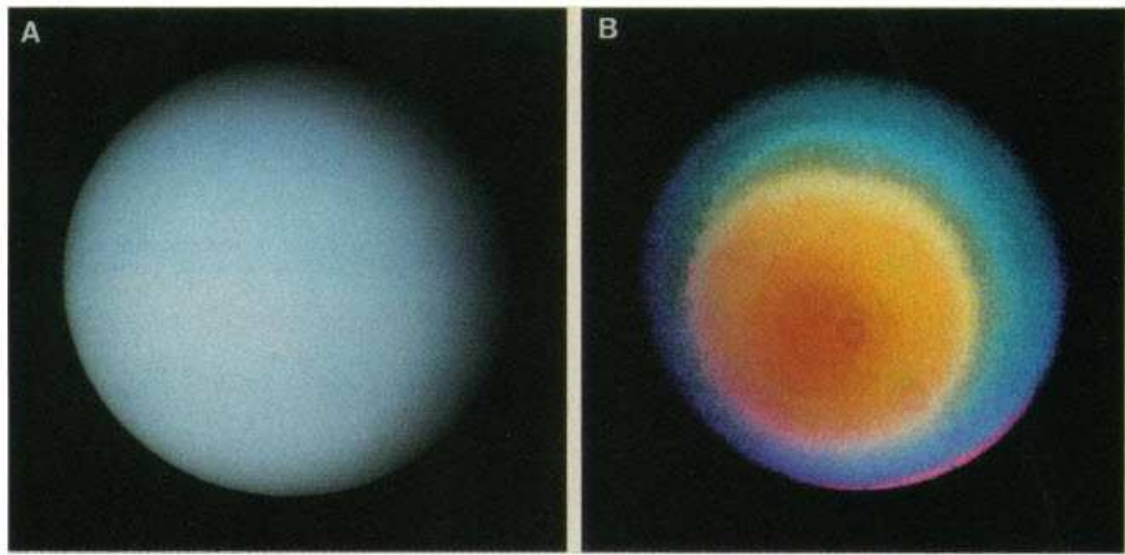


Figure 1.10: Views of Uranus from Voyager II. In panel (A), the color balance was adjusted to simulate the view of human's eyes. In panel (B), blue is from ultraviolet images, green is from violet and blue images, red is from green and orange images. This figure is from Smith et al. 1986[86].

The equinox of Uranus in December 2007 was the first equinox of Uranus in the era of modern astronomy. Because of its 84-year round trip around the Sun, this was the only opportunity in decades to record equinoctial phenomena such as ring-plane crossings, mutual Uranian satellite events, diurnally-driven auroral activity, and atmospheric radiative balance changes driven by seasonal variations in insolation[36]. For atmospheric studies, it was most importantly an opportunity to observe the atmospheric conditions surrounding the first known dark spot on Uranus.

Observations in recent years suggest that Uranus has entered a more dynamic era, compared to the Voyager II encounter in 1986, which occurred near winter solstice and revealed a largely uninteresting atmosphere as far as dynamics were concerned. These seasonal changes may be reflected in changes in a fundamental aspect of the atmospheric dynamics - the zonal wind profile.

Zonal Wind Profile

The zonal wind profile is one of the most important profiles in a planetary atmosphere. It represents the horizontal movement of a planetary atmosphere. As a background wind field of the atmosphere, the zonal wind profile is used as an initial condition in our numerical simulations. Astronomers track the movement of cloud features on a planet over time scales of a less than a planetary rotation. In this way, they can calculate the speed of the clouds at their given latitudes. The velocity of the atmosphere at some latitudes can be determined from these data. However, there are considerable regions where direct tracking measurements of the zonal winds are not possible, leading to interpolative fits to define the complete variation of the zonal wind with latitude. Then the velocity of the atmosphere at other latitudes can be computed from this fit curve.

Since these weather features can typically appear from the lower troposphere to the tropopause, the zonal wind profile often represent the zonal winds in a wide range of altitude. The vertical shear of a zonal wind profile on a planet is ordinarily not strong. In our simulations to the Neptune's atmosphere, vertical shear is investigated and the results show that to sustain a long-lived dark spot, the vertical shear near the spot should be small. In our radiation model, the vertical shear is also studied.

The zonal wind profiles of Neptune and Uranus has proved much smoother than multi-jet versions seen on Jupiter and Saturn. The magnitudes of the zonal winds on Neptune were remarkably large, with the Neptunian winds approaching speeds of near 400 m/s (retrograde) in the vicinity of the equator. Those of Uranus were considerably weaker with the speed near -100 m/s near the equator and near 200 m/s near 60°s.

The standard fit widely used for Neptune was developed in 1993 by Sromovsky et al.[91]. On the other hand, there is not a standard fit for Uranus. Mainly based on the observational results reported by Smith et al. in 1986[86], Karkoschka in 1998

and Sromovsky and Fry in 2005[95], three different versions of the Uranian zonal wind profile have been presented.

Neptune’s Zonal Wind Profile

On Neptune, after the Voyager II observations, Hammel et al. [29] and Smith et al.[87], both in 1989 studied the cloud and vortex features, especially the large scale features (GDS, DS2, Scooter and SPF, see Figure 1.3). They both detected a high speed ($\sim -400\text{m/s}$) retrograde equatorial jet, relative to the 16.11-hr magnetic field rotational period (Warwick et al. 1989[103]).

Later, Limaye and Sromovsky in 1991[53] analyzed more features between 8 and 1.5 rotations before the closest approach of Voyager II. These data showed a maximum westward wind at about -400 m/s near the equator and the maximum eastward wind at about 250 m/s near -70° (see Figure 1.2 in LeBeau 1997[44]). The limited number of cloud observations lead to a not well-defined profile to the north of 30° and to the south of -70° , due to a lack of observations nearer to the poles. The radio occultation wind measurement of Lindal 1992 extended the definition of the zonal wind in the northern hemisphere. His result also supported the idea the Neptune’s winds are mirror-symmetric about the equator. With this symmetric consideration, Sromovsky et al. in 1993[91] fit even-powered polynomials of latitude to the data from Limaye and Sromovsky 1991[53] and Lindal et al. 1990[55]. Figure 1.11 shows the fitting parameters from Sromovsky 1993[91]. The equation is:

$$y(\phi) = k_1 + k_2\phi^2 + k_3\phi^4 + k_4\phi^6, \quad (1.3)$$

where k_i are the parameters from Figure 1.11 and ϕ is the latitude.

Figure 1.12 and Figure 1.13 show the observational data points and fitted curves (including fourth-order and sixth-order fits) to these data points.

Empirical Fits of Even Functions of Latitude to Wind Speed, Drift Rate, and Period Measurements of Limaye and Sromovsky (1991) Combined with One Measurement of Lindal *et al.* (1990)

Variable	Constant term (k_1) \pm SE	ϕ^2 Term (k_2) \pm SE	ϕ^4 Term (k_3) \pm SE	ϕ^6 Term (k_4) \pm SE	Standard deviation
Wind speed	-389 ± 13 m/sec	0.153 ± 0.021 (m/sec)/($^\circ$) ²	$1.01 \pm 0.72E-5$ (m/sec)/($^\circ$) ⁴	$-3.1 \pm 0.7E-9$ (m/sec)/($^\circ$) ⁶	49 m/sec
Wind speed	-398 ± 12 m/sec	0.188 ± 0.014 (m/sec)/($^\circ$) ²	$-1.2 \pm 0.3E-5$ (m/sec)/($^\circ$) ⁴	Not used	48 m/sec
Drift rate, $^\circ$ /hr	-3.19 ± 0.13 / $^\circ$ /hr	$6.7 \pm 1.6E-4$ ($^\circ$ /hr)/($^\circ$) ²	$2.54 \pm 0.31E-7$ ($^\circ$ /hr)/($^\circ$) ⁴	Not used	0.55 $^\circ$ /hr
Period, hr	18.880 ± 0.106 hr	$-9.4 \pm 1.3E-4$ hr/($^\circ$) ²	$-6.8 \pm 2.5E-8$ hr/($^\circ$) ⁴	Not used	0.44 hr

Note. The last column contains the standard deviation of the measurements about the model curve.

Figure 1.11: Fitting parameters to the zonal wind profile on Neptune. This figure is from Sromovsky 1993[91] Table AI.

The 1991, 1994 and 1995 HST data, along with the ground-based and HST observations through 1996 again generally reinforced the zonal wind structure derived from the Voyager data for Neptune[92][33][93]. These results suggest that the Neptune's zonal wind profile is relatively stable over the time frame of the past couple of decades.

Uranian Zonal Wind Profile

Different from Neptune, Voyager observations and later HST observations of Uranus have yielded different wind profiles. With the near 7000 images taken by Voyager II, Smith et al. in 1986 [86] measured some zonal wind speeds on Uranus. But because of the lack of cloud features during the Voyager II passby and the observational angle of Voyager II, the number of zonal wind speeds is very limited and they are all in the southern hemisphere (see Figure 1.14). Based on these, they found that the zonal wind profile reached zero at a latitude of about -20° . A maximum speed might be located at around -50° or -60° .

Based on these data, combined with HST results in Karkoschka 1998[42] and Hammel et al. 2001[34], and assuming a symmetric system, a fitted zonal wind

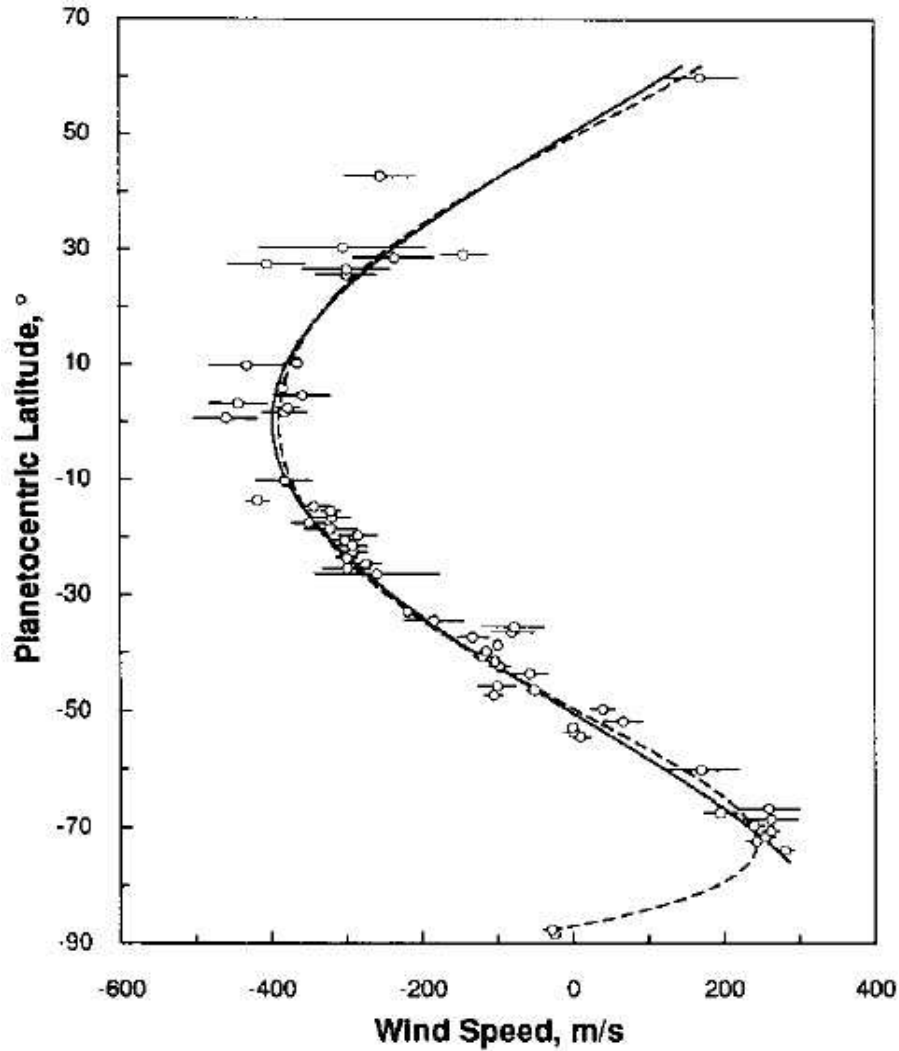


Figure 1.12: Observations of wind speed from Limaye and Sromovsky 1991[53] and Lindal et al. 1990[55], and fitted curves for Neptune. The points at the latitudes $\pm 60^\circ$ are from Lindal et al. 1990. The solid curve is a fourth-order fit, excluding the near polar point; the dashed curve is a sixth-order fit, including all the data. This figure is from Sromovsky 1993[91].

profile equation was achieved as [95]:

$$u(m/s) = 27.46 + 36.568 \cos(\phi) - 175.486 \cos(3\phi). \quad (1.4)$$

In 1998, Karkoschka reported HST observational results from 1997 (see Figure 1.15). Combining these with the Voyager II observational data in 1986, an asymmetric

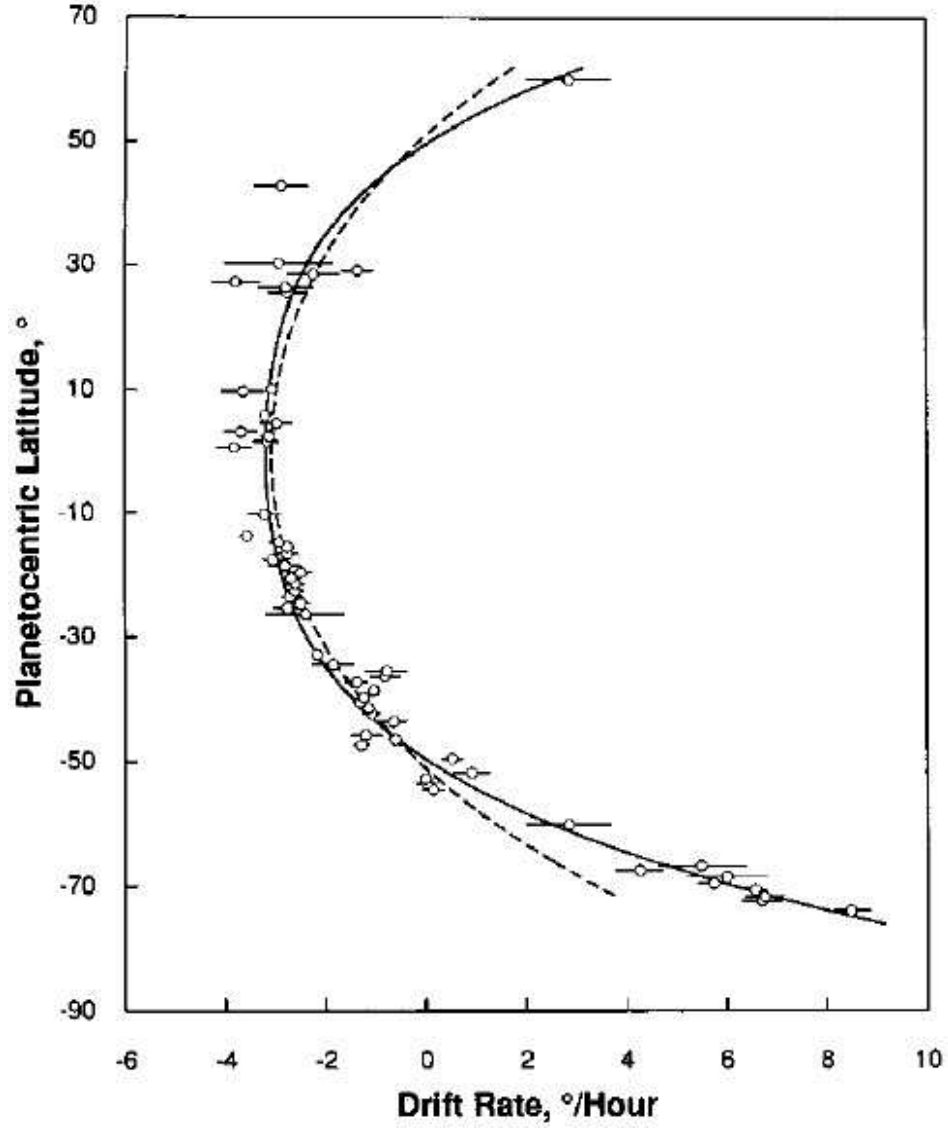


Figure 1.13: Observations of drift rate from Limaye and Sromovsky 1991[53] and Lindal et al. 1990[55], and fitted curves for Neptune. The points and the solid curve are same as Figure 1.12. The dashed curve is the fit to long-term GDS and DS2 motions, for comparison. This figure is from Sromovsky 1993[91].

zonal wind profile absolute rotation rate (in degree/day) equation was proposed[42]:

$$482 - 8 \sin(\phi) + 127 \sin^2 \phi. \tag{1.5}$$

Subtracting the planetary rotation of $501.16^\circ/\text{day}$ and considering the unit and geom-

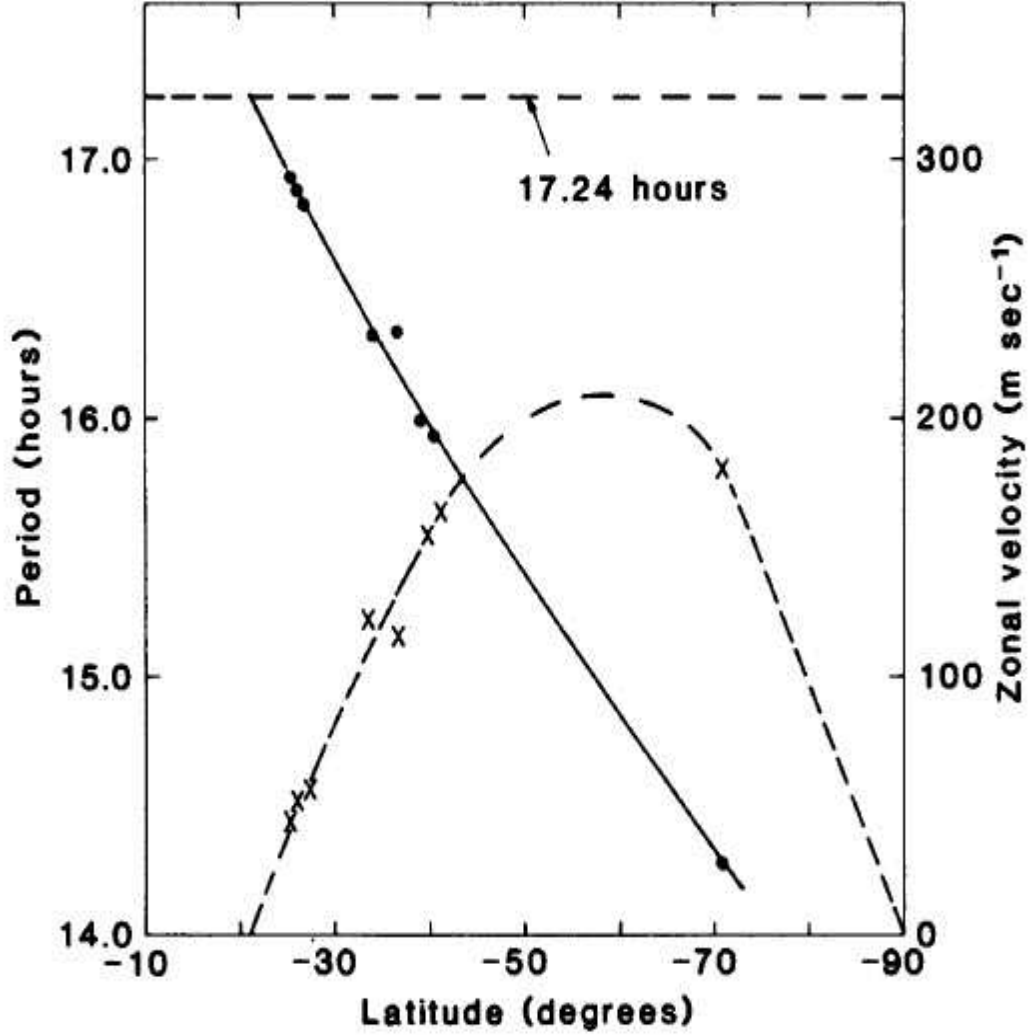


Figure 1.14: Voyager II Measured rotation periods, corresponding zonal velocities and fitted curves for the southern hemisphere of Uranus. The points connected by the solid curve are about the rotation period; the points connected by the dashed curve are about corresponding zonal velocities, relative to the 17.24-hour rotation period of the magnetic field. This figure is from Smith et al. 1986[86].

entry, the relative zonal wind speed can be calculated as:

$$\begin{aligned}
 u(m/s) = & \frac{482 - 8 \sin(\phi) + 127 \sin^2 \phi - 501.16}{24 \times 60 \times 60} \\
 & \times \frac{\pi}{180} \frac{r_e}{\sqrt{1 + \left(\frac{r_p}{r_e} \times \tan \phi\right)^2}}. \quad (1.6)
 \end{aligned}$$

After this, Hammel et al. in 2001 reported HST and Keck observational results,

Cloud	Maximum contrast (%)		Diameter (10 ³ km)	Latitude (°)	Date in 1997				
	Imaged	Modeled			July			October	
					25	28	29	28	29
A	120	900	2	+28	–	25	28	29	–
B	130	750	2	+27	–	25	28	29	–
C	180	600	2.5	+28	–	–	28	–	–
D	120	250	3.5	+30	–	–	28	–	–
E	50	120	3	+29	–	–	28	–	–
F	35	60	2.5	+17	–	–	28	–	16
G	10	25	1.5	+27	–	25	–	29	–
H	18	25	2.5	–25	–	25	28	29	–
I	9	20	1 × 10	–42	–	25	28	–	16
J	8	15	1 × 10	–31	7	25	28	29	–

Figure 1.15: HST observational results of 10 Uranian clouds in 1997. This table is from Karkoschka 1998[42].

showing decreased westward zonal wind speeds. Hammel et al. in 2005 reported further observational results (observations were in 2003) using the Keck telescope. These showed increased wind speeds near 45°N. In 2005, Sromovsky[95] reported observational results from August 2003 to July and August 2004, using the Keck 2 telescope. Based on these, Sromovsky argued that an asymmetric Uranian zonal wind profile had been confirmed. A new fitted zonal wind profile equation was given:

$$\begin{aligned}
 u(m/s) = & 62 - 166.5 \cos(0.052(\phi - 2.9)) \\
 & - 20 \sin(0.27(\phi - 27.5)) \times \exp(-(|\phi - 17.5|/26)^2) \\
 & + 15 \cos(0.026(\phi - 60)).
 \end{aligned}
 \tag{1.7}$$

Here the latitude ϕ is measured in degrees.

If these results reflect actual changes in the zonal winds over time, as opposed to the near stable Neptune’s zonal wind profile, it is a challenging result for astronomers to explain. Certainly, it is possible that the change of zonal wind profile is from better observations. But because of the observed seasonal changes, including more

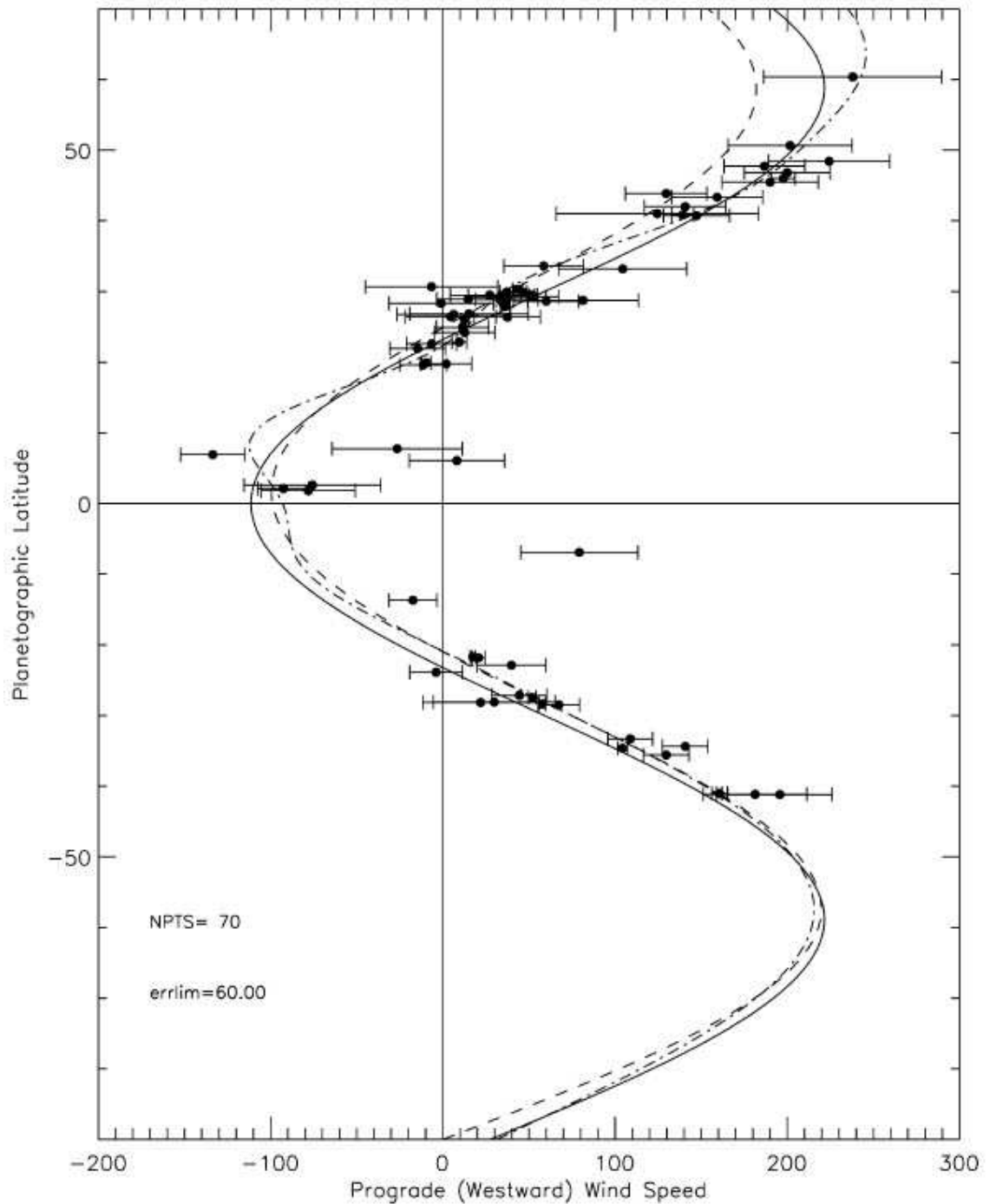


Figure 1.16: Observational results (70 points) from Keck imaging and three zonal wind profiles. These observations were done in August 2003 and July and August 2004. The solid line is the symmetric fitted curve Smith 1986; the dashed line is the asymmetric fitted curve Karkoschka 1998; the dash-dot line is the asymmetric fitted curve Sromovsky 2005. This figure is from Sromovsky 2005[95].

dynamics and more clouds, and the dominant role of solar radiation in the planetary energy balance, it is believable that the zonal wind profile should also have a seasonal change. This is related to the special obliquity of Uranus and the changing angle of solar radiation leads to the changing seasons on Uranus.

Pressure-Temperature Profile

A planetary atmosphere is divided to several layers. The troposphere is the main weather layer of an atmosphere. For a terrestrial planet, it is the bottom layer and contains most of the gas in the atmosphere. For a gas-giant planet, it is the deepest layer of the weather layers and includes all the cloud features. For Earth, this is the layer where people live and the main weather phenomena occur. In this layer, because of the heat of the bottom (for the Earth, it is the ground, for gas-giant planets, the heat source is the gas below the weather layers), temperature increases with pressure (decreases with altitude). Above the troposphere is the stratosphere. In the stratosphere, temperature decreases with pressure (increases with altitude) because of solar radiation absorbed by some species, such as ozone on Earth. The boundary between them is called the tropopause. The troposphere and stratosphere are the two layers used in our simulations. They include most of the mass and most of the energy associated with weather changes. Also, most observations of the atmospheres of Neptune and Uranus are within these two layers.

To represent the vertical changes in a planetary atmosphere, in a CFD model of an atmosphere, the vertical Pressure-Temperature (P-T) Profile is an important profile. Normally, for gas-giant planets, the vertical P-T profile is determined through radio occultation. In the EPIC GCM, the P-T profile is also a standard initial condition.

Because of the similarity of Neptune and Uranus, their pressure-temperature profiles are often studied together. For example, in 1987, Orton et al.[74] presented a Neptune's P-T profile based on ground observations and a Uranian P-T profile based

on Voyager data.

Neptune's P-T profile was improved later by the Voyager radio occultation measurements results [101][55][56]. These profiles varied a little based on different assumed He/H₂ ratios. In 1991, Conrath et al. [13] argued that the best He mole fraction is 19% and the P-T profile was determined as in Figure 2.5. In our simulations of Neptune's atmosphere, the Conrath 1991 profile is used as the baseline P-T profile. As for Uranus, the profile, based on Voyager II observations, presented by Lindal et al. in 1987 is the standard profile used in our numerical simulations (see Figure 2.6).

After these, further analysis of the P-T profiles of Neptune and Uranus were presented by Conrath et al in 1998[14], Marten et al in 2005[60] and Hammel and Lockwood in 2007[37], based on different observations. These analyses do not change the main features of the Conrath and Lindal profiles, and we therefore have continued to use them in this work. Ordinarily, in the observations, the P-T profiles can reach about 2 bars because below that radiation is not able to penetrate. However, in our simulations, we normally need the P-T profile deeper than 7 bars. In this situation, the near-adiabatic extension method discussed in Chapter 2 is be used.

1.3 Fluid Dynamics in Planetary Atmosphere

Fluid dynamics is the mechanism governing the motions of fluids, including planetary atmospheres. When we study a planetary atmosphere, because of the geometry and the rotation of the planets, there are some special equations beyond the basic fluid dynamics theory. The basic fluid dynamics equations can also be manipulated into forms that better meet the requirements for studying planetary atmospheres. To understand the equations and concepts in our CFD study, this section reviews the basic conservation laws and some meteorological concepts used in our projects.

Basic Conservation Laws

In atmospheric fluid dynamics study, the individual molecules in atmospheres are ignored and the atmospheres are regarded as continuous fluid media. Each point of an atmosphere is treated as a small volume containing a large number of molecules. Field variables, e.g., pressure, temperature, density, are continuous functions of space and time. The fundamental equations governing the motions of the atmospheres are expressed in terms of partial differential equations involving the field variables as dependent variables and space and time as independent variables.

The basic equations in fluid dynamics are called the Navier-Stokes equations. These equations were first presented by a French engineer Claude Louis Marie Henri Navier in 1822 and then by a British mathematician-physicist George Gabriel Stokes in 1845. The normal form of the Navier-Stokes equations, including continuity equation, conservation of momentum and conservation of energy, as applied to a planetary atmosphere assuming inviscid flow are:

$$\frac{1}{\rho} \frac{D\rho}{Dt} + \vec{\nabla} \cdot \vec{U} = 0 \quad (1.8)$$

$$\frac{D\vec{U}}{Dt} = -2\vec{\Omega} \times \vec{U} - \frac{1}{\rho} \vec{\nabla} p + \vec{g} \quad (1.9)$$

$$\rho \frac{De}{Dt} + \rho \frac{D}{Dt} \left(\frac{1}{2} \vec{U} \cdot \vec{U} \right) = -\vec{U} \cdot \vec{\nabla} p - p \vec{\nabla} \cdot \vec{U} - \rho g w + \rho J \quad (1.10)$$

Here ρ is density, t is time, \vec{U} is the velocity vector, $\vec{\Omega}$ is the angular velocity, p is pressure, e is internal energy, and J is heat. Gravity \vec{g} is the combination of the gravitational force and the centrifugal force due to the planet's rotation

$$\vec{g} \equiv -g\vec{k} \equiv \vec{g}^* + \Omega^2 \vec{R} \quad (1.11)$$

where \vec{k} designates a unit vector parallel to the local vertical. Except at the poles and the equator, \vec{g} is not directed toward the center of the planet, but is perpendicular

to a geopotential surface. The gravitational force \vec{g}^* is:

$$\frac{\vec{F}_g}{m} \equiv \vec{g}^* = -\frac{GM}{r^2} \left(\frac{\vec{r}'}{r} \right) \quad (1.12)$$

On the right hand side of the momentum equation, the first term is the Coriolis force, which arises from the conservation of angular momentum in a rotating frame. This equation means that the acceleration following the relative motion in the rotating frame equals the sum of the Coriolis force, the pressure gradient force, and effective gravity. This equation is the basis of most work in dynamic meteorology. For the theoretical analysis and numerical prediction, the momentum conservation equation can be expanded into its scalar components, in spherical coordinates:

$$\frac{Du}{Dt} - \frac{uv \tan \phi}{a} + \frac{uw}{a} = -\frac{1}{\rho} \frac{\partial p}{\partial x} + 2\Omega v \sin \phi - 2\Omega w \cos \phi \quad (1.13)$$

$$\frac{Dv}{Dt} + \frac{u^2 \tan \phi}{a} + \frac{vw}{a} = -\frac{1}{\rho} \frac{\partial p}{\partial y} - 2\Omega u \sin \phi \quad (1.14)$$

$$\frac{Dw}{Dt} - \frac{u^2 + v^2}{a} = -\frac{1}{\rho} \frac{\partial p}{\partial z} - g + 2\Omega u \cos \phi \quad (1.15)$$

$$(1.16)$$

Here u , v , w are the zonal, meridional and vertical components of \vec{U} , a is the mean radius of the planet and ϕ is the latitude.

Vorticity

Vorticity is a vector field defined as a curl of velocity. The relative vorticity is defined as

$$\vec{\omega} \equiv \vec{\nabla} \times \vec{U}, \quad (1.17)$$

so that in Cartesian coordinates,

$$\vec{\omega} = \left(\frac{\partial w}{\partial y} - \frac{\partial v}{\partial z}, \frac{\partial u}{\partial z} - \frac{\partial w}{\partial x}, \frac{\partial v}{\partial x} - \frac{\partial u}{\partial y} \right). \quad (1.18)$$

In large-scale dynamic meteorology, only the vertical components of the vorticity is significant because the vertical scale is much smaller than the horizontal scale:

$$\zeta \equiv \vec{k} \cdot (\vec{\nabla} \times \vec{U}). \quad (1.19)$$

When ζ is positive, the vortex rotates counter clockwise and is a cyclone in the northern hemisphere; when it is negative, the vortex is a cyclone in the southern hemisphere. Therefore, ζ is a good diagnostic variable for weather analysis. Ordinarily, we do not add the explicit "vertical component of" in front of "relative vorticity" when we use ζ . There is another vorticity concept in meteorology: absolute vorticity η . The difference between absolute and relative vorticity is planetary vorticity, which is just the Coriolis parameter $f = 2\Omega \sin \phi$. Finally, in Cartesian coordinate, we can get:

$$\zeta = \frac{\partial v}{\partial x} - \frac{\partial u}{\partial y}, \quad \eta = \frac{\partial v}{\partial x} - \frac{\partial u}{\partial y} + f. \quad (1.20)$$

Shallow Water Equations

A shallow water system describes a thin layer of constant density fluid. Conventionally, it is in hydrostatic balance, with a rigid surface below and a free surface above. This can be generalized to multiple layers of immiscible fluids, or to represent stratified layers in a fluid.

The first equation is the hydrostatic equation,

$$\frac{\partial p}{\partial z} = -\rho g. \quad (1.21)$$

Considering the constant density condition, pressure can be written as:

$$p(x, y, z) = -\rho g z + p_0. \quad (1.22)$$

Using η to denote the upper free surface height, $p_0 = \rho g \eta$. Then the pressure equation becomes

$$p(x, y, z) = \rho g(\eta(x, y) - z). \quad (1.23)$$

In cartesian coordinates, without extra forces, this leads to the equation

$$\frac{D\vec{U}_h}{Dt} = \frac{1}{\rho} \vec{\nabla} p = -g \vec{\nabla} \eta. \quad (1.24)$$

Here $\vec{U}_h \equiv u\vec{i} + v\vec{j}$ is the horizontal velocity. In a rotating system, like a planet, the momentum equation becomes

$$\frac{D\vec{U}_h}{Dt} + \vec{f} \times \vec{U}_h = -g \vec{\nabla} \eta. \quad (1.25)$$

Now consider the mass continuity equation. The fluid mass in a column with height h and cross-sectional area A is $\int_A \rho h dA$. Because of the constant density assumption, a net flux of fluid into the column will lead to a increase of h . The mass increase from this is

$$F_m = \frac{d}{dt} \int \rho dV = \frac{d}{dt} \int_A \rho h dA = \int_A \rho \frac{\partial h}{\partial t} dA. \quad (1.26)$$

The mass flow into this column is

$$F_m = - \int_S \rho \vec{U}_h \cdot d\vec{S} = - \oint \rho h \vec{U}_h \cdot \vec{n} dl = - \int_A \vec{\nabla} \cdot (\rho \vec{U}_h h) dA. \quad (1.27)$$

Here $d\vec{S}$ is the small area of the vertical boundary of the column and \vec{n} is its unit direction vector. Combining the above equations, we have the mass continuity equation for a shallow water system:

$$\frac{\partial h}{\partial t} + \vec{\nabla} \cdot (\vec{U}_h h) = 0, \quad (1.28)$$

or equivalently

$$\frac{Dh}{Dt} + h(\vec{\nabla} \cdot \vec{U}_h) = 0. \quad (1.29)$$

Notice the variables \vec{U}_h and h are only functions of x , y , and t , so that material derivative is

$$\frac{D}{Dt} = \frac{\partial}{\partial t} + \vec{U}_h \cdot \vec{\nabla} = \frac{\partial}{\partial t} + u \frac{\partial}{\partial x} + v \frac{\partial}{\partial y}. \quad (1.30)$$

Potential Vorticity

Using the shallow water equations, we can define potential vorticity and prove the conservation of potential vorticity in an inviscid shallow water system.

There are two vector calculation equations:

$$(\vec{U}_h \cdot \vec{\nabla})\vec{U}_h = \frac{1}{2}\vec{\nabla}(\vec{U}_h \cdot \vec{U}_h) - \vec{U}_h \times (\vec{\nabla} \times \vec{U}_h), \quad (1.31)$$

and

$$\begin{aligned} \vec{\nabla} \times (\vec{\omega}^* \times \vec{U}_h) &= (\vec{U}_h \cdot \vec{\nabla})\vec{\omega}^* - (\vec{\omega}^* \cdot \vec{\nabla})\vec{U}_h + \vec{\omega}^* \vec{\nabla} \cdot \vec{U}_h - \vec{U}_h \vec{\nabla} \cdot \vec{\omega}^* \\ &= (\vec{U}_h \cdot \vec{\nabla})\vec{\omega}^* + \vec{\omega}^* \vec{\nabla} \cdot \vec{U}_h. \end{aligned} \quad (1.32)$$

Here $\vec{\omega}^*$ is the curl of the horizontal velocity

$$\vec{\omega}^* \equiv \vec{\nabla} \times \vec{U}_h = \vec{k} \left(\frac{\partial v}{\partial x} - \frac{\partial u}{\partial y} \right) = \vec{k}\zeta. \quad (1.33)$$

The term $\vec{\nabla} \cdot \vec{\omega}^*$ is the divergence of a curl and therefore equals to zero. The variable $\vec{\omega}^*$ is perpendicular to the surface in which \vec{U}_h varies so that $(\vec{\omega}^* \cdot \vec{\nabla})\vec{U}_h = 0$.

The shallow water momentum equation 1.25 can be written as

$$\frac{\partial \vec{U}_h}{\partial t} + (\vec{\omega}^* + f) \times \vec{U}_h = -\vec{\nabla} \left(g\eta + \frac{1}{2}U_h^2 \right). \quad (1.34)$$

Taking the curl of this equation gives the vorticity equation

$$\frac{\partial \zeta}{\partial t} + (U_h \cdot \vec{\nabla})(\zeta + f) = -(\zeta + f)\vec{\nabla} \cdot U_h. \quad (1.35)$$

The shallow water mass continuity equation 1.29 can be written as

$$-(\zeta + f)\vec{\nabla} \cdot U_h = \frac{\zeta + f}{h} \frac{Dh}{Dt}. \quad (1.36)$$

Combining the above equations, we can get

$$\frac{D(\zeta + f)}{Dt} = \frac{\zeta + f}{h} \frac{Dh}{Dt}, \quad (1.37)$$

which can be simplified to

$$\frac{D}{Dt} \left(\frac{\zeta + f}{h} \right) = 0. \quad (1.38)$$

The quantity $Q \equiv (\zeta + f)/h$ is defined as the potential vorticity in a rotating shallow water system, with the equation itself describing the conservation of potential vorticity.

Potential Temperature and Isentropic Coordinate

Potential temperature describes the temperature when a parcel of fluid at pressure P with absolute temperature T adiabatically moves to a standard reference pressure P_0 . The equation for potential temperature θ is

$$\theta = T \left(\frac{P_0}{P} \right)^{\frac{R}{C_p}}, \quad (1.39)$$

where R is the gas constant, C_p is the specific heat capacity.

An isentropic coordinate system use potential temperature. For adiabatic flow, the thermodynamic equation becomes a statement for the conservation of the mass of

fluid with a given value of potential temperature. Because the flow of the atmosphere is largely along isentropic surfaces, the momentum and vorticity equations have a quasi-two-dimensional form. Therefore, using potential temperature can achieve increasing numerical accuracy, and better conservation of potential vorticity, total angular momentum, and total energy for vertically discrete systems[19].

Using $\dot{\theta} = D\theta/Dt$, we can transform the equations from (x, y, z) coordinates to (x, y, θ) coordinates. The material derivative in this coordinate system is

$$\frac{D}{Dt} = \frac{\partial}{\partial t} + u \left(\frac{\partial}{\partial x} \right)_{\theta} + v \left(\frac{\partial}{\partial y} \right)_{\theta} + \frac{D\theta}{Dt} \frac{\partial}{\partial \theta} = \frac{\partial}{\partial t} + \vec{U}_h \cdot \vec{\nabla}_{\theta} + \dot{\theta} \frac{\partial}{\partial \theta}. \quad (1.40)$$

Brunt–Väisälä frequency

Consider an infinitesimal parcel of air with area dA , height dz , pressure $p(z)$ and density $\rho(z)$ in a volume with pressure location p_0 and density ρ_0 . Applying Newton's second law, we have

$$(\rho dA dz) \frac{d^2 z}{dt^2} = -(\rho dA dz)g - dA \frac{dp_0}{dz} dz. \quad (1.41)$$

Dividing $dA dz$ on the both sides, we have

$$\rho \left(\frac{d^2 z}{dt^2} \right) = -\rho g - \frac{dp_0}{dz}. \quad (1.42)$$

In hydrostatic balance, $(dp/dz)_0 = -\rho_0 g$, the above equation becomes

$$\rho \left(\frac{d^2 z}{dt^2} \right) = -\rho g + \rho_0 g \Rightarrow \frac{d^2 z}{dt^2} = -g \frac{\rho - \rho_0}{\rho}. \quad (1.43)$$

When it is at equilibrium status, the only force is the buoyancy force which comes from the density difference. At this time, $p = p_0$. From the ideal gas law $\rho = p/RT$,

$\rho_0 = p_0/RT_0$, then

$$\frac{\rho - \rho_0}{\rho} = \frac{\frac{p}{RT} - \frac{p_0}{RT_0}}{\frac{p}{RT}} = 1 - \frac{T}{T_0}. \quad (1.44)$$

From the definition of potential temperature 1.39 and the equilibrium condition, $T/T_0 = \theta/\theta_0$, then

$$\frac{d^2z}{dt^2} = -g \left(1 - \frac{\theta}{\theta_0} \right). \quad (1.45)$$

From Taylor's expansion, this equation becomes

$$\frac{d^2z}{dt^2} = g \frac{d(\ln \theta_0)}{dz} (z - z_0) \quad (1.46)$$

The frequency of this oscillation equation is

$$N^2 = g \frac{d(\ln \theta_0)}{dz}, \quad (1.47)$$

which is called Brunt-Väisälä frequency. Because the oscillation is related to the chosen density, it is also called the buoyancy frequency.

1.4 EPIC GCM

Currently, there are two popular GCM models used in the study of giant planet planetary atmospheres. One is the MIT GCM, another is the EPIC GCM. Both of them are three dimensional models and run in parallel. The MIT GCM was presented by Marshall et al. in 1997a[61] and 1997b[62]. It can be used for both oceanic and atmospheric simulations. The MIT GCM uses a finite volume method. It supports horizontal orthogonal curvilinear coordinates, including the extended cubic grid[1], which can avoid the singularity problems of poles of a planet. Comparing to this, the EPIC GCM uses a finite difference method and has the traditional latitude-longitude oblate spherical coordinates. The EPIC GCM is designed for the comparison of different planetary atmospheres and people can choose the planet in the initialization

process. The MIT GCM has been widely applied in the study of the oceans ([77], [3], [59] et al.), the interaction of the atmosphere and the sea on the Earth ([28], [89], [63], et al.), and has also recently been applied in the study of the zonal jets on gas-giant planets [51, 52]. The code and more information about MIT GCM can be found at www.mitgcm.org and more applications of MIT GCM can be found in the webpage mitgcm.org/pelican/online_documents/node273.html. The EPIC GCM has been widely applied in the study of the atmospheres of Venus [49, 21], Earth [22], Saturn [25, 26, 70, 84], Jupiter [85, 20, 67, 68, 69, 6, 82, 75, 70], Neptune [45, 20, 98, 22, 46, 16, 47, 48] and Uranus [16, 17, 18, 100, 38], including the zonal winds, vortices, waves and clouds.

In our work, the EPIC GCM is applied, because of its latitude-longitude coordinates, its comparative planetary characteristics and the previous related works. In this section, I will talk about the basic characteristics of the EPIC GCM.

The EPIC GCM was first presented by Dowling et al. in 1998 [19]. The early versions of EPIC use potential temperature as the vertical isentropic coordinate and divide the atmosphere to multiple layers. In each layer, shallow-water theory was used. At the same time, EPIC was applied by LeBeau and Dowling in 1998 to the study of the Great Dark Spot (GDS) of Neptune. Subsequently, Stratman et al. [98] incorporated a simple cloud model into EPIC, which could generate an orographic bright companion cloud next to a vortex. In 2006 and 2007, more detailed simulations on Neptune and Uranus were done with the hybrid version of EPIC [22][46][15][16][47][17].

EPIC uses oblate spherical coordinates as the horizontal coordinates. The relationships between surface Cartesian coordinates and the oblate spherical coordinates are [19]

$$dx = r(\lambda)d\phi; \quad r(\lambda) = \frac{R_e}{(1 + (R_p/R_e)^2 \tan^2 \lambda)^{1/2}}, \quad (1.48)$$

$$dy = R(\lambda)d\lambda; \quad R(\lambda) = \frac{r(\lambda)/\cos \lambda}{\sin^2 \lambda + (R_e/R_p)^2 \cos^2 \lambda}, \quad (1.49)$$

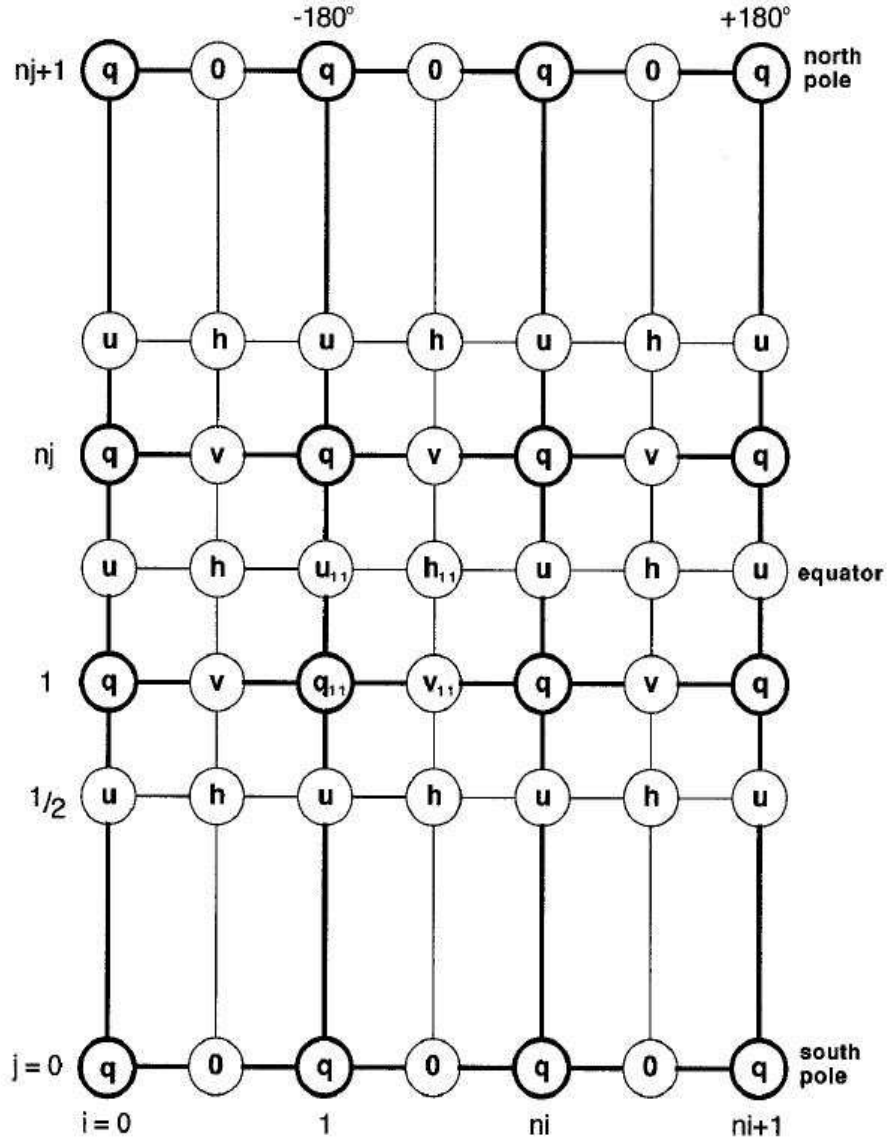


Figure 1.17: Horizontal Discretization of EPIC - distribution of u , v , h and q in the staggered C-grid. This figure is from Dowling et al. 1998.

where R_e and R_p are the equatorial and polar radius of the planets, λ is the planetographic latitude (the angle between the equatorial plane and the local vertical direction) and ϕ is the longitude.

The horizontal discretization of the first version of EPIC model is shown in Figure 1.17, in which we can see the placement and indexing of the variables. Each variable has its own grid. In vertical direction, u , v , q , h are in the same level, while pressure

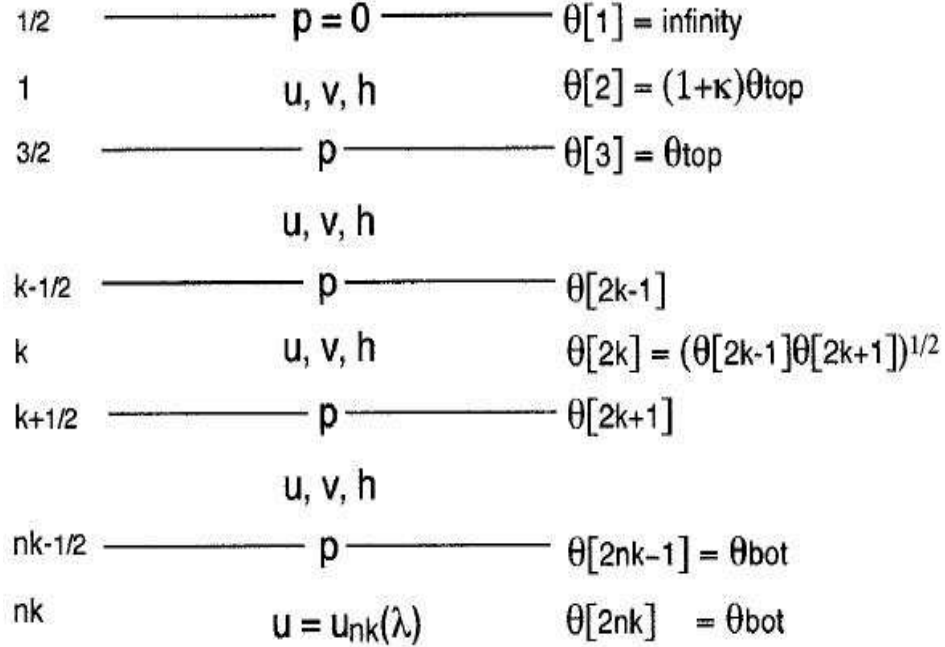


Figure 1.18: Vertical Discretization of EPIC. This figure is from Dowling et al. 1998.

p is staggered in the half layer, see Figure 1.18. Near the poles, the triangle-shape segments get extra latitude spacing to make the continuity and vorticity equations constant (Arakawa and Lamb 1977), shown in Figure 1.19. The new version of EPIC uses similar geometry, but the vertical coordinate is a new hybrid coordinate, not the potential temperature.

The basic equations are the three-dimensional Navier-Stokes equations in the following form:

$$\frac{\partial h}{\partial t} + \nabla \cdot (h\vec{u}) + \frac{\partial}{\partial \zeta}(h\dot{\zeta}) = 0, \quad (1.50)$$

$$\frac{\partial \vec{u}}{\partial t} + q\hat{k} \times (\vec{u}h) = -\nabla(M + K) + \nabla \cdot (\nu \nabla \vec{u}), \quad (1.51)$$

$$\frac{d\theta}{dt} = \frac{\dot{Q}}{\Pi}, \quad (1.52)$$

where $h = -(1/g)\partial p/\partial \zeta$ is the hybrid density, \vec{u} is the horizontal velocity in longitude and latitude, ζ is the hybrid vertical coordinate, q is the potential vorticity, $M = c_p T + gz$ is the Montgomery potential, K is the horizontal kinetic energy per unit

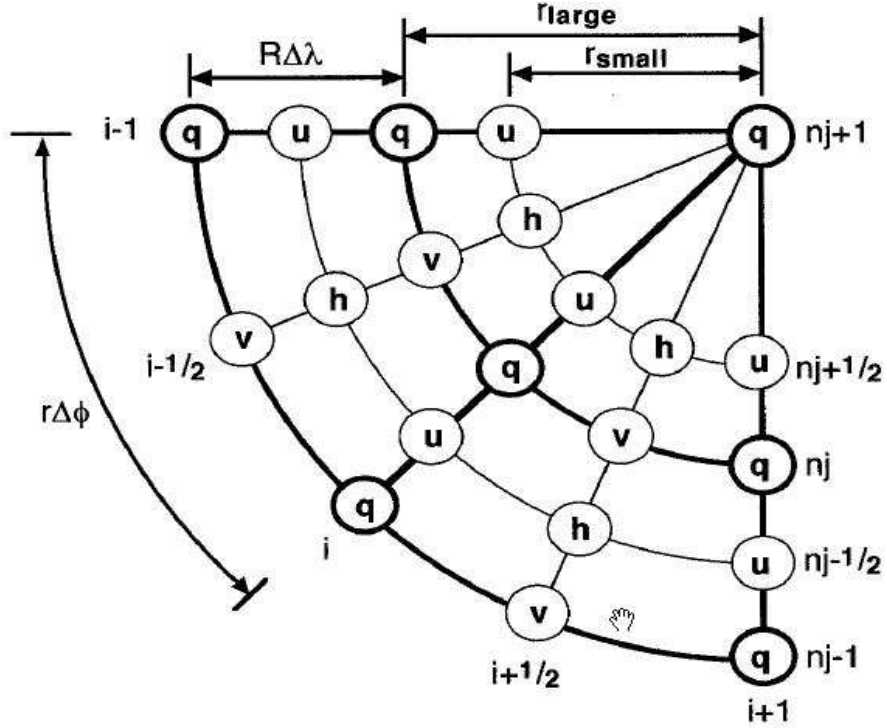


Figure 1.19: C-grid geometry at the north pole in EPIC model. $\pi r_{large}^2 = 2 \times \pi r_{small}^2$; $r_{small} = \frac{1}{2}R \Delta \lambda + \sqrt{\frac{1}{2}R \Delta \lambda} \approx 1.21R \Delta \lambda$. This figure is from Dowling et al. 1998.

mass, ν is the kinematic viscosity, θ is the potential temperature, $\Pi = C_p T / \theta$ is the Exner function, and \dot{Q} is the heat source term. The hybrid vertical coordinate has the form:

$$\zeta = \tilde{f}(\sigma) + \tilde{g}(\sigma)\theta, \quad (1.53)$$

$$\sigma = \frac{\log(p/p_{bot})}{\log p_{top}/p_{bot}}, \quad (1.54)$$

where p is pressure, the subscripts indicating the values at the top and bottom boundaries, and $\tilde{f}(\sigma)$ and $\tilde{g}(\sigma)$ are functions defined as appropriate for the problem ($\tilde{g}(\sigma)$ approaching zero near solid surfaces, yields a pure terrain following pressure coordinate; $\tilde{f}(\sigma)$ approaching zero and $\tilde{g}(\sigma)$ approaching unity when purely isentropic coordinates are desired). Assume $\zeta = F(\theta, p, p_{bot})$, and after some derivations, the

hybrid vertical velocity becomes [22]:

$$\dot{\zeta} = \tilde{g}(\sigma) \frac{\dot{Q}}{\Pi} + \frac{\partial F}{\partial p} \dot{p} + \frac{\partial F}{\partial p_{bot}} \dot{p}_{bot}, \quad (1.55)$$

where the subscripts on F denote partial differentiation, and the direct formula used to calculate $\dot{\zeta}$ on the layer interfaces is:

$$\dot{\zeta}_{k+1/2} = \tilde{g}(\sigma_{k+1/2}) \frac{\dot{Q}_{k+1/2}}{\Pi_{k+1/2}} - \frac{\partial F}{\partial p} \sum_{m=1}^k gh_m D_m \Delta \zeta_m - \frac{\partial F}{\partial p_{bot}} \sum_{m=1}^{nk} gh_m D_m \Delta \zeta_m, \quad (1.56)$$

where $\Delta \zeta_k \equiv \zeta_{k-1/2} - \zeta_{k+1/2}$ and $k = nk$ at the bottom layer.

These equations are solved using finite difference methods on a latitude-longitude grid in vertical layers of constant ζ on an oblate spheroid geometry defined by the measured polar and equatorial radii of the planet. The time integration is explicit, using the third-order Adams-Bashforth algorithm or alternately a Leapfrog algorithm. The equation used to march the prognostic variable u at time $t + \Delta t$ in the third-order Adams-Bashforth scheme is

$$u[t + \Delta t] = u[t] + \frac{\Delta t}{12} \left(23 \frac{\partial u}{\partial t}[t] - 16 \frac{\partial u}{\partial t}[t - \Delta t] + 5 \frac{\partial u}{\partial t}[t - 2\Delta t] \right). \quad (1.57)$$

In addition to the horizontal momentum equation (1.51), a sixth-order numerical hyperviscosity is applied in EPIC. The hyperviscosity terms used in EPIC take the form $(-1)^{n-1} \nu_{2n} \nabla^{2n} \mathbf{v}$, where ν_{2n} are input parameters by the user and n is a positive integer.

Furthermore, a low-pass Fourier filter in the poleward 45° latitude is applied in EPIC. Both hyperviscosity and this filter are used to suppress the numerical instability from the small scale gravity waves and the high-frequency computational modes.

The real atmosphere does not have upper boundary, but numerical models do. To cancel the reflection effect of the upper boundary, EPIC uses a method similar to the

impedance-matching terminator in electronics. Near the top, several sponge layers are set up with a dissipation term used to dampen upward propagating waves and reduce their reflection. The dissipation term used in EPIC is a simple Rayleigh drag term, $-\nu_0^{sp}(\mathbf{v} - \mathbf{v}_0)$.

$$\nu_0^{sp} = \frac{1}{5\Delta t} \frac{1}{2} \left(1 - \cos \left[\pi \frac{k_{sp} + 1 - k}{k_{sp}} \right] \right), \quad (1.58)$$

where k is the layer number, from 1 to the sponge layer k_{sp} . k_{sp} is set to be the integer nearest to $nk/5$, or roughly the upper 20% of the layers, so that when 10 layers are used, $k_{sp} = 2$. When $k = 1$, $\nu_0^{sp} = 1/(5\Delta t)$ is strongest.

The model also includes critical thermodynamic effects (such as ortho-para hydrogen conversion) and chemistry and some basic cloud physics (methane abundance and cloud formation)[98]. The thermodynamic and cloud features can be turned on or shut off. When they are shut off, the model is simply a fluid dynamic one.

In my work, a two-flux radiation model is imported to EPIC, for the study of the seasonal changes of Uranian atmosphere. Also, to study the effects of the bright companions to the dark spots, an advanced methane cloud model is included with vapor to ice phase change, following the scheme presented by Palotai and Dowling[75].

1.5 Computer Resource

In our simulations, four clusters are being used: KFC4, KFC5, KFC6I and KFC6A. These clusters were constructed by the the members in our lab. The information about the these clusters are shown in Table 1.1.

In our simulations, we normally have four simulation domains. The quarter globe domain is often used when we initially do tests. It ranges from -90° to the equator in latitude and -90° to 90° in longitude. The pole to pole half globe domain ranges from -90° to 90° in latitude and -90° to 90° in longitude. Also, in some tests, we use the

Table 1.1: Clusters used in this work

Name	System	Processor	Memory	#	Year
KFC4	cAos 3.4.3	AMD Athlon XP 2500+	512 MB	48	2004
KFC5	cAos 3.4.3	AMD Athlon 64 3200+	512 MB	47	2005
KFC6I	cAos 3.4.3	Intel Core 2 Duo e6400 2.13GHz	1 GB	23	2006
KFC6A	cAos NSA1	AMD Athlon 64×2 4600+ 2.4GHz	1 GB	23	2006

1. Memory is the size of the RAM in each node.
2. # is the number of the nodes.
3. Year is the year when the cluster was constructed.
4. Each cluster has one server, which has the same processor and memory as the nodes, and has hard drives and CD-ROM. The operation system is installed on the server and each node can get the OS from the server via the network when it is booted.

hemisphere domain, which includes 90° in latitude and 360° in longitude. In most cases, the whole globe domain is used, which includes 180° in latitude and 360° in longitude. Our simulations show that to simulate the Great Dark Spots, the whole globe domain is needed.

The horizontal grid spacing is also an important parameter for the cost of the computer resource. Normally, we have two kinds of grid spacing in the simulations of the dark spots. The coarse grid setup has grid spacing 0.7° and the fine grid setup has grid spacing 0.35° . Therefore, for whole globe domain, with coarse grid setup, the horizontal grid number is 256×512 and the time step is 60 seconds; with fine grid setup, the horizontal grid number is 512×1024 and the time step is 30 seconds. In the simulations of the radiation model, because we need to simulate the whole global seasonal changes in 21 years, the horizontal grid spacing is 2.8° and so that the horizontal grid number is 64×128 and the time step is 240 seconds.

In the vertical direction, normally, we use 10 layer setup. Since the top two layers are used as the sponge layers, the center layer of the dark spots should be far away from them. Therefore, the center layer of the simulated phenomena is often set in

from layer 5 to layer 8.

In these clusters, for running the EPIC GCM in parallel, KFC6I is the fastest and KFC6A is second. Normally, for the whole globe simulations, we use eight nodes (16 cores) to run one case, considering the balance of the efficiency of the cluster and the running time of one case. With the coarse grid setup, it will cost about one actual day to simulate one month. With the fine grid setup, it will cost about eight day to simulate one month. The cluster KFC6A (with 8 nodes/16 cores) has 75.2% of the speed of KFC6I; the cluster KFC4 (with 16 nodes) has 55.9% of the speed of KFC6I and the cluster KFC5 (with 16 nodes) has 86.3% of the speed of KFC6I.

Chapter 2 Experimental Methodology

In this chapter, some methods used in the simulations with EPIC and data analysis will be discussed. To apply EPIC to simulate planetary atmospheres, including vortices, radiation heat transfer, clouds, and movement of the atmosphere, we need to input some initial conditions. One is the zonal wind profile. Another is the Pressure-Temperature profile. Besides the fitted curves discussed in chapter 1, we construct profiles with some related theories and methods. Furthermore, to study the vortices in atmospheres, we need to generate vortices to start the evolution. The methods about constructed zonal wind profiles, extended Pressure-Temperature profile and vortex generation will be discussed in section 2.1, 2.2 and 2.3.

2.1 Constructed Zonal Wind Profiles

In 1971, in a study of vortices in air flow, Moore and Saffman [66] determined analytical conditions for a stable elliptical vortex with uniform vorticity in background shear flow with a constant vorticity. In 1981, based on the work of Moore and Saffman, Kida [43] found exact solutions for unsteady elliptical vortices. In 1990, the Kida vortex theory was used by Polvani et al.[76] to interpret the oscillation of the GDS on Neptune. In this model, by adjusting the vorticity difference between the ellipse and the background and the shape of the ellipse, a reasonable match to the observed shape oscillation could be achieved. In 1994, Meacham et al.[65] studied the ellipsoidal vortices with uniform potential vorticity in a three dimensional uniformly stratified background flow with constant buoyancy frequency N .

These previous analytical works indicate the importance of the background vorticity. A suitable background area with constant vorticity seems to be associated with a stably evolving vortex. In our work, we try to modify the background absolute

vorticity to yield suitable constructed zonal wind profiles. That remains consistent with the observational results. As seen in chapter 1, because of the long distance to Neptune and Uranus and the limited number of observations, there are sizeable gaps and considerable uncertainty in the observational results. Fitted curves can give us some sense about the basic zonal wind shapes, but there is still a lot of space for modification within the cloud distributions.

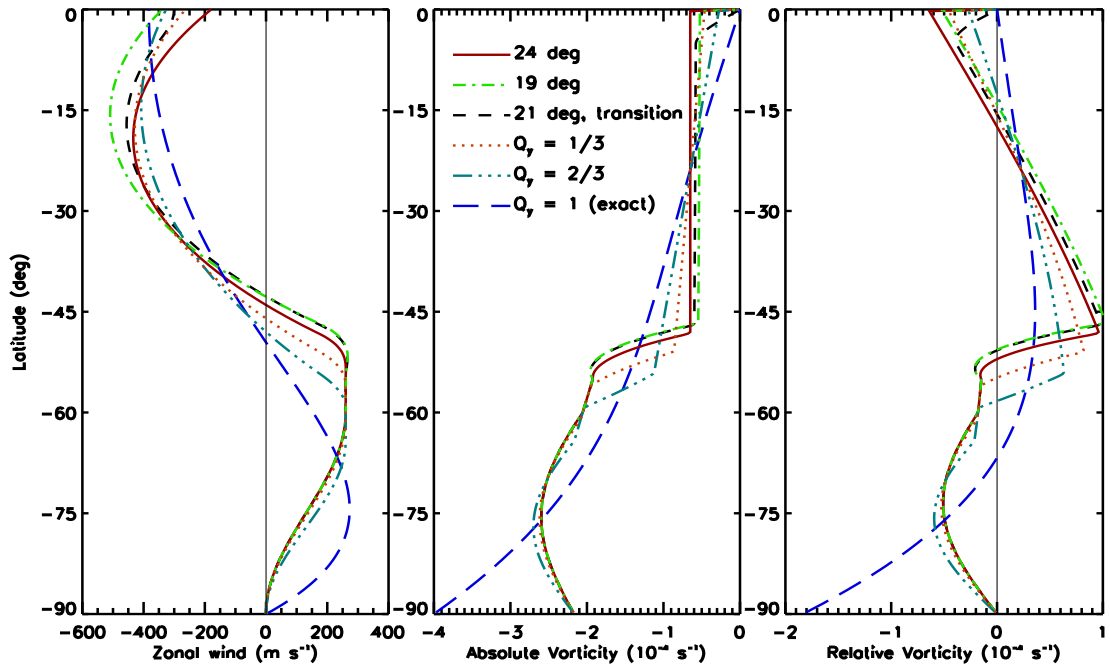


Figure 2.1: Left: Zonal wind profiles used in the Neptune study. Middle: Corresponding absolute-vorticity profiles. Right: Corresponding relative-vorticity profiles. Default $Q_y = 0$, default $\lambda_0 = -24^\circ$, if not mentioned. The wind profiles for the northern hemisphere are symmetric to the southern ones. This figure is from LeBeau and Deng 2007[47].

For Neptune, based on the Sromovsky et al.[91] fit of cloud drift rate ($Q_y=1$ (exact) in Figure 2.1), idealized velocity profiles are constructed to create regions of uniform absolute vorticity. The parameters for the Sromovsky et al. profile are shown

in Figure 1.11. The equation to calculate the fitted curve is

$$u(m/s) = \frac{(-3.19 + 6.74 \times 10^{-4} \times \phi^2 + 2.54 \times 10^{-7} \times \phi^4)}{60 \times 60} \times \frac{\pi}{180} \frac{r_e}{\sqrt{1 + \left(\frac{r_p}{r_e} \times \tan \phi\right)^2}}. \quad (2.1)$$

From Figure 2.1 we can see that the Sromovsky et al. 1993 profile does not have a constant absolute vorticity, but is instead roughly linear with latitude throughout the mid-latitude regions to the equator. To compare with the typical assumption of a uniform background vorticity in Kida theory and Meacham theory of three dimensional oscillating vortices[43][64], we would like to construct a method to achieve a near constant absolute vorticity environment. Considering the absolute vorticity at a reference latitude $(\zeta + f)_0$, we can fix a region of constant absolute vorticity about this latitude. Then we have

$$\zeta + f = (\zeta + f)_0 \Rightarrow -\frac{1}{rR} \frac{\partial(ur)}{\partial\lambda} + f = (\omega + f)_0. \quad (2.2)$$

In order to study the effect of the change of the background absolute vorticity, we can further allow for a linear variation with latitude of the background absolute vorticity, following the approach from LeBeau and Deng[47]. Integration of equation 2.3 with suitable parameters will give suitable wind profiles with fixed values for absolute vorticity gradient:

$$-\frac{1}{rR} \frac{\partial(ur)}{\partial\lambda} + f = (\omega + f)_0 + Q_y \beta^* R_0 (\lambda - \lambda_0), \quad (2.3)$$

$$\beta^* \equiv \left[\frac{1}{R} \frac{\partial}{\partial\lambda} (\omega + f) \right]_{\lambda=\lambda_0}. \quad (2.4)$$

In the above equations, r and R are the longitudinal and meridional radii of curvature. The coriolis parameter is $f = 2\Omega \sin \lambda$, where Ω is the rotation rate of the planet ($1.083 \times 10^{-4} s^{-1}$ for Neptune). The constants $(\omega + f)_0$, β^* , and R_0 are evaluated

at λ_0 . The default reference latitude is $\lambda_0 = -24^\circ$, but to move the turn-off point (the zero gradient point near 18°S) of the zonal wind profile to higher latitudes (so that the crossing-zero point in the relative vorticity is at higher latitudes), some other reference latitudes are also used. The constant $\beta^* = 5.76 \times 10^{-12} m^{-1} s^{-1}$ (from $\lambda_0 = -24^\circ$) with $Q_y = 1$ is the fit Sromovsky et al. profile between the equator and $\sim 50^\circ\text{S}$ (this number changes, because different profiles may reach maximum wind speed at different latitudes). Profiles with fractional Q_y values such as $2/3$, $1/3$, and 0 in Figure 2.1 are also used in different cases. The profiles at higher latitudes are modified to transit smoothly to the zero velocity at the pole (also the zero point at the pole in the relative vorticity curve). Furthermore, to make the velocity cross the equator smoothly, some curves are modified near the equator (see the 21 deg, transition case in Figure 2.1).

For Uranus, a similar approach is used in which the initial zonal wind profiles are the fits based on the observed data. The three fitted curves are shown in Figure 1.16. The related equations are 1.4, 1.6 and 1.7. The modification to construct artificial zonal wind profiles is based on the most recent fitted curve, the Sromovsky and Fry 2005 profile. Besides the basic fitted curves, the main difference from Neptune's artificial zonal wind profiles are the reference latitude and the scale of the modified region. For Uranus, 28°N serves as the reference latitude and $\beta^* = -4.48 \times 10^{-12} m^{-1} s^{-1}$. Different from Neptune simulations, in the Uranus cases the modified regions with near-constant absolute vorticity are much smaller, ordinarily about 10 degrees. Note that the kink in the curve of the Sromovsky and Fry 2005 fit near latitude 28°N and the corresponding absolute vorticity (Figure 2.2), suggests that this may reasonably reflect the current conditions on Uranus. Comparing with the symmetric Smith 1986 curve and the asymmetric Karkoschka 1998 curve and considering the current seasonal change on Uranus northern hemisphere, this may suggest that such configurations are seasonal on Uranus. Based on this, constructed zonal wind profiles are

created near this region, see Figure 2.3 and Figure 2.4.

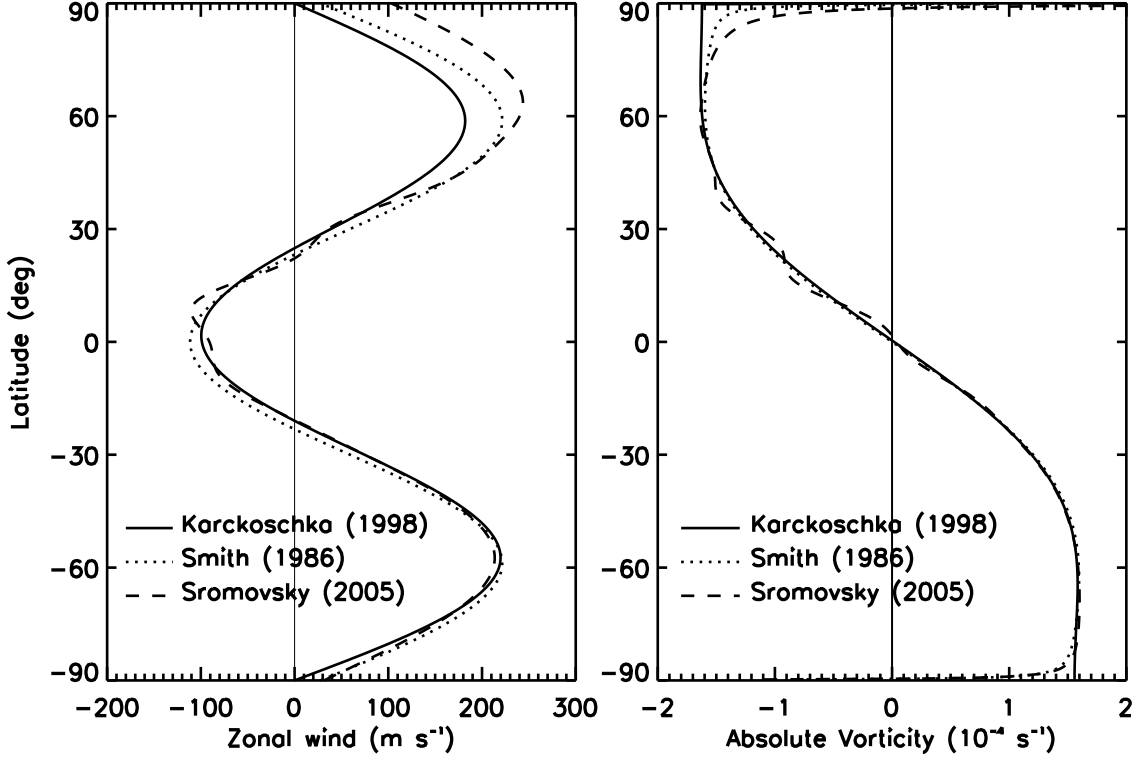


Figure 2.2: Left: Zonal wind profiles used in the Uranus study. Right: Corresponding absolute-vorticity profiles. "Smith (1986)" is a symmetric profile, while the other two are asymmetric. The equations for these profiles are from Sromovsky 2005[95].

Figure 2.3 shows the Sromovsky and Fry 2005 fitted curve and $Q_y = 0, 1/3, 2/3$ curves, together with data points from Hammel et al. 2005[35] and Sromovsky and Fry 2005[95] from the equator to 70°N . In the constructed profiles, the latitude area from 23°N to 33°N is modified and then smoothly connected to the Sromovsky and Fry 2005 profile. The constructed zonal wind profiles are in the error range of the observational data points. Corresponding absolute vorticity profiles are shown in the right panel. The $Q_y = 0$ case shows constant absolute vorticity in the studied region. Because at 28°N the Sromovsky and Fry 2005 profile has a small absolute vorticity gradient, the $Q_y = 1/3$ and $Q_y = 2/3$ profiles also show a small gradient in their

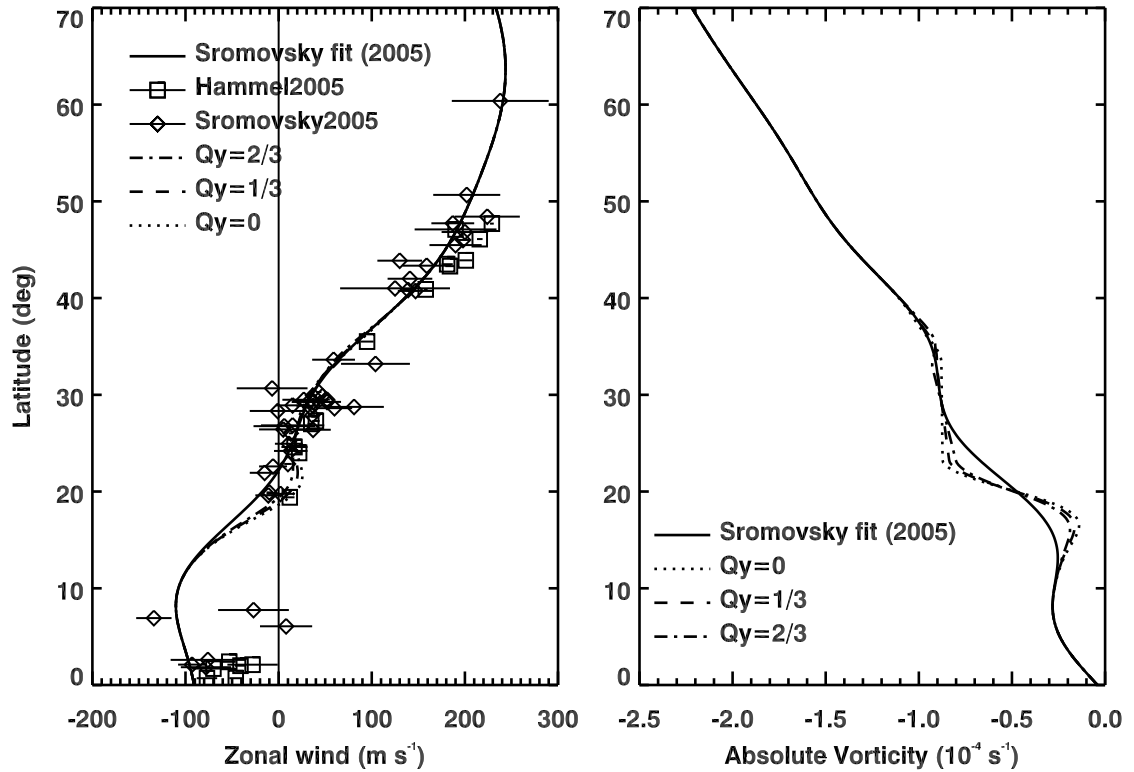


Figure 2.3: Left: Constructed zonal wind profiles used in the Uranus study, from the equator to 70°N. Observational data points [35][95] and Sromovsky and Fry 2005 profile are plotted to compare. Right: Corresponding absolute-vorticity profiles.

absolute vorticity profiles.

Figure 2.4 also shows those profiles, but only between 10°N to 40°N latitude in order to reveal more details in the area near the UDS. This plot also shows an averaged data set calculated from Hammel et al. 2005[35] and Sromovsky and Fry 2005[95] plotted from 21°N to 30°N. Looking at the modified region, the constructed zonal wind profiles are a reasonable representation of the observational data.

2.2 Constructed Pressure-Temperature Profiles

For the vertical P-T profile, the basic approach is to construct temperature-pressure profiles using the known data and then extending it to the deeper regions of the

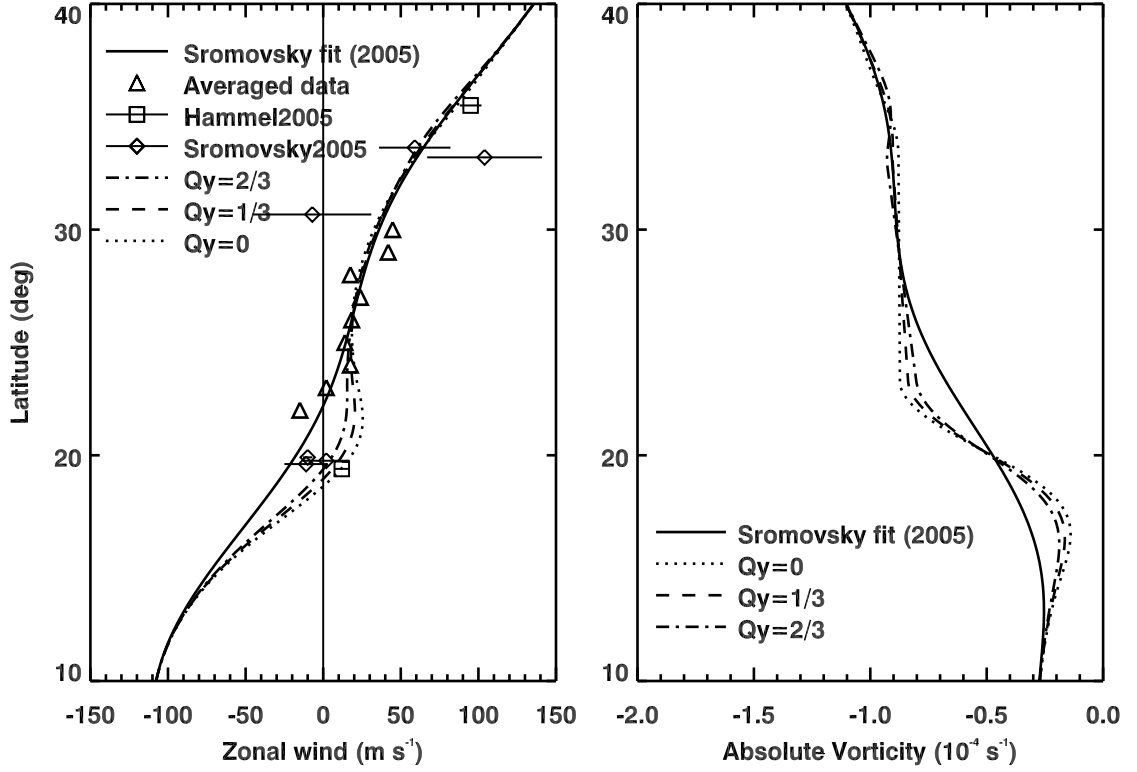


Figure 2.4: Left: Constructed zonal wind profiles used in the Uranus study, from 10°N to 40°N. In the modified region, averaged data points are calculated from the observational results[35][95]. Right: Corresponding absolute-vorticity profiles.

atmosphere with constant buoyancy or Brunt-Väisälä frequency N . The constant buoyancy frequency assumption is consistent with Meacham et al. 1994[65]. This means

$$N^2 = \frac{g}{\theta} \frac{\partial \theta}{\partial z} = \frac{g}{\theta} \frac{\partial \theta}{\partial p} \frac{\partial p}{\partial z} = N_0^2. \quad (2.5)$$

To relate this with the P-T profile, consider the definition of θ in equation 1.39, then[45],

$$\begin{aligned} \frac{\partial \theta}{\partial p} &= \left(\frac{p_0}{p} \right)^{\frac{R}{C_p}} \frac{\partial T}{\partial p} - \frac{RT}{C_p} \left(\frac{p_0}{p} \right)^{\frac{R}{C_p}-1} \frac{p_0}{p^2} \\ &= \frac{\theta}{T} \frac{\partial T}{\partial p} - \frac{R}{C_p} \theta \frac{1}{p}. \end{aligned} \quad (2.6)$$

Now, using the hydrostatic relation $\partial p/\partial z = -\rho g$,

$$N^2 = \frac{\rho g^2}{pT} \left(\frac{R}{C_p} T - p \frac{\partial T}{\partial p} \right). \quad (2.7)$$

Applying the ideal gas law $p = \rho RT$, we can get

$$N^2 = \frac{g^2}{RT^2} \left(\frac{R}{C_p} T - p \frac{\partial T}{\partial p} \right) = N_0. \quad (2.8)$$

When $\partial T/\partial p = 0$, it is an isothermal case. Alternately, integrating the above equation

$$\int_{T_0}^T \left(\frac{R}{C_p} T - \frac{N_0^2 R T^2}{g^2} \right)^{-1} dT = \int_{p_0}^p \frac{1}{p} dp, \quad (2.9)$$

and setting $T_N \equiv \frac{R}{C_p} g^2 / N_0^2 R = g^2 / (N_0^2 C_p)$ yields

$$\left(\frac{T_N - T_0}{T_N - T} \right) \frac{T}{T_0} = \left(\frac{p}{p_0} \right)^{R/C_p}. \quad (2.10)$$

In the above equations, g is gravitational acceleration, R is the ideal gas constant, and C_p is the specific heat at constant pressure. In the test cases, EPIC simulation results were not significantly sensitive to N , so only $N^2 = 0.64 \times 10^{-4} s^{-2}$ is used for most Neptune simulations.

Figure 2.5 shows the P-T profile for Neptune simulations. The left panel shows the constructed P-T profiles with $N^2 = 0.64 \times 10^{-4} s^{-2}$ and $N^2 = 0.36 \times 10^{-4} s^{-2}$, and the nominal profile from Conrath 1991. For the constructed profiles, the Conrath 1991 data is used above 300 mbar. The extension of the $N^2 = 0.64 \times 10^{-4} s^{-2}$ profile starts from pressure 300 mbar with temperature 54.5 K and that of the $N^2 = 0.36 \times 10^{-4} s^{-2}$ starts from pressure 500 mbar with temperature 59.0 K.

For Uranus, a value of $N^2 = 0.09 \times 10^{-4} s^{-2}$ is used in the simulations, Figure 2.6 shows the P-T profile for Uranus simulations. Here, the constructed P-T profiles with $N^2 = 0.64 \times 10^{-4} s^{-2}$ and $N^2 = 0.09 \times 10^{-4} s^{-2}$, and the nominal P-T profile from

Lindal et al. 1987[54]. For Uranus, the both extensions start from pressure 630.96 mbar with temperature 65.3 K.

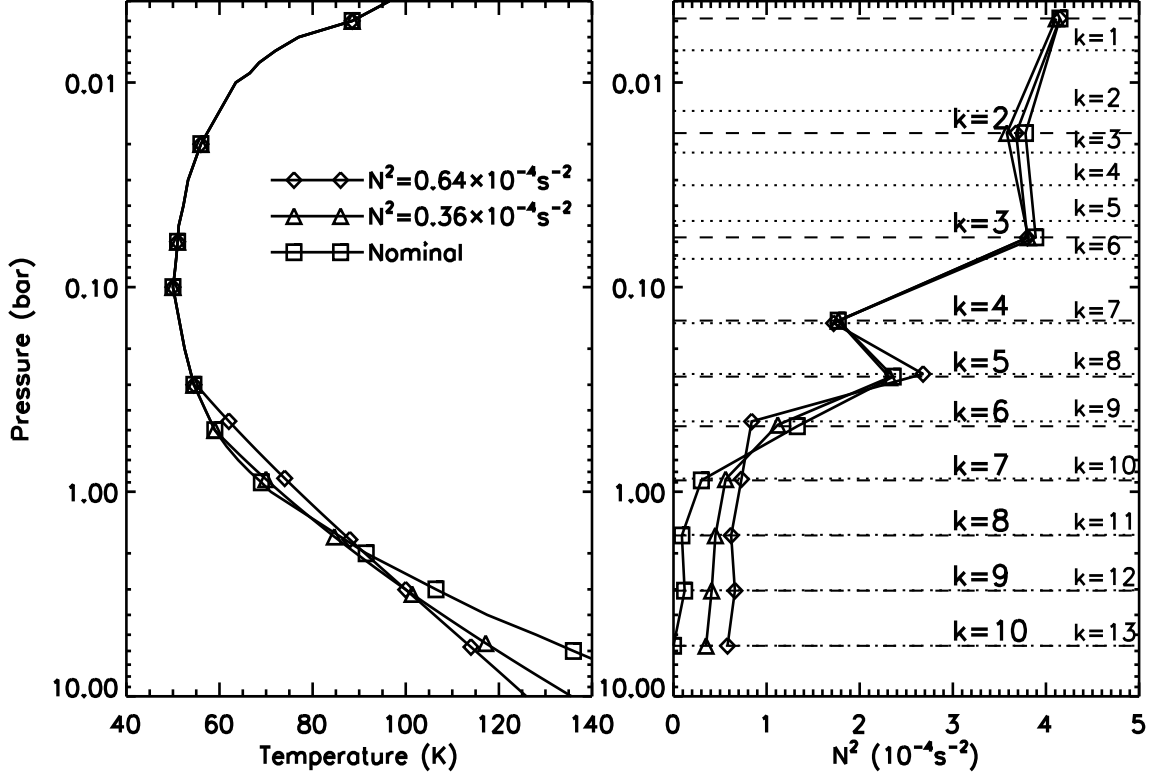


Figure 2.5: Left: Vertical P-T profiles for Neptune, $N^2 = 0.64 \times 10^{-4} \text{ s}^{-2}$ profile is the one used in the current simulations. Right: Corresponding N^2 values in EPIC for different layers. Here 10-layer setup and 13-layer setup are shown on the right plot.

2.3 Vortex Generation

To study the great vortex evolution in the atmospheres, we need to generate vortices in the model. Currently, there are two main methods to insert a vortex into the flow field in EPIC. One is perturbing the Montgomery potential in a manner approximately in geostrophic balance; another is modifying the velocity directly via a stream function.

As discussed previously, in Kida theory[43] and its application to the explanation of GDS-89 by Polvani et al. in 1990[76], there is a vortex region with uniform vorticity

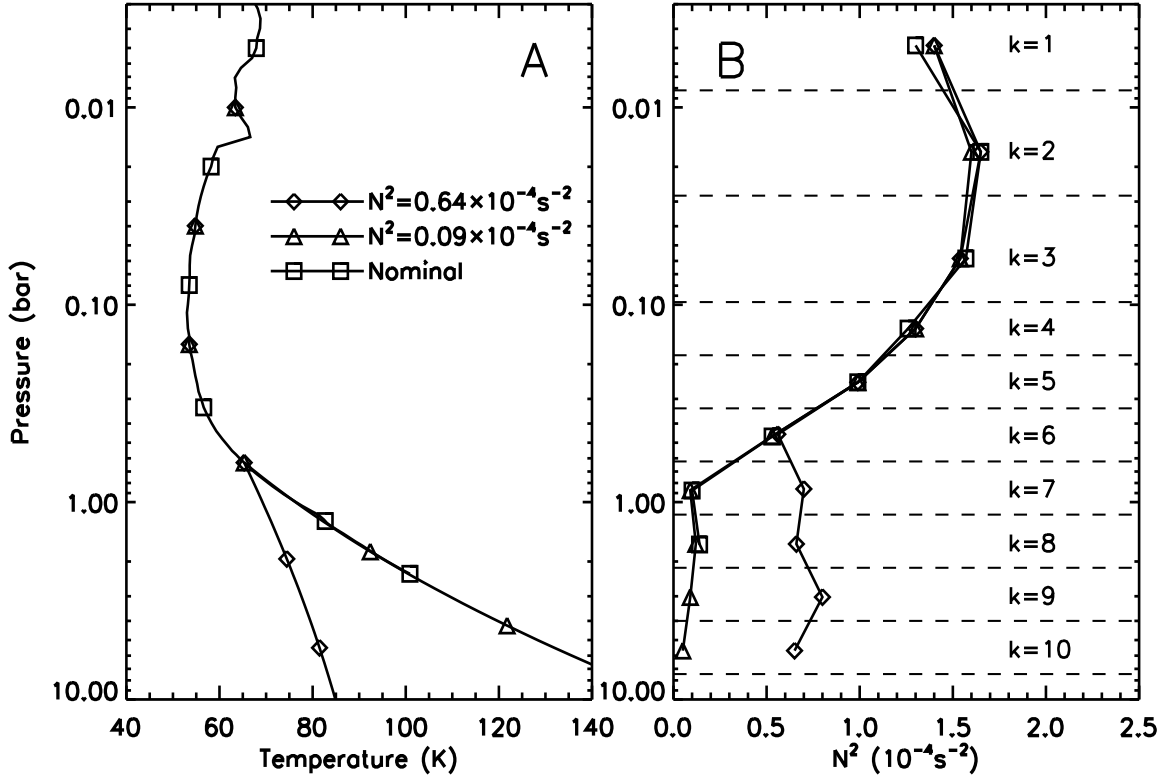


Figure 2.6: Left: Vertical P-T profiles for Uranus, $N^2 = 0.09 \times 10^{-4} \text{ s}^{-2}$ profile is the one used in the current simulations. Right: Corresponding N^2 values in EPIC for different layers.

in a background with another uniform vorticity. Therefore, one idea is to generate a uniform vorticity distribution. This also comes from GRS and White Oval data that suggest a region of uniform potential vorticity in the middle. To achieve this, the following method was presented by LeBeau in 1997[44].

Holton [39] gives the derivations to the inviscid horizontal momentum equation in isentropic coordinates and determines the following momentum conservation equation:

$$\frac{D\vec{v}}{Dt} + f\vec{k} \times \vec{v} = -\vec{\nabla}M, \quad (2.11)$$

where \vec{v} is the horizontal velocity, \vec{k} is the unit vertical vector and M is the Montgomery potential. Assume the vortex is in geostrophic balance and using a constant

Coriolis parameter, then

$$f_0 \vec{k} \times \vec{v} \approx -\vec{\nabla} M. \quad (2.12)$$

Take the divergence and solve for vorticity:

$$\begin{aligned} f_0 \vec{\nabla} \cdot (\vec{k} \times \vec{v}) &\approx -\nabla^2 M, \\ f_0 \vec{v} \cdot (\vec{\nabla} \times \vec{k}) - f_0 \vec{k} \cdot (\vec{\nabla} \times \vec{v}) &\approx -\nabla^2 M, \\ f_0 \zeta &\approx \nabla^2 M \Rightarrow \zeta \approx \frac{1}{f_0} \nabla^2 M. \end{aligned} \quad (2.13)$$

Fixing a constant relative vorticity $\zeta = \zeta_0$ and using radial coordinates, this equation becomes

$$\zeta_0 \approx \frac{1}{f_0} \frac{1}{r} \frac{\partial}{\partial r} \left(r \frac{\partial M}{\partial r} \right). \quad (2.14)$$

One simple solution is $M(r) = a_0 + a_2(r/L)^2$ with $a_2 = f_0 \zeta_0 L^2 / 4$. Since the required vortex region is an elliptical shape, we can design an equation to replace r with elliptical r_{el}

$$r_{el}^2 = x^2 + AR^2 y^2, \quad (2.15)$$

where AR is the aspect ratio of the ellipse. To capture some of the latitudinal variation in the Coriolis parameter, multiply f/f_0 to the second term,

$$M \approx a_0 + \frac{f}{f_0} \left(\frac{f_0 \zeta_0 L^2}{4} \right) \frac{r_{el}^2}{L^2} = a_0 + \frac{f \zeta_0}{4} r_{el}^2. \quad (2.16)$$

To transit smoothly from the central vortex core to the background, LeBeau and Dowling[45] used an equation $M' = (f/f_0) A \operatorname{sech}^2(r_{el}/a_0)$ with A and a_0 defined to make $M = M'$ at $r_{el} = L$. Finally, we have the perturbation equation:

$$\Delta M = \begin{cases} a_0 + \zeta_0 r_{el}^2 f / 4 & , \quad r_{el}^2 \leq L^2 \\ A \operatorname{sech}^2(r_{el}/a_0) f / f_0 & , \quad r_{el}^2 > L^2 \end{cases}, \quad (2.17)$$

This method generates a near constant potential vorticity area on a constant potential vorticity background, as shown in Figure 2.7. The vortex velocity distribution generated with this method is given in Figure 2.8.

After deciding the Montgomery potential perturbation, the velocity can be calculated from the geostrophic approximation:

$$\vec{u}^G = \frac{1}{f} \left(-\frac{1}{R} \frac{\partial M}{\partial \lambda}, \frac{1}{r} \frac{\partial M}{\partial \phi} \right). \quad (2.18)$$

Including gradient-balance correction terms, the correction to the velocity field is:

$$\vec{u}^C = \left(u^G - \frac{1}{f} \left\{ \zeta^G u^G + \frac{1}{R} \frac{\partial K^G}{\partial \lambda} \right\}, v^G - \frac{1}{f} \left\{ \zeta^G v^G - \frac{1}{r} \frac{\partial K^G}{\partial \phi} \right\} \right), \quad (2.19)$$

where the G superscript refers to the geostrophic winds and the C superscript is the total correction to the existing zonal wind velocity field, K is kinetic energy per mass, r and R are the map factors from equations 1.48 and 1.49.

In 2001, Stratman et al.[98] provided a Gaussian style spot equation when they study the bright companion around the Great Dark Spot:

$$\Delta M = u_s (1.2 f_s R_e b_s) \exp \left\{ - \left[\frac{\phi - \phi_s}{a_s} \right]^2 - \left[\frac{\lambda - \lambda_s}{b_s} \right]^2 - \left[\frac{\ln p - \ln p_s}{c_s} \right]^2 \right\}, \quad (2.20)$$

where “s” denotes “spot”; ϕ_s , λ_s , p_s are the longitude, latitude and pressure position of the spot’s center; a_s , b_s and c_s set the spot’s size in longitude, latitude and pressure height, respectively; u_s sets the velocity amplitude. An example potential vorticity shape generated by this method is also shown in Figure 2.7, and the vortex velocity distribution generated with this method is given in Figure 2.8.

In the Uranus simulations, a new spot maker is being used, which changes veloc-

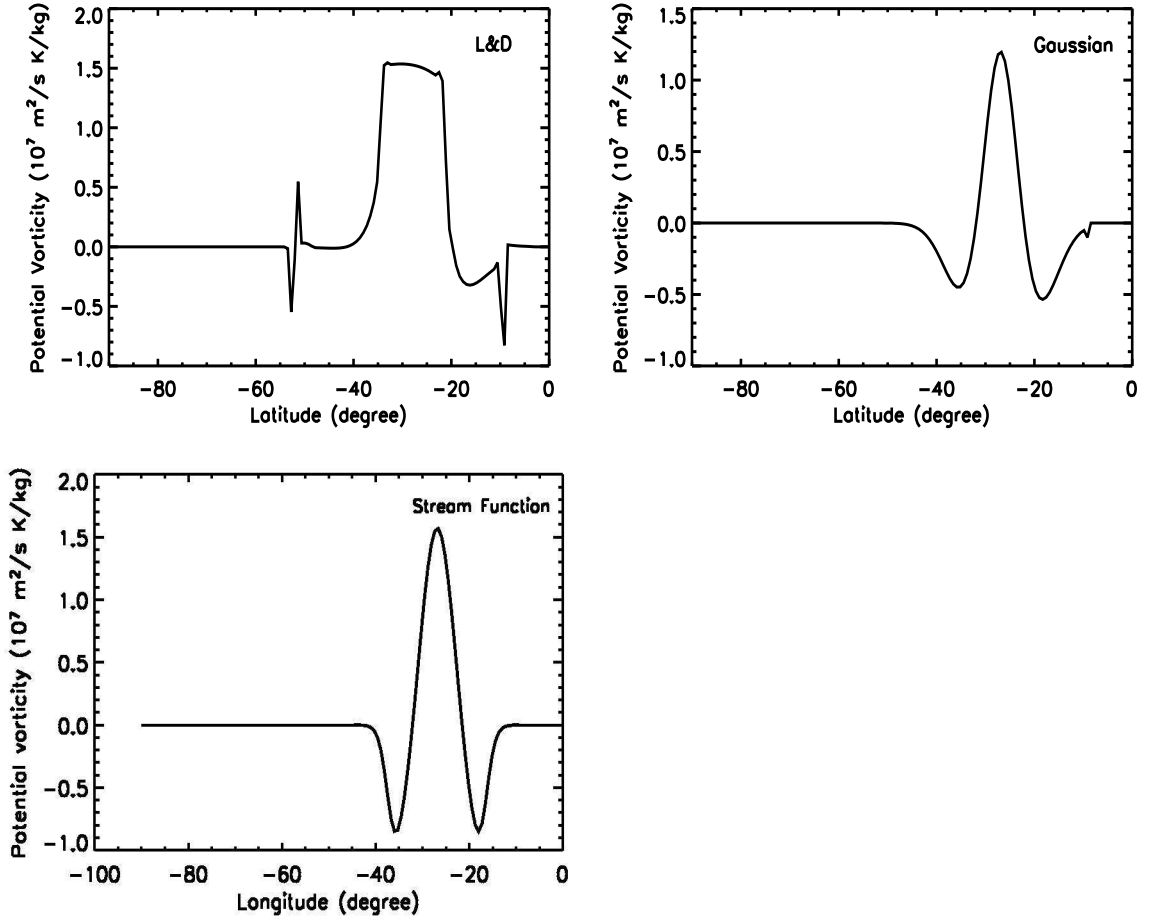


Figure 2.7: The three vortex shapes used in the simulations. The one from LeBeau and Dowling 1998 [45] is called L&D; the Gaussian one is from Stratman et al. 2001[98]; the last one is calculated from stream functions. These figures are from LeBeau and Deng[46].

ities from stream function. The stream function is defined in a Gaussian shape,

$$\psi = \psi_0 \times \exp \left\{ - \left[\frac{\phi - \phi_s}{a_s} \right]^2 - \left[\frac{\lambda - \lambda_s}{b_s} \right]^2 - \left[\frac{\ln p - \ln p_s}{c_s} \right]^2 \right\}. \quad (2.21)$$

ψ_0 is the constant used to modify the equation so that the calculated maximum velocity is as required. Other parameters are same as those in the above Gaussian method.

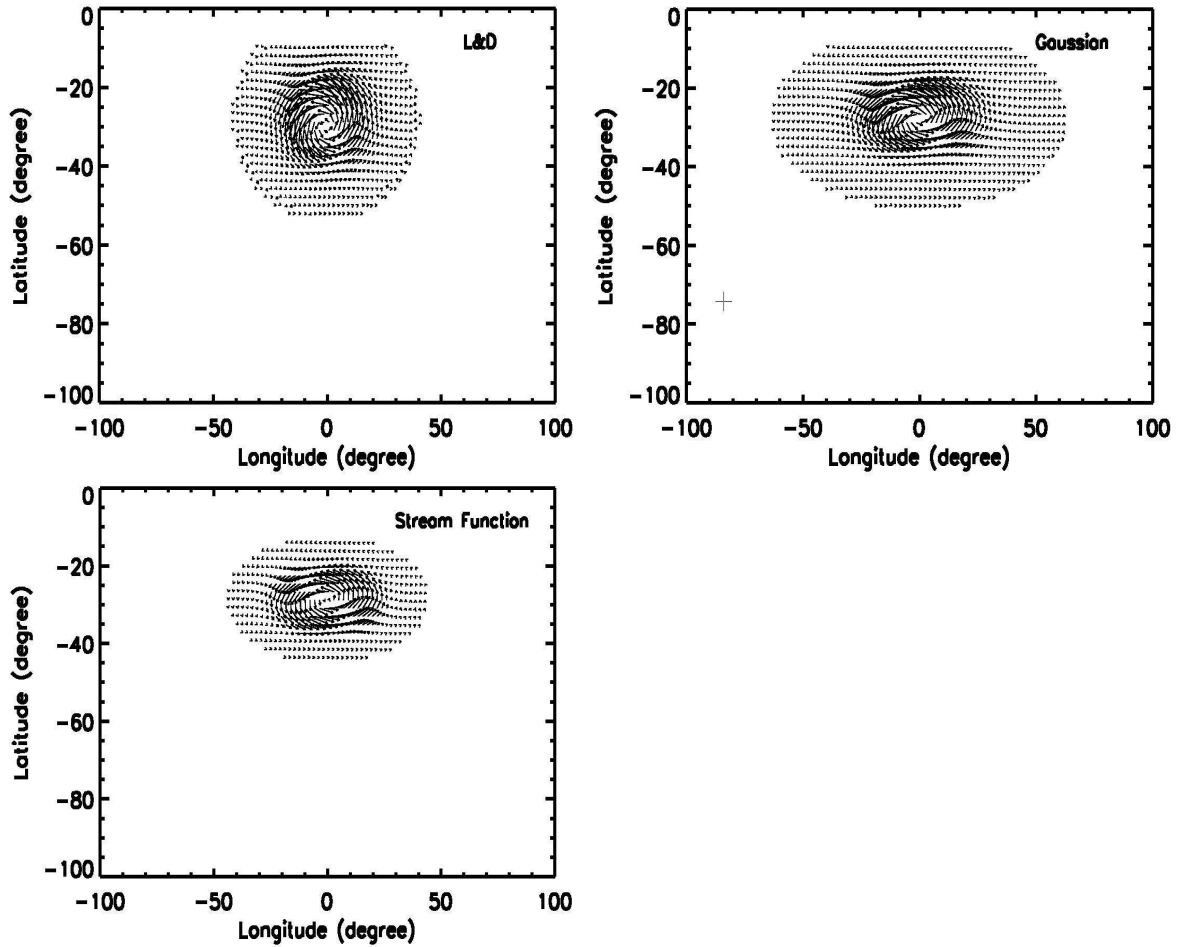


Figure 2.8: The vortex velocity distributions from the three vortex generation methods. The one from LeBeau and Dowling 1998 [45] is called L&D; the Gaussian one is from Stratman et al. 2001[98]; the last one is calculated from stream function. These figures are from LeBeau and Deng[46].

Then the velocities are calculated

$$u = -\frac{1}{R} \frac{d\psi}{d\lambda}, \quad v = \frac{1}{r} \frac{d\psi}{d\phi}. \quad (2.22)$$

An example of the potential vorticity shape generated with stream function method is shown in Figure 2.7. The vortex velocity distribution generated with this method is in Figure 2.8.

From Figure 2.7, we can see that in the two vortices generated by different Montgomery potential perturbation methods, the Gaussian one is relatively smoother.

However, from our simulations, this smoother vortex leads to weaker shape oscillations, which is not what we want when we study the Great Dark Spots on Neptune. The vortex generated via the stream function method shows the smoothest potential vorticity profile. In the Uranian Dark Spot simulations, we want to study the sustainability of the background environment and hope the spot can be stable as long as possible. Therefore, this smoothest shape is used in the UDS simulations. Furthermore, when we tried to simulate vortices near the ground on terrestrial planets, the methods based on the perturbation of Montgomery potential are all not suitable because of the solid bottom topography. In these cases, the stream function method still works well and generates clean vortices.

2.4 Fitting GDS with Least Squares Method

After the simulations, we need to analyze the resulting data. In the study of the Great Dark Spots on Neptune, because of the oscillation character, fitting the vortex with an ellipse is important. Only after we get the fitted ellipse can we study the oscillation of the aspect ratio and the orientation angle of the vortex.

In previous study of the GDS-89 by Polvani et al.[76] with Kida theory and Sromovsky et al.[91], the shape and size of the observed GDS-89 were defined by subjective visual estimates. In our study, we fit the contour of the potential vorticity of the simulated vortex with an ellipse, using Least Squares Method (LSM). The basic LSM method is discussed below[99].

The vector \vec{x} that minimizes $\|Ax - b\|^2$ is the solution to the normal equations

$$A^T A \vec{x} = A^T b. \quad (2.23)$$

This vector $\vec{x} = (A^T A)^{-1} A^T \vec{b}$ is the least squares solution to $A \vec{x} = \vec{b}$.

This can be summarized as: If $A \vec{x} = \vec{b}$ has no solution, multiply by A^T and solve

$$A^T A \vec{x} = A^T \vec{b} [99].$$

Given the measurements b_1, \dots, b_m at time t_1, \dots, t_m , the line $y = C + Dt$ which minimizes the error $\|e\|^2 = \|\vec{b} - A\vec{x}\|^2$ is determined by [99]

$$A^T A \vec{x} = A^T \vec{b}, \quad (2.24)$$

or

$$\begin{bmatrix} m & \Sigma t_i \\ \Sigma t_i & \Sigma t_i^2 \end{bmatrix} \begin{bmatrix} C \\ D \end{bmatrix} = \begin{bmatrix} \Sigma b_i \\ \Sigma t_i b_i \end{bmatrix}. \quad (2.25)$$

The best line is $y = \bar{b} + D(\bar{t} - \bar{t})$, with $D = \frac{\Sigma(t_i - \bar{t})b_i}{\Sigma(t_i - \bar{t})^2}$ and so $C = \bar{b} - D\bar{t}$.

In our case, notice the ellipse equation has the following form:

$$\frac{x'^2}{a^2} + \frac{y'^2}{c^2} = 1, \quad (2.26)$$

and so

$$y'^2 = c^2 + \left(-\frac{c^2}{a^2}\right)x'^2. \quad (2.27)$$

Letting $y = y'^2$, $t = x'^2$, $C = c^2$ and $D = -\frac{c^2}{a^2}$, we can get the form $y = C + Dt$ and so this theory and related equations can be applied in fitting the GDSs with ellipse lines.

To locate the spot in the simulation data, a prediction method on relative potential vorticity (local potential vorticity minus background potential vorticity) is applied. By subtracting the background potential vorticity, the remained relative potential vorticity field is clearer and the calculation can be more accurate.

To get the center of the Great Dark Spot, there are three method. One is locating the point with highest relative potential vorticity. This is the simplest method. But when there is high amplitude noise at some point or the spot is evolving, this method can be inaccurate. The second method is averaging the relative potential vorticity

with location weight. This method is more accurate. But still, when there are some noises, especially when additional vortices are generated, it is possible that the program will catch the wrong one and get wrong result. The third method is predicting the spot center from previous step. This method is helpful to locate the spot at a estimated area. But itself cannot give accurate spot center.

In our program, the three methods are all used to locate the spot center. When the program deals with the first data file, the prediction method cannot be used. The first two methods are combined to locate the spot center. The program uses method one to find the highest relative potential vorticity point, and then uses method two to calculate the weighted center. In later files, method two and method three are combined to locate the center.

After locating the center of the vortex, around this weighted center, the program looks for the positions of some points on the contour with a given critical value, similar to the contour plot method. The latitudes and longitudes of these points are in the vectors \vec{b}'' and \vec{t}'' , respectively. Considering the orientation angle α (in the program, a range of α values are tested to get the best fit),

$$b'_i = b''_i \sin(\alpha) + t''_i \cos(\alpha), \quad t'_i = b''_i \cos(\alpha) + t''_i \sin(\alpha). \quad (2.28)$$

Letting $b_i = b_i'^2$ and $t_i = t_i'^2$, we can get the two measurement vectors \vec{b} and \vec{t} . Applying the above theory and calculate C and D , then we can get $c = \sqrt{C}$ and $a = \sqrt{-C/D}$. In this way, the fitted elliptical equation is decided.

2.5 Power Spectrum Calculation

After fitting the potential vorticity contour with ellipse, we can get the data of aspect ratio vs. time and the data of orientation angle vs. time. These data points change with time to show the oscillation of the simulated Great Dark Spots. With these

data points, we can calculate the power spectrum. In our simulations, we extract a simulation data file after every 400 steps (6.67 hours). From the Nyquist-Shannon sampling theorem, this sampling frequency sets a limit to the analyzed frequency to have a period longer than 13.34 hours, which is much smaller than the observed 8-day period of GDS-89. Since in a simulation, the Great Dark Spot needs about one month for the adjustment, when we calculate the power spectrum, we use the data starting from 27.7 days (2,400,000 steps). Also, after several months, the simulated dark spot drifts closer to the equator and may lose its shape and steady movement. In this situation, we cut the later part to make sure the data used for the power spectrum calculation are in the time interval of steady drift and good oscillation.

The Fast Fourier Transform (FFT) is the most popular method to calculate a power spectrum. When FFT is used, evenly sampled data are required. In astronomy, people often need to deal with observational data, which are often unevenly sampled. When there are only a few gaps in the data, people can interpolate the data to get a evenly spaced data and then use FFT to calculate the power spectrum. When there are a lot of gaps or even most of the data points are not spaced equally, another method developed by Lomb can be used. This method is then called the Lomb method. In our work, although the data from the simulation results are spaced evenly, we follow the tradition of dealing with astronomical data and use the Lomb method.

Here, I follow the method presented in the book Numerical Recipes in C[78] to show the related equations and parameters. Consider N data points $h_i \equiv h(t_i)$, $i = 1, \dots, N$ with time series t_i and time span $T \equiv \max(t_i) - \min(t_i)$, the mean and variation can be calculated

$$\bar{h} \equiv \frac{1}{N} \sum_1^N h_i, \quad \sigma^2 \equiv \frac{1}{N-1} \sum_1^N (h_i - \bar{h})^2. \quad (2.29)$$

Then the Lomb normalized periodogram can be calculated from equation

$$P_N(\omega) \equiv \frac{1}{2\sigma^2} \left\{ \frac{\left[\sum_j (h_j - \bar{h}) \cos \omega(t_j - \tau) \right]^2}{\sum_j \cos^2 \omega(t_j - \tau)} + \frac{\left[\sum_j (h_j - \bar{h}) \sin \omega(t_j - \tau) \right]^2}{\sum_j \sin^2 \omega(t_j - \tau)} \right\}. \quad (2.30)$$

Here $\omega \equiv 2\pi f$ is the angular frequency, τ is a constant from

$$\tan(2\omega\tau) = \frac{\sum_j \sin 2\omega t_j}{\sum_j \cos 2\omega t_j}, \quad (2.31)$$

which makes the above $P_N(\omega)$ equation completely independent of shifting t_i by any constant. Different from FFT method, Lomb method weights the data on a "per point" basis without dealing with any time interval. Therefore, Lomb method can be used to deal with unevenly spaced data.

In this normalized equation, the significance level of a positive number z is calculated via equation

$$P(> z) \equiv 1 - (1 - e^{-z})^M, \quad (2.32)$$

where M is estimated from

$$M = 2N_p/ofac. \quad (2.33)$$

Here, $N_p = ofac \times hifac \times N/2$ is the number of different frequencies, $ofac$ is the oversampling factor, $hifac$ is the ratio of highest frequency f_{hi} to the Nyquist frequency calculated from $f_{nyquist} = N/(2T)$. In our work, we use $ofac = 4$ and $hifac = 1.2$. A smaller significance level indicates a more significant periodic signal and that the data are further departing from the null hypothesis - the data are independent Gaussian random points. In our work, we calculate z values for different significance levels 50%, 10%, 5%, 1%, 0.5% and 0.1% via the equation

$$z = -\ln(1 - (1 - P(> z))^{\frac{1}{M}}). \quad (2.34)$$

After these calculations, the power spectrum plot including the z values for different significance levels can be generated. Since we have the data for both aspect ratio oscillation and orientation angle oscillation, we can calculate two power spectra for one case. The result show that when the simulated dark spot is in a roughly good shape, these two power spectra are similar to each other with similar peak frequencies and similar magnitudes. This is consistent with a Kida model of the ellipse oscillations. Therefore, we use the data of orientation angle of the fitted ellipse to calculate a power spectrum. The z values for significance levels 1% and 0.1% are plotted with dashed horizontal straight lines in the power spectrum plots.

Chapter 3 Dynamic Simulations of Great Dark Spots on Neptune

In this chapter, we will talk about our dynamic simulations of Neptune's Great Dark Spots.

The discovery of GDS-89 and close observations by Voyager II [29][30][31][87][91] provide us an opportunity to study the environment of Neptune and great vortex phenomena in a planetary atmosphere. Similar to Jupiter, Neptune is a gas-giant planet and so has a bottomless atmosphere. The internal heat energy is also stronger than the solar insolation. Both Neptune and Jupiter have great vortices in their atmospheres. But different from Jupiter, which has a multi-jet zonal wind profile, Neptune has a much smoother zonal wind profile and the potential-vorticity gradient of the background zonal winds is mainly positive. The characteristics of relatively smooth zonal wind profile and the mainly positive potential-vorticity gradient are similar to the Earth. Studying the great vortex on Neptune provides an opportunity to understand the vortices on different planets and may be helpful to predict the behavior of great vortices on the Earth.

To study a great vortex, one approach is to track the small features in the vortex to get the velocity distribution. This was done on Jupiter to study the Great Red Spot and the white ovals. But on Neptune, because of the lack of cloud tracers, the rapid evolution of the GDS-89 and the covering of the bright companion, tracking the small features in GDS-89 was impossible. For NGDS-32 and NGDS-15, because of the long distance of the observations, people were not able to identify the detailed velocity distributions. Therefore, indirect methods were used to study the vortices. Smith et al. in 1989 estimated a vorticity number $0.9 \times 10^{-5} \text{s}^{-1}$ for the GDS-89 by dividing 2π by the 8.3-day oscillation period, and a vorticity number $2.3 \times 10^{-5} \text{s}^{-1}$ for the local background by assuming a difference in velocity of 100 m/s over 10° of

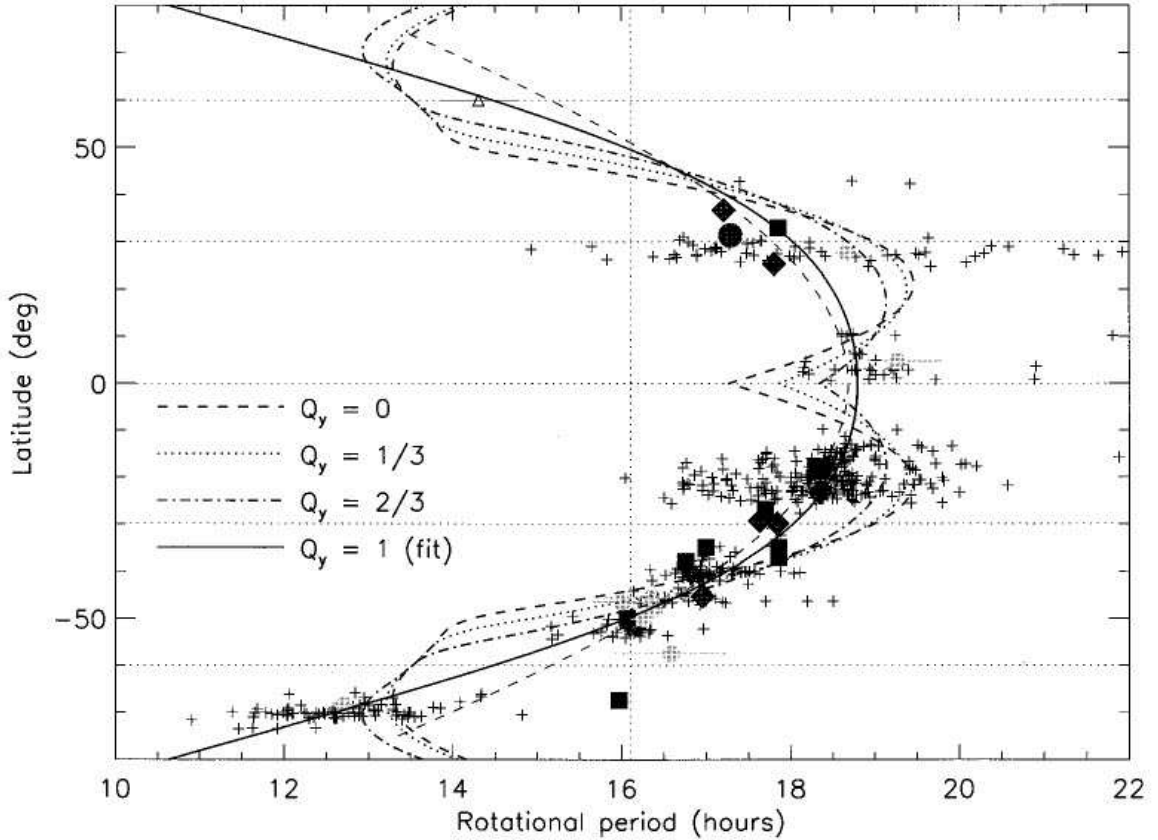


Figure 3.1: Sromovsky et al. 1993 fitted zonal wind profile and three constructed zonal wind profiles, comparing with the full set of cloud tracking data for Neptune. The $Q_y = 1$ curve is the fitted curve using the Limaye and Sromovsky 1991 data[53] (crosses) and the Lindal et al. 1990 data[55] (points). Lighter squares are pre-Voyager ground-based observations; darker squares are Voyager cloud-tracking data from Hammel et al. 1989[29]; circles and diamonds are post-Voyager HST observations from Hammel et al. 1995[32], Sromovsky et al. 1996[93], and Hammel and Lockwood 1997[33]. The lighter dashed line is the GDS-DS2 fit of Sromovsky et al. 1993[91]. Constructed profiles staying in the error range of the observational data points show that a range of possible change on the profile is permitted. This figure is from LeBeau and Dowling 1998[45].

latitude. This result showed that the GDS-89 vorticity was estimated to be smaller than the background vorticity, which was opposite from that of the Great Red Spot on Jupiter. Later, Polvani et al in 1990 applied the Kida theory [43] to study GDS-89 and its background and got the vorticity number $2.02 \times 10^{-5} \text{ s}^{-1}$ for the GDS-89 and the vorticity number $0.96 \times 10^{-5} \text{ s}^{-1}$ for the background zonal wind environment. Comparing to the above results in Smith et al 1989, this result shows a higher vorticity

for the vortex than that of the background.

Later, in 1998, LeBeau and Dowling[45] used EPIC to simulate GDS-like features and got the best match to the drift rate with a potential vorticity (PV) gradient one third that of the fitted Voyager zonal wind profile. They tested the GDS on Neptune with different Q_y (see equation 2.3 and Figure 3.1 and 3.2). In their simulations, shape oscillations and the tail-like features were also achieved. Their results prefer a background zonal wind profile near the GDS with $Q_y = 1/3$. In 2006, Dowling et al.[22] tested several Neptune cases with the new version of EPIC and found that $Q_y = 0$ is best to meet the observed drift rate $1.24^\circ/\text{month}$.

These previous works are relatively limited because of the lack of computer resources at that time or different goals of their own projects. Some qualitative results and a few quantitative results are achieved. The main values they study are the background Q_y , simplified oscillations, and drift rate. They did not investigate the effects of many parameters systematically. The constructed zonal wind profiles were also simple, just for what was, in effect, an initial study. All these need more work to get better understanding of the Neptune's atmosphere and the Great Dark Spots.

In this project about the dynamic simulations of GDSs, different parameters about the background and the great vortex are investigated systematically. GDS-89 is the main Great Dark Spot we will study. The drift rate 1.24 deg/month , the oscillation of the aspect ratio and the orientation angle with a period of 8.0 days are the main simulation targets. The size and its change as shown in equation 1.1 and Figure 1.5 and Figure 1.6 will also be used to judge the behavior of a simulation. Also, the effects of the CFD parameters are investigated.

The simulated Great Dark Spot will be defined as a closed contour of potential vorticity, which tracks the material movement of the vortex. This contour will be fitted with an ellipse applying the least squares method shown in Chapter 2. The drift rate will be calculated based on the location of the center of this closed contour.

The aspect ratio will be defined as the semi-minor axis/semi-major axis of this fitted ellipse.

3.1 Basic Parameters

In our simulations, different parameters are investigated, including Q_y , the reference latitude, vertical shear, and P-T profile of the background environment and the relative size, relative strength, initial aspect ratio, starting latitude and center layer of the vortex. Each parameter has its default value. If it is not mentioned in a simulation case, the default value is used.

For generating GDSs in EPIC, the default aspect ratio, AR , is 1.5. Since the observed GDS-89 drifted from 27°S to 17°S, the default starting latitude is $\lambda_0 = 28^\circ\text{S}$, giving some space for initial adjustment. The observed longitudinal size of the GDS-89 was 30° to 45° (12,000-18,000 km); the observed latitudinal extent was 12° to 17° (5200 - 7400 km); average size was 38°×14°. The perturbation of the Montgomery potential is similar to equation 2.17[22]:

$$\Delta M = \alpha(k)M_0 \frac{f}{f_0} \times \begin{cases} A_0 + A_2(r_{el}/L_{in})^2 & , \quad 0 \leq r_{el} \leq L_{in}, \\ \text{sech}^2(r_{el}/a_0) & , \quad L_{in} \leq r_{el} \leq L_{out}, \end{cases} \quad (3.1)$$

where $M_0 = 35,000 \text{ m}^2\text{s}^{-2}$, $f = 2\Omega\sin(\lambda)$ is the Coriolis parameter, $f_0 = f(\lambda_0)$, $a_0 = 5057 \text{ km}$, $A_2 = -(L_{in}/a_0)\text{sech}^2(L_{in}/a_0)\tanh(L_{in}/a_0) = -0.305$, and $A_0 = \text{sech}^2(L_{in}/a_0) - A_2 = 0.835$. To generate a GDS with suitable size, in the simulations, the range of the perturbation to the Montgomery potential is $L_{out} = 15171.4 \text{ km}$ and the inner flat part is $L_{in} = 4248 \text{ km}$. These are used as default numbers. When we give a relative size in a simulation case, it is multiplied to the L_{out} and L_{in} in the program to generate the spot with the corresponding size.

The vertical extent of GDS-89 was not well defined from the observations. In our simulations, in order to cover the main troposphere and part of the stratosphere,

the 10-layer set up in Table 3.1 is used as the default. In most cases, the vortex is generated through layer 5, 6, 7, 8 and 9 with amplitude parameter $\alpha(k)$ equal to 0.2, 0.6, 1., 1., and 0.5, respectively. When a relative strength is given in a simulation case, it will be multiplied to $\alpha(k)$ to generate the spot with corresponding strength. The default Brunt-Väisälä frequency in the deeper layer is $N = 0.8 \times 10^{-2} s^{-1}$.

Table 3.1: The default 10-layer setup on Neptune in the dynamic simulations

Layer	ζ [K]	P [mbar]	T [K]	θ [K]	N^2 [1/s ⁻²]
1.0	926.8	4.86505e+00	108.0	926.8	0.000415
2.0	345.6	1.76667e+01	68.7	345.6	0.000378
3.0	176.4	5.73261e+01	56.2	176.4	0.000380
4.0	115.6	1.50043e+02	54.1	115.6	0.000172
5.0	95.9	2.65731e+02	56.4	95.9	0.000276
6.0	85.1	4.53515e+02	62.0	85.1	0.000070
7.0	77.3	8.67930e+02	74.1	78.7	0.000055
8.0	64.1	1.63628e+03	87.0	71.9	0.000068
9.0	57.9	3.04411e+03	100.2	65.1	0.000057
10.0	51.6	5.66316e+03	113.7	58.2	0.000052

1. ζ is the hybrid vertical coordinate.
2. θ is the potential temperature.
3. N^2 is the square of the Brunt-Väisälä frequency (buoyancy frequency).

Because GDS-89 is relatively large (38° in longitude and 14° in latitude) and did not change too quickly (its oscillation period was 8 days and its drift rate was $1.24^\circ/\text{month}$), it is possible to simulate this phenomena with the relatively coarse grid setup (grid spacing 0.7°) and relatively long time step (60 seconds). After testing the grid spacing 1.4° , 0.7° and 0.35° , the 0.7° is the best one to balance the accuracy and the simulation time. With this grid spacing, after testing the time steps 80 seconds, 60 seconds, 30 seconds and 20 seconds, we found that when it is smaller than 60 seconds, the change of the simulation results is small compared to the 60-second case. Considering the balance between the accuracy and the simulation time, we

keep using time step 60 seconds in the simulations of Great Dark Spots on Neptune.

The first simulations conducted are on a quarter globe domain (latitude from south pole to equator, longitude from -90° to 90° with a periodic boundary, grids 128 in latitude times 256 in longitude). Then, we compare the quarter globe cases with whole globe (latitude from south pole to north pole, longitude from -180° to 180° , grids 256×512) cases. After that, we choose two basic zonal wind profiles and investigate the effects of different parameters. The vertical extent of most simulations is from about 2.3 mbar to 7.4 bar with 10 vertical layers. The basic time step is 60 seconds.

3.2 Quarter Globe Simulations

As a starting point, the quarter globe was chosen to investigate the effects of background zonal wind profiles, spot strength, starting latitude, and other parameters to give a basic idea about the nature of the dynamic simulations.

The first thing we investigate is the zonal wind profile. The used constructed zonal wind profiles are shown in Figure 3.2. In this plot, each Q_y corresponds to a constant gradient of absolute vorticity in a wide range below the equator. When $Q_y = 0$, we can get a profile with constant absolute vorticity.

Using standard spot parameters of relative strength 1, relative size 1 and initial aspect ratio 1.5, we constructed flat shape spots (LeBeau_Dowling) and started the spots from latitude $S32^\circ$. This yielded the simulation results shown in Figure 3.3.

From these simulations, we can see that when Q_y increases (so that the gradient of the absolute vorticity of the background zonal wind profile increases), the drift rate also increases. We can conclude that to get the observed small drift rate ($1.24^\circ/\text{month}$), we need small Q_y .

We also ran some cases with the Gaussian initial vortex shape and got the results shown in Figure 3.4. In this plot, we tried constructed zonal wind profiles $Q_y = 0$,

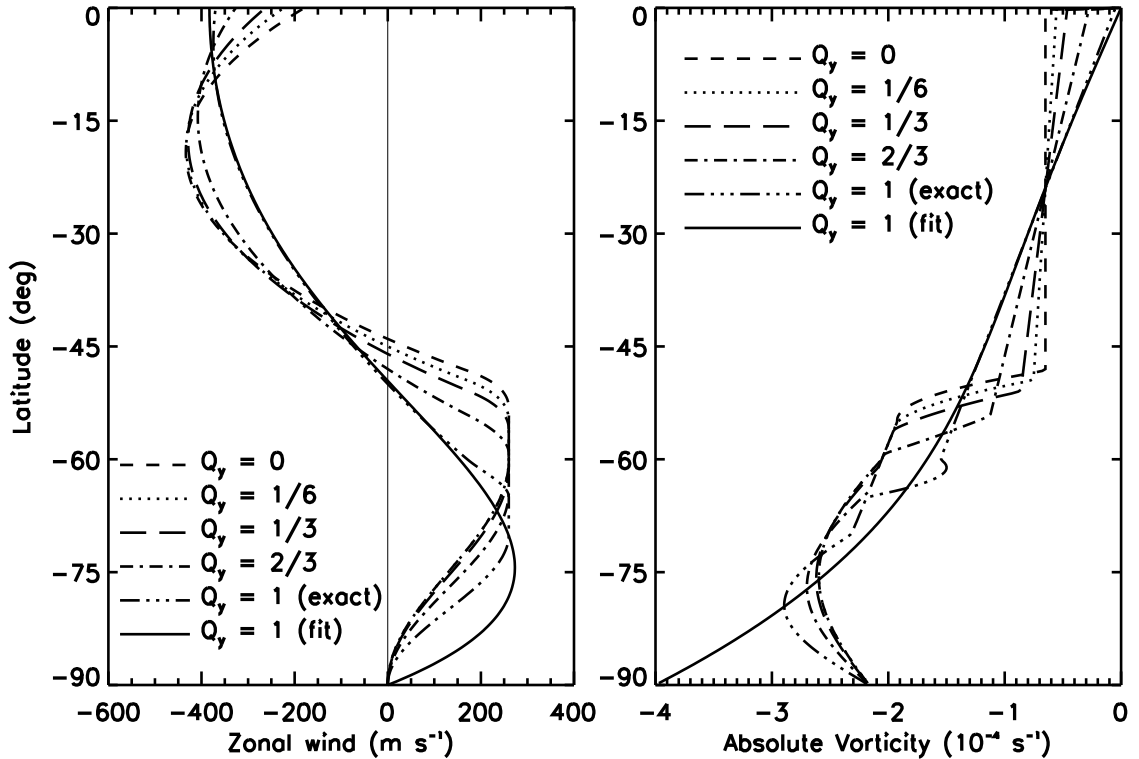


Figure 3.2: Fitted ($Q_y = 1$ (fit)) and constructed ($Q_y = 0$, $Q_y = 1/6$, $Q_y = 1/3$, $Q_y = 2/3$ and $Q_y = 1$ (exact)) Neptune’s zonal wind profiles. Left plot shows the zonal wind profiles in the southern hemisphere; right plot shows the absolute vorticity profiles corresponding to these zonal wind profiles.

$Q_y = 1/6$ and $Q_y = 1/3$ and altitude pressure 200 mbar, 500 mbar and 1000 mbar.

The results also show that the drift rate increases with Q_y and we need $Q_y \sim 0$ to get slow drift. For a higher Q_y value, deeper spots drift faster than shallower spots. Comparing the results of LeBeau and Dowling and Gaussian shape spots, we can also see that when Q_y is small, flat shape spots showed periodic oscillations, while Gaussian shape spots showed minimal oscillations. This is reasonable since a flat shape means sharp change of the absolute vorticity. Since the observation results showed strong oscillations, we use LeBeau and Dowling spots as default in our future simulations to Neptune’s GDSs.

As we know, the two main observational results known about Neptune’s GDS-89

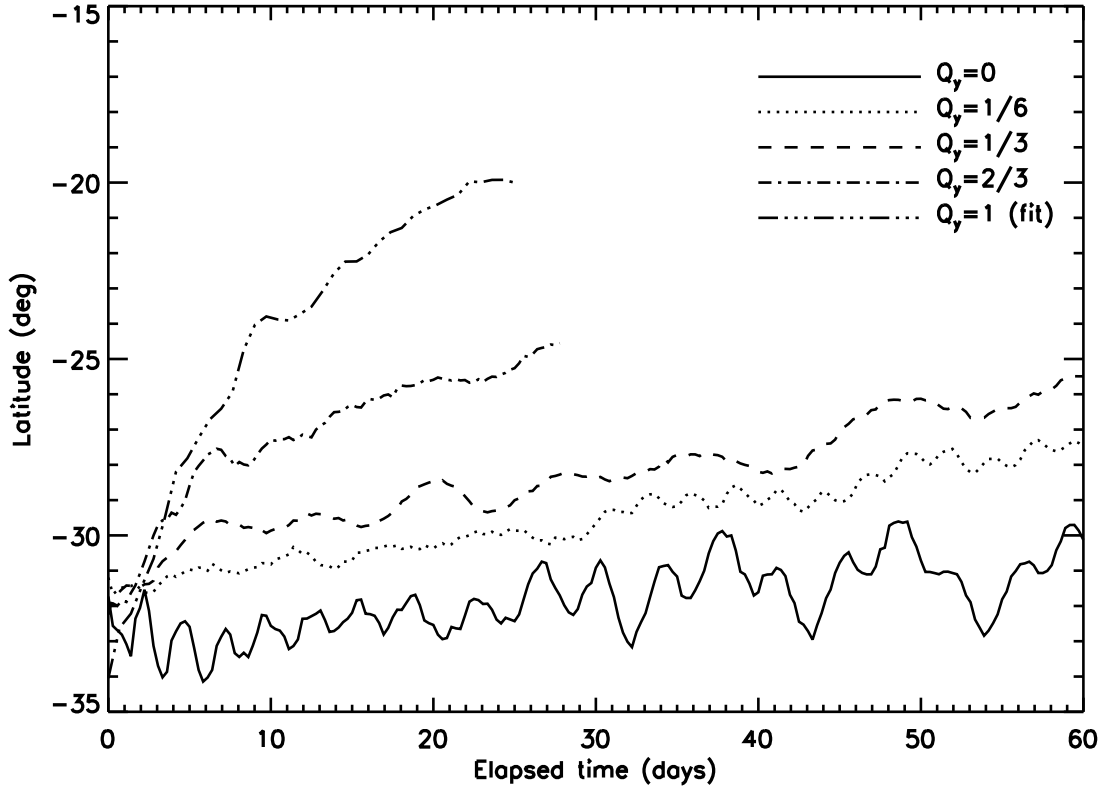


Figure 3.3: Drift curves of simulation results with different zonal wind profiles for LeBeau_Dowling spots. Other parameters used here are: reference strength 1, reference size 1, initial AR 1.5, and starting latitude S32°.

are drift rate and oscillation. Previously, some drift curves were shown in Figure 3.3 and Figure 3.4. Figure 3.5 shows the oscillation and tail formation of a spot including the ellipse fit to the spot with reference size 1, reference strength 1 with $Q_y = 0$ and starting latitude 28°. This plot is in layer 7 (868 mbar). Figure 3.6 shows the shape oscillation at layer 7 (868 mbar), layer 8 (1636 mbar) and layer 9 (3044 mbar). This case shows a 3-4 days period of oscillation in aspect ratio, angle and tail formation. Comparing with the observational results, the aspect ratio is too big and the oscillation period is about half of the observed 8-day period.

With suitable parameters, we can also get ≥ 8 day period oscillations with quarter globe domain, although it needs fine adjustment. Figure 3.7 and Figure 3.8 are similar

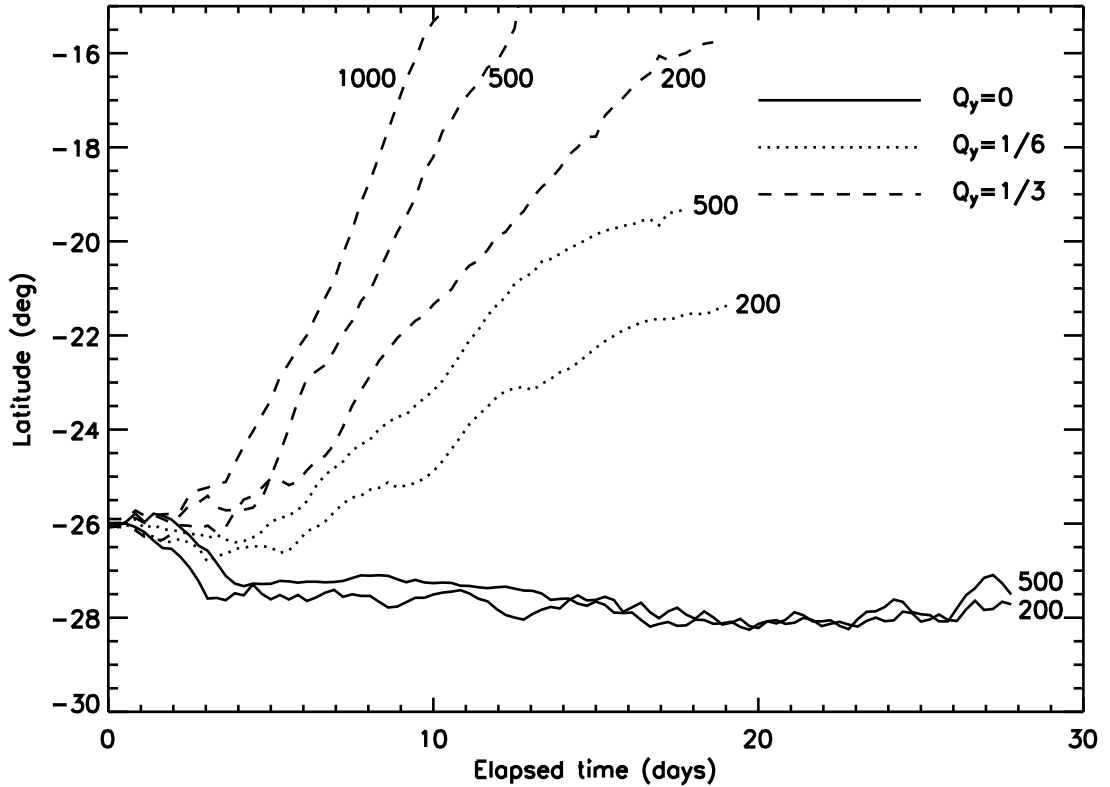


Figure 3.4: Drift curves of simulation results with different zonal wind profiles for Gaussian Spots at different altitudes. These cases all start from 26°S at 200 mbar, 500 mbar or 1000 mbar. The initial maximum velocity of these cases is 50 m/s.

to Figure 3.5 and Figure 3.6, but with $Q_y = 0.214$, relative strength 0.6 and starting from 32°S . We can see a ~ 9 -day oscillation from these plots.

Figure 3.9 shows the oscillation of the inverse aspect ratio (b/a) and the orientation angle ϕ (radians). Also, the power spectrum calculated from the ϕ (radians) oscillation is shown at the bottom. We can see that the S28 and S26 with $Q_y = 0$ cases show good oscillation with period ~ 3 days. The S31 with $Q_y = 0.214$ and the S32 with $Q_y = 0.286$ cases show longer period oscillations. However, these oscillations are not simple and not strong. Multiple peaks appear from frequency 0.1 to 0.2.

Figure 3.10 shows the phase plot of six cases with different period oscillations. The $Q_y = 0$, $\lambda_0 = -28$ and $\lambda_0 = -26$ cases give similar orientation angle vs. aspect

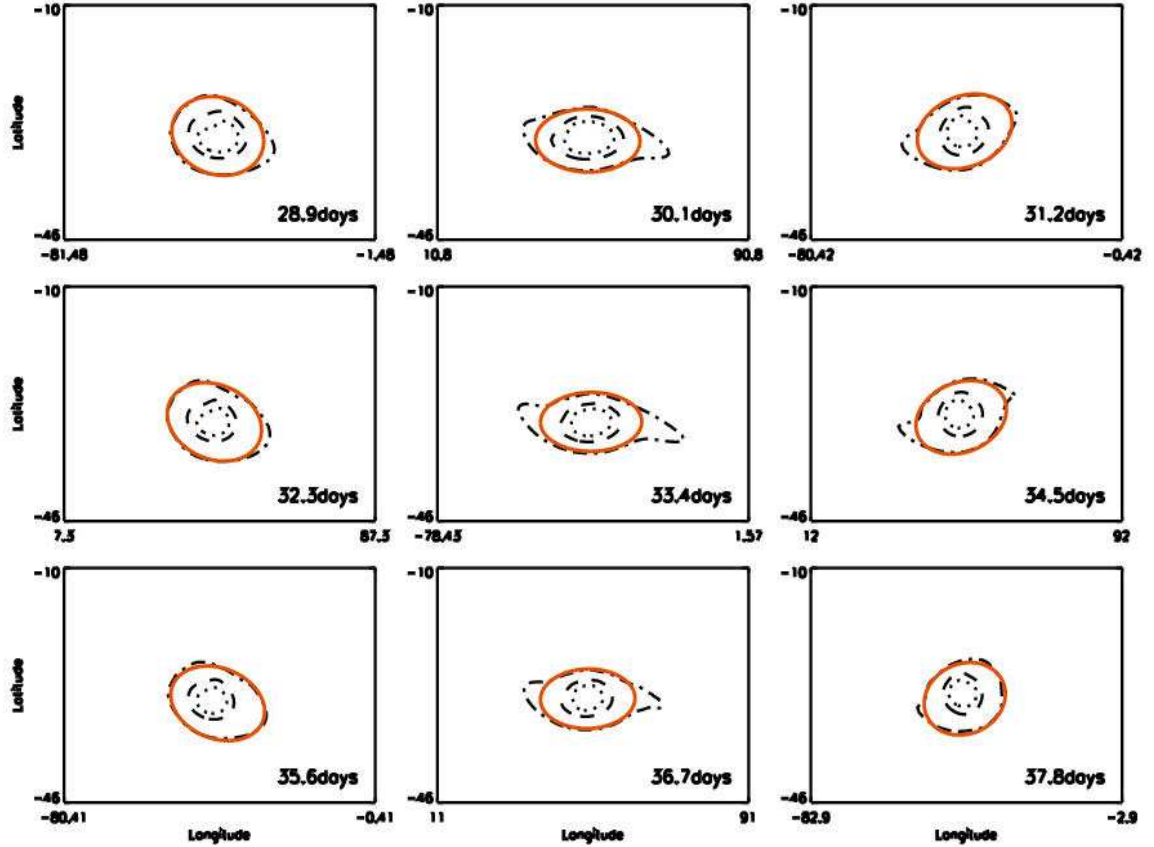


Figure 3.5: Oscillation and tail formation of GDS with $Q_y = 0$, reference size 1, reference strength 1 and starting latitude 28° . Solid curve is the ellipse fit. This plot is on layer 7 (868 mbar).

ratio shape as the top GDS and Kida plots. The problem here is that the aspect ratios are higher than the observed one. Also, as we can see Table 3.2, these two cases have ~ 3 day period oscillations. Other cases have ≥ 8 day oscillations, but from this table we can see that their oscillations are not strong and their average aspect ratios are small.

Previous simulations are all in the southern hemisphere, corresponding to GDS-89. Figure 3.11 shows the drift profile of the simulation to NGDS-32, comparing with the symmetric vortex in the southern hemisphere. We can see that their behaviors are totally symmetric. This is reasonable since the background profiles and the spots are totally symmetric. Therefore, in future simulations, we focus on the southern

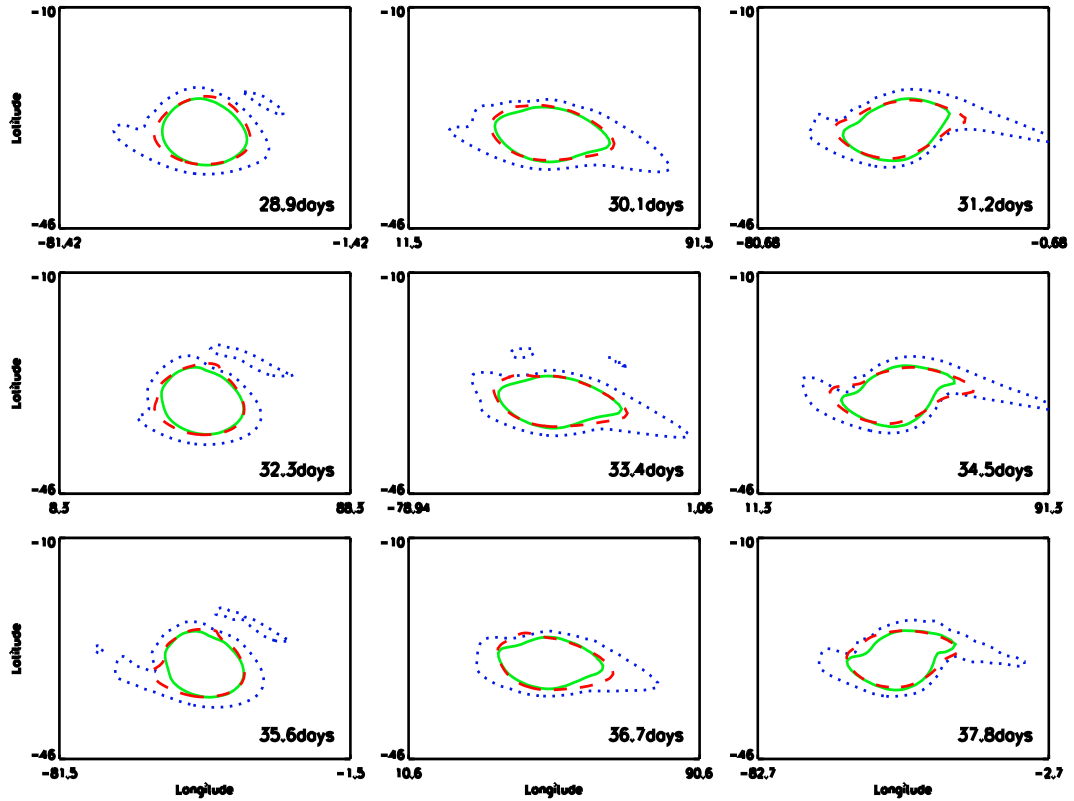


Figure 3.6: Oscillations of GDS at different layers with $Q_y = 0$, reference size 1, reference strength 1 and starting latitude 28° . Dotted contour is in layer 7 (868 mbar); solid contour is in layer 8 (1636 mbar); dashed contour is in layer 9 (3044 mbar).

hemisphere and the northern ones could be obtained from the corresponding southern cases.

In Table 3.2, most of the cases are quarter globe cases, but those marked with an * are pole-to-pole simulations. From this table, we can see that it is relatively easy to get ~ 3 -day oscillation, while it is much harder to get ~ 8 -day oscillation under these circumstances.

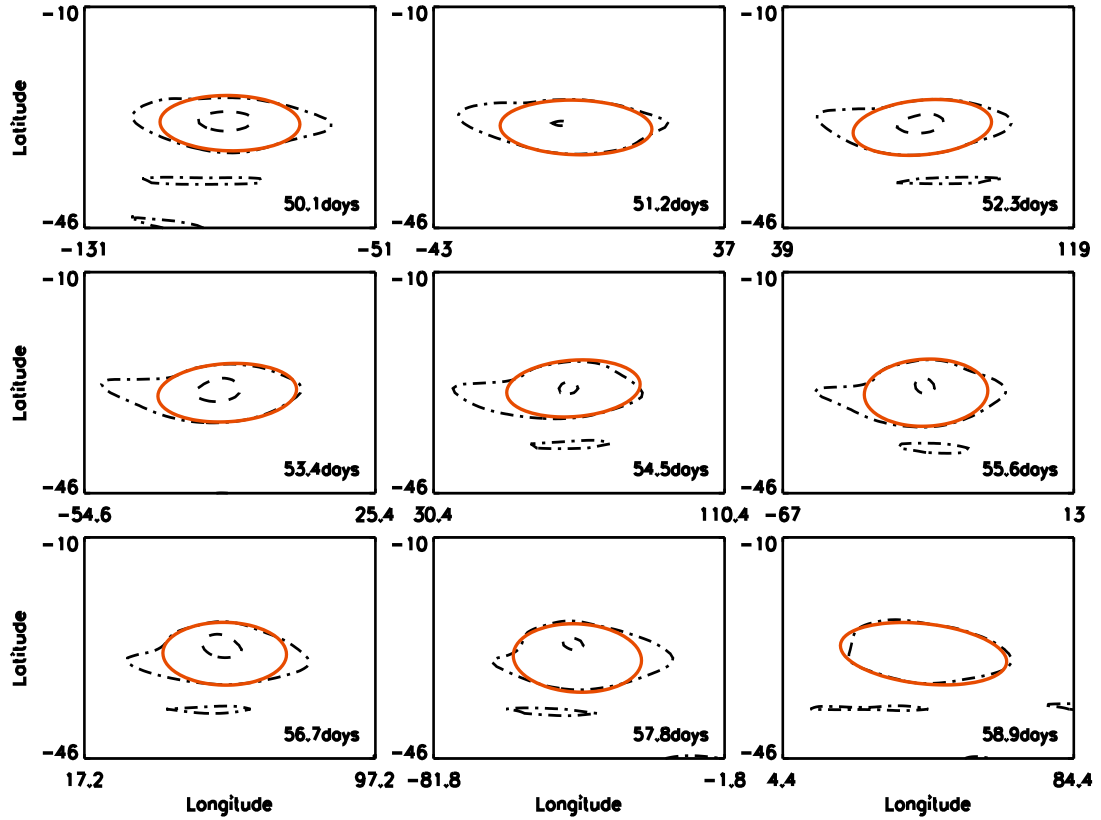


Figure 3.7: Oscillation and tail formation of GDS with $Q_y = 0.214$, reference size 1, reference strength 0.7 and starting latitude 32° . Solid curve is the ellipse fit. This plot is on layer 7 (868 mbar).

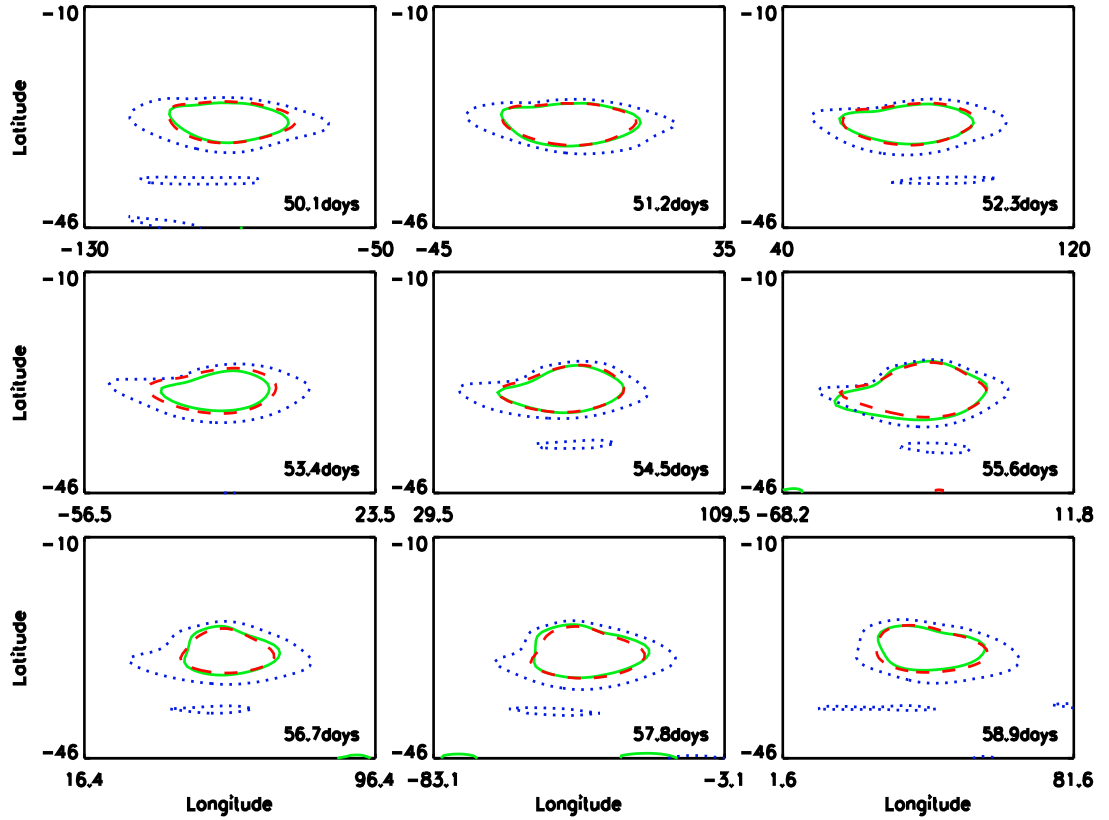


Figure 3.8: Oscillations of GDS at different layers with $Q_y = 0.214$, reference size 1, reference strength 0.7 and starting latitude 32° . Dotted contour is in layer 7 (868 mbar); solid contour is in layer 8 (1636 mbar); dashed contour is in layer 9 (3044 mbar).

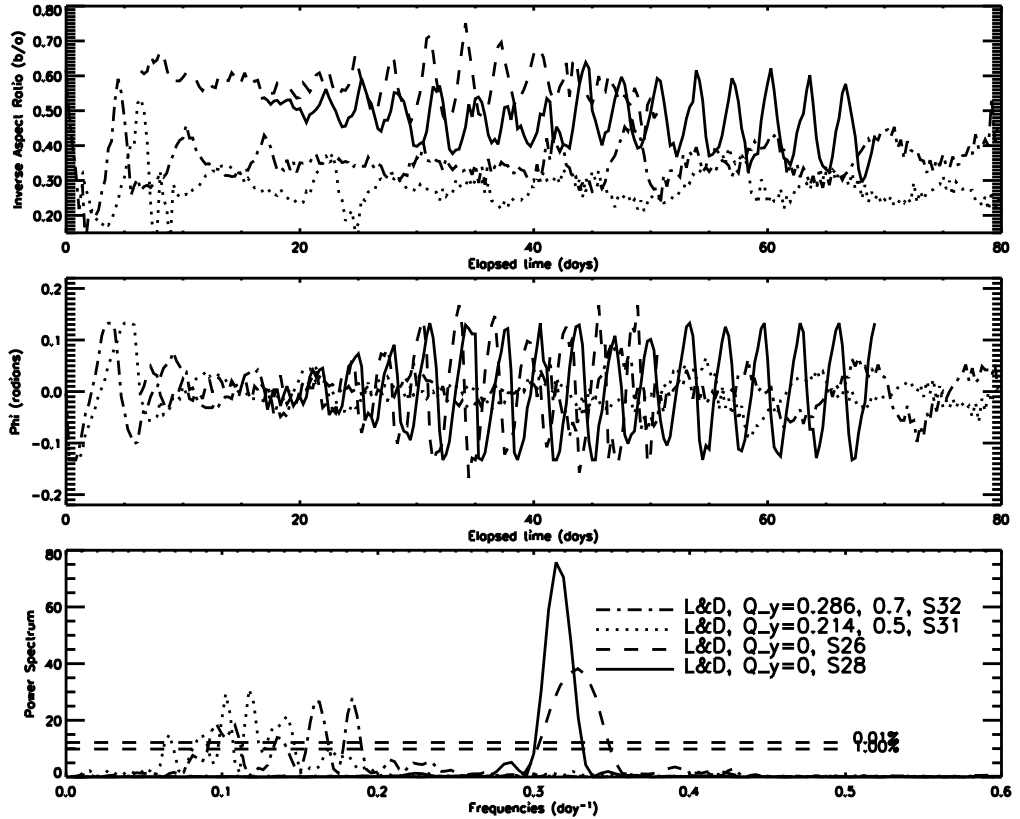


Figure 3.9: Oscillations of simulated GDS starting with different parameters. The top subplot is for the inverse aspect ratio (b/a); the middle one is for the orientation angle (radians); the bottom subplot shows the power spectrum calculated from the orientation angle oscillation data. The S26 and S28 cases are in $Q_y = 0$ background zonal wind profile and with reference strength 1, reference size 1 and initial AR 1.5. The S31 case is in $Q_y = 0.214$ profile and with reference strength 0.5. The S32 case is in $Q_y = 0.286$ profile and with reference strength 0.7.

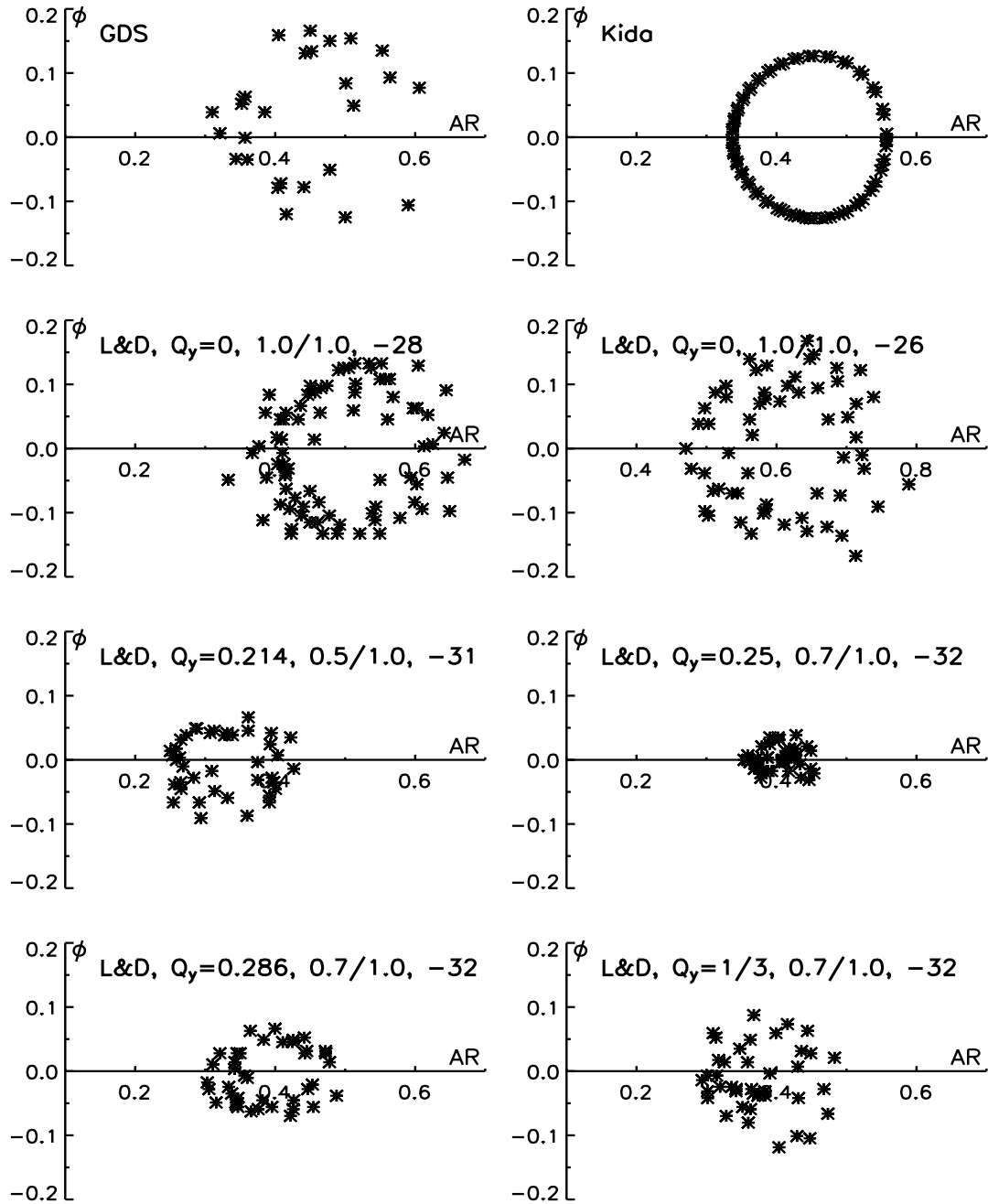


Figure 3.10: Phase plot for six LeBeau-Dowling vortices, having different initial conditions, starting from different latitudes and in the constructed zonal wind profiles with different Q_y . Top left plot is from Voyager-II observational results of GDS-89; top right plot is from Kida theory; others are as the parameters shown on them. All these cases are in quarter globe domain and the initial aspect ratios of the spots are all 1.5.

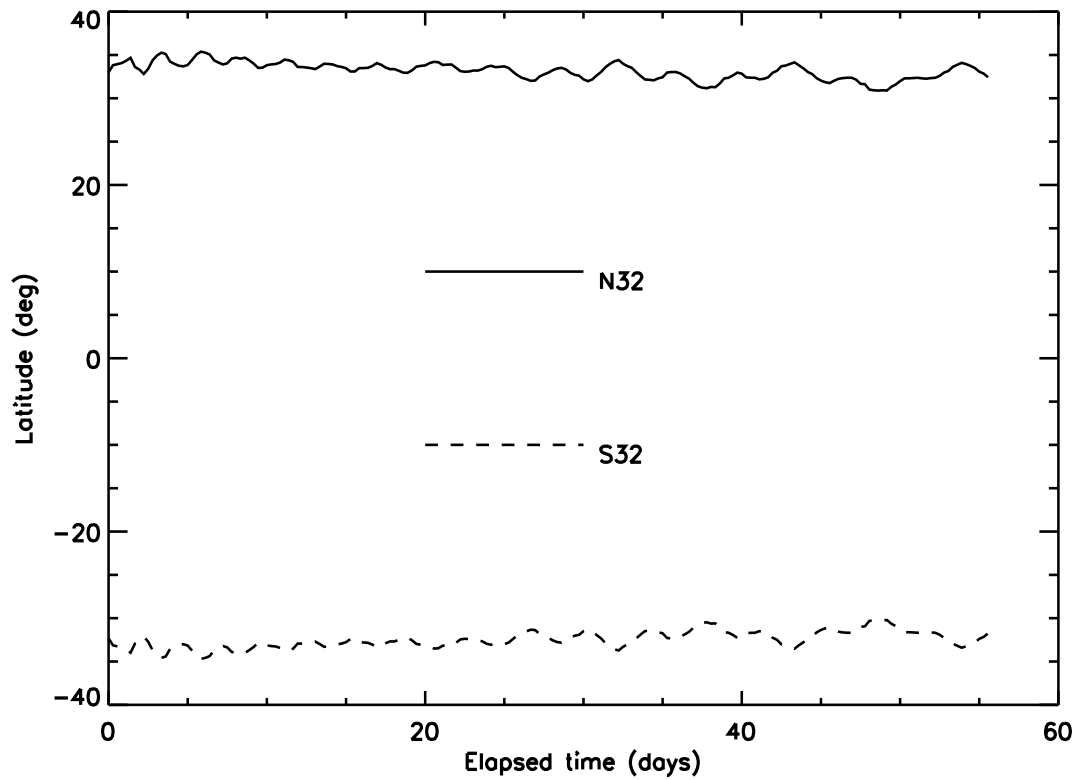


Figure 3.11: Simulation to NGDS-32, comparing with the symmetric case in the southern hemisphere. Basic parameters are: $Q_y = 0$, reference strength 1, reference size 1, initial AR 1.5 and starting latitude 32° .

Table 3.2: Selected simulation results for GDS-89 on Neptune. The Q_y values marked with an * are pole-to-pole simulations. Others are quarter globe simulations with latitude region from south pole to equator and longitude region from -90° to 90° .

Q_y	λ_0	Str./Size/AR	Drift	Period	Inverse AR	$\phi(\text{rad})$
	GDS-89 -18°S		1.24	8.0	0.42 ± 0.12	0 ± 0.15
	GDS-89 -22°S		1.24	8.0	0.35 ± 0.11	-
0	26°S	1.0/1.0/1.5	1.0	3.0	0.59 ± 0.14	0 ± 0.17
0*	26°S	1.0/1.0/1.0	-2.3	3.0	0.41 ± 0.16	0 ± 0.13
0*	26°S	1.0/1.0/1.7	-0.7	2.9	0.69 ± 0.13	0 ± 0.18
0	28°S	1.0/1.0/1.5	1.3	3.1	0.51 ± 0.16	0 ± 0.16
0	28°S	1.0/1.0/0.8	1.3	3.3	0.31 ± 0.11	0 ± 0.13
0	28°S	1.0/1.0/3.0	2.8	0.8	0.72 ± 0.22	0 ± 0.13
0	28°S	0.7/1.0/1.5	1.3	3.2	0.33 ± 0.21	0 ± 0.13
0*	28°S	1.0/1.0/1.5	0.9	3.2	0.48 ± 0.14	0 ± 0.13
0*	28°S	1.2/1.1/1.5	0.3	3.1	0.58 ± 0.13	0 ± 0.14
0	28°S	1.5/1.3/1.5	1.4	3.1	0.49 ± 0.27	0 ± 0.14
0	28°S	2.0/1.3/1.5	3.3	1.4	0.81 ± 0.20	0 ± 0.15
0*	28°S	2.0/1.3/1.5	0.5	1.7	0.75 ± 0.25	0 ± 0.13
0	30°S	1.0/1.0/1.5	0.7	3.1	0.49 ± 0.14	0 ± 0.17
0	32°S	1.0/1.0/1.5	1.2	3.6	0.40 ± 0.15	0 ± 0.14
0	32°N	1.0/1.0/1.5	-1.2	3.6	0.40 ± 0.15	0 ± 0.14
0	32°S	2.0/1.3/1.5	0.5	3.9	0.45 ± 0.07	0 ± 0.08
0	34°S	1.0/1.0/1.5	-0.8	4.3	0.36 ± 0.13	0 ± 0.13
0	34°S	2.0/1.3/1.5	-0.1	4.8	0.38 ± 0.02	0 ± 0.03
1/6	32°S	1.0/1.0/1.5	2.1	2.7	0.38 ± 0.04	0 ± 0.05
1/6	34°S	1.5/1.3/1.5	1.1	2.8	0.33 ± 0.07	0 ± 0.05
1/3	32°S	1.0/1.0/1.5	3.8	7.7	0.39 ± 0.05	0 ± 0.03
1/3	36°S	1.5/1.3/1.5	0.3	4.2	0.33 ± 0.02	0 ± 0.02
1/3	32°S	0.7/1.0/1.5	1.6	11.1	0.37 ± 0.08	0 ± 0.09
0.286	32°S	0.7/1.0/1.5	1.9	10.3	0.35 ± 0.07	0 ± 0.07
0.286	32°S	0.6/1.0/1.5	1.6	9.5	0.27 ± 0.06	0 ± 0.05
0.25	32°S	0.6/1.0/1.5	1.3	8.3	0.28 ± 0.07	0 ± 0.06
0.25	31°S	0.5/1.0/1.5	1.5	12.2	0.31 ± 0.09	0 ± 0.05
0.214	32°S	0.6/1.0/1.5	1.3	9.3	0.29 ± 0.06	0 ± 0.05
0.214	31°S	0.5/1.0/1.5	1.6	10	0.30 ± 0.08	0 ± 0.06

1. λ_0 is the starting latitude.
2. The unit of Drift is $^\circ/\text{month}$.
3. The unit of Period is days.
4. Str./Size/AR is Initial Strength/Initial Size/Initial Aspect Ratio.
5. $\phi(\text{rad})$ is the oscillation orientation angle amplitude, in radian unit.

3.3 Comparison to Whole Globe Simulations

After some basic investigations using a quarter globe domain, some cases were investigated with a latitudinal half globe domain (southern hemisphere, latitude from south pole to equator, longitude from -180° to 180°), some cases were investigated with a longitudinal half globe domain (south pole to north pole, longitude from -90° to 90°), and some cases were investigated with a whole globe domain. These simulations show that the simulation domain affected the resulting motions of GDS-like great vortices.

Figure 3.12 is an example of the effect of different simulation domains. These cases are all in the zonal wind profile with $Q_y = 0$ and reference latitude 24°S . The vertical P-T profile is the one with $N^2 = 0.64 \times 10^{-4} \text{s}^{-2}$. The inserted spots all have relative size 1, relative strength 1, initial aspect ratio 1.5 and start from 28°S . The only difference is the simulation domain, which is presented by the grid number of each case. We can see that when the domain is the longitudinal half globe domain, we can only see a ~ 3 -day oscillation; when the domain includes all the longitude, we can see another oscillation mode whose period is close to 8 days.

The differences among these simulations with different domains tell us that although quarter globe simulations can show the effect of some parameters, we need to use the whole globe domain to simulate the GDS if we want to get more accurate results and study the real effects of the parameters. This is especially important when we want to simulate the ~ 8 -day period oscillations of GDS-89.

Figure 3.13 shows the oscillation of the spot in a whole globe domain. We can see the change of the orientation angle, the change of the ellipse aspect ratio and the tail evolution. Comparing with Figure 3.5, a roughly eight-day period oscillation is apparent.

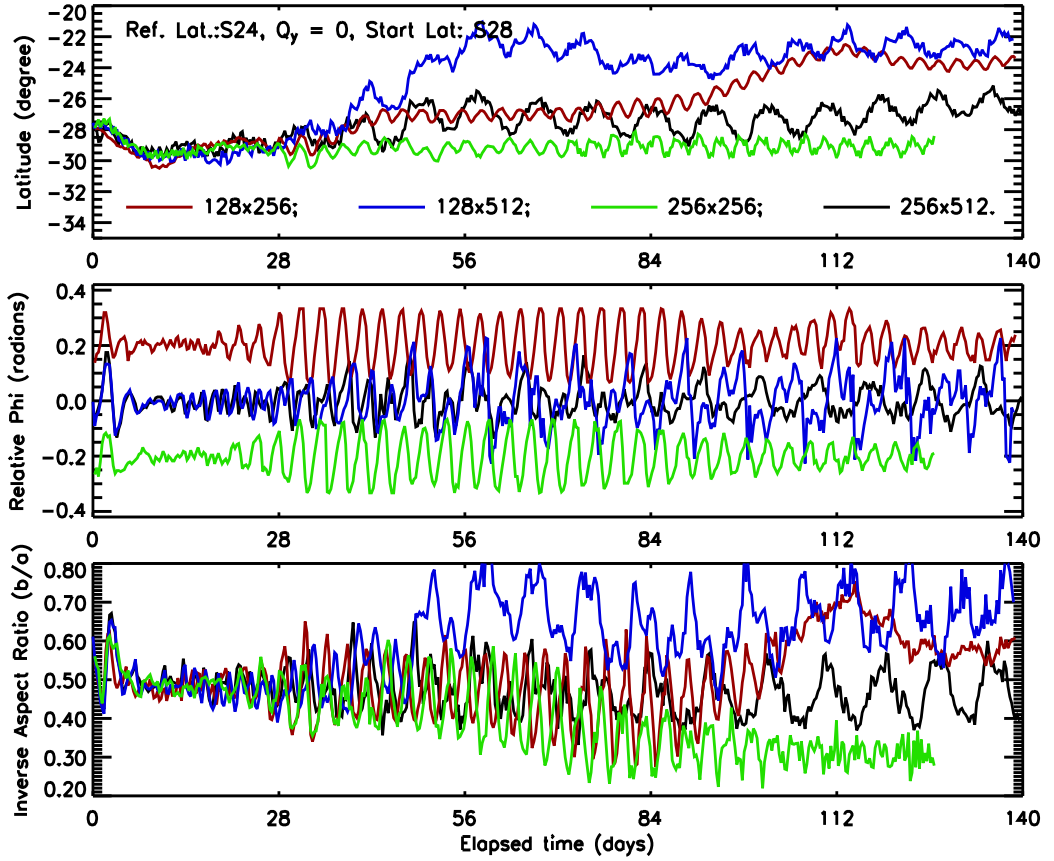


Figure 3.12: Comparison of simulations with different simulation domains. Simulation parameters are: $Q_y = 0$, reference strength 1, reference size 1, initial AR 1.5, starting latitude S28°. The top subplot is the drift curves; the middle subplot is the oscillation of the orientation angle (notice here the quarter globe case is shifted +0.2 radians and the longitudinal half globe case is shifted -0.2 radians, for clarity); the bottom subplot is the oscillation of the inverse aspect ratio (b/a).

3.4 Whole Globe Domain Simulations

Comparing to the quarter globe domain, the whole globe domain requires four times the computer resources. But since their grid spacings are the same, the time step is unchanged.

The parameters we use to investigate the simulation results include: Q_y , reference latitude, vertical shear, P-T profile, initial spot size, initial spot strength, initial spot aspect ratio, initial spot layer, and initial spot location. Furthermore, in some

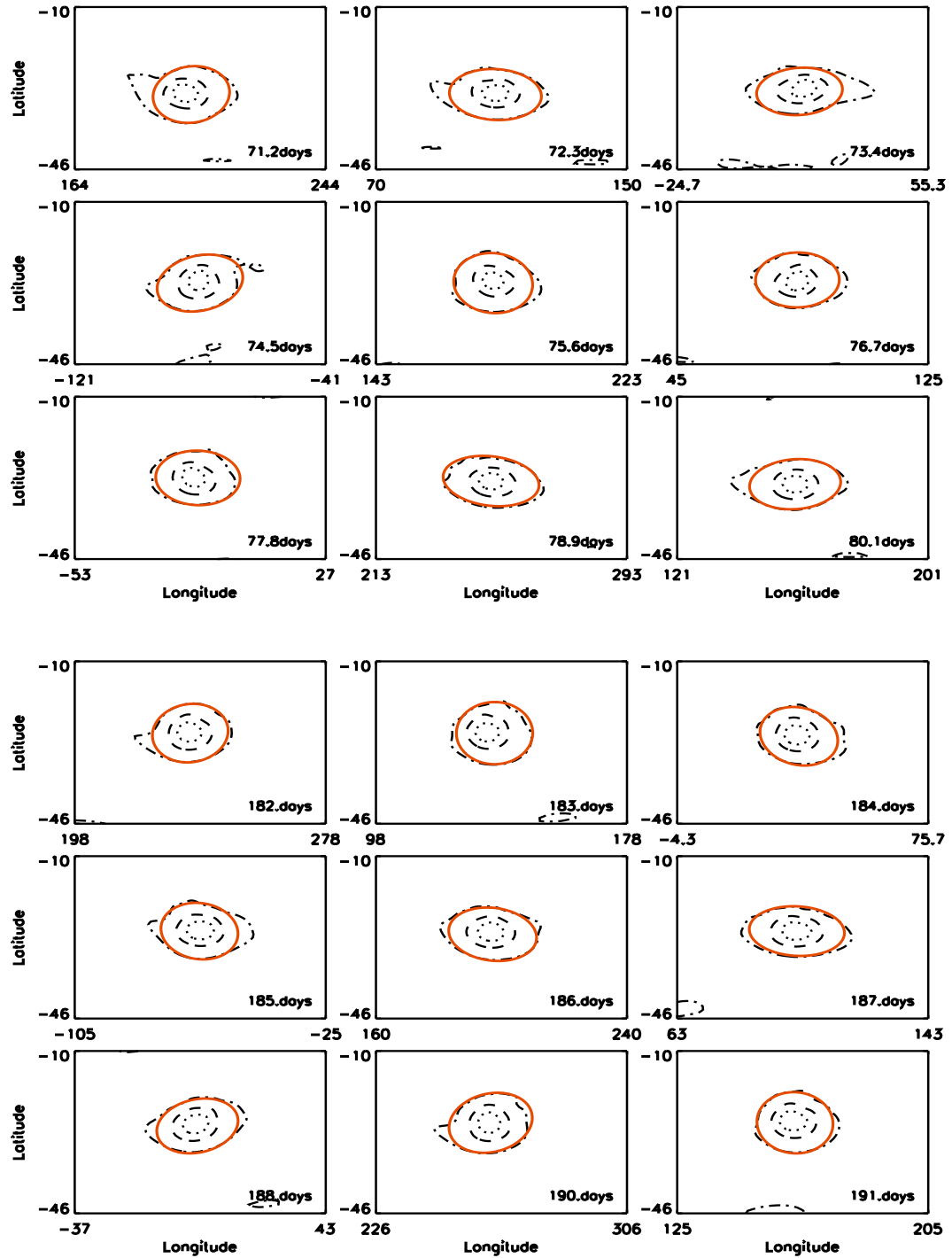


Figure 3.13: The contour plots of the whole globe simulation with $Q_y = 0$, reference strength 1, reference size 1 and initial AR 1.5. The top plot is from 71.2 days to 80.1 days; the bottom plot is from 182 days to 191 days. The contour plot of potential vorticity is on layer 7 (867.9 mbar).

cases, we modify the zonal wind profile to limit the small Q_y area to a smaller region in latitude and make the constant Q_y area transit to the upper and lower bounds smoothly.

Effects of Q_y

As shown in the coarse grid simulations, Q_y is one of the key parameter for the behavior of the simulated Great Dark Spot. The drift rate of the GDS is sensitive to this parameter. Here, we start the parametric simulations from Q_y . At this point, to investigate the effect of Q_y , we still use the zonal wind profiles shown in Figure 3.2.

Figure 3.14 shows the drift rate of simulated great dark spots in the background with different Q_y . Different from Figure 3.3, in Figure 3.14, all spots start from 28°S . One more zonal wind profile used in Figure 3.14 is the $Q_y = 1/12$ case, which is between the $Q_y = 0$ and $Q_y = 1/6$ profiles. Figure 3.14 shows that the behavior of the great dark spot is sensitive to the gradient of the absolute vorticity of the background zonal wind profile. To get a small drift rate, the background zonal wind profile should be close to $Q_y = 0$. Therefore, our later simulations will focus on the zonal wind profiles with near constant absolute vorticity in the studied region. The drift rates are also shown in Table 3.3.

To calculate the drift rate, we use the data after one month if the spot lasts for more than two months. Otherwise, we use the data after 15 days. In this way, the main part of the initial adjustment can be avoided. Also, we cut the final unsteady drift part to avoid the disperse time. At last, we can fit the drift rate in a relatively steady period. This basic idea is also applied when we analyze the following cases.

Effects of Spot Size

With the default parameters and $Q_y = 0$, we studied the behavior of the simulated great dark spots with different spot sizes. Figure 3.15 shows the effect of the spot

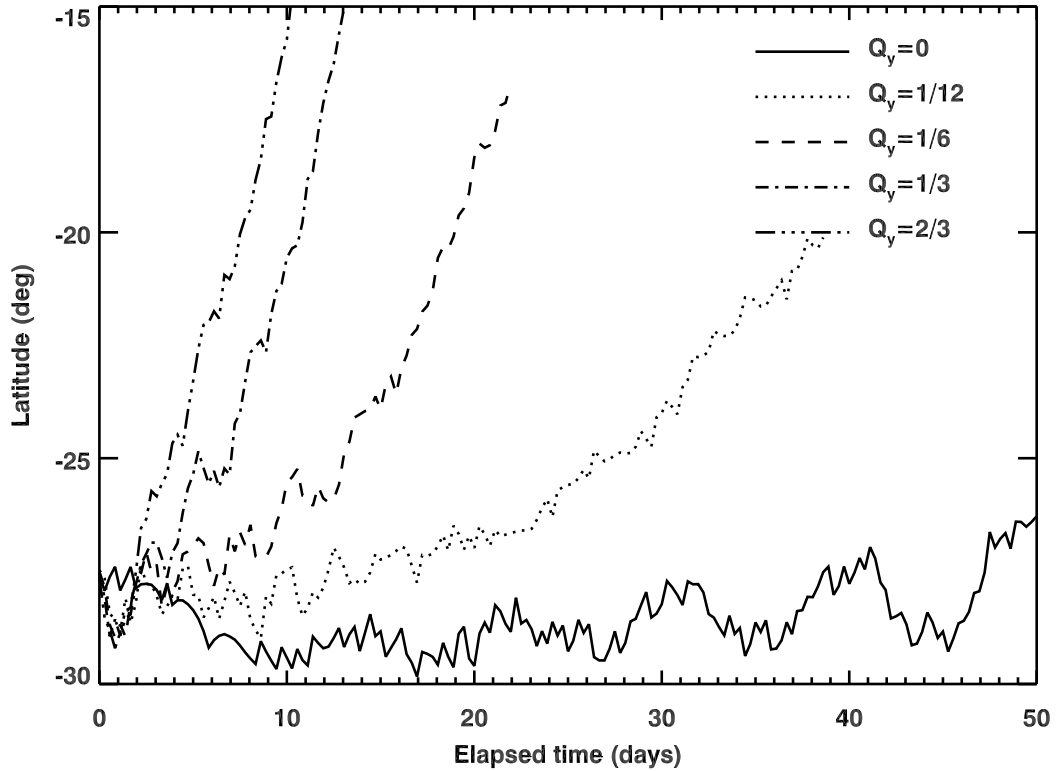


Figure 3.14: Drift rate of great dark spot in the zonal wind profiles with different Q_y : 0, 1/12, 1/6, 1/3, and 2/3 with reference latitude 24°S. Except Q_y , all other parameters are default: starting from 28°S, relative strength 1, relative size 1, and layer 5 to 9.

size to the drift rate, oscillation of inverse aspect ratio and oscillation of orientation angle. When the spot size becomes relatively small (0.6), the drift rate becomes faster. Studying the plot, we can see that in the first month they are similar. Near 50-60 days both 1.0 and 0.8 cases show a turn point at which the drift rates become flat, while the 0.6 case does not have this turn point. We can also see that when the spot becomes smaller, the inverse aspect ratio becomes higher, which means the spot becomes rounder. Also, smaller spot size leads to stronger oscillation.

These simulations tell us that to get suitable drift rates and oscillations, we need to use the spots with suitable relative sizes. Also, although the defined size of the simulated spot can vary in a range with different critical contour values, the spot

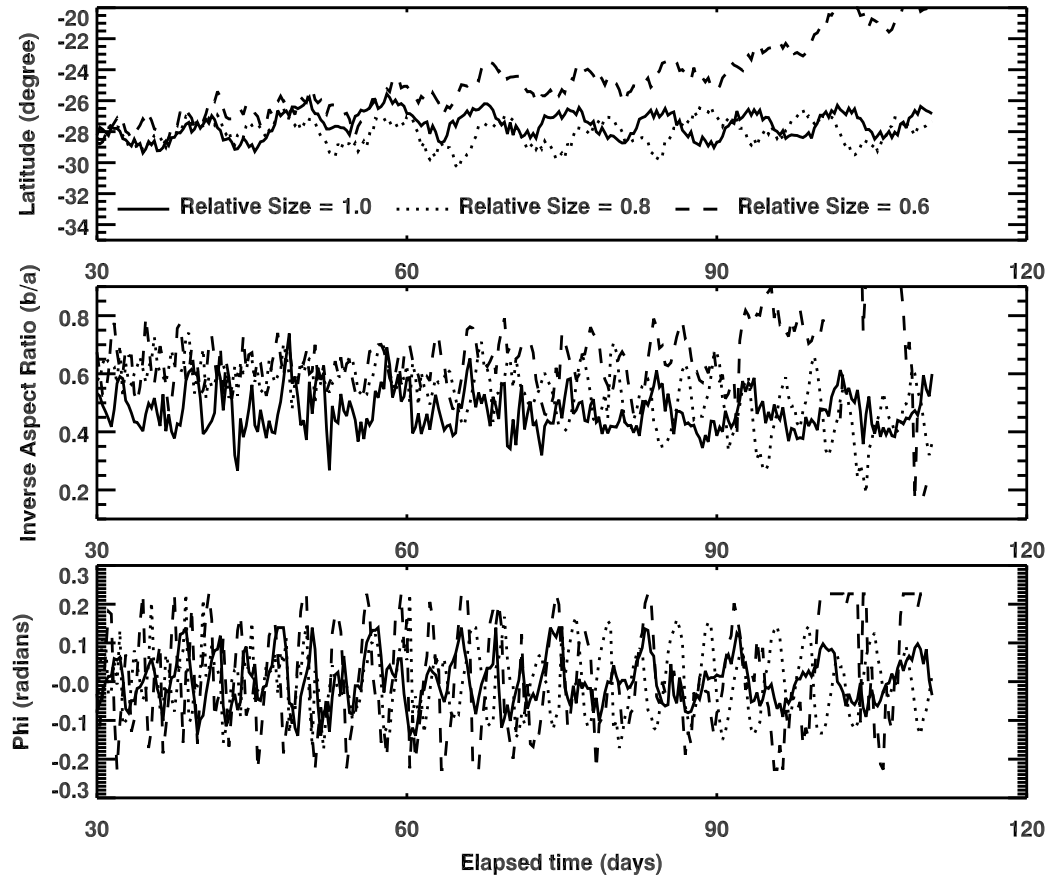


Figure 3.15: Drift rate (top panel), oscillation of inverse aspect ratio (middle panel) and oscillation of orientation angle (bottom panel) of great dark spot with different initial spot size. Except relative spot size, all these spots have the default parameters: starting from 28°S ; relative strength 1; layer 5 to 9; $Q_y = 0$ with reference latitude 24°S . All plots start from 30 days, after the initial adjustment. In the "Relative size = 0.6" case, when the spot passes 23° (~ 100 days), the spot becomes not regular so that the inverse aspect ratio and the orientation angle are not defined well.

size from the observations is still a limitation and so that the initial relative size of the spot cannot be too small. Obviously, relative size 0.6 is insufficient to generate a simulated great dark spot with observed size (see Figure 3.16). Therefore, most our future simulations will have the relative size 0.8 or 1.0.

As we see in the the oscillation plots, the amplitude and the center of the oscillation can change with time. This effect is especially obvious for the inverse aspect ratio. To compare them, we choose a whole period near the simulated elapsed time 80-90

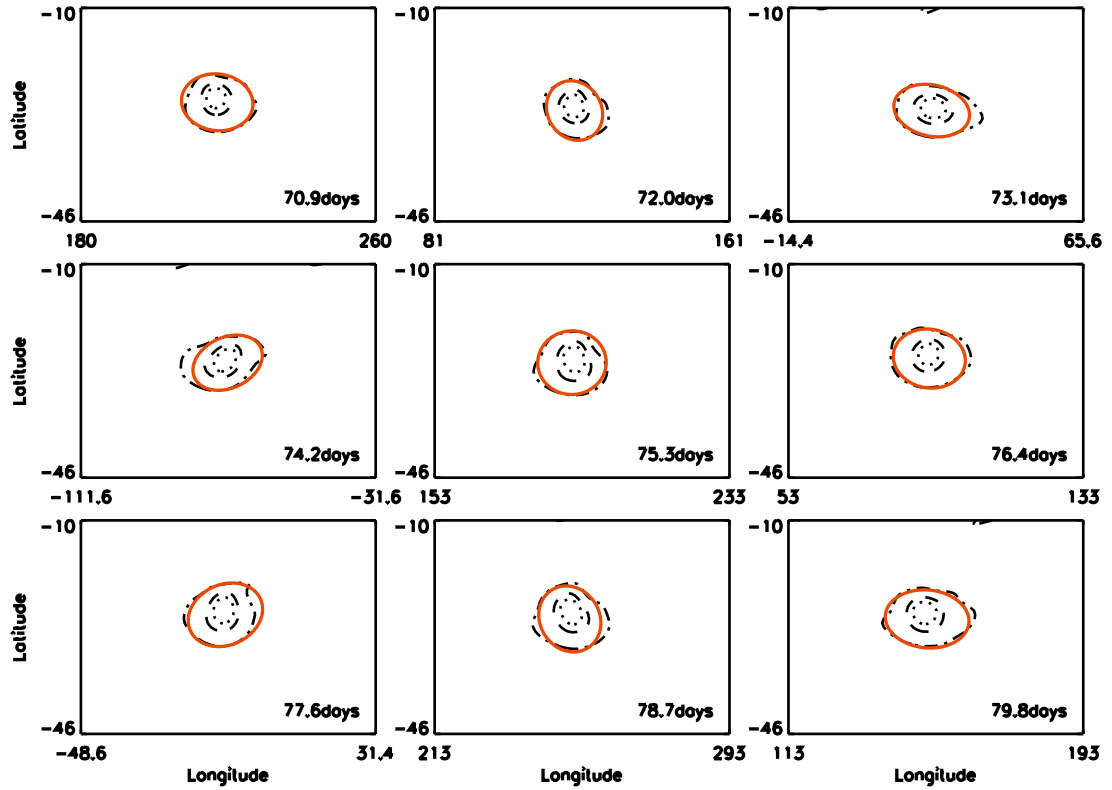


Figure 3.16: Oscillation and tail formation of GDS with $Q_y = 0$, relative size 0.5, relative strength 1 and starting latitude 28°S . Solid curve is the ellipse fit. The contour plot of potential vorticity is on layer 7 (867.9 mbar). The levels for the contour are 0.2, 0.6 and 0.8 times of the peak value of the potential vorticity.

days and get the center and amplitude from this. If that case does not show good oscillation or does not have good data near this region, we use the last good-shape oscillation to get the data. This method is also used in the following study. This may cause occasional difficulties when the spot is unstable, like the relative strength equals 0.5 case, which cannot keep its shape for a long time. Still the main trends do not change with this problem.

Effects of Spot Strength

To test the effects of the strength of the simulated great dark spot, we modify the relative strength from 1.0 to 0.5. Figure 3.17 shows the effect of the spot strength

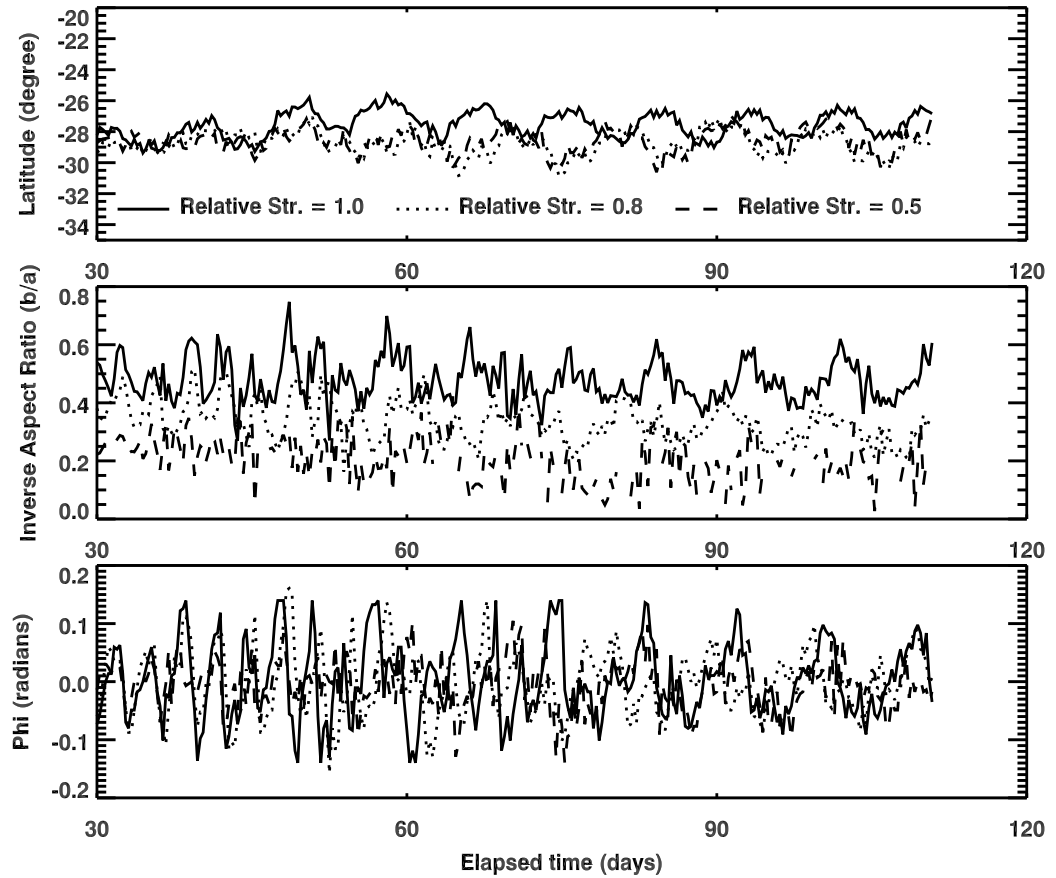


Figure 3.17: Drift rate (top panel), oscillation of inverse aspect ratio (middle panel) and oscillation of orientation angle (bottom panel) of great dark spot with different initial spot strength. Except relative spot strength, all these spots have the default parameters: starting from 28°S ; relative size 1; layer 5 to 9; $Q_y = 0$ with reference latitude 24°S . All plots start from 30 days, after the initial adjustment.

on the drift rate, oscillation of inverse aspect ratio and oscillation of orientation angle. Obviously, a weaker spot has smaller drift rate, smaller inverse aspect ratio (so a stronger spot is rounder) and smaller oscillation. Also, the oscillation period increases when the spot is weaker.

Since the inverse aspect ratio of the observed GDS-89 (see Table 3.2) is about 0.3 to 0.4 in the region from 27°S to 17°S , the relative strength cannot be too small. Here, with relative size 1 and relative strength 0.5, the inverse aspect ratio is 0.19 at about 28° , which is too small compared to the observational result.

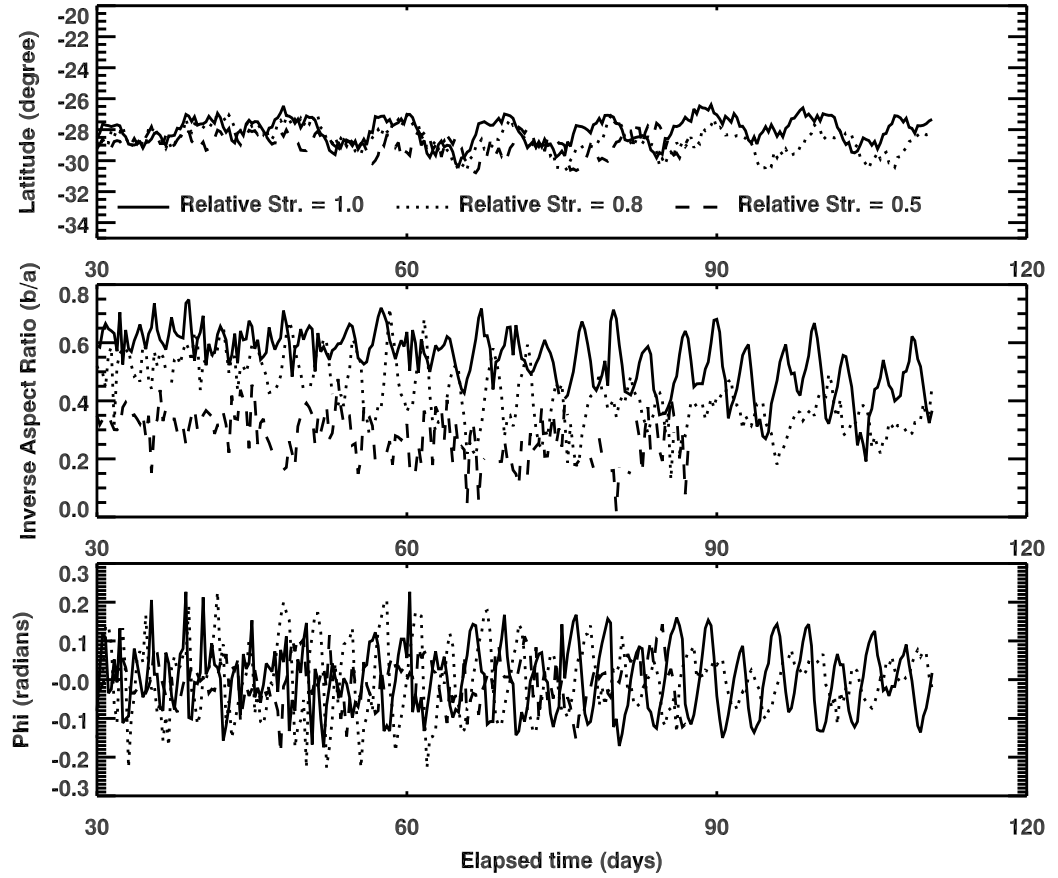


Figure 3.18: Drift rate (top panel), oscillation of inverse aspect ratio (middle panel) and oscillation of orientation angle (bottom panel) of great dark spot with different initial spot strength. The relative size for these cases are all 0.8. Except relative size and relative spot strength, all these spots have the default parameters: starting from 28°S , layer 5 to 9, and $Q_y = 0$ with reference latitude 24°S . All plots start from 30 days, after the initial adjustment.

From above discussion, we know that the size of the spot will also influence the oscillation and the aspect ratio. A smaller spot has a rounder shape. Therefore, we tried some cases with relative size smaller than 1 and/or relative strength bigger than 0.5 to try to fit the observed aspect ratio.

Figure 3.18 shows the cases with relative size 0.8 and relative strength 0.5. From the plots, we can see that the above results still stand: a weaker spot has a smaller drift rate, smaller inverse aspect ratio (stronger spot is rounder) and smaller oscilla-

tion (see the oscillations after 90 days, when the good shape oscillations are found).

Comparing those cases with relative size 1, we can also get the similar trends regardless the effects of size change: a smaller spot has a rounder shape and a stronger oscillation.

Effects of Brunt–Väisälä Frequency

As discussed in the last chapter, the vertical P-T profile is based on the nominal (Conrath 1991[13]) data and is extended to deeper layers with constant Brunt–Väisälä frequency from a pressure of 300 mbar and a temperature of 54.5 K. Here we investigate the effects of the Brunt–Väisälä frequency.

Figure 3.19 shows the effects of different P-T profiles. We can see that relatively speaking the nominal one makes the spot less stable than the other two. In the first 50 days, $N^2 = 0.36 \times 10^{-4} \text{s}^{-2}$ is close to the $N^2 = 0.64 \times 10^{-4} \text{s}^{-2}$ case. After that the $N^2 = 0.36 \times 10^{-4} \text{s}^{-2}$ case shows smaller drift. These results suggests that after initial adjustment, smaller N^2 leads to slightly smaller drift rates and slightly smaller inverse aspect ratios. Basically, the three P-T profiles show similar shapes. This means that the vertical P-T profile does not have significant influence on the dynamics of the great dark spot. With the three profiles, the $N^2 = 0.64 \times 10^{-4} \text{s}^{-2}$ case shows the best performance as far as the steady drift and good oscillations. Therefore, in most simulations, we use the vertical P-T profile with $N^2 = 0.64 \times 10^{-4} \text{s}^{-2}$.

Effects of Vertical Shear

To study the effects of vertical shear, we apply the method used in García-Melendo et al. 2007[25]. They used four parameters to control the vertical shear shape. The equation used to calculate the zonal wind velocity at each layer is[25]

$$U(\phi, P) = u_h(\phi)u_v(P), \quad (3.2)$$

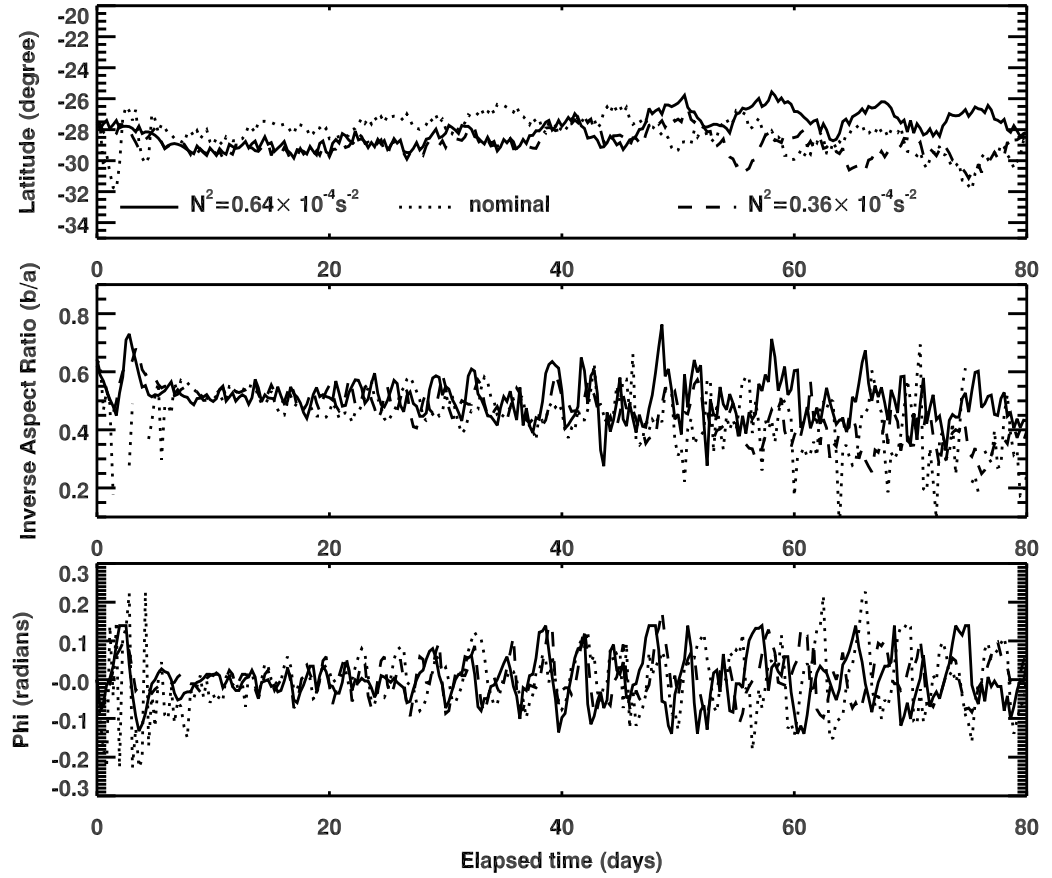


Figure 3.19: Drift rate (top panel), oscillation of inverse aspect ratio (middle panel) and oscillation of orientation angle (bottom panel) of great dark spot with different P-T profiles. The $N^2 = 0.64 \times 10^{-4} s^{-2}$ and $N^2 = 0.36 \times 10^{-4} s^{-2}$ cases are constructed P-T profiles with constant Brunt–Väisälä frequency. The nominal one is from Conrath 1991[13]. Except the P-T profile, all these spots have the default parameters: relative size 1, relative strength 1, starting from $28^\circ S$; layer 5 to 9; $Q_y = 0$ with reference latitude $24^\circ S$. All plots start from 0 days to show the effect of the P-T profile from the beginning.

where $u_h(\phi)$ is the zonal wind profile calculated via the methods discussed above. The variable P_0 is the standard level, at which $u_v(P_0) = 1$. The variable $u_v(P)$ is the non-dimensional equation used to control the vertical shear of the zonal winds. When $P \leq P_1$ [25],

$$u_v(P) = \left(1 + m_1 \ln \left(\frac{P}{P_0} \right) \right). \quad (3.3)$$

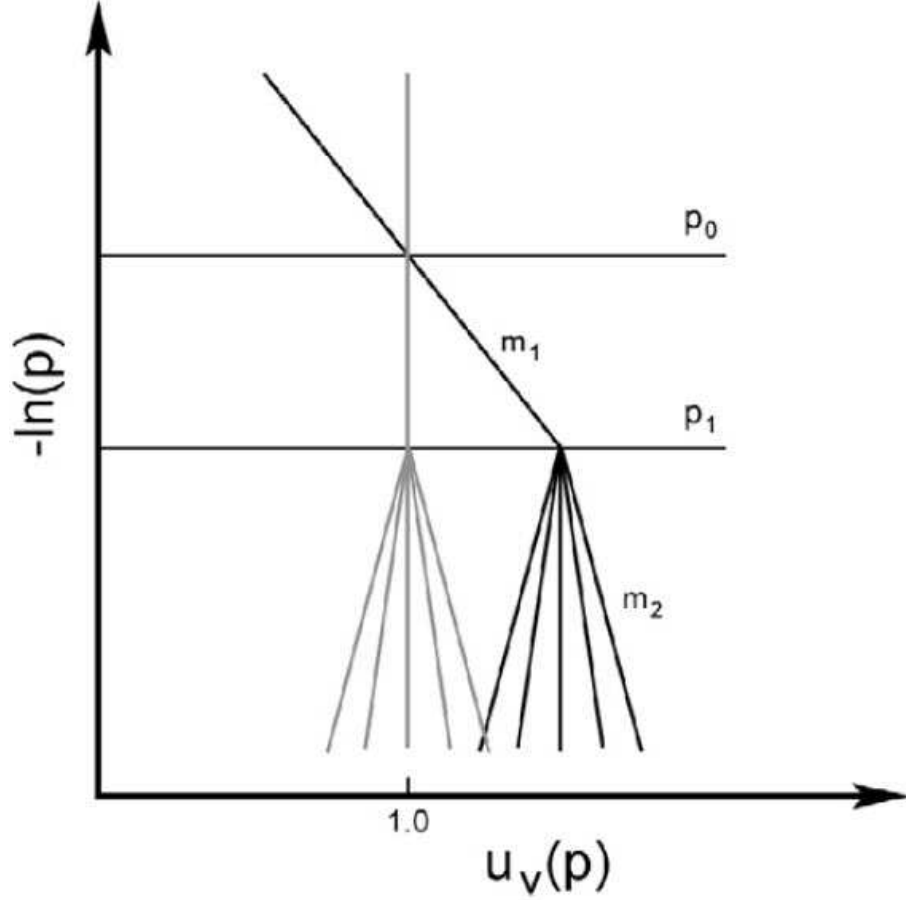


Figure 3.20: The structure scheme used to modify the vertical shear. Above p_1 , $m_1 = 0.0$ case (gray) and $m_1 = 0.2$ case (solid) are shown here. Below P_1 , different m_2 cases are shown. $P_0 = 500$ mbar is the level where $u_v(P_0) = 1$. This figure is from García-Melendo et al. 2007[25].

When $P > P_0$ [25],

$$u_v(P) = \left(u_1 + m_2 \ln \left(\frac{P}{P_1} \right) \right), \quad (3.4)$$

$$u_1 = 1 + m_1 \ln \left(\frac{P_1}{P_0} \right). \quad (3.5)$$

Figure 3.20 shows the vertical structure scheme of this method. The observations show that the vertical shear of the zonal winds near the GDS layer is not significant. In our simulations, we keep $m_1 = 0$, $P_0 = 500$ mbar, $P_1 = 1000$ mbar and modify m_2 to see its effects on the behavior of the simulated great dark spot.

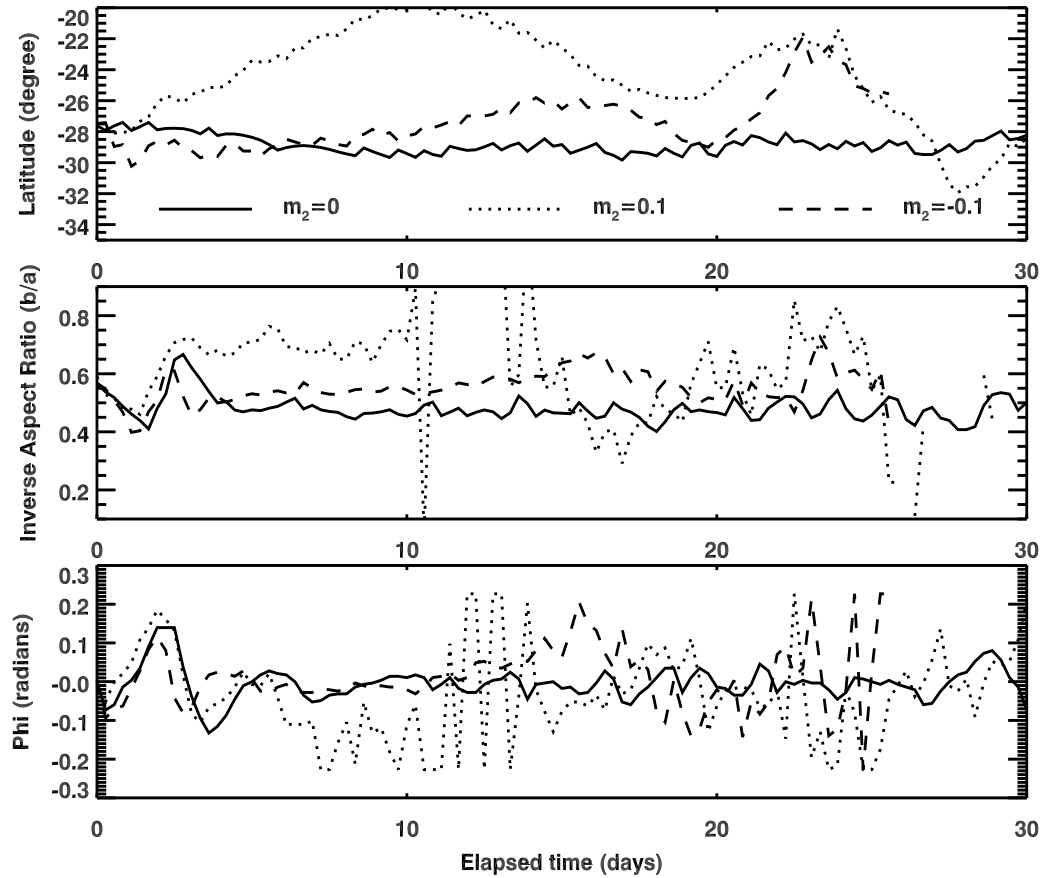


Figure 3.21: Drift rate (top panel), oscillation of inverse aspect ratio (middle panel) and oscillation of orientation angle (bottom panel) of great dark spot with different vertical shear. These cases include $m_2 = 0, 0.1$ and -0.1 . Except the vertical shear, all these spots have the default parameters: relative size 1, relative strength 1, starting from 28°S , layer 5 to 9, and $Q_y = 0$ with reference latitude 24°S . These plots start from 0, because the sheared winds cannot sustain the spots for a long enough time.

Figure 3.21 shows the changes of drift rate, inverse aspect ratio and orientation angle when m_2 is changed to 0.1 and -0.1. The case with $|m_2| = 0.1$ shows fast drift both equatorward and poleward and has irregular oscillations so we can believe that this number is too big and the vertical shear of the Neptune winds must be not strong near the GDS layer. The drift rates shown in Table 3.3 are calculated using the steady drift regions before day 10.

Figure 3.22 shows the changes of drift rate, inverse aspect ratio and orientation

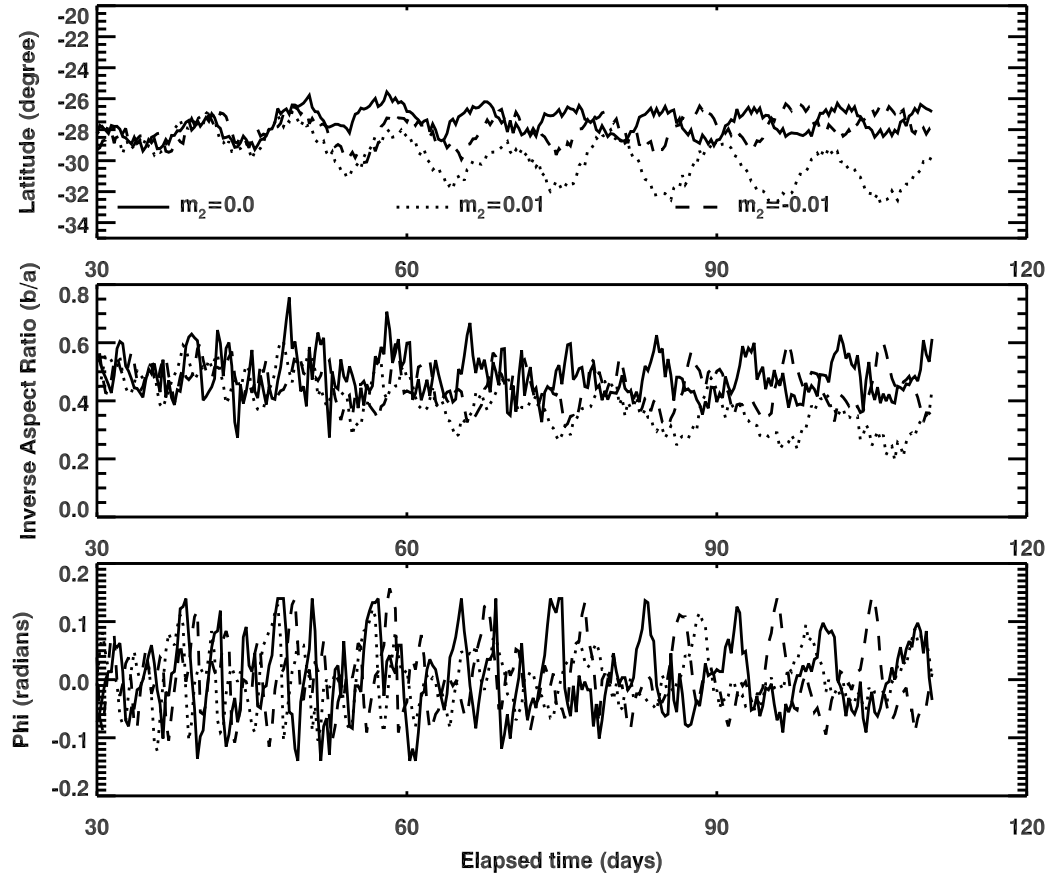


Figure 3.22: Drift rate (top panel), oscillation of inverse aspect ratio (middle panel) and oscillation of orientation angle (bottom panel) of great dark spot with different vertical shear. These cases include $m_2 = 0$, 0.01 and -0.01 . Except the vertical shear, all these spots have the default parameters: relative size 1, relative strength 1, starting from 28°S , layer 5 to 9, and $Q_y = 0$ with reference latitude 24°S .

angle when m_2 is changed to 0.01 and -0.01 . From this figure, positive m_2 leads to a smaller drift rate and a smaller inverse aspect ratio. Both cases show longer oscillation periods in both short-term and long-term oscillations (see Table 3.3).

Figure 3.23 shows the changes of drift rate, inverse aspect ratio and orientation angle when m_2 is changed to 0.03 and -0.03 . When $|m_2| = 0.03$, the oscillations of the spots become strong. Both cases show faster drift rates than the $m_2 = 0$ case. In the $m_2 = -0.03$ case, the spot drifts fast at first and then the drift rate becomes flat (In Table 3.3, its drift rate is calculated from the fast drift phase between 30 days

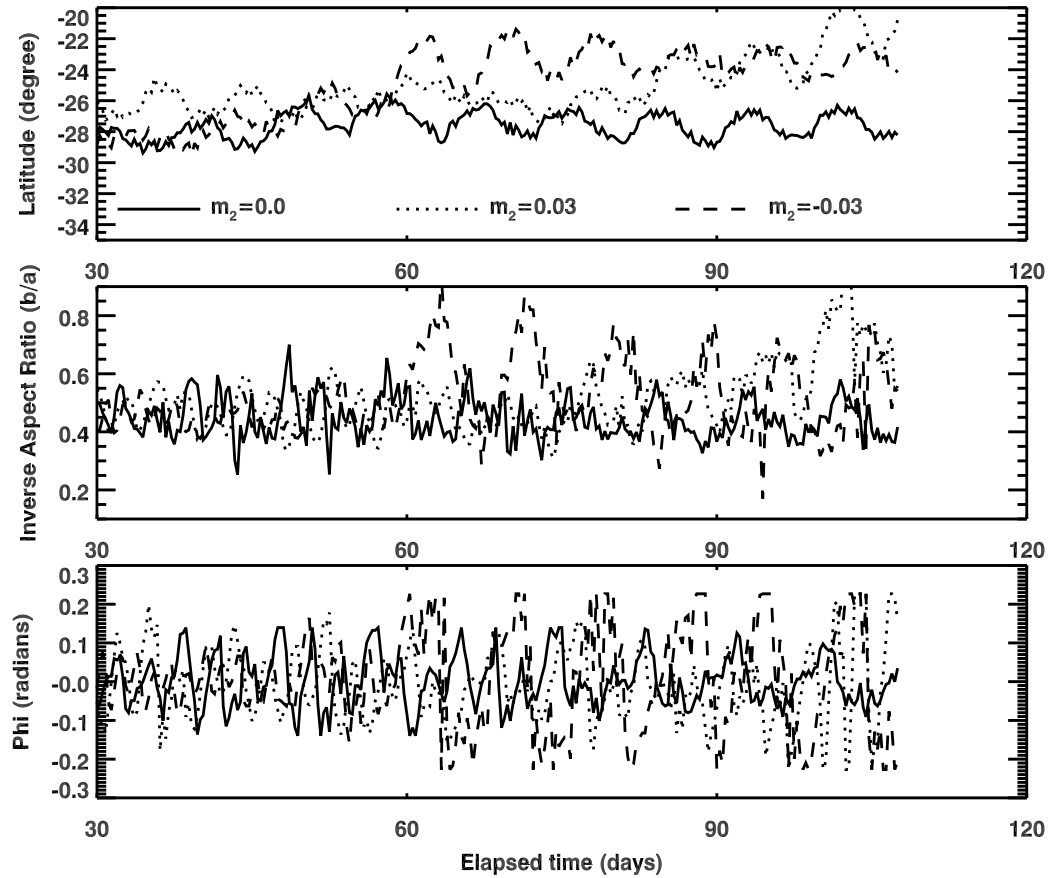


Figure 3.23: Drift rate (top panel), oscillation of inverse aspect ratio (middle panel) and oscillation of orientation angle (bottom panel) of great dark spot with different vertical shear. These cases include $m_2 = 0, 0.03$ and -0.03 . Except the vertical shear, all these spots have the default parameters: relative size 1, relative strength 1, starting from 28°S , main layer 7, and $Q_y = 0$ with reference latitude 24°S .

and 60 days.). In the $m_2 = 0.03$ case, the spot drift is relatively more steady. But after it reaches 24°S (~ 85 days), its drift rate becomes faster and its shape becomes irregular (so that we see multiple spikes in the oscillation plots).

Effects of Initial Aspect Ratio

Figure 3.24 shows the effect of the initial aspect ratio. This plot indicates that the initial aspect ratio does not change the drift rate and the oscillation amplitude. The main effect is that with higher initial aspect ratio the spot evolves to a rounder shape.

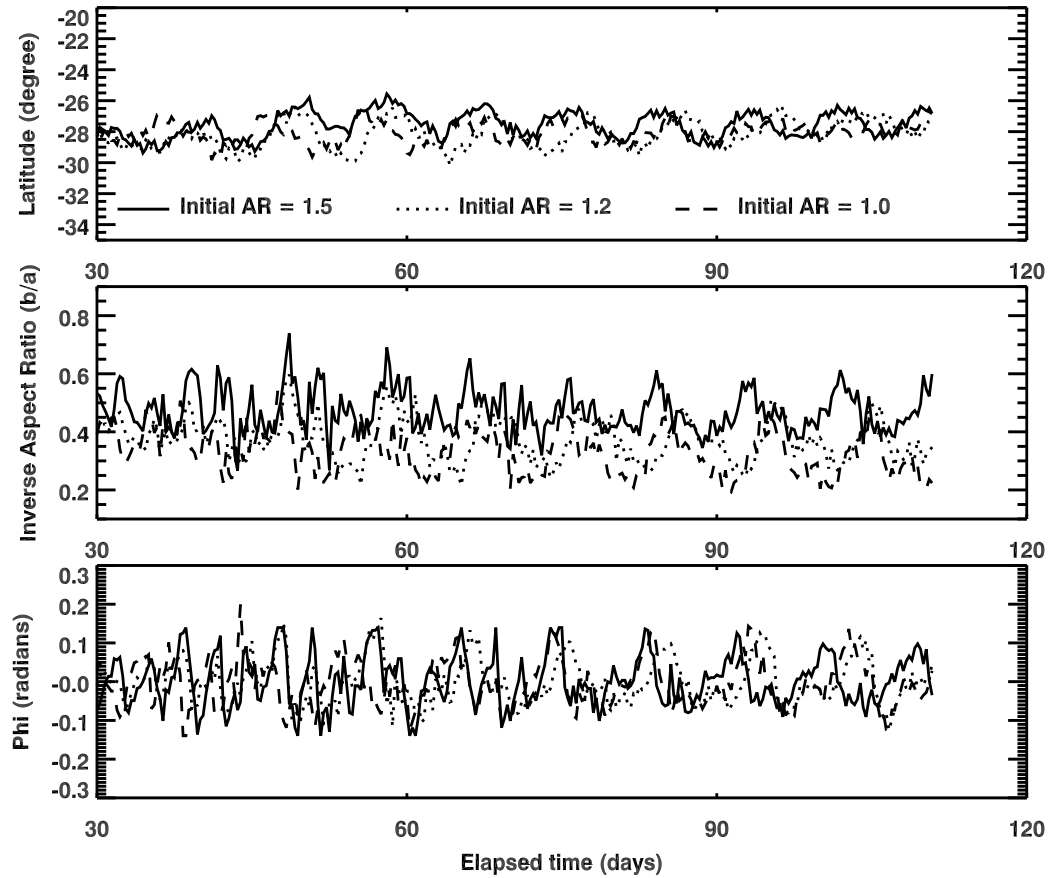


Figure 3.24: Drift rate (top panel), oscillation of inverse aspect ratio (middle panel) and oscillation of orientation angle (bottom panel) of great dark spot with different initial aspect ratios. The initial aspect ratios are 1.5, 1.2 and 1.0, respectively. In each figure, except the initial aspect ratio, all these spots have the default parameters: relative size 1, relative strength 1, layer 5 to 9, starting from 28°N , and $Q_y = 0$.

Effects of Vortex Layer

Figure 3.25 shows the effect of vertical central spot layer. We can see that the main layer 7 and 8 cases show close results. The layer 6 case shows smaller inverse aspect ratio than the other two. From this plot, the effect of the vertical layer on the dynamics of great vortex is not strong.

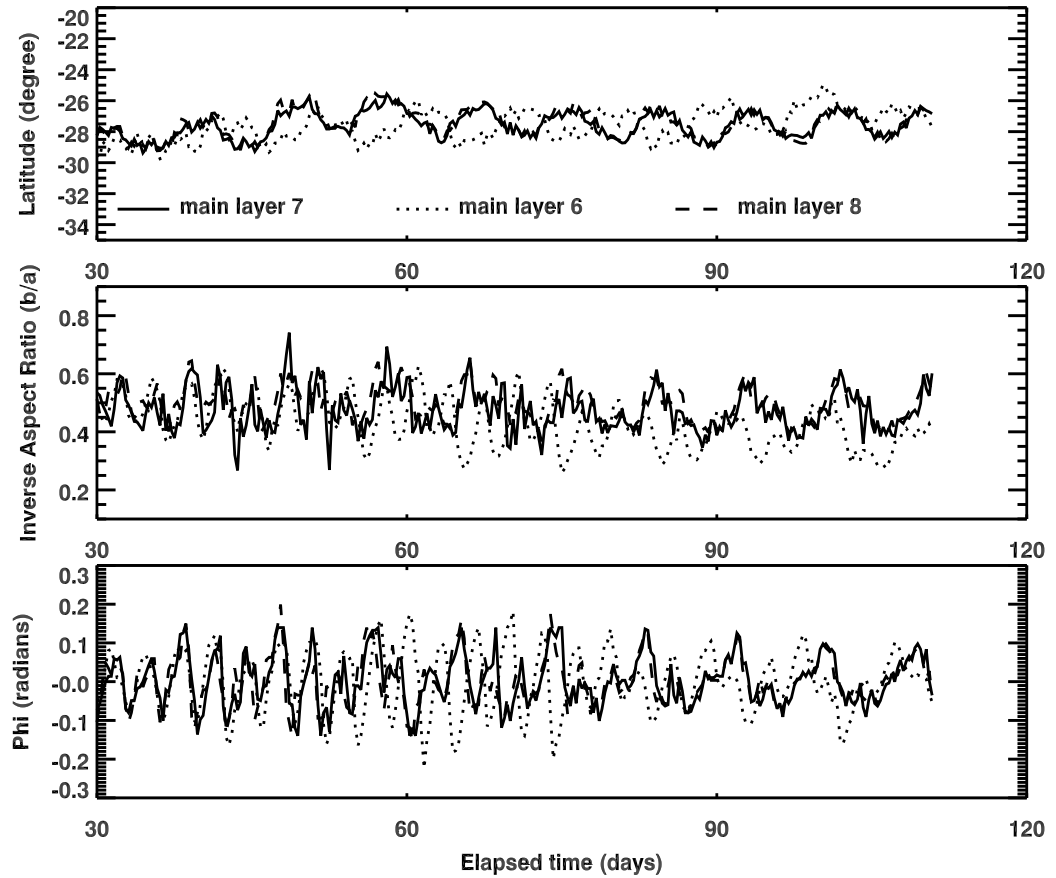


Figure 3.25: Drift rate (top panel), oscillation of inverse aspect ratio (middle panel) and oscillation of orientation angle (bottom panel) of great dark spot with different central spot layers. In these cases, the spots are at layer 6, 7 and 8, respectively. In each figure, except the spot layer, all these spots have the default parameters: relative size 1, relative strength 1, AR 1.5, starting from 28°N , and $Q_y = 0$.

Effects of Reference Latitude

Changing the reference latitude of the constructed zonal wind profile will change the constant absolute vorticity (and so potential vorticity) and the turn point of the zonal wind profile (related with the crossing-zero point of the relative vorticity) curve near the equator. Figure 3.26 shows the constructed zonal wind profiles with different reference latitudes, together with the Sromovsky 1993 fitted profile.

Figure 3.27 shows the changes of drift rate, inverse aspect ratio and orientation angle when the reference latitude is changed to 21°S , 20°S , 19°S , 18°S and 16°S . It

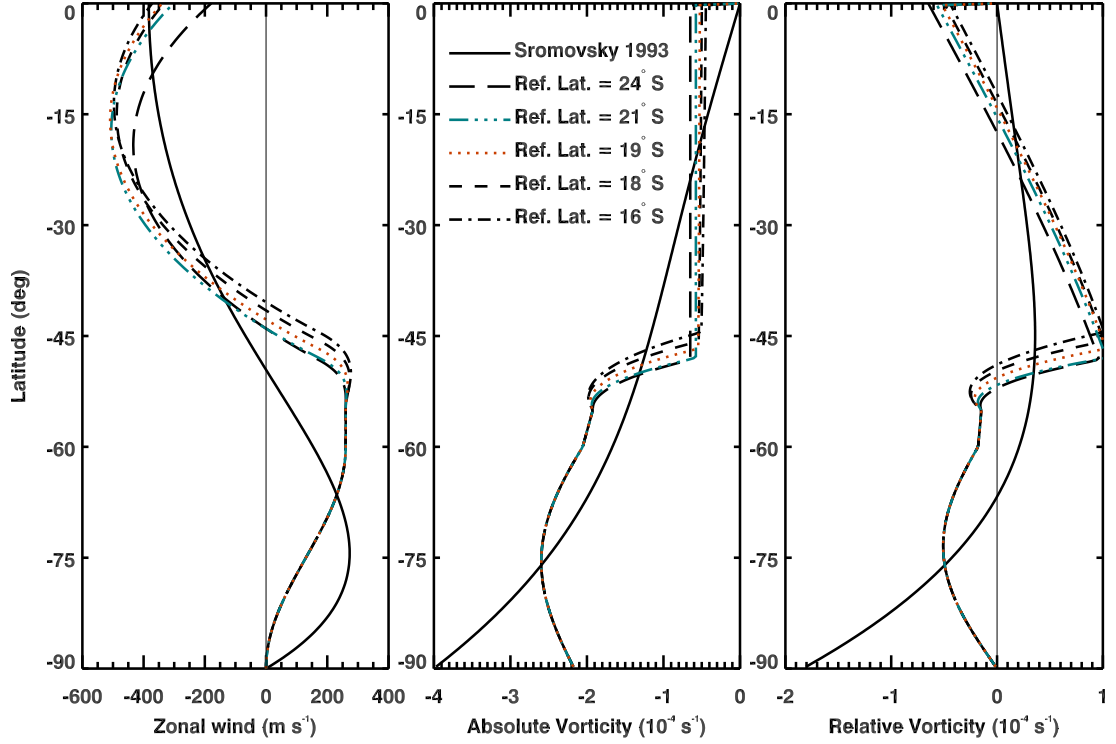


Figure 3.26: Zonal wind profiles (left panel) and their corresponding absolute vorticity profiles (middle panel) and relative vorticity profiles (right panel) for different reference latitude. All the constructed profiles are $Q_y = 0$ ones so that their absolute vorticities are all constant above $\sim 45^\circ\text{S}$. When the reference latitude is closer to the equator, the constant absolute vorticity is higher and the crossing-zero point of the relative vorticity profile is closer to the equator.

shows that when the reference latitude is closer to the equator, the spot drift faster. When the reference latitude is too close to the equator (16°S), the oscillation and the drift are not as steady. For all the other reference latitudes, oscillation amplitudes are similar. Also, the oscillation periods are similar. But when the reference latitude is closer to the equator, the short-term oscillation becomes more dominant than the long-term oscillation. This suggests that the zonal wind profile has significant effects on the oscillation period.

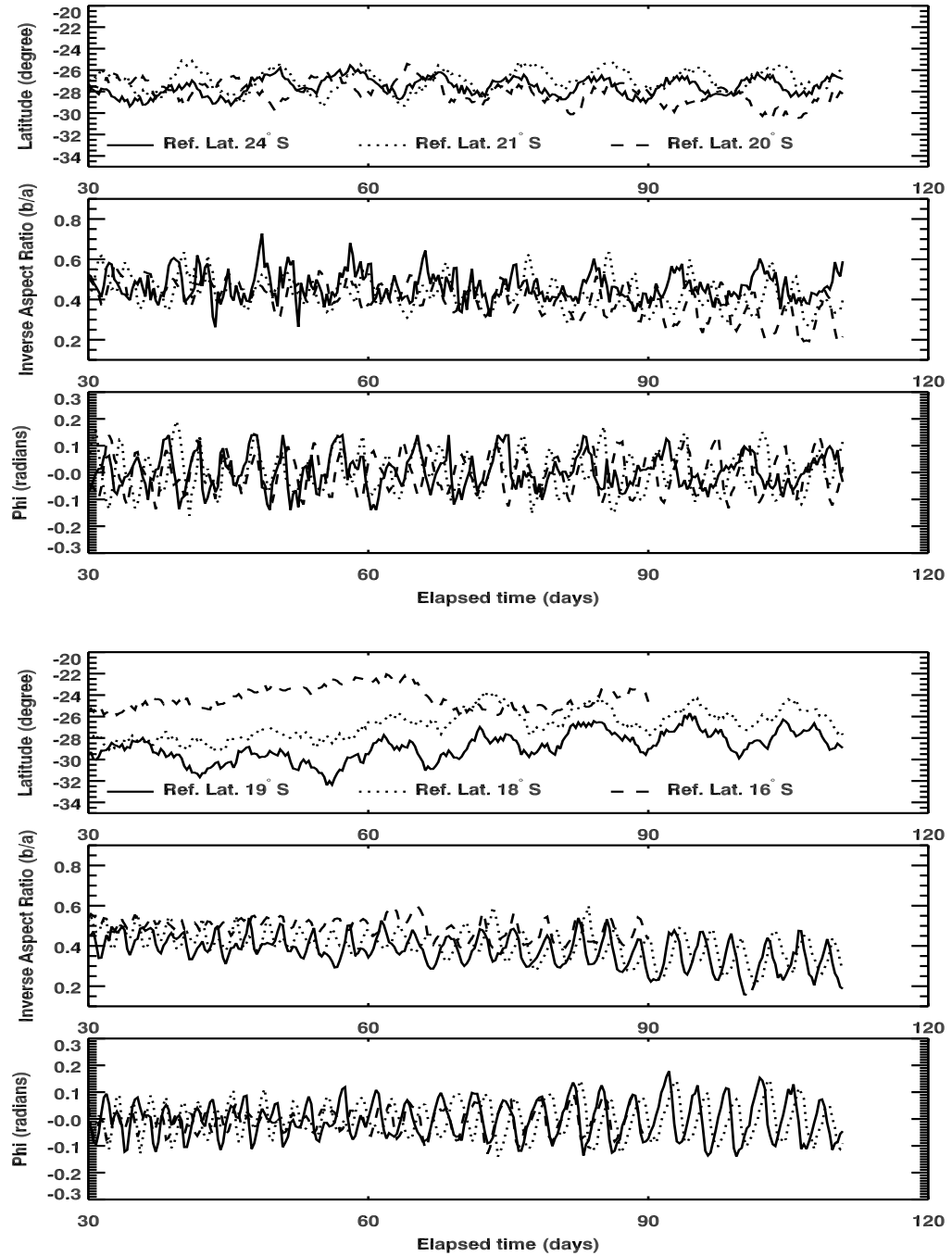


Figure 3.27: Drift rate (top panel), oscillation of inverse aspect ratio (middle panel) and oscillation of orientation angle (bottom panel) of great dark spot in the zonal wind profiles with different reference latitude. These cases include reference latitude = 24°S (default), 21°S, 20°S, 19°S, 18°S and 16°S. Except the reference latitude, all these spots have the default parameters: relative size 1, relative strength 1, starting from 28°S, layer 5 to 9 and $Q_y = 0$.

Effects of Starting Latitude

In our simulations, we need to generate a vortex at a particular latitude. This latitude can be different for different simulations. Here we want to investigate the effects of the starting latitudes.

Figure 3.28 and Figure 3.29 show the effects of different starting latitudes with background $Q_y = 0$. In Figure 3.28, the starting latitude 24° case shows similar oscillation period and similar drift rate in the center latitude plot. But in the other two plots, the oscillation amplitudes are big and the curves are not smooth, showing that the shape of the spot is not good. The reference latitude 21°S plot shows better oscillations for the spot with starting latitude 24°S . The reference latitude 17°S plot shows good oscillations for the spot with starting latitude 24°S , but not good for starting latitude 22°S . One obvious result for all the plots is that when the starting latitude is too close to the equator, the spot will drift quickly to the equator and break or kick back near some latitude. At the same time, the oscillations are not good when the spot is close to the equator.

When the reference latitude of the constructed zonal wind profile is closer to the equator, the turn point of the profile (the crossing-zero point of the relative vorticity profile) is closer to the equator, then the background zonal winds can sustain a spot closer to the equator. This is one benefit of using a lower reference latitude. Also, there is another way to move the turn point closer to the equator - changing Q_y smoothly from the low Q_y area to the high Q_y area near the equator, but this will be considered later. Since the observational results showed that the GDS-89 moved to at least 17°S , the turn point of the zonal wind profile must be higher than that of the $Q_y = 0$ profile with reference latitude 24° . This means one or both of the methods are needed.

For the same reference latitude with constant background Q_y and different starting latitudes, the drift rates of the spots become similar after several months. Starting

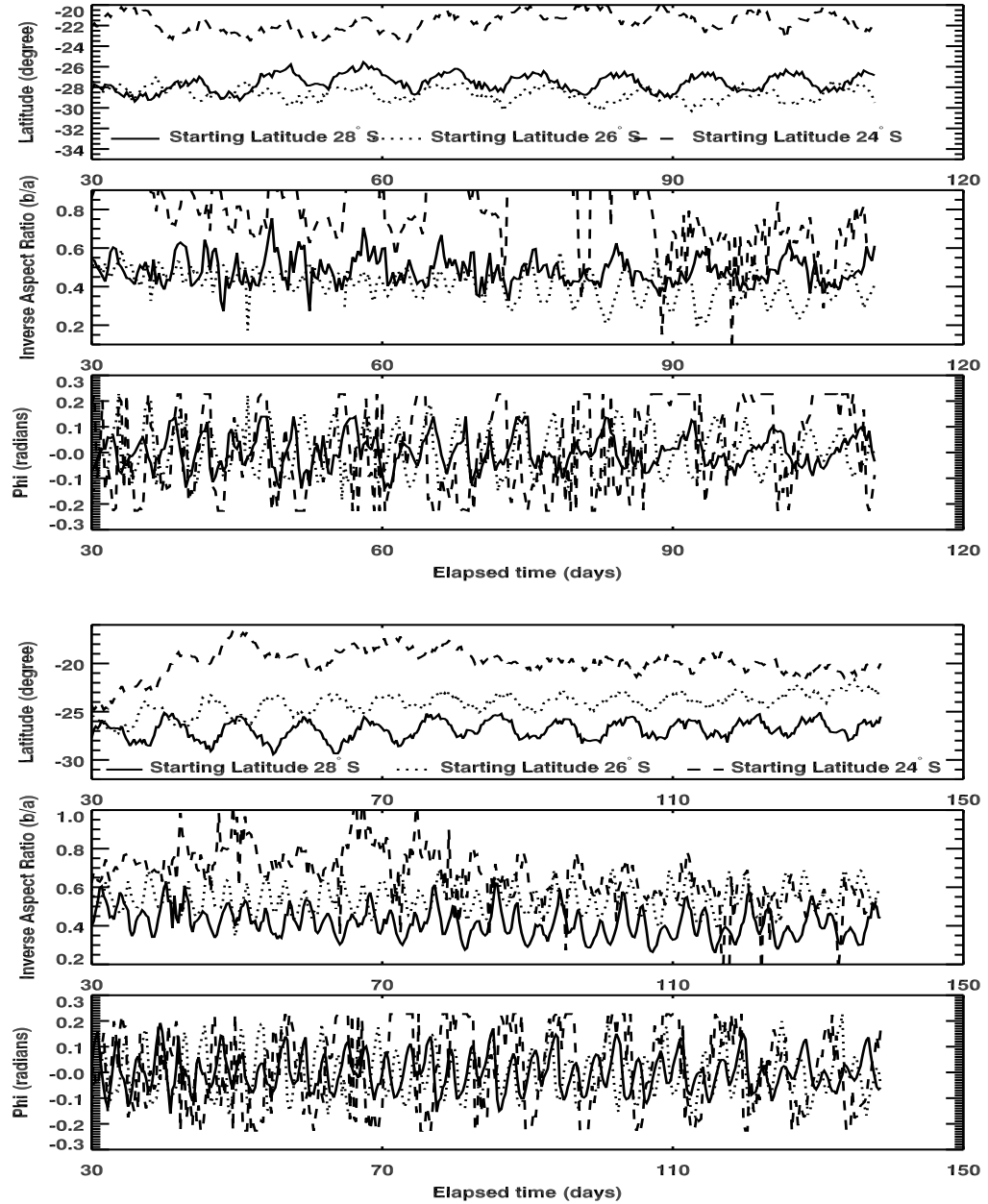


Figure 3.28: Drift rate (top panel), oscillation of inverse aspect ratio (middle panel) and oscillation of orientation angle (bottom panel) of great dark spot starting from different latitudes. The top figure is in the constructed zonal wind profile with reference latitude 24°S and the spots start from 28°S, 26°S and 24°S, respectively. The lower one is in the constructed zonal wind profile with reference latitude 21°S and the spots also start from 28°S, 26°S and 24°S, respectively. In each figure, except the starting latitude, all these spots have the default parameters: relative size 1, relative strength 1, layer 5 to 9, and $Q_y = 0$.

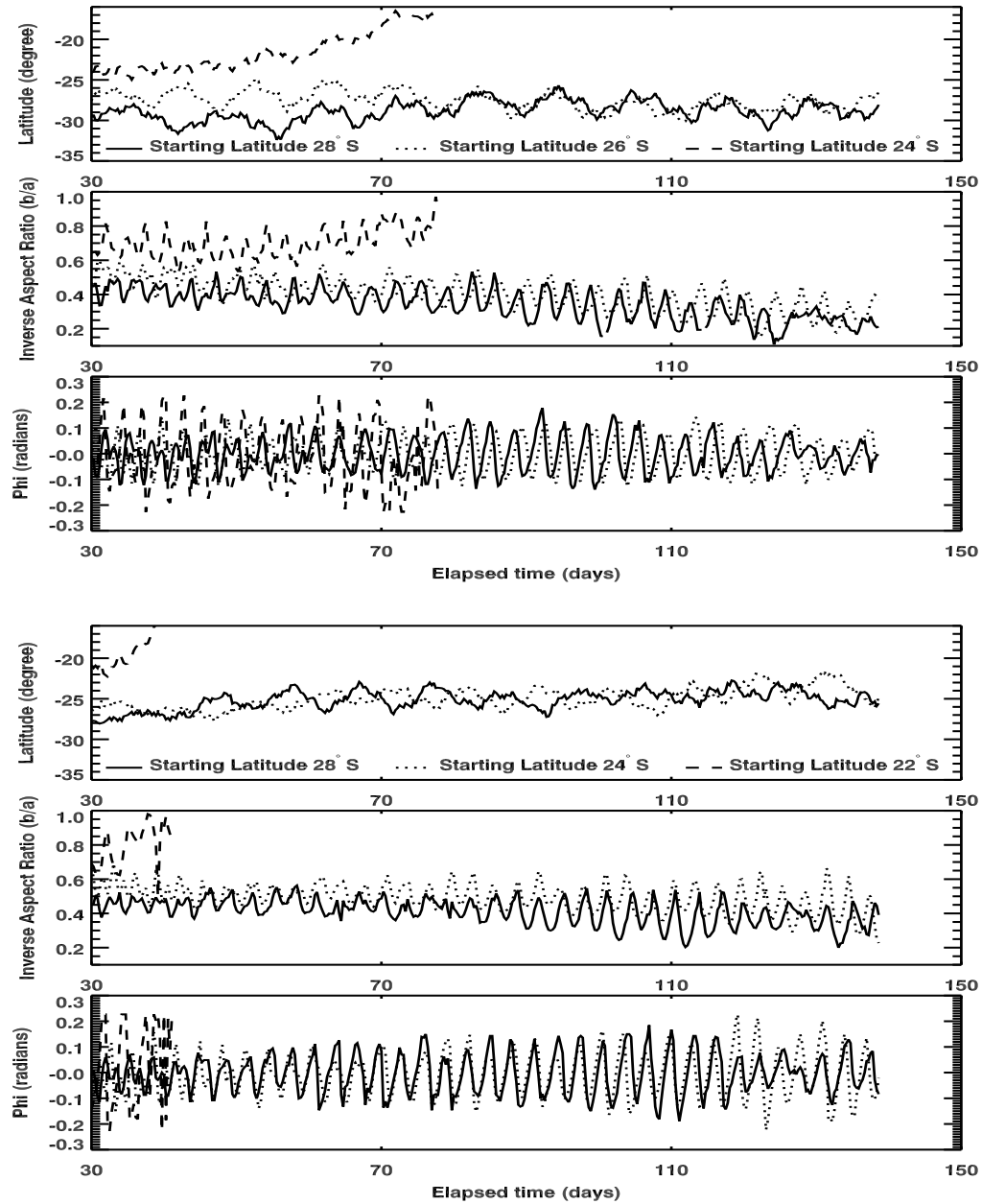


Figure 3.29: Drift rate (top panel), oscillation of inverse aspect ratio (middle panel) and oscillation of orientation angle (bottom panel) of great dark spot starting from different latitudes. The top figure is in the constructed zonal wind profile with reference latitude 19°S and the spots start from 28°S , 26°S and 24°S , respectively. The lower one is in the constructed zonal wind profile with reference latitude 17°S and the spots also start from 28°S , 24°S and 22°S , respectively. In each figure, except the starting latitude, all these spots have the default parameters: relative size 1, relative strength 1, layer 5 to 9, and $Q_y = 0$.

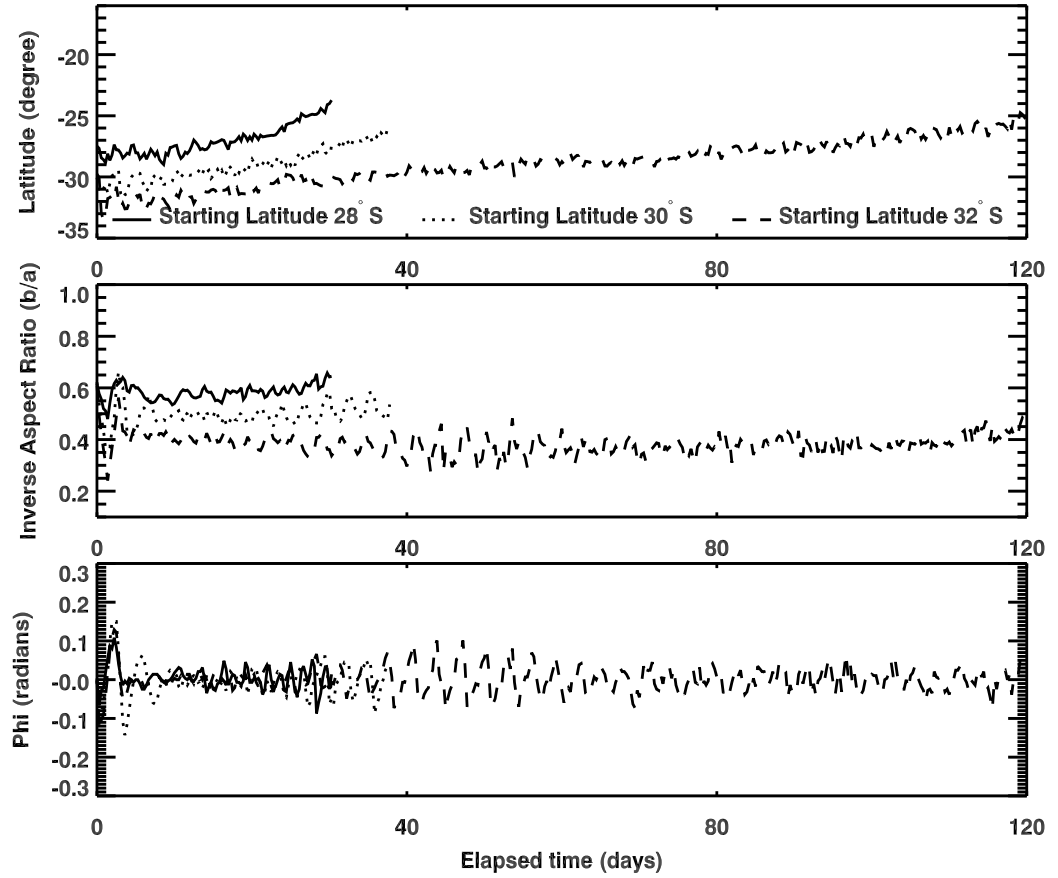


Figure 3.30: Drift rate (top panel), oscillation of inverse aspect ratio (middle panel) and oscillation of orientation angle (bottom panel) of great dark spot starting from different latitudes. This plot is in the constructed zonal wind profile with reference latitude 24°S and the spots also start from 28°S , 30°S and 32°S , respectively. Except the starting latitude, all these spots have the default parameters: relative size 1, relative strength 1, layer 5 to 9, and $Q_y = 1/12$. Starting time is from 0 so that we can see the evolution of the 28°S case and 30°S case more clearly.

from higher latitude often means the inverse aspect ratio is higher in the future. This is consistent with the observational result. But in a single case, it is still hard to get a increasing inverse aspect ratio when the time increases. As to the amplitude of the oscillations, normally, closer-to-equator cases show stronger oscillations.

Figure 3.30 shows the constructed zonal wind profile with $Q_y = 1/12$ and reference latitude 24°S . It is clear that when Q_y is higher, we need to generate the initial vortex at a higher latitude to end in steady drift. Still, the drift rate under $Q_y = 1/12$ is

higher than that under $Q_y = 0$.

Generating a Smoother Constructed Zonal Wind Profile

From Figure 3.2 and Figure 3.26, we can see that the Sromovsky 1993 fitted zonal wind profile has zero gradient near the equator so that the zonal winds change smoothly from the south hemisphere to the north hemisphere. In the absolute vorticity plots, we can also see that the Sromovsky 1993 profile goes to zero to the equator. But the constructed zonal wind profiles show different shapes. They change sharply near the equator and so there is a jump at the equator in the absolute vorticity plots. The real world should have continuous vorticity profiles. This suggests modifying the constructed zonal wind profiles near the equator to get smooth profiles. Also, the constructed zonal wind profiles change relatively sharply near 45°S to meet the upper limit of the observational data near this latitude and transit smoothly to the poles. This makes the constructed zonal wind profiles farther from the Sromovsky 1993 fitted curve. These can be modified to get smoother zonal wind profiles.

We use two methods to modify the constructed zonal wind profiles to make them transit smoothly across the equator or to another curve. Method 1 is to use an exponential interpolation equation to modify the zonal wind profile itself. Method 2 is to use an linear interpolation equation to modify Q_y smoothly so that the zonal wind profile will also be modified. As discussed previously, moving the turn point of the zonal wind profile is needed. This method can also move that point closer to the equator.

In Figure 3.31, the profiles marked by "Trans" are all transition cases. The mark 0-5 means that the transition happens from 5°S to the equator to make the profiles pass the equator smoothly. The mark 0-28 means that the transition is from 28°S to the equator to get zero absolute vorticity and relative vorticity at the equator. And the mark 38-66 means that the transition is from 38°S to 66°S to the $Q_y = 1$ zonal

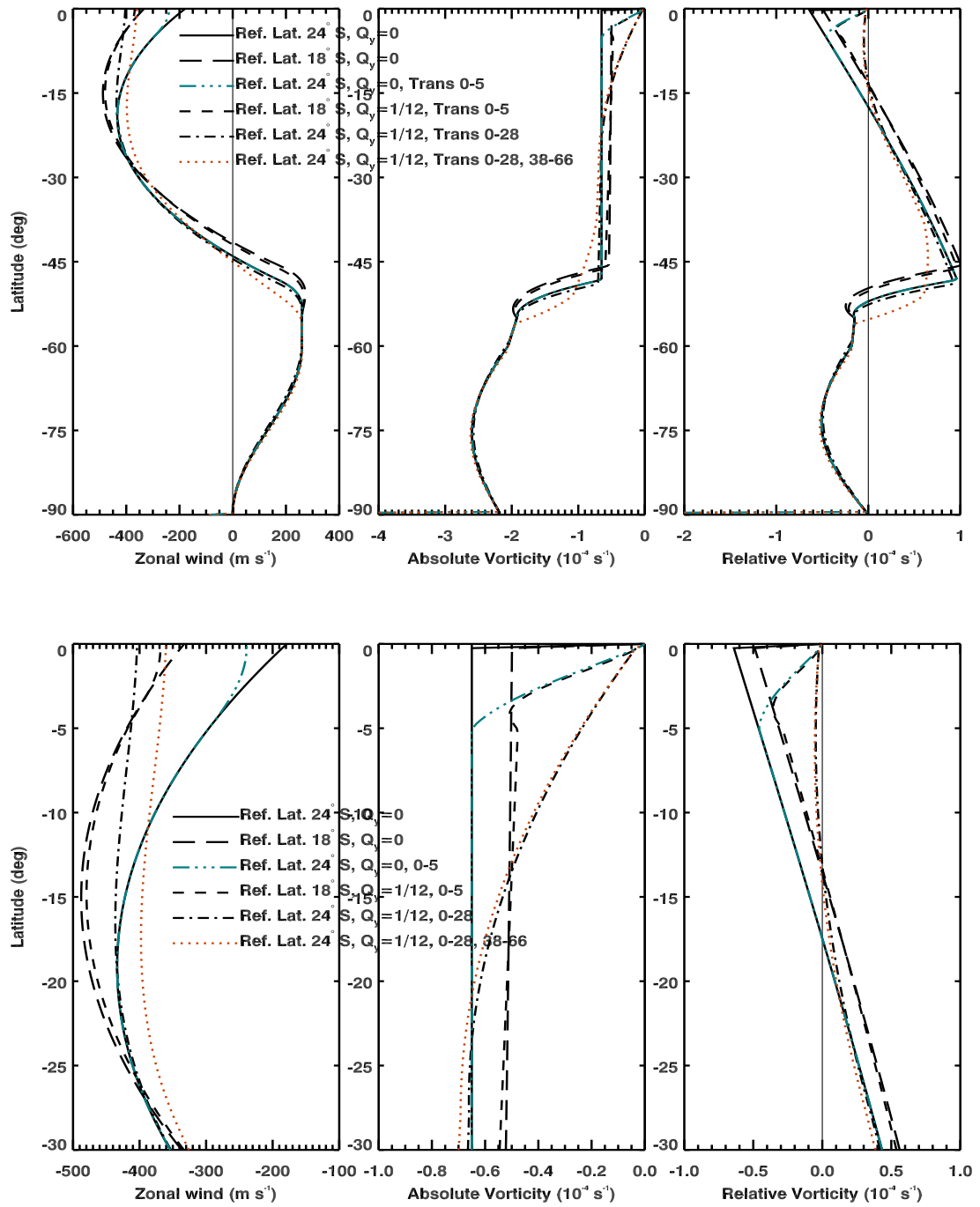


Figure 3.31: Zonal wind profiles (left panel) and their corresponding absolute vorticity profiles (middle panel) and relative vorticity profiles (right panel) for different reference latitudes and different transition methods. The bottom figure shows the detail plots from the equator to 30°S of the top figure.

wind profile, to avoid sharp changes near the 45°S. The 0-5 cases are all calculated from method 1 and the 0-28 and 38-66 cases are calculated from method 2.

Considering the effects of above parameters, we know that to get a good oscillation with slow drift rate, Q_y should be close to 0. But the pure $Q_y = 0$ cases generally showed too small drift rates, compared with the observed value of 1.24 deg/month. This means Q_y should be a little higher than 0. We choose $Q_y = 1/12$ in most of our later simulations and modify the constructed zonal wind profiles with the methods discussed above.

Based on current simulation results, relative strength 1 is too strong to get a small enough inverse aspect ratio of the fitted ellipse. Therefore, we like to use smaller relative strength. In our future simulations, relative strength is often set to 0.5.

Simulation results show that relative size 1 is also big in many cases, especially when we use smaller relative strength. To get suitable size in the simulations, we need to decrease the relative size of the simulated spot. The number 0.8 is often used.

Also, based on above discussion, the turn point of the zonal wind profile should be moved equatorward to allow the vortex drift closer to the equator. We study two main constructed zonal wind profile:

1. With $Q_y = 1/12$ and reference latitude 18°S, transit the profile smoothly from 5°S to the equator. Notice, with this method, the turn point of the zonal wind profile is same as that of the $Q_y = 1/12$ and reference latitude 18°S profile without transition.
2. Construct a constant Q_y between 28°S and 38°S, then transit the profile smoothly from 66°S to 38° and from 28°S to the equator.

These two constructed zonal wind profiles are shown in Figure 3.31.

From now on, simulation results based on these two profiles will be presented and discussed.

3.5 Simulations with $Q_y = 1/12$ and Reference Latitude 18°S

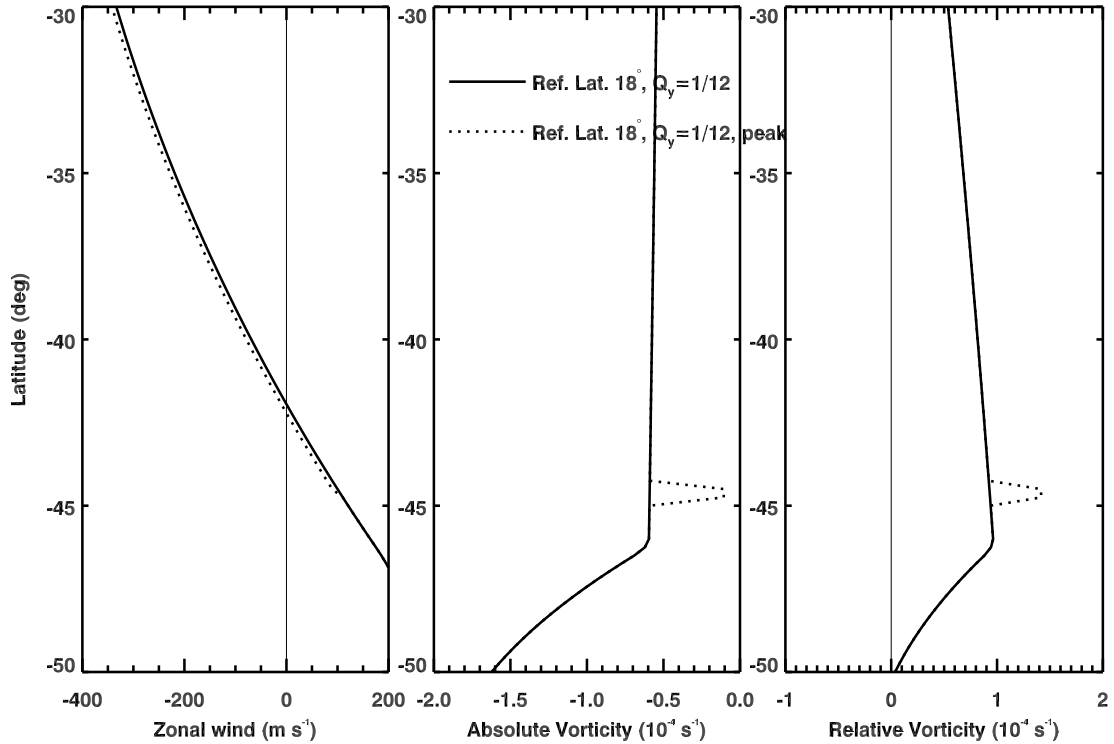


Figure 3.32: Zonal wind profiles (left panel) and their corresponding absolute vorticity profiles (middle panel) and relative vorticity profiles (right panel) for $Q_y = 1/12$, reference latitude 18°S and transition between 5°S and the equator, with and without peak.

In this section, we will talk about the simulations with $Q_y = 1/12$ and reference latitude 18°S . Again, we will investigate the effects of other parameters to check the validity of their effects in this profile. As discussed previously, in most cases we use relative size 0.8 and relative strength 0.5. Our simulations show that the effect of the spot strength cancels part of the effect of $Q_y = 1/12$ on the drift rate, so that

in these simulations the drift rate is small. This make it suitable to use $Q_y = 1/12$ zonal wind profiles.

The whole smooth $Q_y = 1/12$ with reference latitude 18°S profile is shown in Figure 3.31. Based on this, we constructed a profile with a small jump near 45°S . In Figure 3.32 we can see the two profiles are close to each other. The zonal wind profile marked by peak has a small jump near 45°S and so has a peak near this latitude in the corresponding vorticity profiles.

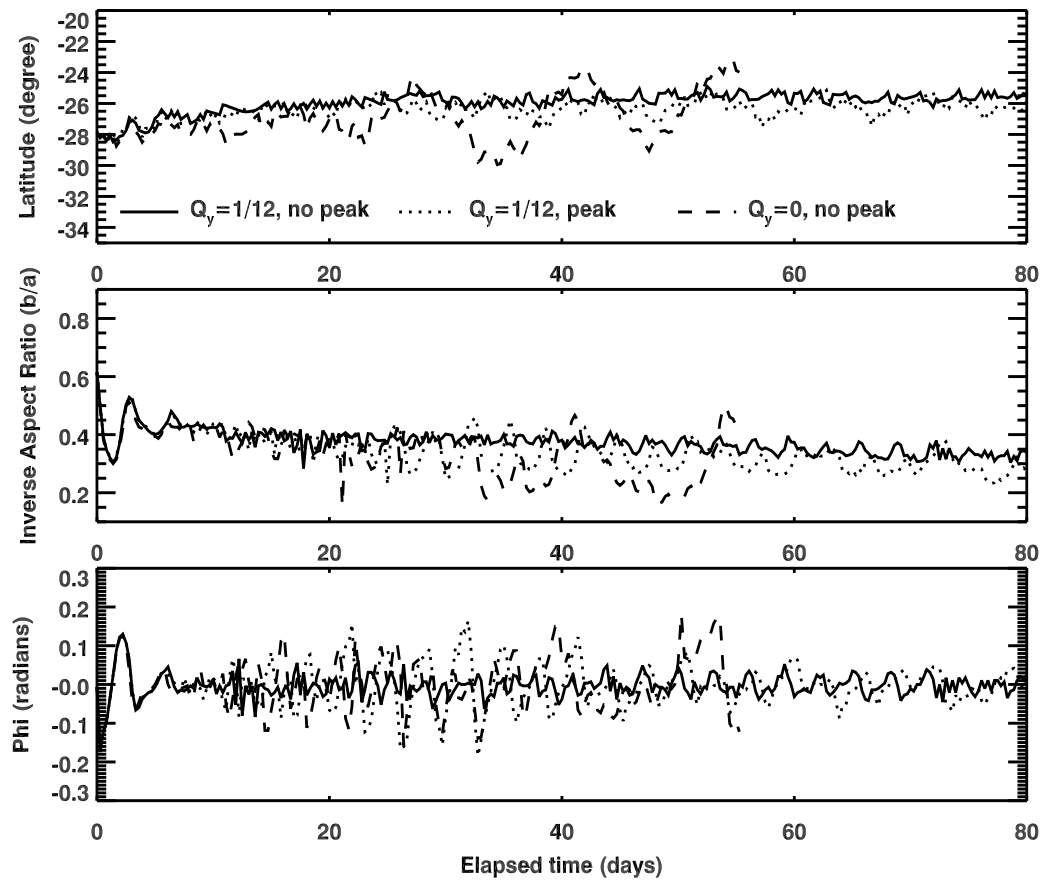


Figure 3.33: Drift rate (top panel), oscillation of inverse aspect ratio (middle panel) and oscillation of orientation angle (bottom panel) of great dark spot in different zonal wind profiles. In these cases, the spots are at layer 7, with relative size 0.8, relative strength 0.5 and initial aspect ratio 1.5, and start from 28°S . The zonal wind profiles all have reference latitude 18°S .

Figure 3.33 shows that the $Q_y = 0$ profile is better for the spot oscillations,

comparing with the two $Q_y = 1/12$ cases. This is similar to what we knew before: constant absolute vorticity tends to be better for the oscillations of the great dark spots. With $Q_y = 1/12$, the zonal wind profile with a peak near 45°S is better for the oscillations. This should come from the perturbation of the small peak. Since the reference latitude 18°S without peak case does not show good oscillations, we did some simulations based on the reference latitude 18°S with peak profile.

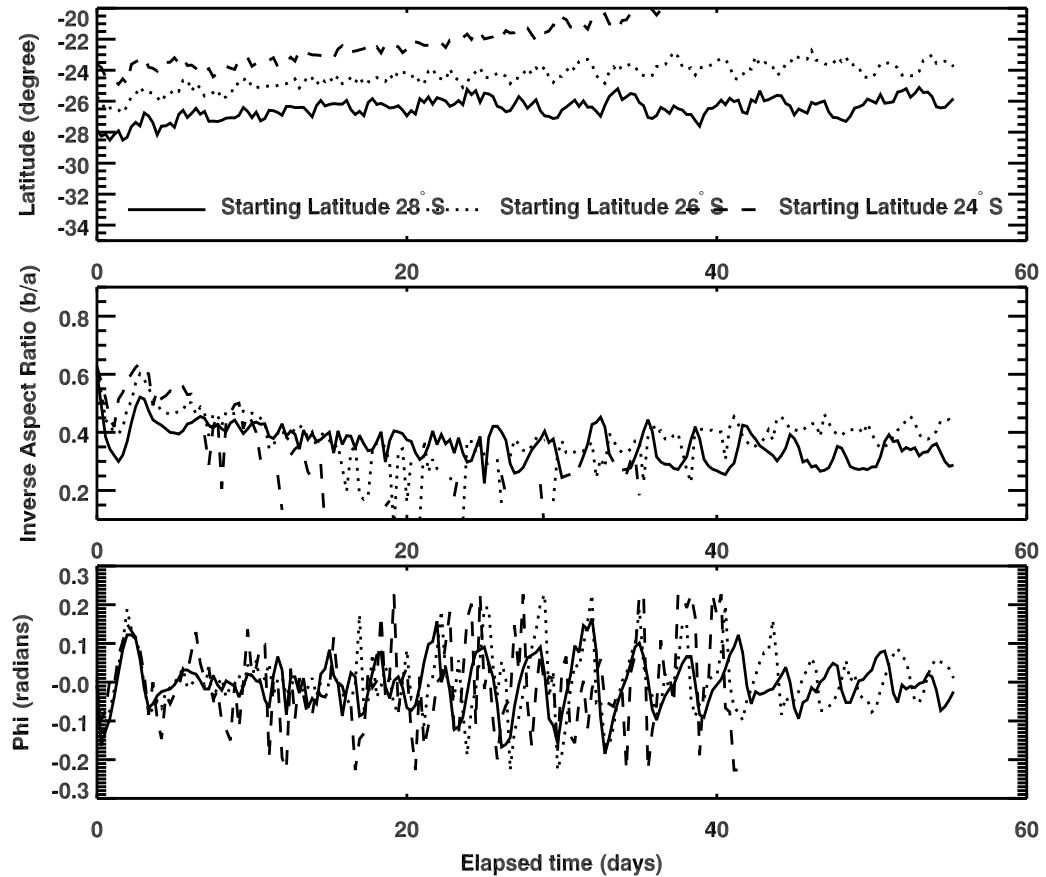


Figure 3.34: Drift rate (top panel), oscillation of inverse aspect ratio (middle panel) and oscillation of orientation angle (bottom panel) of great dark spots starting from different latitudes. In these cases, the spots are at layer 7, with relative size 0.8, relative strength 0.5 and initial aspect ratio 1.5. The zonal wind profile has a reference latitude 18°S and $Q_y = 1/12$ with peak near 45°S .

Figure 3.34 shows the effect of the starting latitude. As before, a starting point too close to the equator is not good for the oscillation of the great dark spot.

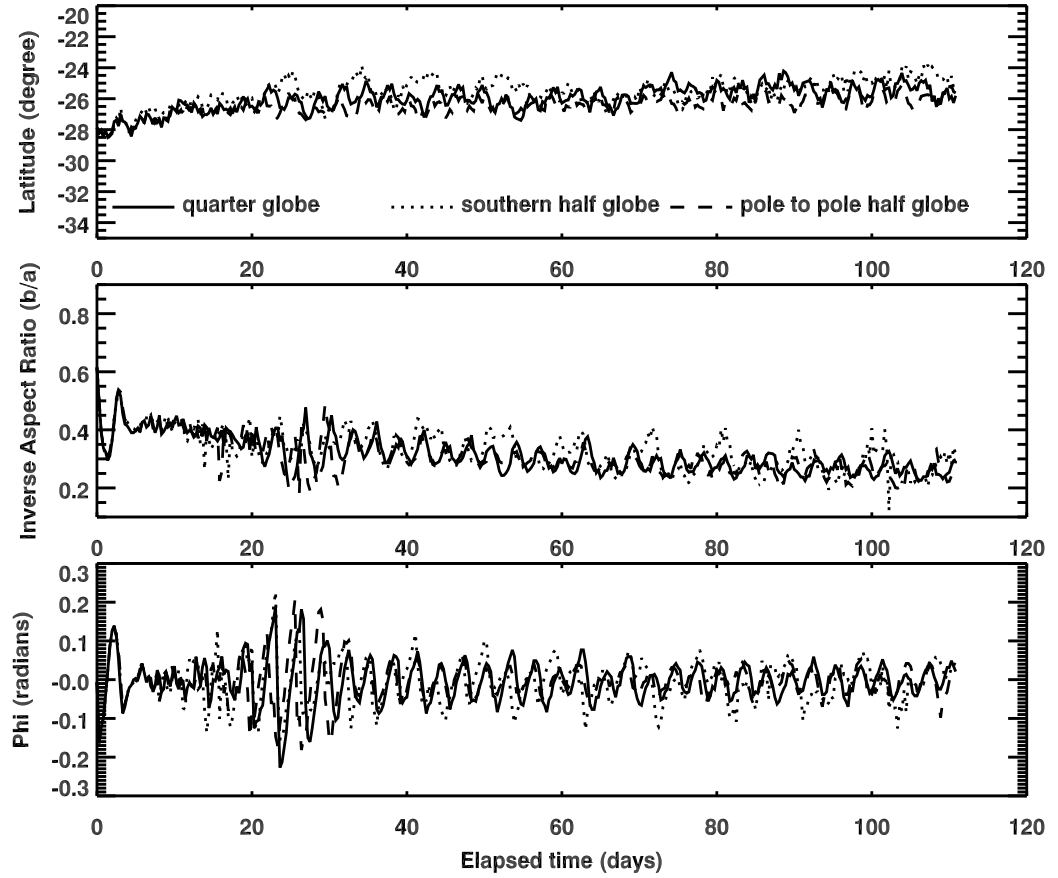


Figure 3.35: Drift rate (top panel), oscillation of inverse aspect ratio (middle panel) and oscillation of orientation angle (bottom panel) of great dark spots in different simulation domains. In these cases, the spots are at layer 7, with relative size 0.8, relative strength 0.5 and initial aspect ratio 1.5, and start from 28°S. The zonal wind profile has a reference latitude 18°S and $Q_y = 1/12$ with peak near 45°S.

Figure 3.35 shows that the south hemisphere domain gives the best long period oscillation among these three cases. Comparing with other figures, the whole globe case is better than this south hemisphere domain in long-period oscillation. This is consistent with our previous result that to get good 8-day period oscillations, we need to simulate the great vortex in the whole globe domain.

Figure 3.36 shows that with a smaller initial aspect ratio, the simulated spot has smaller inverse aspect ratio. With higher AR, the long-period oscillation becomes weaker. Other characteristics, like the drift rate and the oscillation amplitude, are

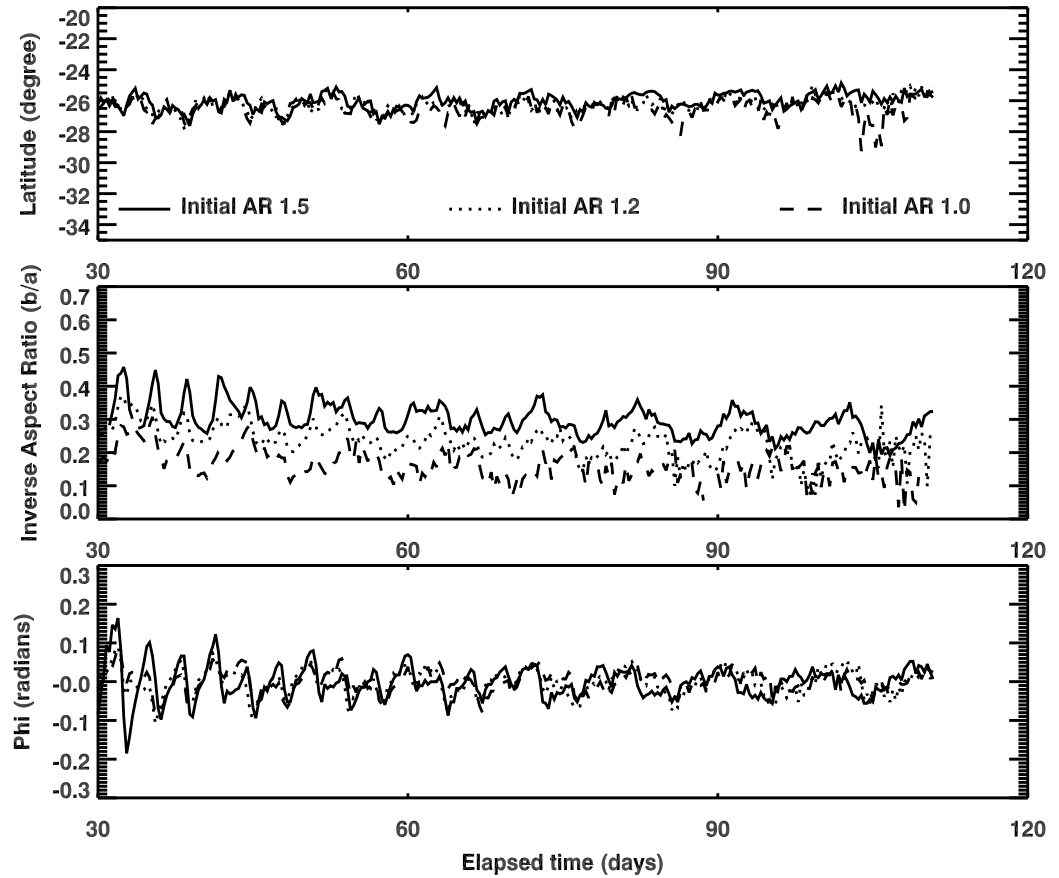


Figure 3.36: Drift rate (top panel), oscillation of inverse aspect ratio (middle panel) and oscillation of orientation angle (bottom panel) of great dark spots with different initial aspect ratios. In these cases, the spots are at layer 7, with relative size 0.8, relative strength 0.5 and initial aspect ratio 1.5, and start from 28°S. The zonal wind profile has a reference latitude 18°S and $Q_y = 1/12$ with peak near 45°S.

similar for different initial AR. This is also same as what we saw previously.

Figure 3.37 shows that the layer effect to the dynamics of the spot is not significant. They have similar drift rates and similar oscillations. With this zonal wind profile, the spot centered in layer 7 shows the smallest inverse aspect ratio.

Figure 3.38 shows the effects of different P-T profiles. Again, we get that N^2 does not change the dynamics of the great dark spot much. Relatively speaking, the nominal vertical profile leads to stronger and more irregular oscillations.

Figure 3.39 shows the effects of the relative strength of the great dark spots.

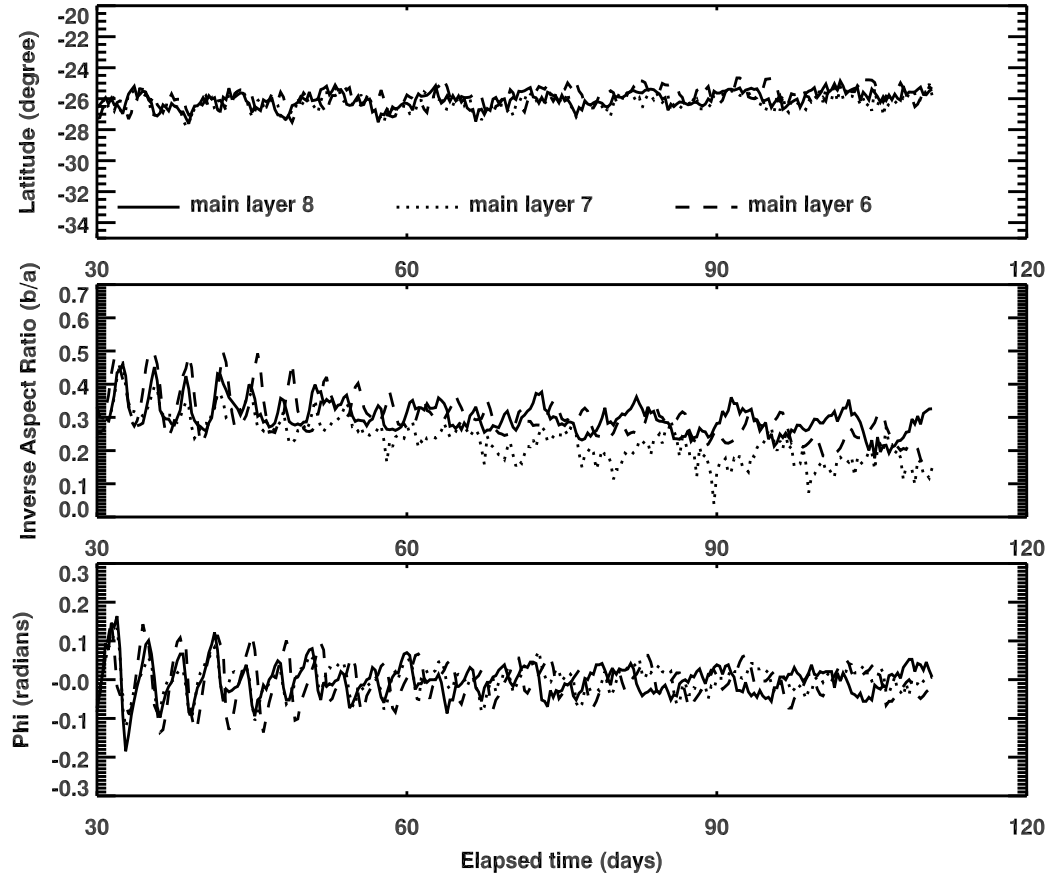


Figure 3.37: Drift rate (top panel), oscillation of inverse aspect ratio (middle panel) and oscillation of orientation angle (bottom panel) of great dark spots at different layers. In these cases, the spots are at layer 8, 7 and 6, respectively. Other parameters are: relative size 0.8, relative strength 0.5 and initial aspect ratio 1.5. All these spots start from 28°S . The zonal wind profile has a reference latitude 18°S and $Q_y = 1/12$ with peak near 45°S .

Again, we get that a stronger spot evolves to a rounder shape.

The above investigations show that our previous results with reference latitude 24°S and $Q_y = 0$ without transition still exist. This means that these effects are independent of the zonal wind profile. Also, as shown above, a small perturbation on the zonal wind profile is helpful for the great dark spot to get stronger oscillations. Since the real zonal winds on a planet cannot be extremely smooth, our results show that maybe just because of some small perturbation in the zonal winds, the GDS-89

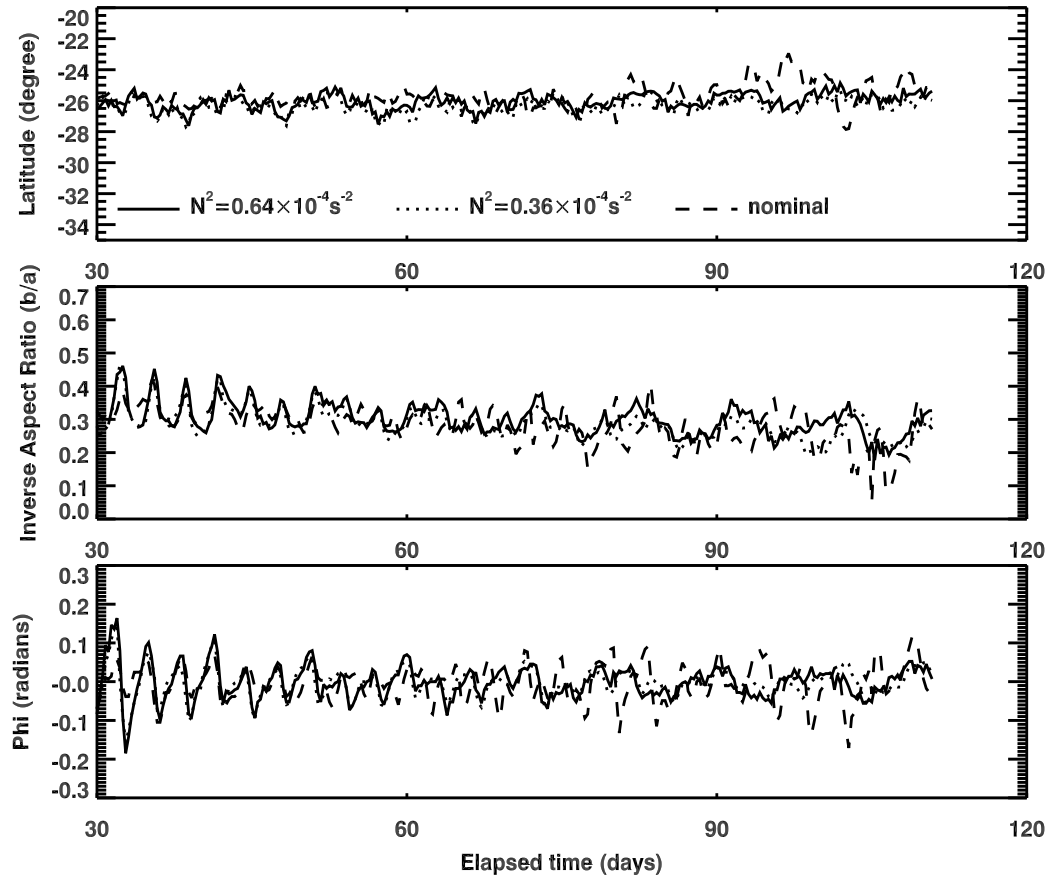


Figure 3.38: Drift rate (top panel), oscillation of inverse aspect ratio (middle panel) and oscillation of orientation angle (bottom panel) of great dark spots with different P-T profiles. In these cases, the spots are at layer 7 with relative size 0.8, relative strength 0.5 and initial aspect ratio 1.5. All these spots start from 28°S . The zonal wind profile has a reference latitude 18°S and $Q_y = 1/12$ with peak near 45°S .

showed strong oscillations. Certainly, there are other parameters that can influence the oscillations, like Q_y , the starting latitude and the vertical layer. Since we do not have enough information about all these parameters, currently we cannot conclude which one is the main parameter for the spot oscillations. The Neptune atmosphere system is a complex system. Many parameters are correlated with each other. We just want to test the effects of different parameters and give a possible range for some parameters.

For the next step we will consider the second method of getting a higher turn

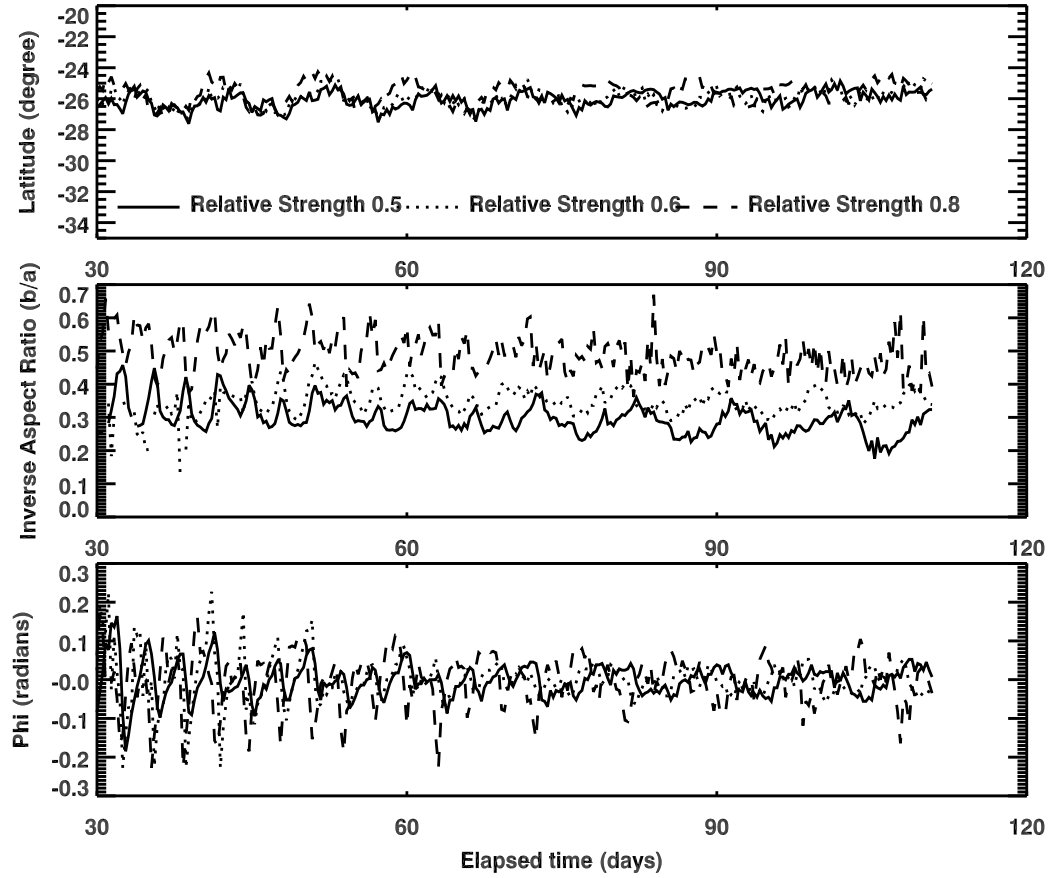


Figure 3.39: Drift rate (top panel), oscillation of inverse aspect ratio (middle panel) and oscillation of orientation angle (bottom panel) of great dark spots with different initial relative strength. In these cases, the spots are at layer 7 with relative size 0.8 and initial aspect ratio 1.5. All these spots start from 28°S . The zonal wind profile has a reference latitude 18°S and $Q_y = 1/12$ with peak near 45°S .

point latitude without moving the reference latitude. Instead of keeping constant Q_y in a big area, which is hard to get in the real world, we try to narrow it to about 10° and continuously transit to both ends.

3.6 Simulations with Smooth Q_y Change

Now, we come back to reference latitude 24°S . We construct zonal wind profiles with constant Q_y near the starting latitude of observational GDS-89 and transit it to both the equator and higher latitude. This method has several benefits. First, it can

generate a constant Q_y region, which is what we want for the survival of the great dark spots. Second, it can eliminate the sharp change at about 45°S. Third, it can increase the turn point of the zonal wind profile to a lower latitude, closer to the equator. Finally, it has continuous profile near the equator. All these are what we want based on our previous discussion.

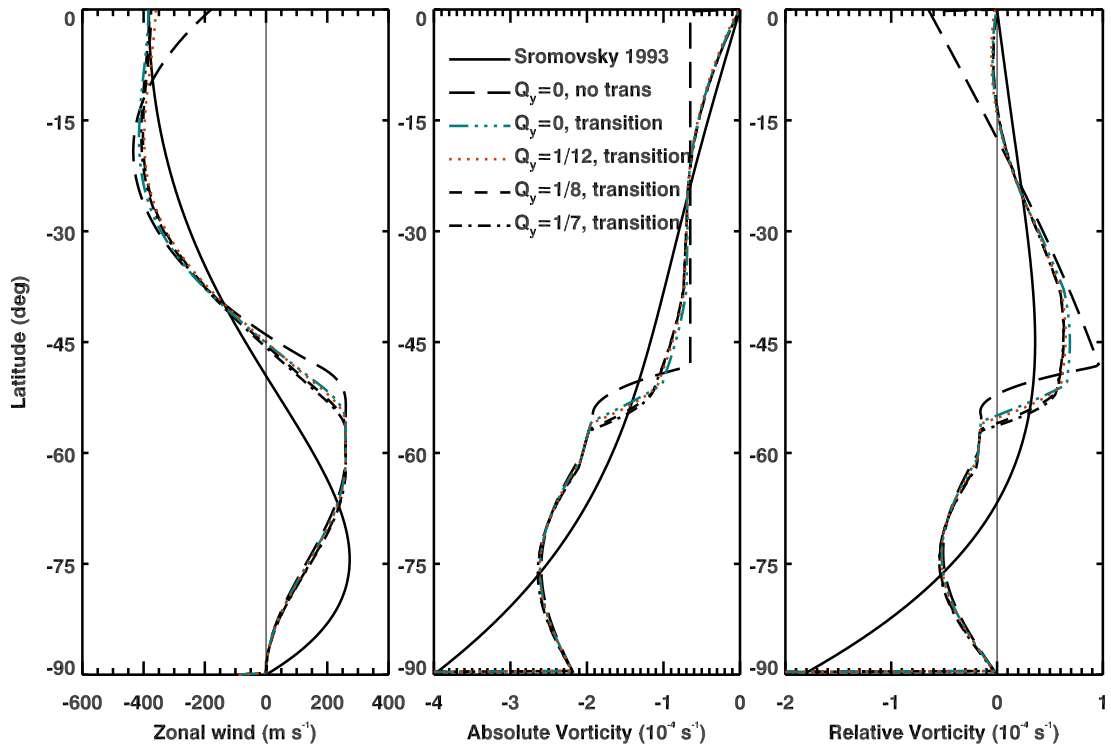


Figure 3.40: Zonal wind profiles (left panel) and their corresponding absolute vorticity profiles (middle panel) and relative vorticity profiles (right panel) for different Q_y with transition on both ends. The constant Q_y region is 28°S to 38°S.

We constructed several profiles with constant Q_y from 28°S to 38°S. Figure 3.40 shows the profiles with $Q_y = 0, 1/12, 1/8$ and $1/7$. We can see how they transit from the constant Q_y region to the equator and to the higher latitudes.

Figure 3.41 shows the effects of Q_y . As what we see before, higher Q_y leads to faster drift. $Q_y = 1/7$ drifts too fast and lose its shape after 90 days.

Figure 3.42 is similar to Figure 3.41, but at a deeper layer. Still, the $Q_y = 1/7$ case

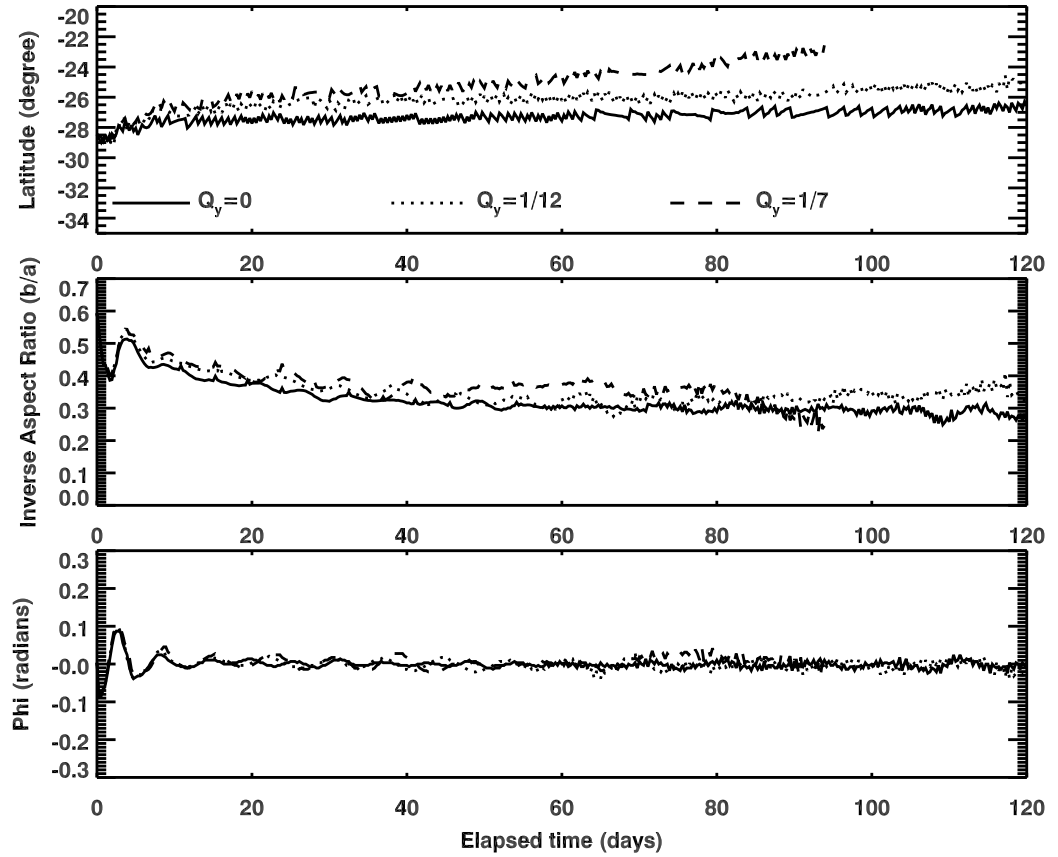


Figure 3.41: Drift rate (top panel), oscillation of inverse aspect ratio (middle panel) and oscillation of orientation angle (bottom panel) of great dark spots with different Q_y . In these cases, the spots are at layer 7 with relative size 0.8, relative strength 0.5 and initial aspect ratio 1.5. All these spots start from 29°S . The zonal wind profile has a reference latitude 24°S .

drifts quickly to the equator and cannot keep its shape for a long time. Different from those simulations in Figure 3.41, which is one layer up, we can see good oscillations in the $Q_y = 0$ case. The amplitude increases when the spot drifts to the equator. This does not appear in previous simulations. It seems that this effect comes from the changing Q_y . At last, the $Q_y = 0$ case breaks at about 25°S , after four-month steady drift. Also, the $Q_y = 1/12$ case shows fast increase in the oscillation amplitude and breaks its shape after 60 days. In these cases, we cannot see the three-day oscillations, which always exist in previous simulation cases. The difference between these zonal

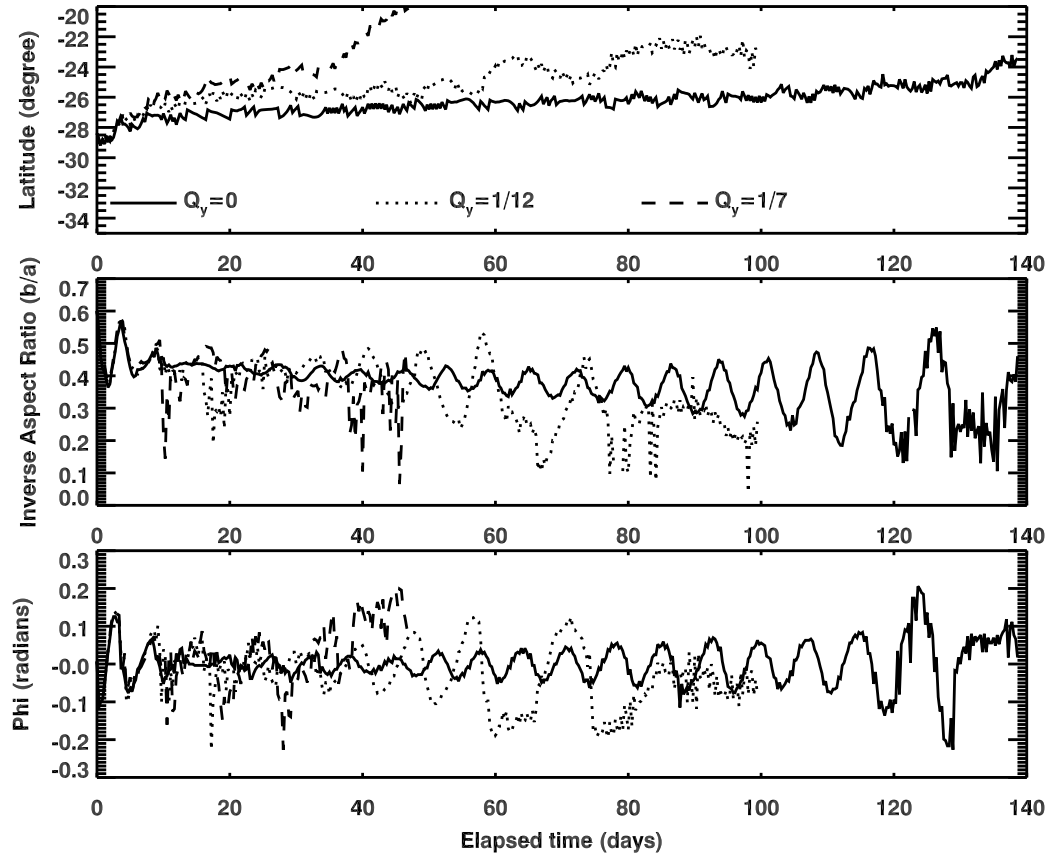


Figure 3.42: Drift rate (top panel), oscillation of inverse aspect ratio (middle panel) and oscillation of orientation angle (bottom panel) of great dark spots with different Q_y . In these cases, the spots are at layer 8 with relative size 0.8, relative strength 0.5 and initial aspect ratio 1.5. All these spots start from 29°S . The zonal wind profile has a reference latitude 24°S .

wind profiles from previous profiles is the transition at higher latitudes. This suggests that the three-day oscillation mode may be related to the sharp changes near 45°S in previous zonal wind profiles.

Oscillations

In the quarter globe simulations, we can get a ~ 3 day oscillation easily. We can also get some long period oscillations, but on the quarter globe, it is not easy and the long-term oscillations are not strong and clear. In the whole globe domain simulations, in

many cases we see long period oscillations. But the short period oscillations are often there as well. Looking at Table 3.3, we can see two periods for many cases, they are about the short period (~ 3 day) and the long period (≥ 8 days) oscillations.

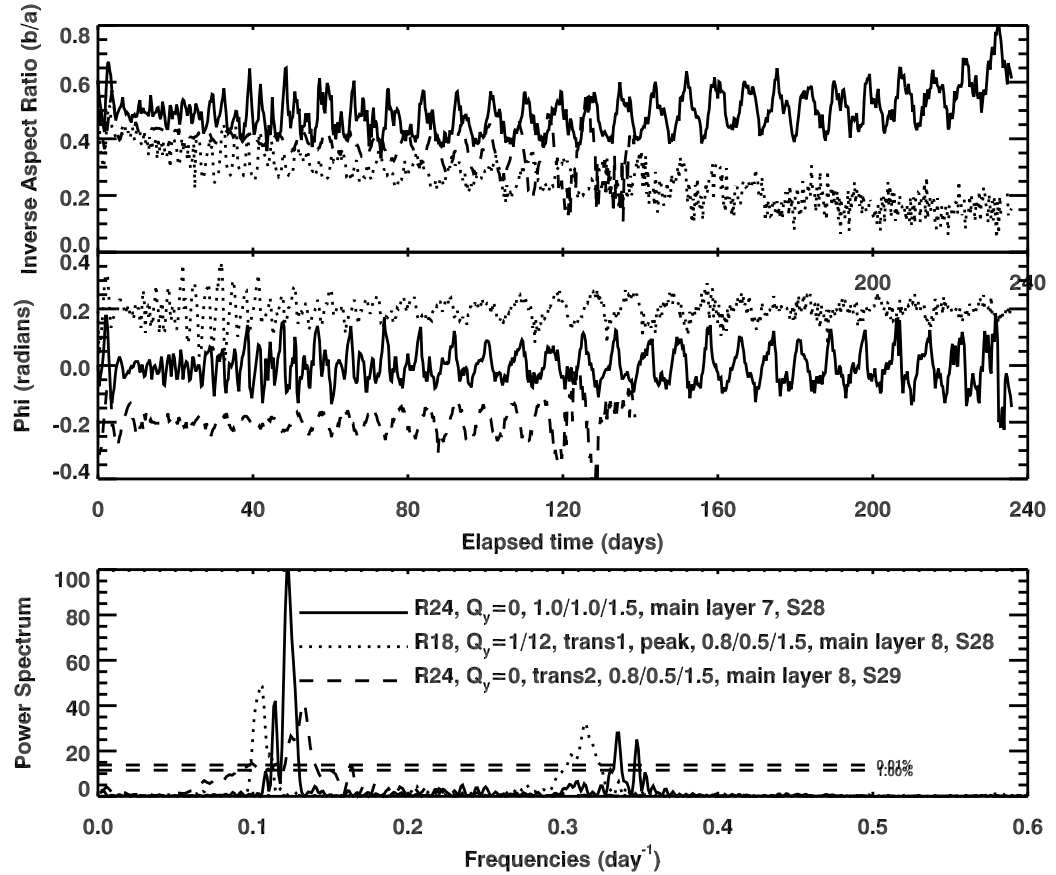


Figure 3.43: Oscillations of three simulation cases. The top panel shows oscillation of inverse aspect ratio, the middle panel shows oscillation of orientation angle and the bottom panel shows the power spectrum calculating from the angle oscillations. In the middle panel, the dotted line is shifted 0.2 above and the dashed line is shifted 0.2 below to make their curves clearer in the plot. R24 means reference latitude 24°S and R18 means reference latitude 18°S . The three numbers separated by slash are initial relative size/relative strength/aspect ratio. The notation trans1 means transition from 5°S to the equator; the notation trans2 means transition from 28°S to the equator and 38°S to 66°S . The notation "peak" means there is a small jump on the constructed zonal wind profile near 45°S . The last numbers are starting latitudes.

Figure 3.43 shows the oscillations of three cases over eight months. The "R24, $Q_y = 0, 1.0/1.0/1.5, \text{S28}$ " case shows a much stronger long period oscillation than

short period oscillation. In the "R18, $Q_y = 1/12$, trans1, 0.8/0.5/1.5, S28" case, the long period oscillation is weaker, but still stronger than the short period oscillation. These two cases both show two mode oscillations. In the "R24, $Q_y = 0$, trans2, 0.8/0.5/1.5, S29" case, the short period oscillation disappears and we can only see one peak near 0.13 day^{-1} (period = 7.7 day).

The short period oscillations, as we see, appears when the zonal wind profile changes sharply near 45°S . When the southern boundary of the constant Q_y region is connected with higher latitudes smoothly by modifying Q_y , this oscillation mode disappears. Therefore, we can believe that this mode is related to the latitudinal change of the zonal wind profile.

As to the long period oscillation, in the quarter globe and pole to pole half globe simulations, this mode is hard to achieve. In the south hemisphere and whole globe simulations, this mode appears. A possible explanation is that the long period oscillation is related to the longitudinal circle effects when the GDS rotates globally in the atmosphere.

From Figure 3.43 we can see that there is an evolution of the oscillations. The short period oscillation appears first and then gradually transit to the long period oscillation. Figure 3.44 shows both the short period oscillation (top panel) and long period oscillation (lower panel) of the "R18, $Q_y = 1/12$, trans1, 0.8/0.5/1.5, main layer 8, S28" case. In the top panel, an obvious ~ 3 day period oscillation can be observed. In the bottom panel, the short period oscillation disappears and a roughly 9 day period oscillation can be observed. Figure 3.45 shows the oscillation of the "R24, $Q_y = 0$, trans2, 0.8/0.5/1.5, main layer 8, S29" case. A near 8-day period oscillation can be observed.

The transition from short period oscillation to long period oscillation may show that the short period oscillation is related to the initial adjustment of the great dark spot. When the spot is better balanced, the short period oscillation is weaker.

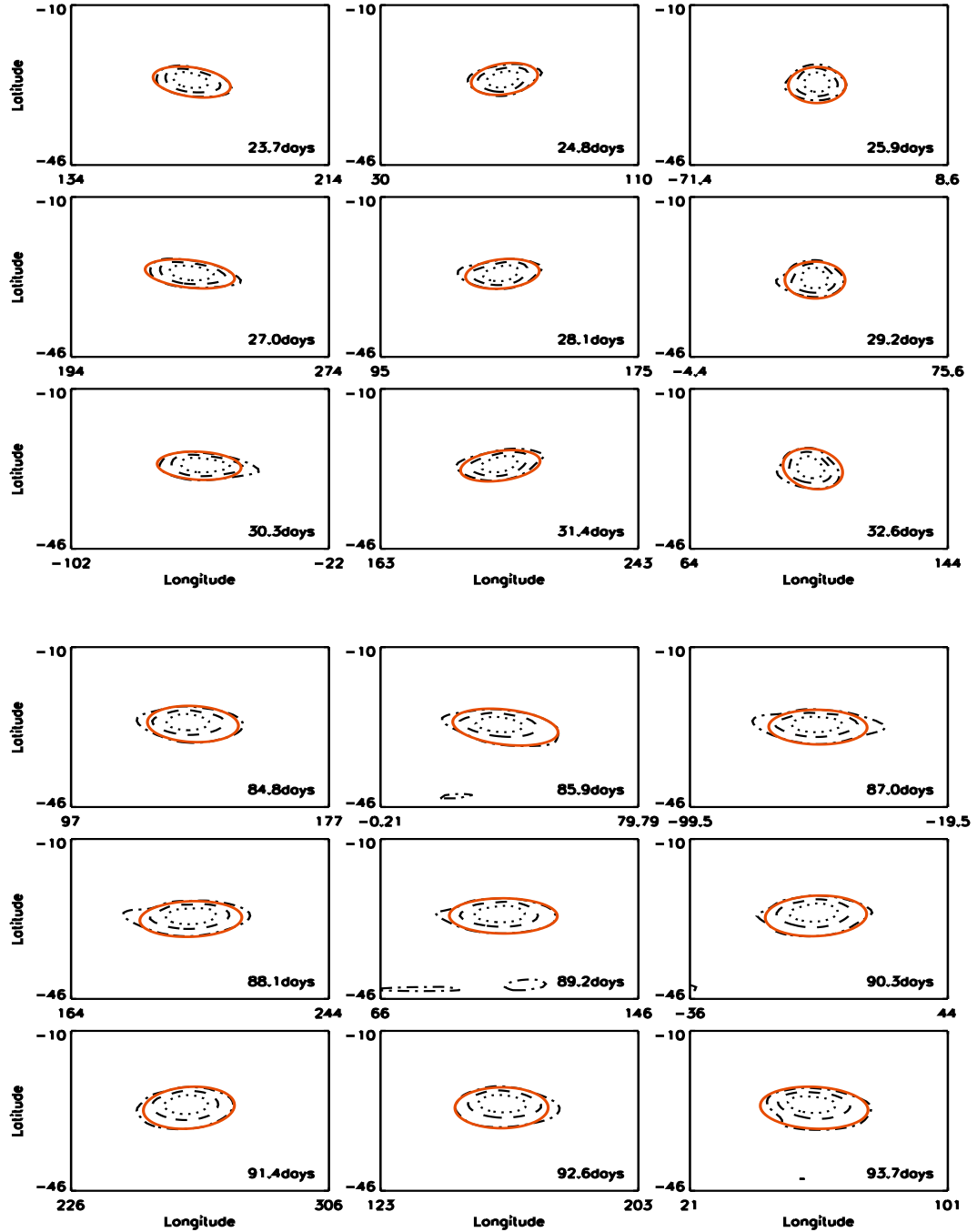


Figure 3.44: The contour plots of the whole globe simulation with $Q_y = 1/12$, reference latitude 18°S , relative size 0.8, relative strength 0.5 and initial AR 1.5. The zonal wind profile transit from 5°S to the equator and has a peak near 45°S . The spot is generated at main layer 8 and starts from 28°S . The top plot is from 23.7 days to 32.6 days; the bottom plot is from 84.8 days to 93.7 days. The contour plot of potential vorticity is on layer 8 (1636 mbar).

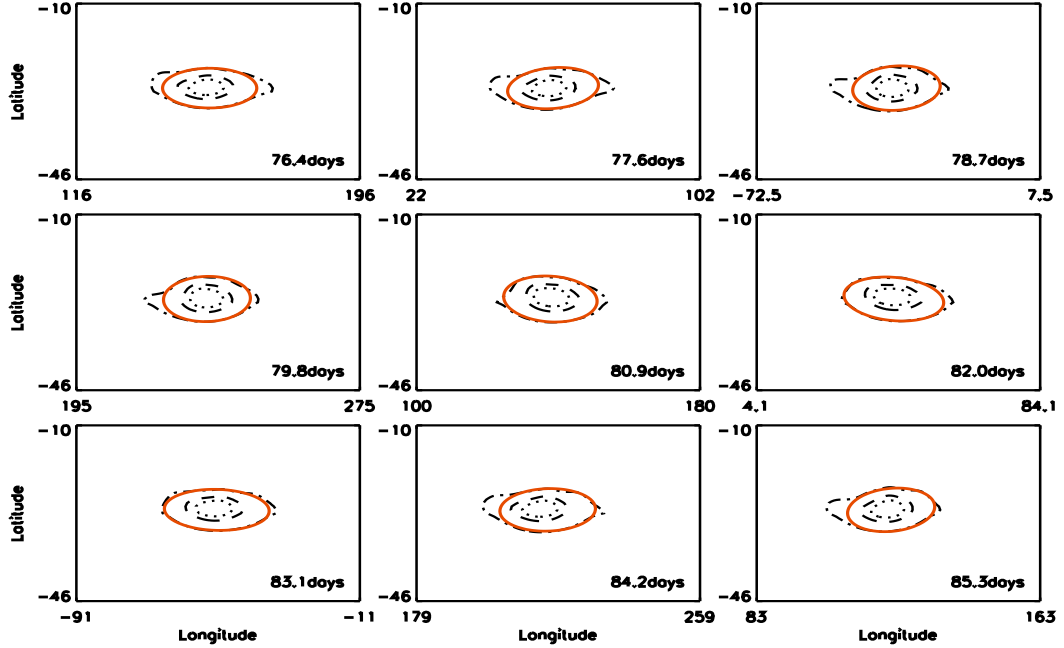


Figure 3.45: The contour plots of the whole globe simulation with $Q_y = 0$ between 28°S and 38° , reference latitude 24°S , relative size 0.8, relative strength 0.5 and initial AR 1.5. The zonal wind profile transit smoothly to both the equator and the high latitudes. The spot is generated at main layer 8 and starts from 29°S . The contour plot of potential vorticity is on layer 8 (1636 mbar).

Figure 3.46 shows the oscillations of three cases with different initial aspect ratios. The AR=1.5 case shows smaller long period oscillation amplitude in the power spectrum than in Figure 3.43 because here we only use the first four months data. The later oscillations are dominated by the long period oscillation. Therefore, cutting the data after 120 days decreases the amplitude of the long period oscillation.

In Figure 3.46, the AR=1.2 and AR=1.0 cases show smaller amplitudes near 0.33 day^{-1} and have stronger amplitude near 0.1 day^{-1} . This shows that the AR=1.2 case and the AR=1.0 case are better balanced than the AR=1.5 case and need less adjustment at the beginning. This can also be observed in the top panel and the middle panel.

More power spectra are plotted in Figure 3.47. From the top panel and the middle

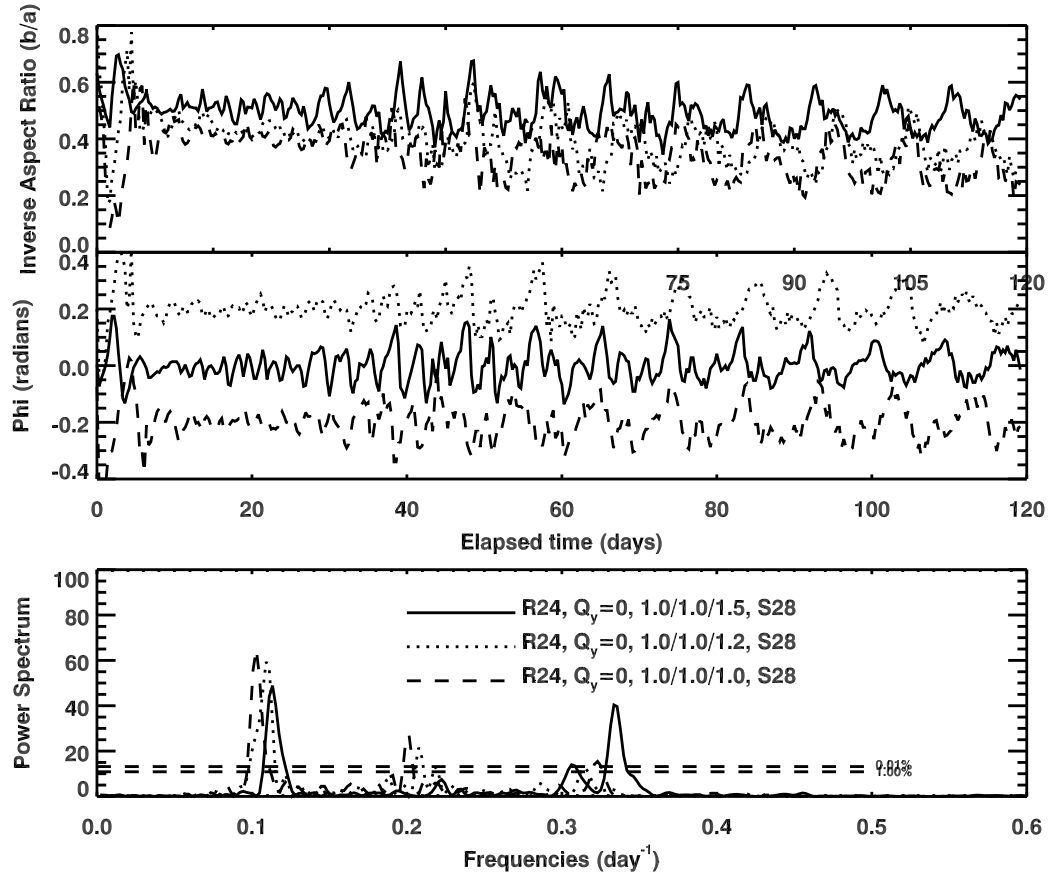


Figure 3.46: Oscillations of three simulation cases with different initial aspect ratio. The top panel shows oscillation of inverse aspect ratio, the middle panel shows oscillation of orientation angle and the bottom panel shows the power spectrum calculating from the angle oscillations. In the middle panel, the dotted line is shifted 0.2 above and the dashed line is shifted 0.2 below to make their curves clearer in the plot. R24 means reference latitude 24°S . The three numbers separated by slash are initial relative size/relative strength/aspect ratio. The last numbers are starting latitudes.

panel we can see that the 360° in the longitudinal direction is needed to get long period oscillations. From the bottom panel we can see that the short period oscillation does not exist any more. This means the zonal wind profiles from transition method 2 do not support short period oscillation. Since the main difference from them to other profiles are the smooth transition at higher latitudes, we can believe that the poleward bound of the near constant Q_y region is responsible for the short period oscillations. Also, with this kind of zonal wind profile, a spot in a deeper layer has

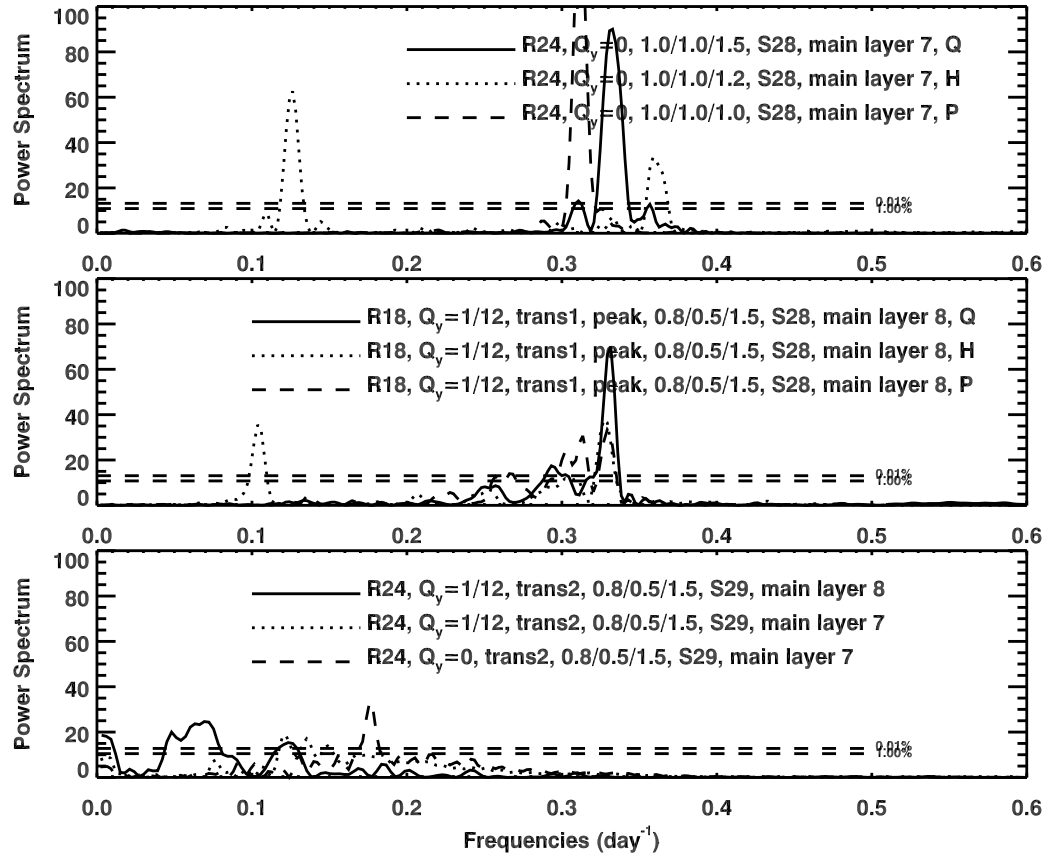


Figure 3.47: Oscillations of nine simulation cases. The top panel and the middle panel show the effects of simulation domain. The character "Q" means quarter globe; "H" means southern hemisphere; "P" means pole to pole half globe. The bottom panel shows the effect of different layer and the effect of modifying a constructed zonal wind profile with method 2. The notation "trans1" and "trans2" mean transition method 1 and transition method 2 as discussed above.

stronger oscillations than a spot in a upper layer.

Figure 3.48 shows the phase plots of observed GDS-89, Kida theory and six whole globe simulation results. We can see that smaller initial AR leads to smaller inverse AR. $Q_y = 0$ cases show strong oscillations. The "R24, $Q_y = 0$, trans2, 0.8/0.5/1.5, S29" case shows increasing strength of the oscillations.

3.7 Discussion

The investigations of GDS-89 with a purely dynamical model suggest several ideas about its physics. First, in order to get small drift rate and strong and clear oscillations, the background zonal wind profile should have near constant absolute vorticity gradient near the great dark spot area. Second, the turn point of the zonal wind profile influences the lifetime of the great dark spot. It sets a limit latitude for the spot: when the spot moves close to this point, it will break or be kicked back. Third, a small perturbation in the zonal wind profile may drive the oscillation of the great dark spot. Fourth, the vertical P-T profiles with different N^2 do not have significant influence on the drift and oscillations. The vertical velocity shear near the great dark spot layer cannot be big while keeping the GDS oscillations smooth and drift steady. Furthermore, as we see in several cases, in order to accurately simulate a great vortex in Neptune's atmosphere, a whole globe domain is needed. Smaller domains will have boundary effects on the equator and eliminate the global circulation effect of the atmosphere.

About the characteristics of the GDS, the simulations suggests that a weaker spot will have smaller drift rate and smaller inverse aspect ratio; a smaller spot will have faster drift rate and higher inverse aspect ratio; and a spot with smaller initial aspect ratio will have smaller inverse aspect ratio. In the study of the oscillation periods, the simulation results indicate that a near three day period oscillation is related to the latitudinal effect of the zonal wind profile and a near 8 day (which is the observed oscillation period of GDS-89) period oscillation is related to the longitudinal effects of the zonal wind profile. This suggests that the oscillations may be related to the waves in these two directions. Finally, a better balanced Great Dark Spot can get stronger long period oscillation and weaker short period oscillation.

As mentioned before, the Neptune atmosphere is a complex system. There are many parameters correlating with each other. Also, the observational data are limited

because of the limited number of observations and the long distance from Neptune to Earth. Therefore, it is maybe impossible to determine all the parameters through simulating a perfect great dark spot with all the observed characteristics. What we can do is to give a possible range for these parameters. In this chapter, we investigated different zonal wind profiles, different spots and different vertical layer setups. Through this kind of parametric simulations, we achieved some results as shown above. This is helpful for people to understand the Neptune atmosphere better and understand the simulations of great vortices on a planet better. The knowledge we get here will be applied to our later simulations, including the Uranian Dark Spot and the cloud model.

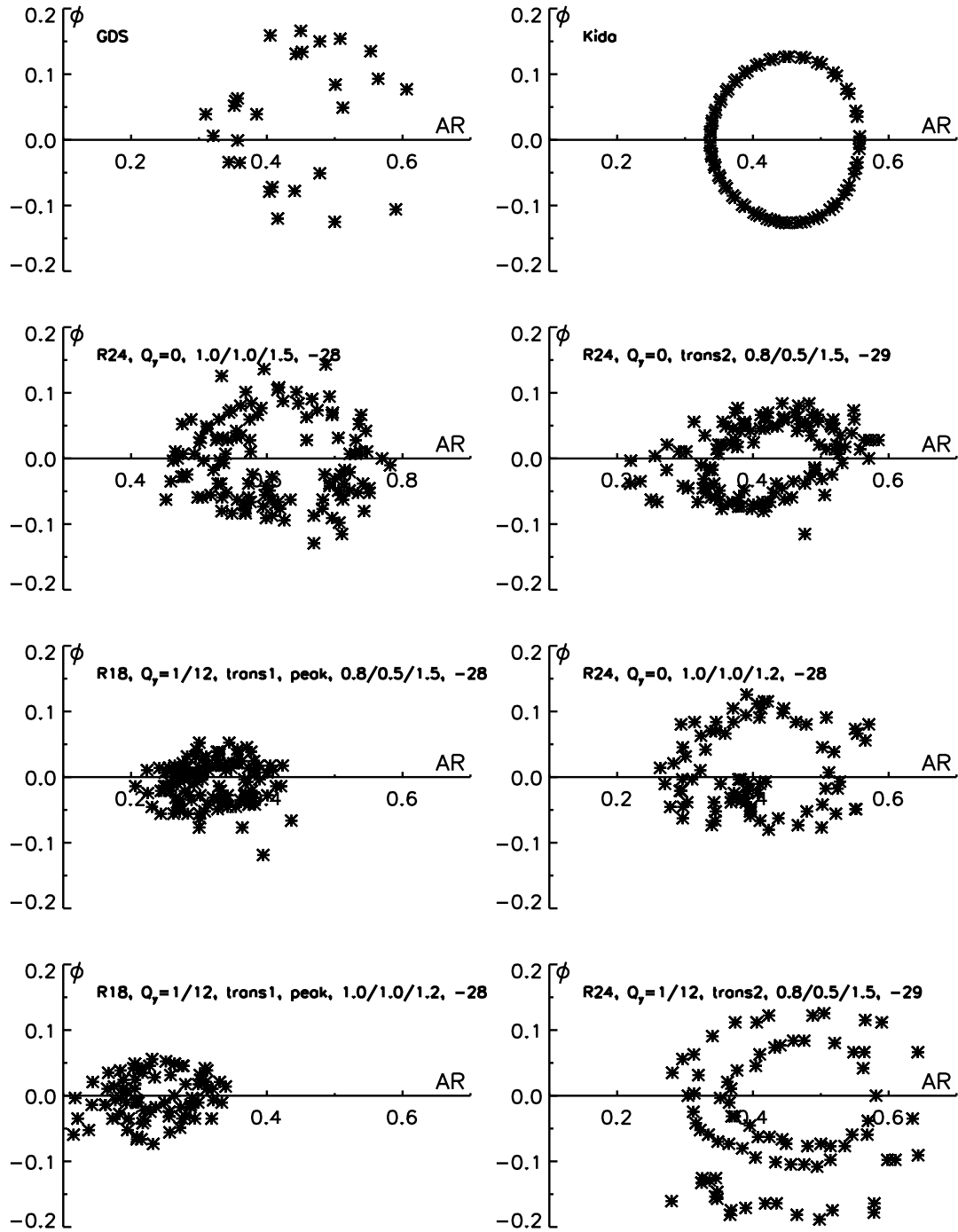


Figure 3.48: Phase plot for six LeBeau_Dowling vortices, having different initial conditions, starting from different latitudes and in different constructed zonal wind profiles. Top left plot is from Voyager-II observational results of GDS-89; top right plot is from Kida theory; others are as the parameters shown on them. All these cases are in whole globe domain. The explanation of the parameters used here are same as Figure 3.43.

Table 3.3: Selected simulation results for GDS-89 on Neptune in whole globe region.

Q_y	λ_0	Str./Size/AR	Drift	Periods	Inverse AR	$\phi(\text{rad})$	Others
	GDS-89 -18°S		1.24	8.0	0.42±0.12	0±0.15	
	GDS-89 -22°S		1.24	8.0	0.35±0.11	-	
0	28°S	1.0/1.0/1.5	0.1	2.9&8.8	0.48±0.12	0.01±0.09	
1/12	28°S	1.0/1.0/1.5	13.7	N/A	N/A	N/A	
1/6	28°S	1.0/1.0/1.5	31.7	N/A	N/A	N/A	
1/3	28°S	1.0/1.0/1.5	38.9	N/A	N/A	N/A	
2/3	28°S	1.0/1.0/1.5	53.6	N/A	N/A	N/A	
0	28°S	1.0/0.8/1.5	0.0	3.2&9.5	0.52±0.17	0.01±0.14	
0	28°S	1.0/0.6/1.5	2.5	3.0&8.7	0.58±0.15	0.02±0.21	
0	28°S	0.8/1.0/1.5	0.0	3.2&10.0	0.30±0.10	0.01±0.09	
0	28°S	0.5/1.0/1.5	0.0	3.2&10.5	0.19±0.14	0.01±0.09	
0	28°S	0.8/0.8/1.5	-0.3	3.3&10.0	0.32±0.14	-0.01±0.09	
0	28°S	0.5/0.8/1.5	-0.1	3.3&10.8	0.27±0.13	0.01±0.13	
0	28°S	1.0/1.0/1.5	-0.7	3.2&10.0	0.35±0.15	0.0±0.09	$N^2 = 0.36 \times 10^{-4} s^{-2}$
0	28°S	1.0/1.0/1.5	-1.6	3.7/N/A	0.40±0.20	-0.02±0.12	nominal
0	28°S	1.0/1.0/1.5	26.3	N/A	N/A	N/A	$m_2 = 0.1$
0	28°S	1.0/1.0/1.5	7.6	N/A	N/A	N/A	$m_2 = -0.1$
0	28°S	1.0/1.0/1.5	-1.1	3.2&10.4	0.35±0.09	0.03±0.09	$m_2 = 0.01$
0	28°S	1.0/1.0/1.5	0.3	3.1&9.4	0.41±0.07	0.02±0.10	$m_2 = -0.01$
0	28°S	1.0/1.0/1.5	0.2	2.8&8.3	0.48±0.12	-0.04±0.14	$m_2 = 0.03$
0	28°S	1.0/1.0/1.5	4.3	2.9&8.3	0.55±0.25	0.01±0.24	$m_2 = -0.03$
0	28°S	1.0/1.0/1.2	0.4	3.2&9.5	0.36±0.12	0.01±0.08	
0	28°S	1.0/1.0/1.0	0.1	3.1&9.5	0.32±0.12	0.03±0.11	

1. All the parameters are same as those in Table 3.2.
2. Two periods of the oscillations are shown in this table.

Table 3.3: Selected simulation results for GDS-89 on Neptune in whole globe region. - Continued

Q_y	λ_0	Str./Size/AR	Drift	Periods	Inverse AR	ϕ (rad)	Others
0	28°S	1.0/1.0/1.5	0.8	3.2&9.8	0.45±0.15	0.00±0.10	main layer 6
0	28°S	1.0/1.0/1.5	0.2	3.0&8.9	0.50±0.10	0.02±0.11	main layer 8
0	28°S	1.0/1.0/1.5	0.1	2.9&8.9	0.47±0.17	0.01±0.16	Ref. Lat. 21°S
0	28°S	1.0/1.0/1.5	-0.8	3.2&11.1	0.38±0.14	0.00±0.12	Ref. Lat. 20°S
0	28°S	1.0/1.0/1.5	0.4	3.4&11.2	0.39±0.16	0.00±0.13	Ref. Lat. 19°S
0	28°S	1.0/1.0/1.5	0.6	3.3&11.0	0.42±0.17	0.00±0.13	Ref. Lat. 18°S
0	28°S	1.0/1.0/1.5	0.9	2.9&10.0	0.45±0.12	0.00±0.14	Ref. Lat. 17°S
0	28°S	1.0/1.0/1.5	2.7	3.3&9.1	0.45±0.08	0.00±0.09	Ref. Lat. 16°S
0	28°S	1.0/1.0/1.5	4.2	3.0&N/A	0.49±0.08	0.00±0.11	Ref. Lat. 15°S
0	26°S	1.0/1.0/1.5	-0.2	3.2&9.5	0.37±0.16	0.02±0.13	
0	24°S	1.0/1.0/1.5	0.4	2.8&8.5	0.85±0.45	0.0±0.27	
0	26°S	1.0/1.0/1.5	0.3	2.7&8.0	0.53±0.15	0.01±0.19	Ref. Lat. 21°S
0	24°S	1.0/1.0/1.5	8.7	3.6&7.5	0.57±0.16	0.02±0.27	Ref. Lat. 21°S
0	26°S	1.0/1.0/1.5	-0.4	3.1&10.4	0.43±0.13	0.00±0.11	Ref. Lat. 19°S
0	24°S	1.0/1.0/1.5	1.9	2.7&N/A	0.63±0.14	0.00±0.22	Ref. Lat. 19°S
0	24°S	1.0/1.0/1.5	0.8	3.1&10.3	0.52±0.12	0.00±0.14	Ref. Lat. 17°S
0	22°S	1.0/1.0/1.5	5.9	2.8&N/A	0.73±0.14	0.00±0.22	Ref. Lat. 17°S
1/12	32°S	1.0/1.0/1.5	1.4	3.1/N/A	0.37±0.08	0.01±0.08	
1/12	30°S	1.0/1.0/1.5	4.7	2.9/N/A	0.52±0.05	0.00±0.08	
1/12	28°S	0.8/0.5/1.5	0.1	3.0/N/A	0.37±0.03	0.01±0.03	Ref. Lat. 18°S, trans1, main layer 8
1/12	28°S	0.8/0.5/1.5	0.3	3.1/9.8	0.29±0.07	0.00±0.04	Ref. Lat. 18°S, trans1, peak, main layer 8
0	28°S	0.8/0.5/1.5	2.6	N/A/13.3	0.32±0.15	0.06±0.11	Ref. Lat. 18°S, trans1, main layer 8

1. The notation "trans1" means the zonal wind profile transit from 5°S to the equator smoothly and get vorticity 0 at the equator.
2. The notation "peak" means on the reference latitude 18°S constructed zonal wind profile, near 45°S, there is a small jump so that a peak exists on the vorticity profiles.

Table 3.3: Selected simulation results for GDS-89 on Neptune in whole globe region. - Continued2

Q_y	λ_0	Str./Size/AR	Drift	Periods	Inverse AR	ϕ (rad)	Others
1/12	26°S	0.8/0.5/1.5	1.1	2.8/8.3	0.42±0.08	-0.02±0.09	Ref. Lat. 18°S, trans1, peak, main layer 8
1/12	24°S	0.8/0.5/1.5	5.1	N/A	N/A	0.00±0.22	Ref. Lat. 18°S, trans1, peak, main layer 8
1/12Q	28°S	0.8/0.5/1.5	0.3	3.0/N/A	0.29±0.05	-0.01±0.06	Ref. Lat. 18°S, trans1, peak, main layer 8
1/12H	28°S	0.8/0.5/1.5	0.3	3.1/9.8	0.30±0.10	-0.01±0.09	Ref. Lat. 18°S, trans1, peak, main layer 8
1/12P	28°S	0.8/0.5/1.5	0.3	3.0/N/A	0.26±0.06	0.00±0.05	Ref. Lat. 18°S, trans1, peak, main layer 8
1/12	28°S	0.8/0.5/1.2	0.2	3.1/10.0	0.22±0.07	-0.01±0.06	Ref. Lat. 18°S, trans1, peak, main layer 8
1/12	28°S	0.8/0.5/1.0	-0.1	3.1/10.0	0.14±0.06	0.00±0.05	Ref. Lat. 18°S, trans1, peak, main layer 8
1/12	28°S	0.8/0.5/2.0	0.2	3.1/N/A	0.35±0.05	-0.01±0.05	Ref. Lat. 18°S, trans1, peak, main layer 8
1/12	28°S	0.8/0.5/2.5	0.4	3.1/N/A	0.36±0.06	0.00±0.07	Ref. Lat. 18°S, trans1, peak, main layer 8
1/12	28°S	0.8/0.5/1.5	0.4	3.2/10.0	0.27±0.07	0.00±0.07	Ref. Lat. 18°S, trans1, peak, main layer 6
1/12	28°S	0.8/0.5/1.5	0.2	3.1/10.3	0.19±0.09	0.00±0.06	Ref. Lat. 18°S, trans1, peak, main layer 7
1/12	28°S	0.8/0.5/1.5	0.2	3.1/10.0	0.25±0.05	0.00±0.04	R. L. 18°S, trans1, peak, layer 8, N236
1/12	28°S	0.8/0.5/1.5	0.4	3.7/N/A	0.29±0.10	-0.01±0.10	R. L. 18°S, trans1, peak, layer 8, nominal
1/12	28°S	0.8/0.6/1.5	0.2	3.1/9.5	0.34±0.05	0.00±0.04	Ref. Lat. 18°S, trans1, peak, main layer 8
1/12	28°S	0.8/0.8/1.5	0.2	3.0/10.0	0.46±0.06	-0.01±0.08	Ref. Lat. 18°S, trans1, peak, main layer 8
0	29°S	0.8/0.5/1.5	0.2	N/A/10.5	0.30±0.02	0.00±0.01	Ref. Lat. 24°S, trans2, main layer 7
1/12	29°S	0.8/0.5/1.5	0.4	N/A/8.0	0.32±0.02	0.00±0.01	Ref. Lat. 24°S, trans2, main layer 7
1/7	29°S	0.8/0.5/1.5	1.3	N/A/10.3	0.35±0.04	0.00±0.02	Ref. Lat. 24°S, trans2, main layer 7
0	29°S	0.8/0.5/1.5	0.5	N/A/6.9	0.37±0.08	0.00±0.07	Ref. Lat. 24°S, trans2, main layer 8
1/12	29°S	0.8/0.5/1.5	1.6	N/A/14.3	0.39±0.09	-0.01±0.10	Ref. Lat. 24°S, trans2, main layer 8
1/7	29°S	0.8/0.5/1.5	7.8	N/A/9.0	0.34±0.14	-0.02±0.10	Ref. Lat. 24°S, trans2, main layer 8

1. The Q_y marked with Q means quarter globe domain.
2. The Q_y marked with H means southern hemisphere domain.
3. The Q_y marked with P means pole to pole half globe domain.
4. N236 means the vertical P-T profile is the $N^2 = 0.36 \times 10^{-4} s^{-2}$ one.

Chapter 4 Dynamic Simulations on Uranian Dark Spot

The Uranian Dark Spot (UDS) was observed in the northern hemisphere of Uranus in 2006. This discovery raised several questions, including:

1. Why had no one observed a dark spot on Uranus in the last several decades? As the sister planet of Neptune, Uranus is regarded as similar to Neptune in many aspects. Since Voyager II, people had observed dark spots on Neptune multiple times. What difference between these two planets leads to the lack of spots on Uranus?
2. Why did the dark spot appear at this time? Was it connected to the equinox in December 2007 in which the northern hemisphere and the southern hemisphere of Uranus received same amount of solar radiation. This was the first time that the mid latitudes of the northern hemisphere of Uranus received significant radiation for the first time in the last decades. Was UDS related to the seasonal change of Uranian atmosphere?
3. Why did UDS appear at the latitude about 28°N and is there any special reason for UDS to stay at this latitude?

With these questions in mind, we started our simulations on the UDS. First, a horizontal coarse grid setup (whole globe, 256×512 , grid spacing 0.7° , time step 60s) was used to test parameters and simulate the UDS. Then, we used a finer horizontal grid setup (whole globe, 512×1024 , grid spacing 0.35° , time step 30s) to do more accurate simulations. Since the Uranian Dark Spot was much smaller than GDS-89 on Neptune, the finer grid setup is needed in the simulations. But as we can see later, while the finer grid spacing will lead to longer lifetimes, it will not change the trends of the simulation results. In the vertical direction, the layer setup is same as

that shown in Table 3.1. Using 8 nodes (16 cores) of the fastest cluster KFC6I, we can simulate about one month in one real day for the coarse grid cases and about one month in eight real days for the finer grid cases. Therefore, to get the simulation result of one finer grid case, we normally need to spend two to three weeks, depending on how many months we need to simulate. The grid setup and the time step is also the result of a balance between accuracy and simulation time.

There are several restrictions about the observations to Uranian atmosphere and UDS that limit our ability to analyze this phenomena.

1. The distance from the Earth to the Uranus is about three billion kilometers, which is about 20 times of the distance from the Earth to the Sun. Even with the best observatories - Hubble Space Telescope (in the space) and Keck Telescope, the long distance means the observations only get coarse images. Comparing with this, GDS-89 was observed when Voyager II passed by Neptune in 1989. The Voyager II observations to Neptune were much closer and so obtained more detailed images.
2. Each group can only apply for limited observation times of the HST or Keck telescope. Each year, these telescopes can only be used to observe Uranus for at most several days. Therefore the observations of the UDS were discrete and could only read limited evolution information about UDS. In comparison, Voyager II monitored GDS-89 over three months as it approached Neptune.
3. The Uranian Dark Spot was much smaller than GDS-89 - about one twenty-fifth of the area, which made it more difficult to get accurate images and evolution information.

Therefore, people could observe more details about GDS-89, including the shape oscillations and the tail formation. But for the UDS, what we know is essentially its latitude, its approximate size, and an estimate of its lifespan.

The observations, from June through October, suggest a relatively stable vortex with a lifespan of at least 120 days centered on the latitude of 28°N , without obvious latitudinal drift. Our simulations therefore examine the relative viability of vortices as functions of zonal wind profile and vortex strength in the vicinity of this latitude. The objective is to determine which conditions are most opportune for a vortex-like feature to persist on time scales similar to that of the observed feature. Specifically, the simulations examine several zonal wind profiles proposed for Uranus and assess the relative viability and behavior of a vortex within those profiles at various latitudes in the region of the observed dark spot.

4.1 Model Setup

The basic methods used in this project are similar to those in the simulations of GDS-89. Similar approaches are used to create constructed zonal wind profiles and the vertical pressure-temperature profile. For Uranus, the constant Brunt-Väisälä frequency used to extend the P-T profile is $N = 0.003\text{s}^{-1}$, compared to Neptune, where we ordinarily use $N = 0.008\text{s}^{-1}$. The baseline P-T profile used here is from Lindal et al. 1987[54] and is shown in Figure 4.1.

The atmosphere was divided into ten layers in altitude covering pressures from about 2 mbars to 7.5 bars (Figure 4.1). The current simulations assume a uniform zonal wind profile with depth except within the top two layers of the model, above the proposed vortex region. Under these conditions in the EPIC model, layer thickness is roughly uniform across the globe, meaning variations in potential vorticity corresponded directly to those in absolute vorticity.

As with previous EPIC vortex studies (LeBeau and Dowling, 1998[45]; Stratman et al., 2001[98]; Morales-Juberias and Dowling 2005[68]; Deng and LeBeau, 2007[16, 17]; Dowling et al., 2007[23]; Legarreta and Sanchez-Lavega 2008[50]; Sanchez-Lavega et al 2008[80]), these simulations did not attempt to generate the initial vortex.

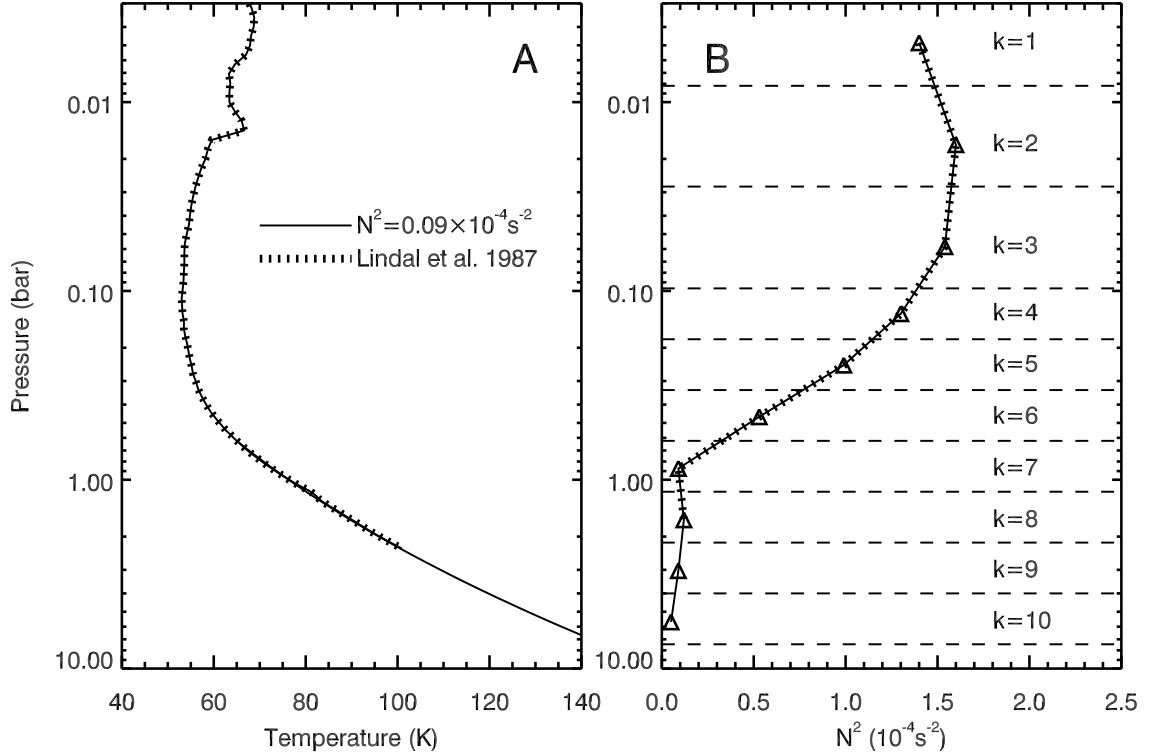


Figure 4.1: Uranus vorticity-model input parameters. (a) Vertical temperature-pressure profiles are shown for Uranus. The $N^2 = 0.09 \times 10^{-4} \text{s}^{-2}$ profile corresponds to that used in the current simulations: the Lindal et al. (1987) profile above 630 mbars, and the constant N^2 profile below 630 mbars. (b) The values for the square of the Brunt-Väisälä (buoyancy) frequency N - computed with EPIC for the two profiles in panel (a) - are overlaid by the locations of the layer boundaries (dashed lines) in the simulation grid. The triangles represent the the location of the layer midpoints for the constant N^2 profile.

Rather, we placed the vortex into the background defined by the zonal wind profile and then allowed it to evolve. The observations showed that the physical extent of the UDS is roughly 2° in latitude and 5° in longitude[38]. Since the inserted vortex will evolve and shrink to a smaller size, the initial dimensions of the ellipsoidal vortex were set at a bigger size: 3.9° in latitude and 7.8° in longitude. From the wavelengths at which the UDS was detected, the bright companion clouds were probably in the 200-600 mbars range and the UDS lay between 1000 and 4000 mbars[38]. Therefore, in our simulations, the central layer of most inserted vortices are placed at about

1000 mbars. For comparison, some simulations are at 4000 mbars.

In our numerical investigation, the other key background parameter is the shape of the zonal wind profile. Several different curves have been fit to the data available for the Uranian zonal wind profile as shown in Figure 4.2, which compares these profiles against cloud-tracking data (Hammel et al., 2005[35]; Sromovsky and Fry, 2005[95]). A symmetric model best fit the data from the Voyager 2 encounter (Smith et al., 1986[86]; Allison et al., 1991[2]), and also provided a good fit to Keck data taken in 2003 (Hammel et al., 2005[35]). Asymmetric fits have also been suggested (Karkoschka, 1998[42]; Sromovsky and Fry, 2005[95]). These fitted profiles are shown in Figure 1.16. In Figure 2.2, the corresponding absolute vorticity profiles can also be seen.

The three fit profiles are not that dissimilar in terms of their absolute vorticity magnitudes. However, the mid-latitude variations in the Sromovsky and Fry 2005[95] profile results in a region of near-constant absolute vorticity about latitude 32°N . Previous simulations of Neptune's GDS-89 suggested that a region approaching uniform potential vorticity was advantageous to stable vortices on Neptune (LeBeau and Dowling, 1998[45]; Dowling et al. 2006[22]; and see Chapter 3 for more discussion), hence this correlation may not be coincidental. We thus constructed an additional profile to extend this "fixed vorticity" a few more degrees southward and fully encompass the region of the Uranian dark spot.

The method of modifying the absolute vorticity equation to construct artificial zonal wind profiles, as discussed in Chapter 2, is used here. For this set of constructed profiles, we modified the profile of Sromovsky and Fry 2005[95] between 23°N and 33°N . In the equation 2.3, λ_0 is defined as 28°N and the constant R_0 is the meridional radius at λ_0 . The value $(\omega + f)_0$ and the parameter β^* are evaluated at 28°N from the Sromovsky and Fry profile, representing the local vorticity. The parameter Q_y scales β^* , with a value of zero corresponding to a region of constant absolute vorticity; our

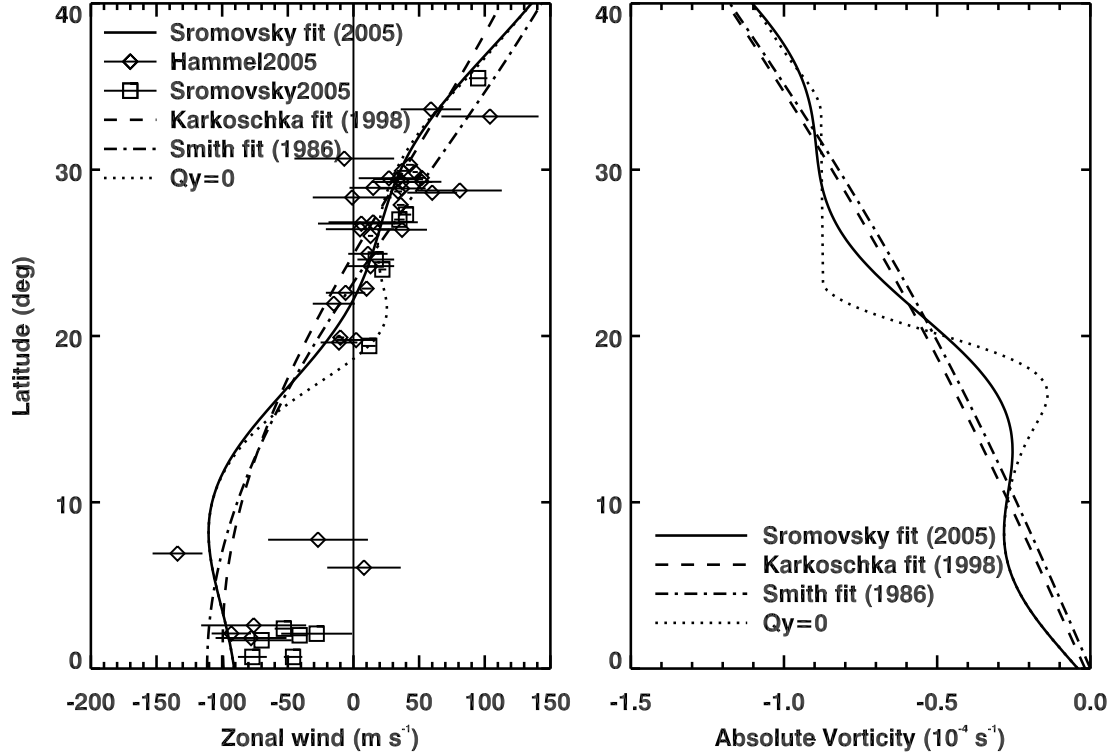


Figure 4.2: Uranus zonal wind profiles and initial constructed profiles. (a) We show zonal wind profiles, including fitted and constructed profiles, compared with the cloud-tracking data (open symbols) from Hammel et al. 2005[35] and Sromovsky and Fry 2005[95]. (b) This panel shows the correlating profiles in absolute vorticity based on the profiles in the left panel.

profile corresponds to $Q_y = 0$. Between 14°N and 23°N, as well as from 33°N to 40°N, the constructed profile is gradually merged back into the original profile. Figure 2.3 and Figure 2.4 in Chapter 2 give the $Q_y = 0$, $Q_y = 1/3$ and $Q_y = 2/3$ constructed zonal wind profiles, compared with the observational data and the averaged data. Here, Figure 4.2 shows the constructed profile $Q_y = 0$ and its absolute vorticity profile, compared to the three fitted curves and the observational data from Hammel et al. 2005[35] and Sromovsky and Fry 2005[95]. This profile is a reasonably close match to the observed zonal wind data; however, it notably does not capture the three data points near 22°N. This constructed profile allows us to further investigate the conditions most likely to produce long-lived vortices on Uranus.

The vortex was subsequently defined by a closed potential vorticity contour, which is approximately a material boundary in the EPIC code. The vortex was placed in the flow field by changing the local winds to reflect the superposition of an ellipsoidal vortex onto the background wind profile, as previously discussed in Chapter 2. The flow-field modification for the vortex used the Gaussian shape stream function. The resulting initial potential vorticity distribution had a Gaussian profile and its strength was defined by the maximum vortex velocity. We considered maximum velocities between 30 and 130 m/s. The initial vortex then evolved within the numerical simulation.

4.2 Coarse Grid Simulations

We summarize the simulation results for the coarse grid in Table 4.1. The essential output was the lifespan of the vortex, given in the tables in terms of days (i.e., 24 hours). We assessed the vortex lifespan by tracking the evolving potential vorticity contour that defines the vortex. Once the vortex had stretched to a longitudinal dimension of more than 20° or had lost the coherence of a single, compact vortex, it was considered to have been effectively sheared out by the zonal wind.

Table 4.1 also indicates the center latitude of both the initial vortex and the vortex when it reached the end of its lifespan. The standard evolution of these vortices was to drift equatorward during the simulation, with the most rapid drift occurring in the first several days of the simulation. This drift is one reason why multiple initial vortex latitudes are considered in these simulations.

Effect of Zonal Wind Profile

Figure 4.3 illustrates the effect of the background zonal wind profile on vortex shearing. Here, initial vortices of the same dimensions and same strength ($u_{max} = 70$ m/s) were placed in four different zonal wind fields on the coarse grid with initial latitude

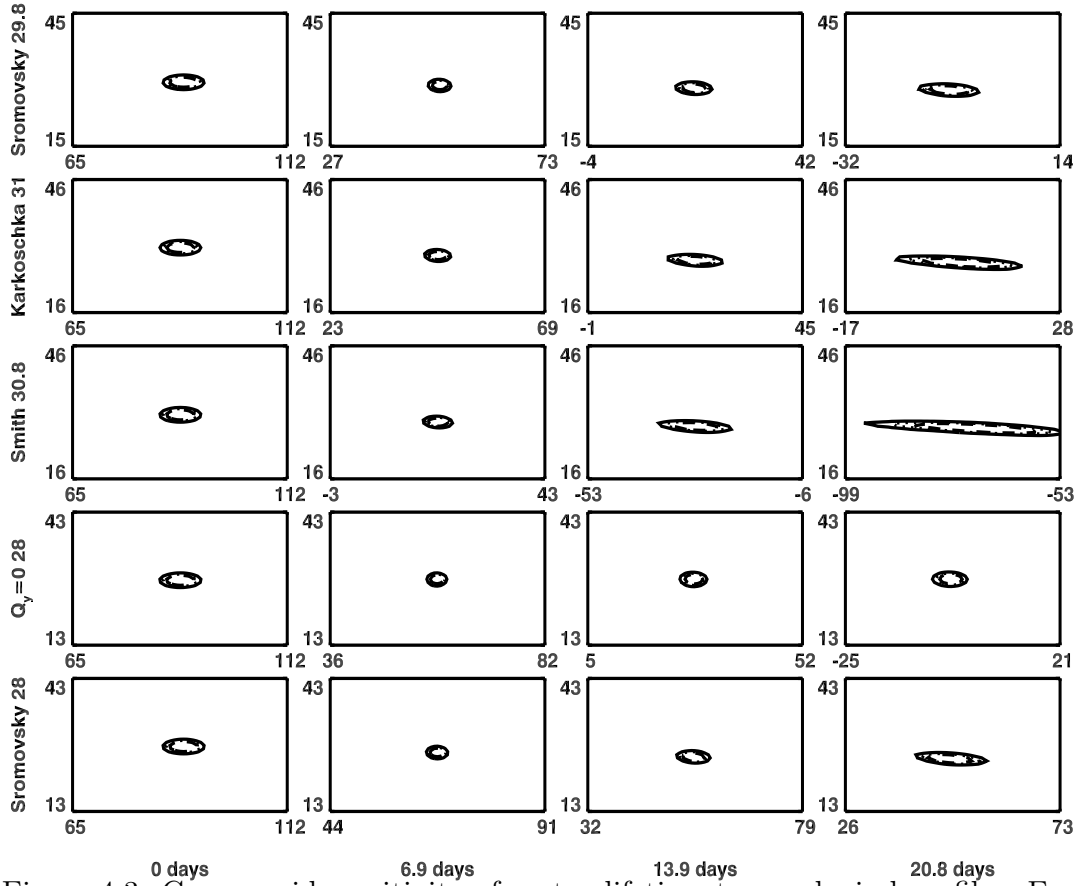


Figure 4.3: Coarse-grid sensitivity of vortex lifetime to zonal wind profiles. For these simulations, a 70 m/s vortex was initially placed in five different zonal wind profiles using a whole-globe domain. The number indicates the initial latitude of the vortex, all of which are between 28°N and 31°N. The dimensions of each frame are 47° by 30°. The vortices placed in the profiles of Karkoschka 1998[42] and Smith et al. 1986[86] are clearly shearing by 20 days. The Sromovsky and Fry 2005[95] vortices remain more compact, while the $Q_y = 0$ vortex evidences the least amount of shearing.

near 28°N. The evolution of the vortex contour in the central layer (layer 7) for each profile is shown in a 47° by 30° frame centered on the vortex. The vortices placed in the Smith profile sheared most rapidly, steadily losing coherence as a vortex-like feature. The Karkoschka and Sromovsky profiles' vortices sheared more slowly, although the rate is sensitive to the initial vortex latitude. Unlike the fit profiles, the constructed profile maintains a compact spot with little noticeable shearing through most of the run, never reaching 20° in length. Instead, these spots disappear due to interaction with the equatorward shear region located about the bend in the absolute

vorticity profile at 22°N, eventually merging into the shear.

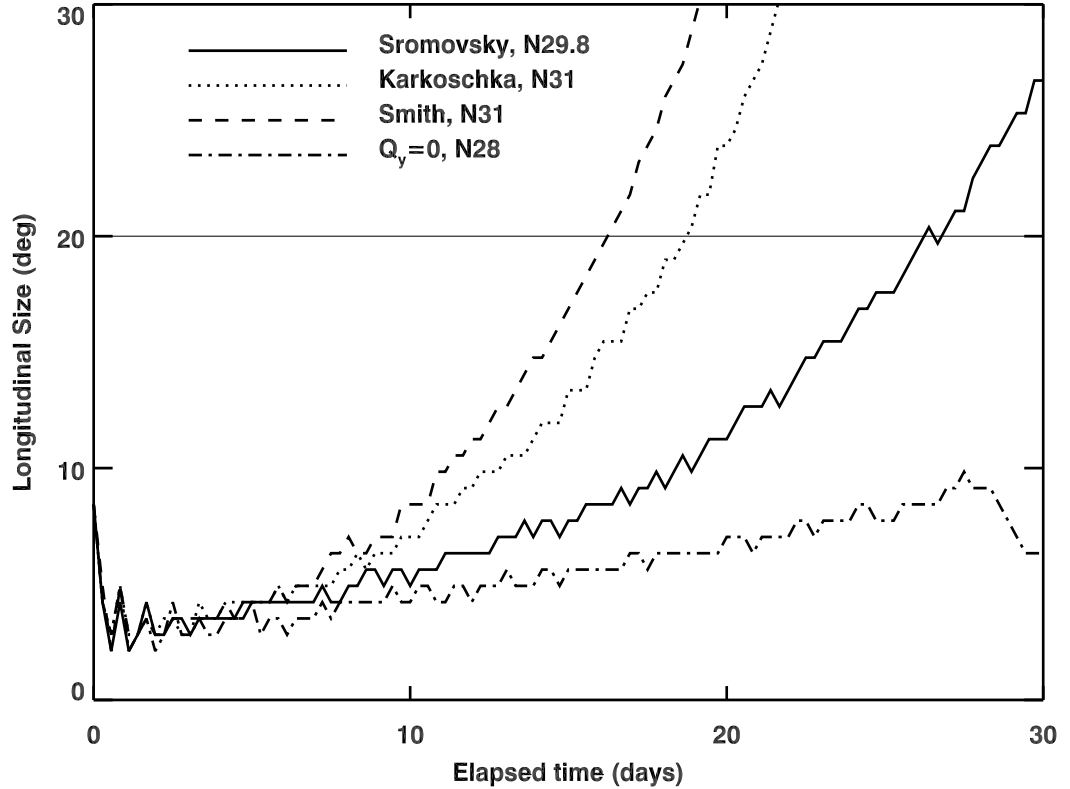


Figure 4.4: Longitudinal size change with time for different fit zonal wind profiles and $Q_y = 0$ constructed zonal wind profile. These four cases all drift roughly to the same latitude, 28°N, although they start from different initial latitudes.

Figure 4.4 shows the longitudinal size change of the three cases drifting to near 28°N. Among these cases, Sromovsky 29.8 keeps compact for a longer time than the other two, which suggests that the Sromovsky and Fry 2005 zonal wind profile is the best among these fitted profiles for sustaining a UDS in this latitude region. The constructed $Q_y = 0$ profile works better than the three fit profiles, suggesting that near constant local absolute vorticity is helpful to sustain a great vortex.

As shown in Table 4.1, the rate of vortex drift appears to be somewhat correlated to the gradient in absolute vorticity. The Smith and Karkoschka profiles, with a stronger gradient in the vicinity of 28°N, drifted equatorward faster than the Sro-

movsky profile, while the $Q_y = 0$ profile exhibited minimal drift over the lifespan of the vortex. Shifting the initial vortex location northward in an attempt to have the vortex drift to 28°N rather than starting at that latitude yielded a few day increase in the lifespan of the vortex in the Sromovsky profile. Similar efforts with the Smith and Karkoschka profiles reduced the lifespan by several days.

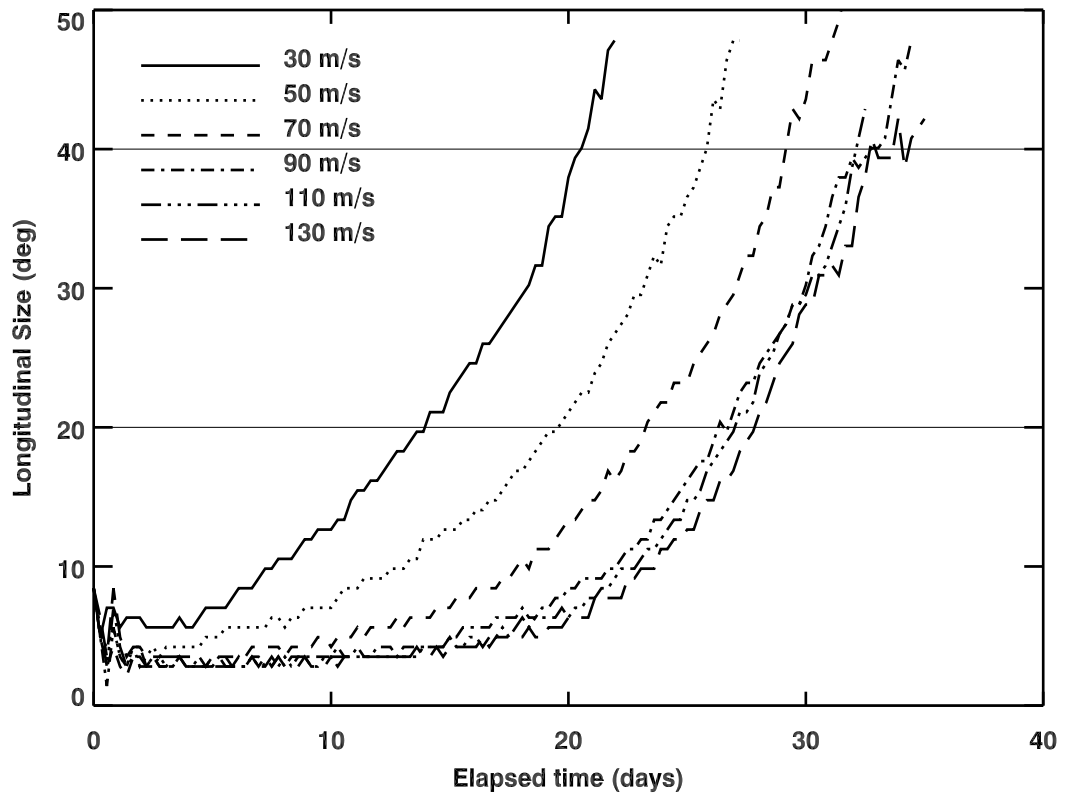


Figure 4.5: Sensitivity of vortex lifetime to maximum vortex wind velocity. We examined the evolution of different strength vortices initially placed at 28°N in the profile of Sromovsky and Fry 2005. This plot presents the evolution of the vortex major axis measured in degrees of longitude with the time to a 20° length being defined as the vortex lifespan. There are considerable gains in lifespan from 30 m/s to 90 m/s, but after this the increases in lifespan are muted.

Effect of Vortex Strength

In an attempt to extend the vortex lifespan, we considered several different maximum vortex velocities in the Sromovsky and Fry profile (Figure 4.5). While increasing the vortex strength from 30 m/s to 90 m/s did increase the lifespan steadily, the effect appears to asymptote beyond 90 m/s. Furthermore, we can see that a stronger vortex leads to faster drift in Figure 4.6. These suggest that just increasing the vortex strength is not a means to significantly increase vortex lifespan. Similar results occurred with the $Q_y = 0$ profile as seen in Table 4.1.

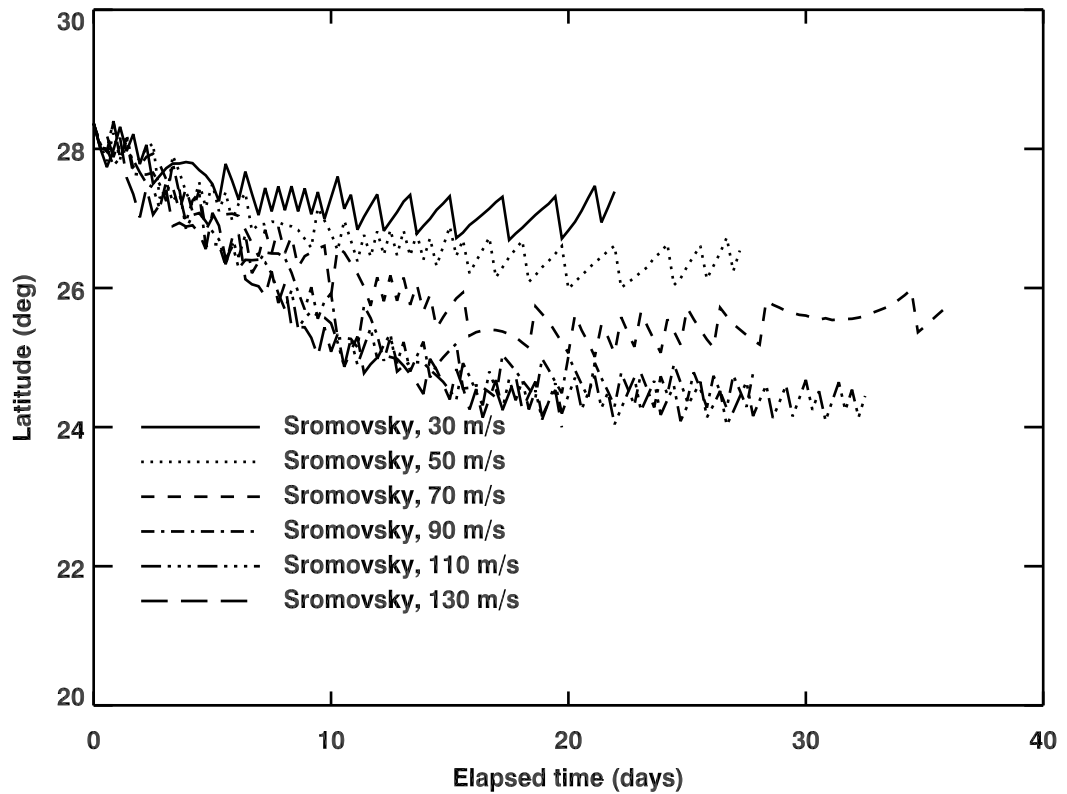


Figure 4.6: Sensitivity of vortex drift rate to maximum vortex wind velocity. This plot has the same cases as Figure 4.5. Similar results can be achieved as Figure 4.5: from 30 m/s to 90 m/s, drift rate increases significantly; after 90 m/s, the change in drift rate is muted.

The contour plots of these cases with different strengths are shown in Figure 4.7.

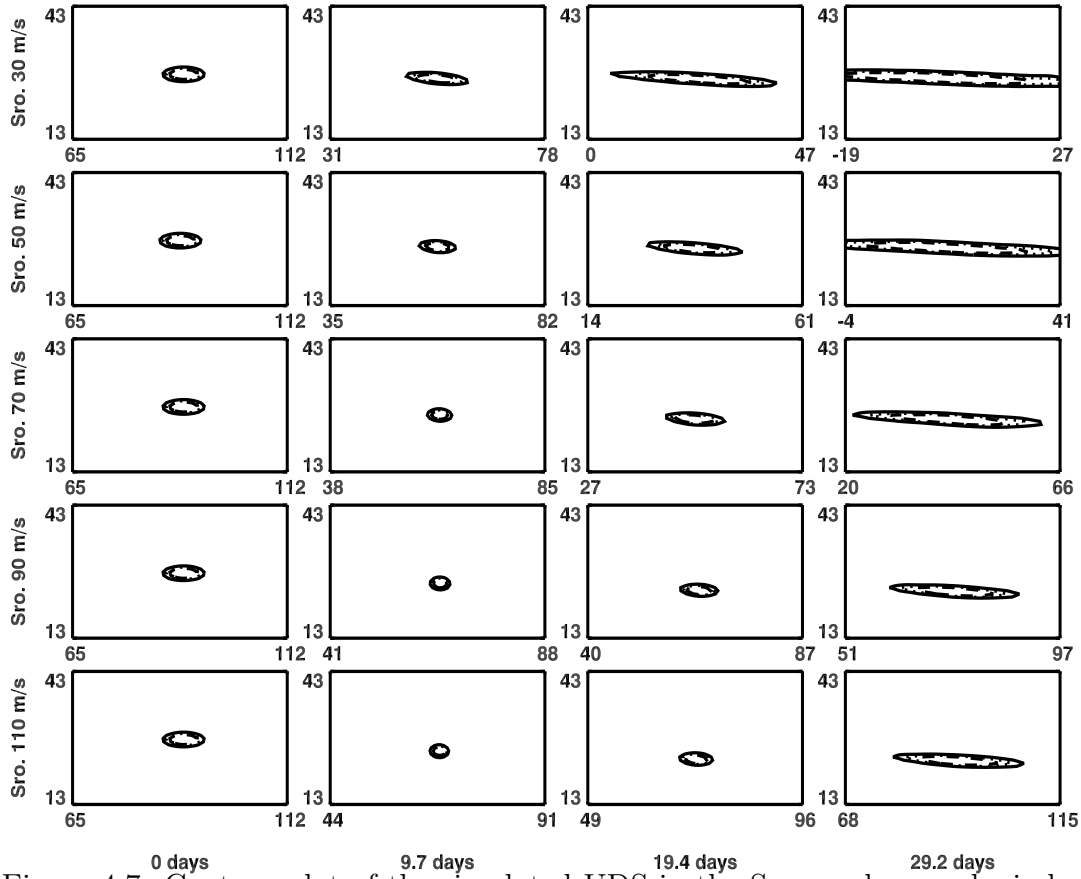


Figure 4.7: Contour plot of the simulated UDS in the Sromovsky zonal wind profile with different initial maximum wind velocities. These simulations all start from 28°N . The same runs are plotted in Figure 4.6 about their lifetime.

When the initial maximum wind velocity is small, increasing it will help to sustain the spot for a longer time. When the initial maximum velocity is bigger than 90 m/s , the effect is not so significant. This is consistent with Figure 4.5. In Table 4.1, we show the simulation results for different initial vortex strengths with $Q_y = 0$ profile. Similar to the above simulations in Sromovsky and Fry 2005 profile, the effect to the lifetime of increasing vortex strength is less significant after 70 m/s .

Drift of UDS

Figure 4.8 shows the drift of some simulation cases. The first group includes four cases: Sromovsky 29.8° , Karkoschka 31° , Smith 31° and $Q_y = 0$ 28° . In this group, in the three fitted zonal wind profiles, Sromovsky is the one with the smallest drift,

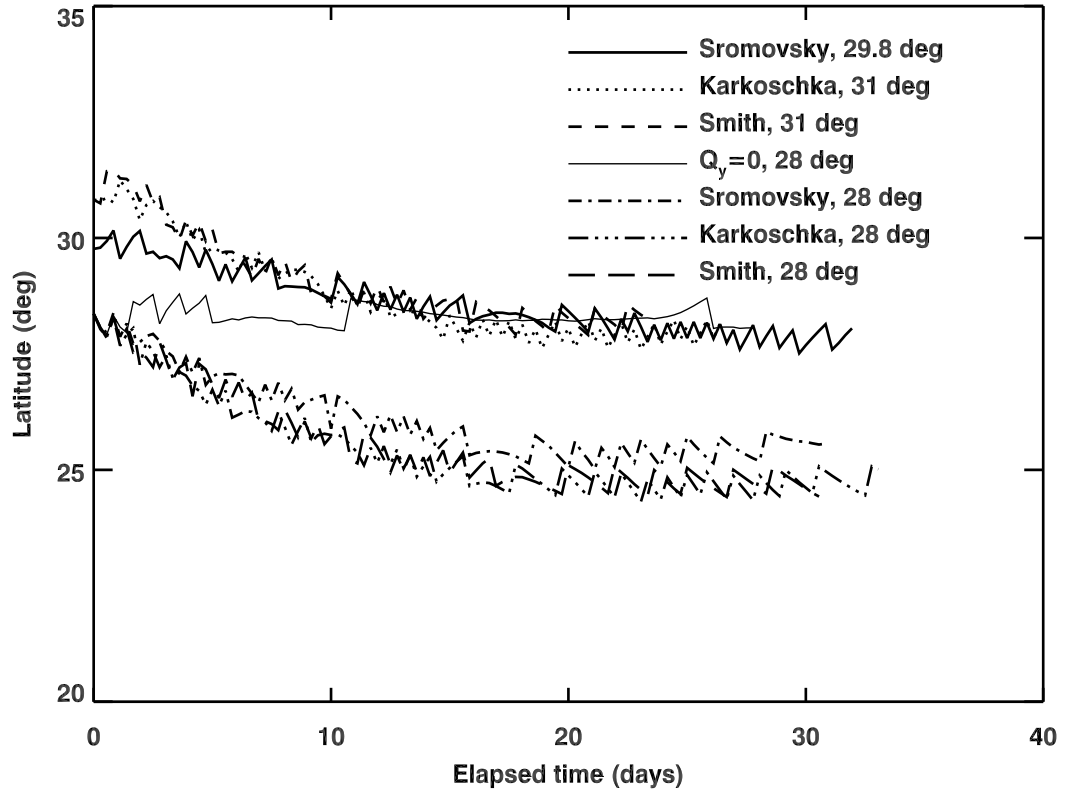


Figure 4.8: Drift of Uranian Dark Spot. Two groups of cases are shown in this figure. One is about those cases drift to 28° with different zonal wind profiles; another is about those cases drift from 28° . All these spots have a 70 m/s initial maximum velocity.

so that near 28°N this profile does the best keeping the spot at a constant latitude. The second group also includes four cases: Sromovsky 28° , Karkoschka 28° , Smith 28° and again $Q_y = 0$ 28° . Among the fitted curves, again, the Sromovsky profile provides the best environment for the UDS to stay at its initial latitude. Moreover, the $Q_y = 0$ case is better than all the fitted profiles. It keeps constant latitude from the beginning to about one month. In Table 4.1, we can also see that $Q_y = 0$ constructed zonal wind profile works better than $Q_y = 1/3$ and $Q_y = 2/3$ profiles in keeping the initial latitude. When Q_y increases, the drift rate to the equator also increases. These suggest that a near constant background absolute vorticity is helpful

for keeping the UDS at a fixed latitude.

Suitable Location for UDS

In Table 4.1, for each fitted zonal wind profile, several simulations with different initial latitudes are listed. Simulations on Smith 1986 profile and Karkoschka 1998 profile all indicate that on Uranus a near equator latitude is more suitable than a higher latitude for sustaining a UDS. Since their background absolute vorticities all have similar gradients at these latitudes (Figure 4.2), this effect is mainly about the latitude itself, not the background absolute vorticity.

For the Sromovsky profile, things become more complex. Figure 4.2 shows two regions with small absolute vorticity gradients: one is centered at about 30°N , which is the interest area of UDS; another is centered at about 10°N . From Table 4.1 we can see that this is also a good region for vortices, so a case starting from 18°N also had a long lifespan (at least 58 days).

Figure 4.9 shows the change of the longitudinal sizes with different initial latitudes of the spot centers. The most notable case is the 18°N one, which keeps a constant axis length of $\sim 5^{\circ}$ after the first 10 days. Figure 4.10 shows the drift of the spots in these simulations. In the 18°N case, the spot also almost keeps a constant latitude at about 13.4°N . Notice 13° is about the latitude with a local maximum of the absolute vorticity profile in Figure 4.2. These results confirm our idea about the UDS sustainability that near constant absolute vorticity is needed to keep a UDS stable on both latitude and size. Although the gradient is still relatively small below this point, it does become negative.

In Figure 4.9, except for the discussed 18°N case, the 29.8°N case is the best to keep compact. The 29.8°N case is just the one drifting to 28°N . This suggests that a latitude $\sim 28^{\circ}\text{N}$ is a preferable location for the UDS to survive. The spots above this point and below this point all shear more quickly. This may explain why we saw

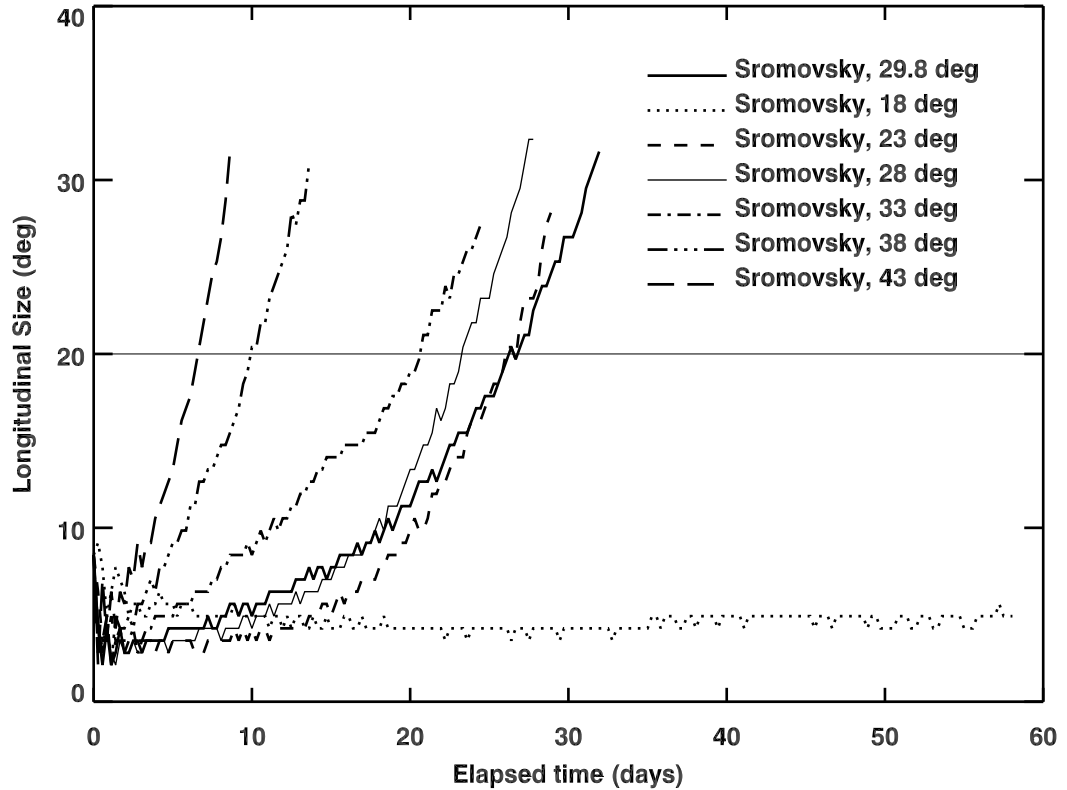


Figure 4.9: Longitudinal size change of spot vs. initial latitude of spot center, with Sromovsky and Fry 2005 zonal wind profile and maximum wind velocity 70 m/s.

UDS in 2006 at this latitude.

But since the simulation results show that 13.4° is more suitable for UDS survival, why near this latitude no spots were found before? Also, from Table 4.1 we can see that for Karkoschka 1998 profile and Smith 1989 profile, when the latitudes are near the equator, the lifespan of the spots can also be longer than that of the spot at 28° in the Sromovsky zonal wind profile. So, why we did not see any great vortex in the lower latitudes? Because of the limitation of the observations and lack of data, we cannot draw solid conclusion about this currently. Previous data are shown in Figure 1.16 and Figure 4.2, where we can see that the observed zonal wind velocities near the equator have shown significant diversity and do not change as smoothly with latitude as the mid-latitude region. They have more differences and peaks than the winds in

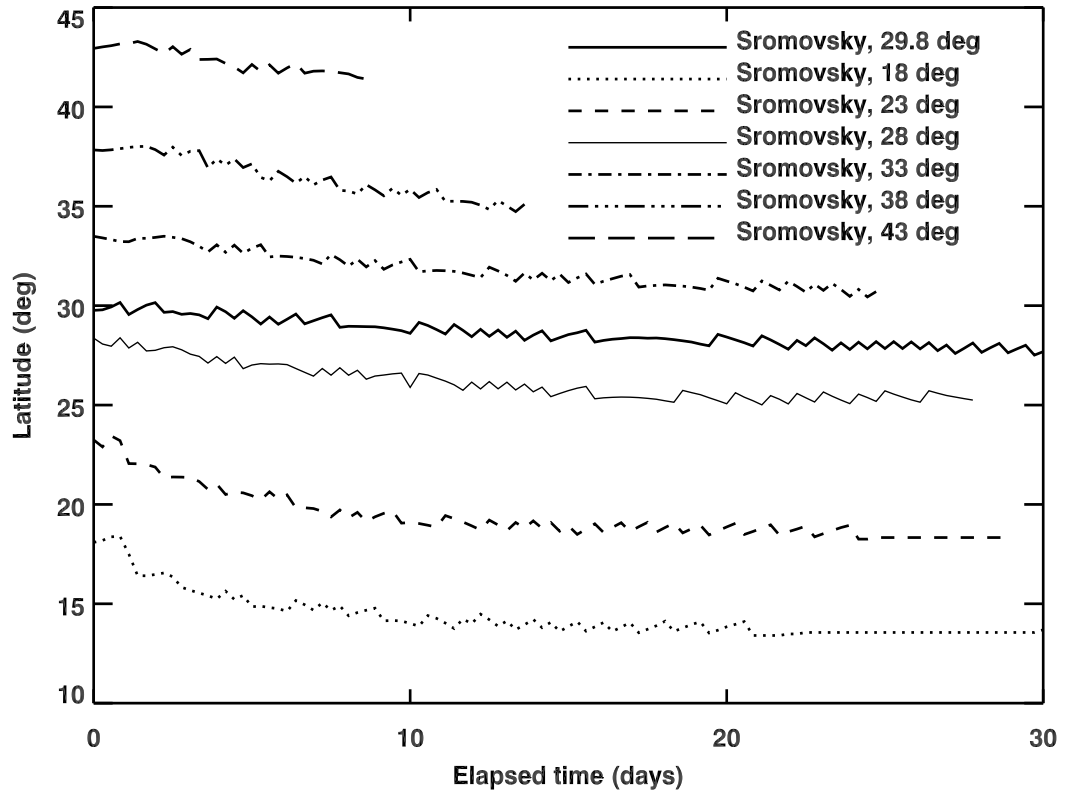


Figure 4.10: Drift of spot vs. initial latitude of spot center, with Sromovsky and Fry 2005 zonal wind profile and maximum wind velocity 70 m/s.

higher latitudes. Also, there are sizeable regions in which observational data do not exist. In the northern hemisphere, between 10° and 20° , there is no observational point. In the southern hemisphere, there is only one point from the equator to 10°S and it is far away from the fitted curves. In other words, the fitted curves erase possible sharp changes of the observed zonal wind velocities and so that the absolute vorticities change smoothly near the equator. Therefore, the simulations based on the fitted zonal wind profiles may not reflect the real world of Uranus near the equator. Since sharp changes in the zonal winds tend to destabilize vortices, a great vortex may not be able to survive for a long time near the equator of Uranus, unlike what we see in our simulations.

The Sromovsky 2005 profile was fit mainly based on the data observed in 2003.

Three years later the first UDS was observed in 2006. Since the Uranus was moving to its equinox and its northern hemisphere was approaching its spring during these years, the zonal wind profile near 28° may have changed. It is possible that the small gradient absolute vorticity region extended to a wider region. It is also possible that a local maximum similar to the 13.4°N in Figure 4.2 appeared near 28° . Therefore, the background zonal wind environment of Uranus near this latitude may have become more suitable for sustaining a great vortex than the zonal winds shown in Sromovsky and Fry 2005. Currently, we do not have enough observational zonal wind data near 28°N at the time of UDS. Either of these two changes might be sufficient to explain the UDS phenomenon.

4.3 Finer Grid Simulations

Because the simulated UDS size is relatively small, a finer grid setup was applied to check if the trends obtained in and conclusions from the coarse grid simulations would remain consistent. We should note that since the finer grid simulations have four times the cells (the horizontal grid spacing of 0.35° is half of that of coarse grid cases) and half of the time step (30s), to simulate a similar case with the same computational resources require an eightfold increase in simulation time. From our previous simulations of the Neptune's GDSs, we know that to simulate a great dark spot on a giant planet with a long time evolution, a whole global domain is needed to enable waves to form on the global scale. This may be critical for some characteristics of the simulation results. Therefore, in our simulations of the UDS, all the finer grid simulations are also in whole global domains.

Table 4.2 shows some of the simulations of the UDS with finer grids. Basically, finer grid simulations with smaller time steps have longer lifespans, indicating that grid resolution issues were affecting the simulations. Moreover, the simulations show the same basic trends observed in the coarse grid simulation results.

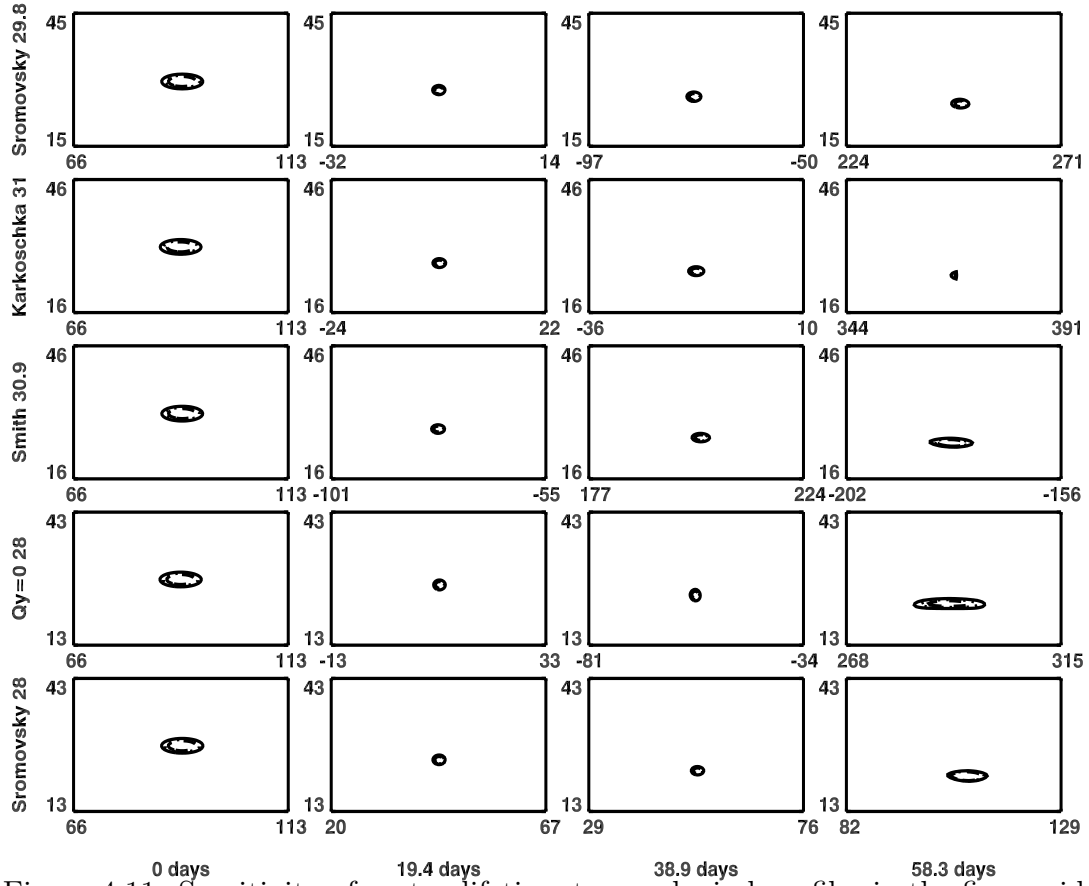


Figure 4.11: Sensitivity of vortex lifetime to zonal wind profiles in the finer grid. For these simulations, a 70 m/s vortex was initially placed in five different zonal wind profiles using a whole-globe domain. To compare with the coarse grid simulations, in these finer grid simulations, the starting latitudes of the vortices are same as the cases shown in Figure 4.3.

Effect of Zonal Wind Profile

As before, we apply the Sromovsky and Fry 2005, Karkoschka 1998, Smith 1989 and $Q_y = 0$ profiles to test which one is most suitable to sustain a great dark spot. Figure 4.11 and Figure 4.12 show the contour shape of the vortices in the background with different zonal wind profiles. Cases in Figure 4.11 have the same corresponding starting latitudes as the coarse grid cases in Figure 4.3. Cases in Figure 4.12 end at $\sim 28^\circ$ in their drifting, except the last case. The last case starts from 28°N in the Sromovsky and Fry 2005 zonal wind profile. Similar to the coarse grid simulations, the Sromovsky and Fry 2005 profile is the best at sustaining a great dark spot on

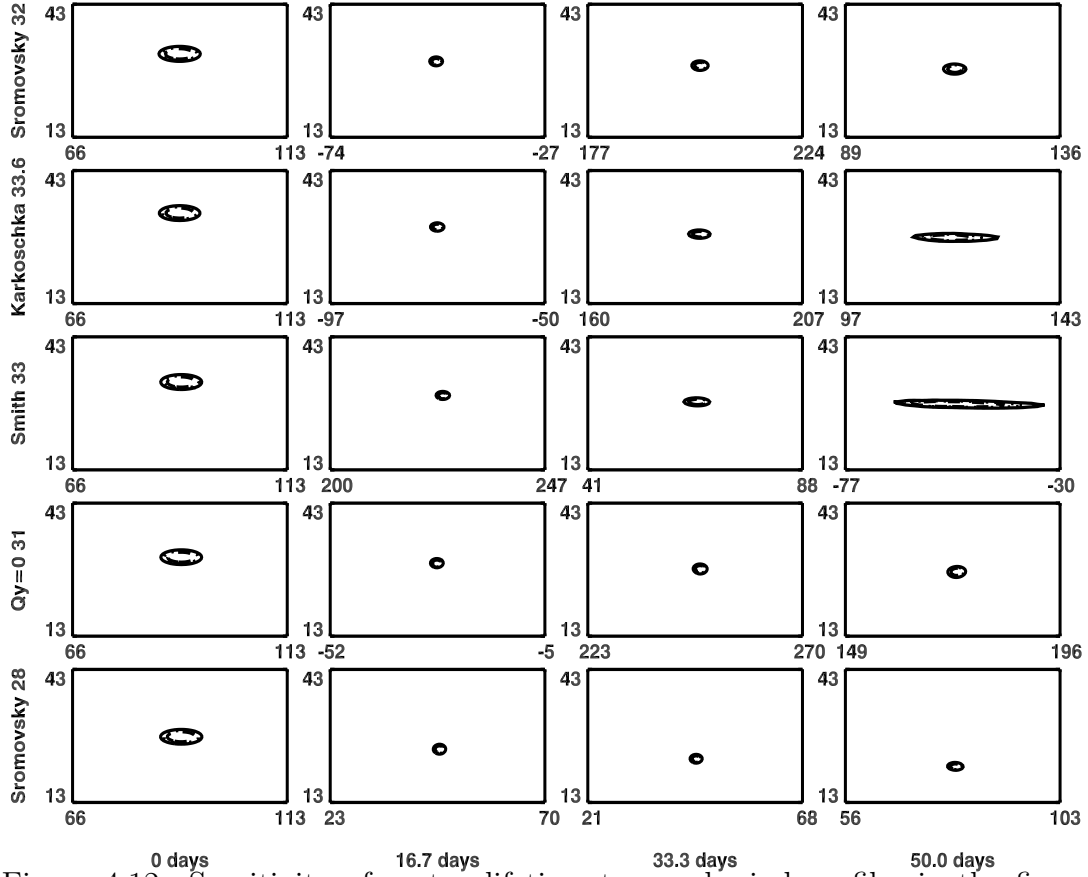


Figure 4.12: Sensitivity of vortex lifetime to zonal wind profiles in the finer grid. This plot is similar to Figure 4.11, just starting from different latitudes. The first four simulation cases all drift to 28°N , comparing with the last case, which starts from 28°N .

Uranus. However, the $Q_y = 0$ 28 fine grid case is not as good as the $Q_y = 0$ 28 coarse grid case both in terms of keeping a constant latitude and sustaining the dark spot for a longer time. This is likely because of the boundary effect of the $Q_y = 0$ region. The $Q_y = 0$ region is generated and connected to the other regions. In coarse grid simulations, the grid spacing is bigger so that the effect of the boundary change is smoothed. In finer grid simulations, grid spacing is smaller and this leads to waves and more generated vortices around the boundary. These have feed back to the simulated UDS itself.

Figure 4.13 shows the evolution of the simulated UDS in the $Q_y = 0$ constructed zonal wind background, starting from 28°N . The vortex drifted to the south boundary

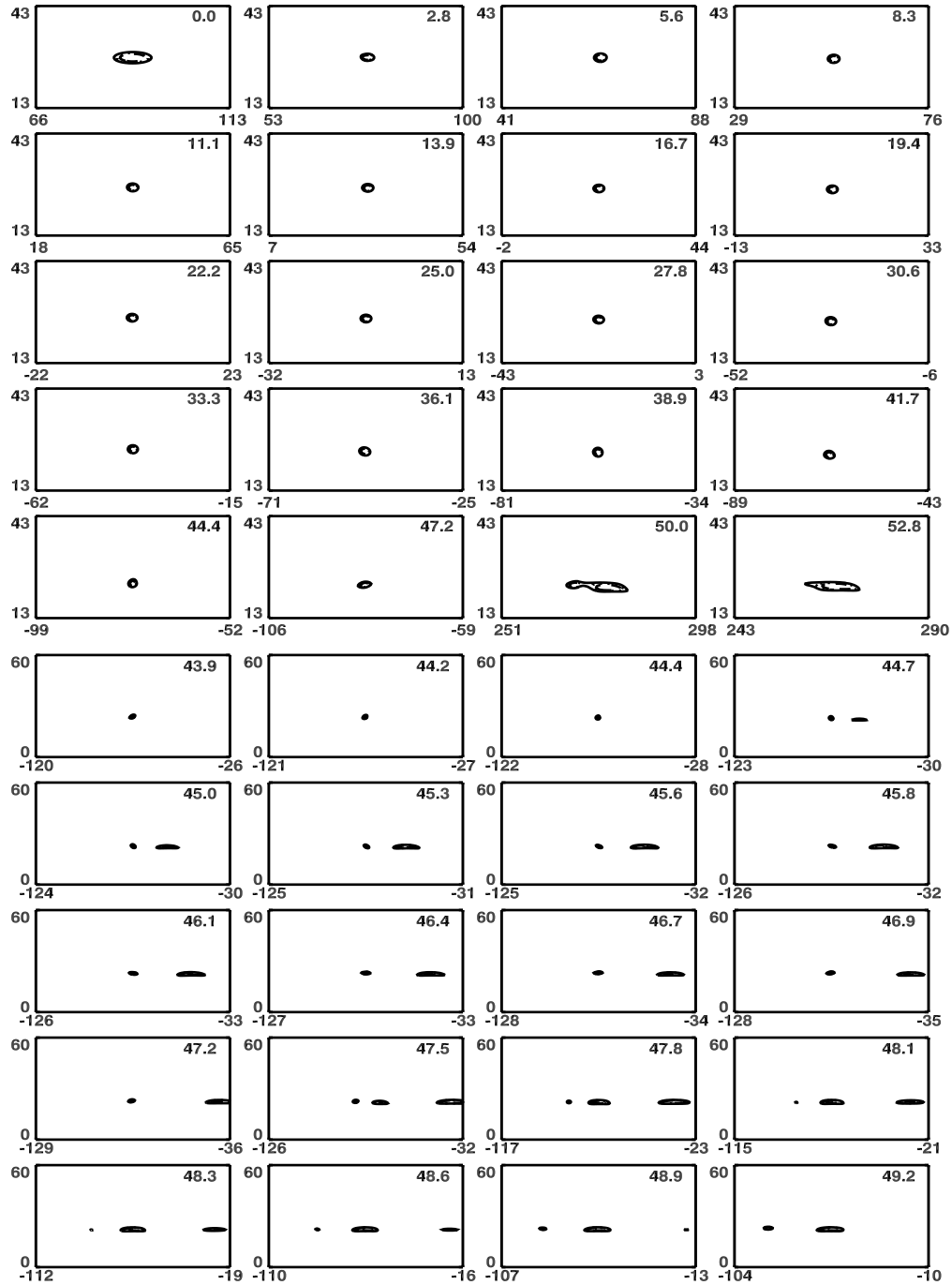


Figure 4.13: Contour plots of the simulated UDS on $Q_y = 0$ constructed zonal wind profile. In this simulation, a vortex with initial maximum velocity 70 m/s was placed in a whole-globe domain, starting from 28°N. The upper panel is for the whole life of the simulation; the lower panel is about the last stage of the simulation to show the effect of the vortex on the boundary of the $Q_y = 0$ area. The scale of the plot in the lower panel is doubled than that of the upper panel to show a wider area. The numbers in the subplots are the times of the simulations, in unit days.

of the $Q_y = 0$ area and there generated other vortices.

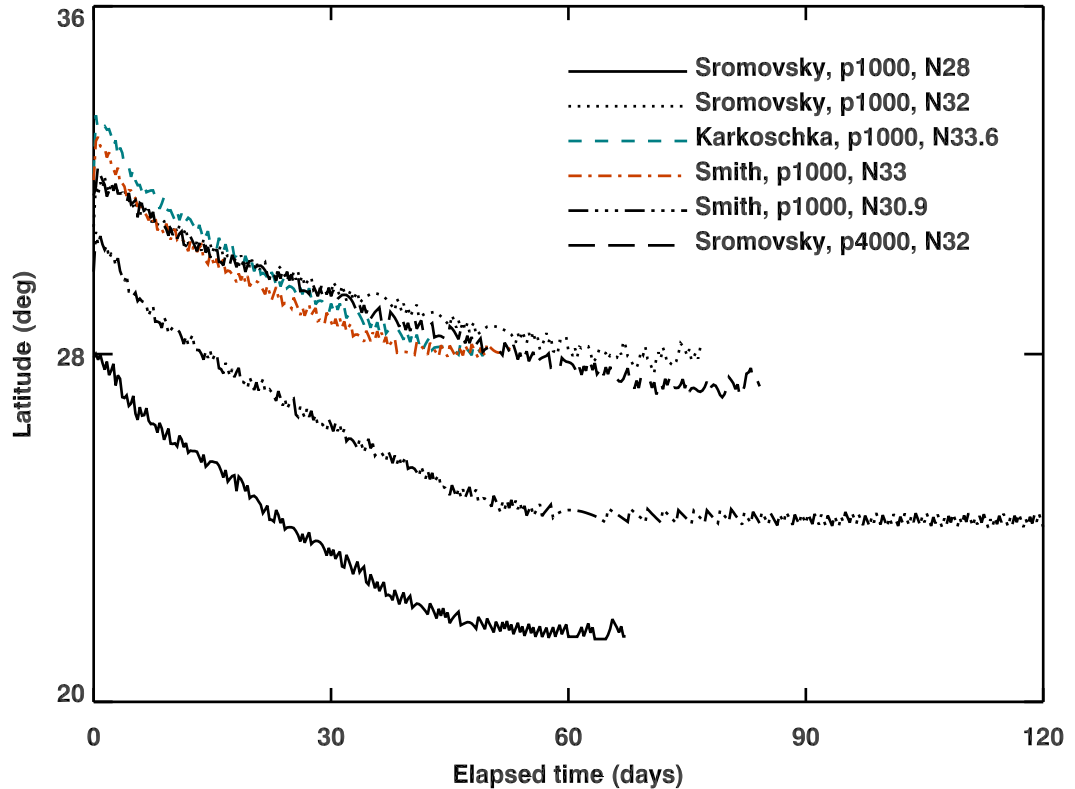


Figure 4.14: Finer-grid drift of spots with different zonal wind profiles, initial latitudes and layers. p is the pressure of the central vortex layer, so $p1000$ is 1000 mbar pressure and $p4000$ is 4000 mbar pressure.

Figure 4.14 shows the drift of the spots with different zonal wind profiles, starting from different latitudes and centered on different pressure layers. Obviously, among those cases drift to near 28°N , Sromovsky, $p1000$, $N32$ case is the best.

Figure 4.15 shows the size change of the spots with different zonal wind profiles. The dotted line - the Sromovsky $p1000$ $N32$ case - shears most slowly among those cases laying on 1000 mbar pressure. The deeper case, Sromovsky $p4000$ $N32$, drifts closer to the equator and keeps compact for a longer time. This shows that a deeper vortex may be more robust than a shallower vortex.

In general, of the fitted profiles, the Sromovsky one has the best ability to sustain

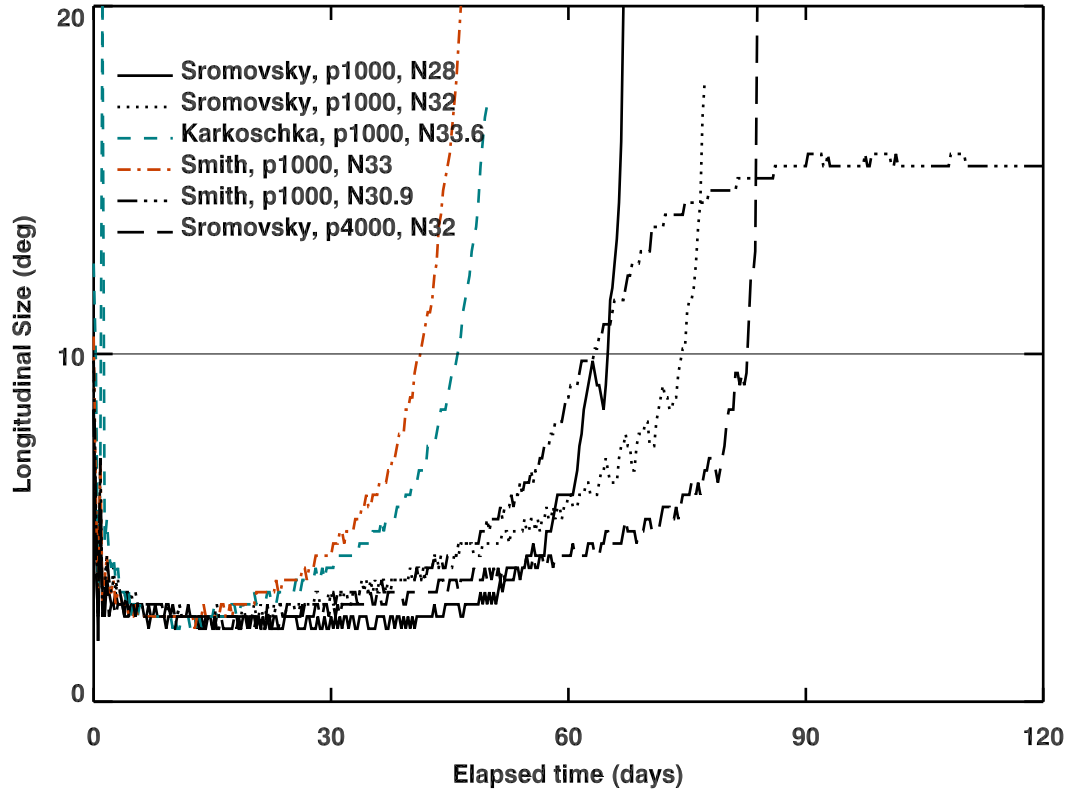


Figure 4.15: Longitudinal size change of spots in finer grid with different zonal wind profiles, initial latitudes and layers.

a great dark spot on Uranus, in terms of both keeping it at a constant latitude and keeping its size compact.

Effect of Vortex Strength

Similar to the coarse grid simulations, we arranged some cases to test the effect of vortex strength. These simulations are also in the Sromovsky and Fry 2005 profile. From Figure 4.16 we can also get the result that just increasing the vortex strength is not a means to significantly increase vortex lifespan. The 90 m/s case has longer lifespan than the 110 m/s case, because of the latter's strong oscillation. Also, we can see that a stronger spot leads to a faster drift, consistent with the coarse grid cases.

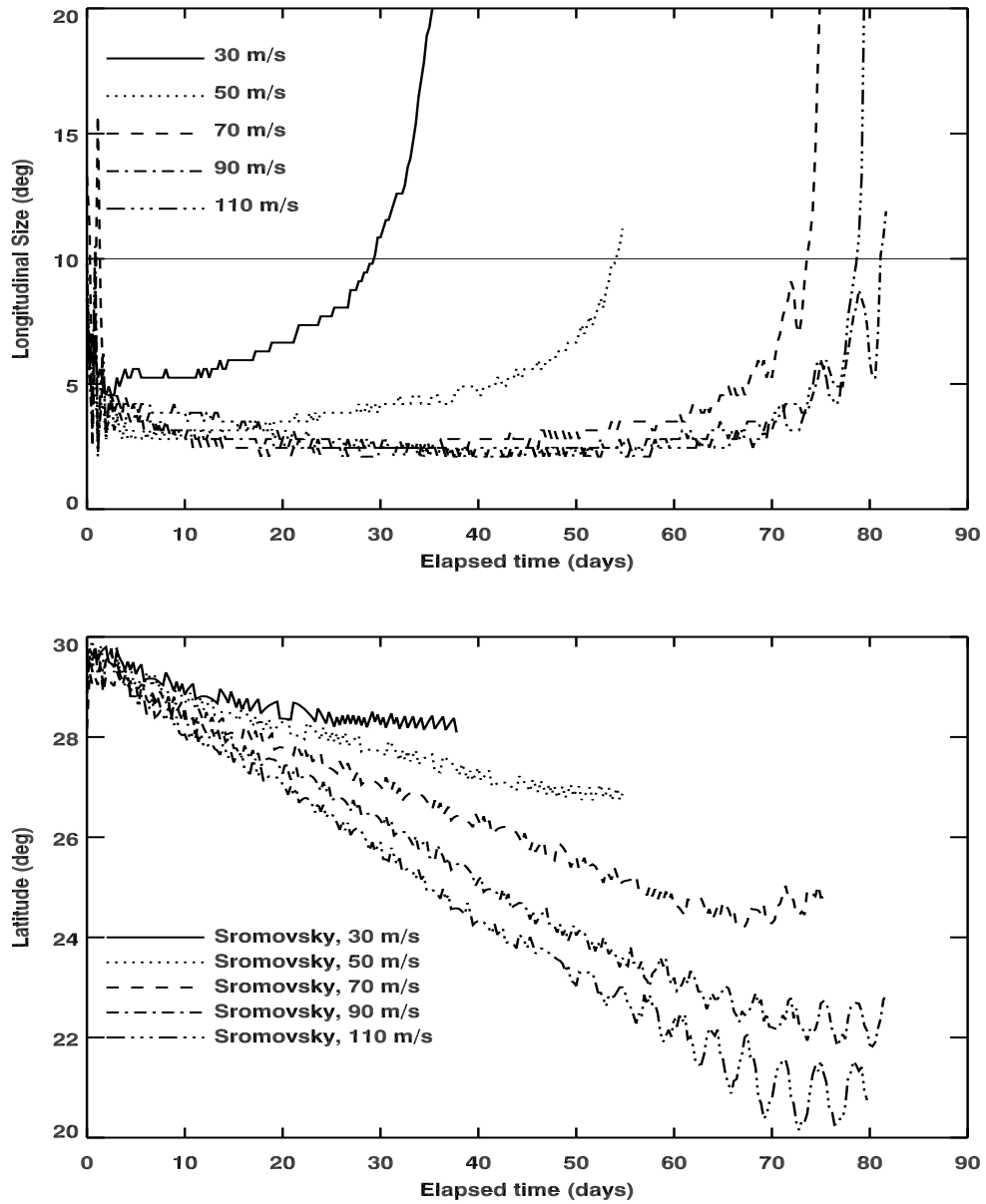


Figure 4.16: Upper panel: sensitivity of vortex lifetime to maximum vortex wind velocity. Lower panel: sensitivity of vortex drift rate to maximum vortex wind velocity. These plots are about finer grid simulations. We examined the evolution of different strength vortices initially placed at 29.8°N in the profile of Sromovsky and Fry 2005. This plot presents the evolution of the vortex major axis measured in degrees of longitude with the time to a 10° length being defined as the vortex lifespan. There were considerable gains in lifespan from 30 m/s to 90 m/s, but after this the increases in lifespan are muted. The lifespan of the 110 m/s case is even shorter than that of the 90 m/s case. After 50 days, the 90 m/s case and the 110 m/s case show fluctuations with ~ 3 days periods.

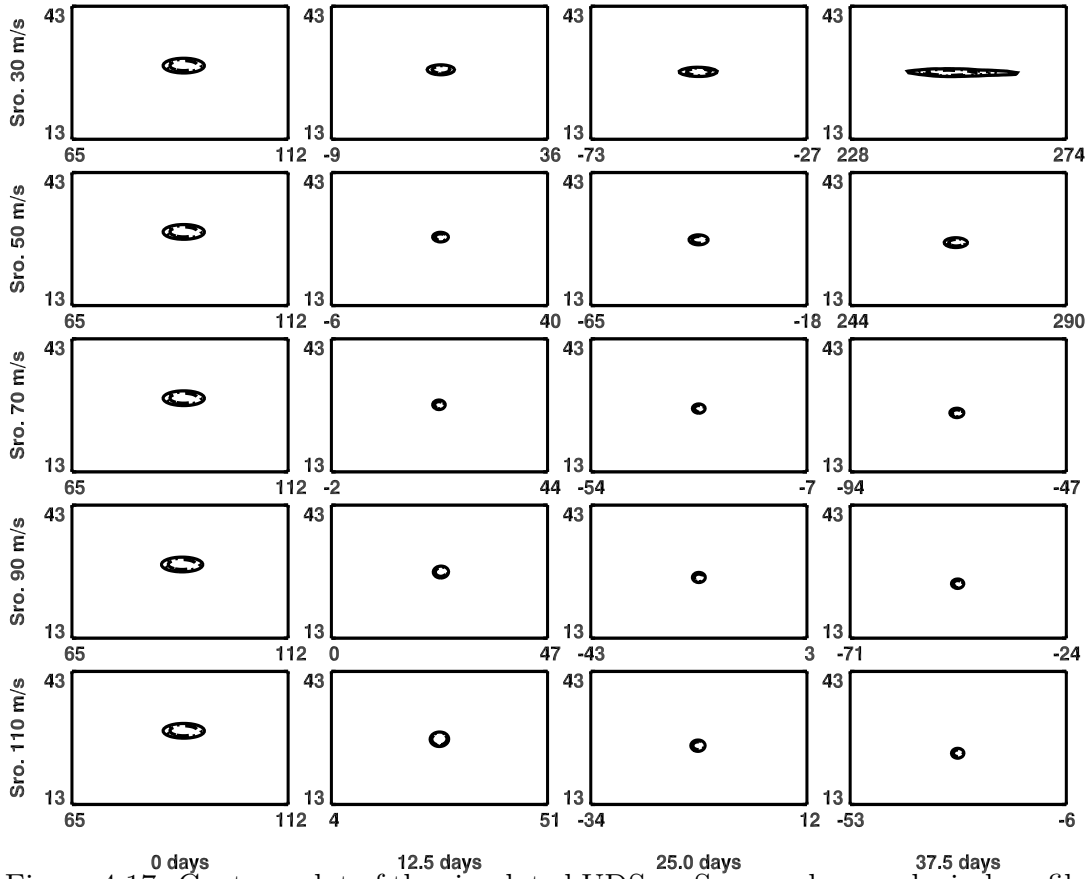


Figure 4.17: Contour plot of the simulated UDS on Sromovsky zonal wind profile with different initial maximum wind velocity. This plot is about finer grid simulations. These simulations all start from 29.8°N .

The contour plot about the finer grid simulations on Sromovsky and Fry 2005 profile with different strength is shown in Figure 4.17. Similar results to the coarse grid simulations can be achieved. Suitable strength is helpful for the spot to keep compact for a longer time. But when the strength is too strong, it will have strong interaction with the environment, which will harm the sustainability.

Suitable Location for UDS

Figure 4.19 shows the longitudinal change of spots at different latitudes. Since the finer grid dark spots stay more compact, 10° is used as the critical value when we calculate lifespan. Basically, we still have the result that high latitude spots shear faster than low latitude spots. The case starting from 32°N shows a longer lifespan

in the region around 28° , although the 28°N case is at the lower latitude.

One interesting phenomenon is the comparison between the Sromovsky 28°N and the Sromovsky 32°N cases. The 28°N initial latitude has a smaller size and flatter size change before 50 days. However, after that, this case shears more rapidly than the 32°N case. This appears to be related to the drift of the spot (see Figure 4.20), since after the spot in the 28°N case drifts out of the region with a small gradient of absolute vorticity, it shears rapidly. The spot in the 32°N case drifts to 28°N - a location that can sustain a long-lived dark spot. Therefore, in regard the earlier stages of the vortex revolution, starting point 28° is the better location; in regard the later stage, starting from 32° is better.

Figure 4.20 shows the drift of the simulated UDS starting from different latitudes. There is one interesting phenomenon here. The Sromovsky 18° case shows a location oscillation around 13° . Noticing that 13° is the local maximum of the absolute vorticity profile in Figure 4.2b, this shows that the spot moves around this local maximum point and gradually shrinks (see Figure 4.19 and Table 4.2). As discussed previously in the coarse grid simulations, the fitted zonal wind profiles near the equator are not well defined. They lack data and smooth the sharp change of the observed zonal winds, so the simulated spots near the equator do not represent the real world. This may explain why no one has observed a dark spot near the equator of Uranus.

4.4 Discussion

In this chapter, simulations on Uranian Dark Spot are performed. The investigations are mainly on the effects of different zonal wind profiles, the latitudes of the UDS, the strength of the UDS and the effects of grid spacing. The simulation results show that the Sromovsky and Fry 2005 zonal wind profile is the best in the three fitted zonal wind profiles to sustain a dark spot. Also, 28°N is about the best location to sustain a dark spot in the Sromovsky and Fry zonal wind profile in the middle and

high latitudes. The kink of Sromovsky and Fry profile near 28°N is important for the sustainability of the UDS. This may explain why no dark spots were observed before until 2006 and why the UDS appeared at 28°N . This also suggests that the zonal wind profile of Uranus changes with time and the kink of the Sromovsky and Fry 2005 profile may be the result of the seasonal change on Uranus.

The simulation results show that the latitudes near the equator are more suitable for the survival of a dark spot. But no dark spots were observed near the equator. This may be related to the real zonal winds near the equator and the vertical shear of the zonal winds. Since the observational wind speed data near the equator do not change smoothly and in many latitudes there are not zonal wind data, the fitted zonal wind profile near the equator cannot reflect the real world on Uranus. Therefore, the possible great vortex near the equator may be destroyed by the diversity of the zonal winds or the strong vertical shear near the equator.

As to the strength of the dark spot, our simulations show that considerable strong dark spot can survive longer, but too strong (maximum velocity > 90 m/s) dark spot cannot get longer lifetime.

Our simulations include the coarse grid cases (grid spacing equals to 0.7°) and the fine grid cases (grid spacing equals to 0.35°). The simulation results show that the fine grid cases show longer lifetime than the coarse grid cases. But the qualitative sustainability results related to the zonal wind profiles, to the latitudes and to the strength of the dark spot do not change. This means that the trends observed in the simulations is believable. The only exception is the constructed $Q_y = 0$ zonal wind profile, which shows better performance in the coarse grid cases than that in the fine grid cases. This is related to the effect of the connection of the $Q_y = 0$ region to the Sromovsky and Fry profile. In the coarse grid simulations, the big grid spacing smoothed the connection, while in the fine grid simulations, the connections generate waves and small vortices, which affect the dynamics of the UDS and lead to a worse

behavior.

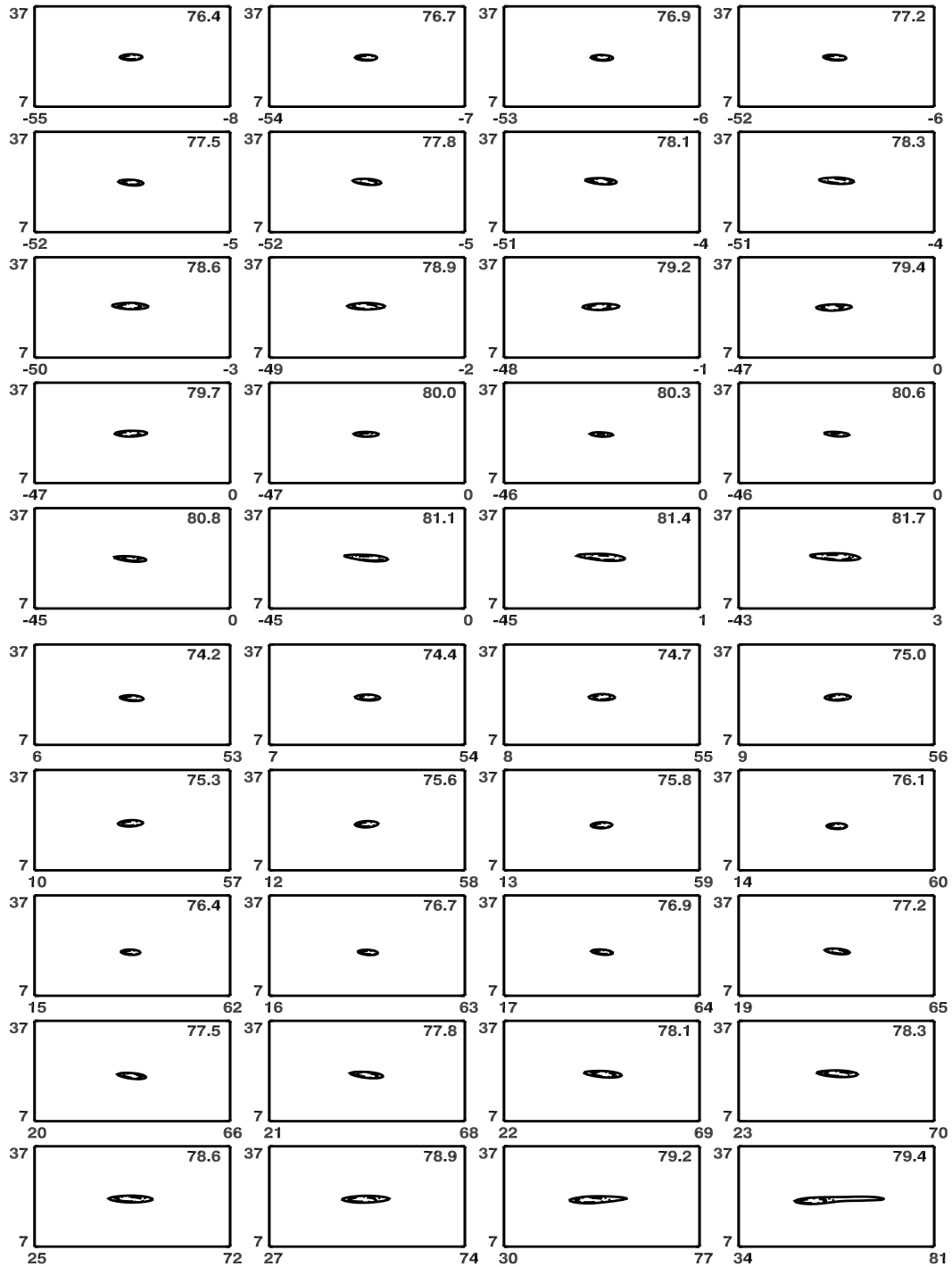


Figure 4.18: Contour plot of the simulated UDS on Sromovsky zonal wind profile with initial maximum wind velocity 90 m/s and 110 m/s. This plot is about finer grid simulations. These simulations all start from 29.8°N. The final stages of these two simulations are shown. We can see the fluctuations near the end of their lives (10° longitudinal extent). The numbers in the subplots are the times of the simulations, in unit days.

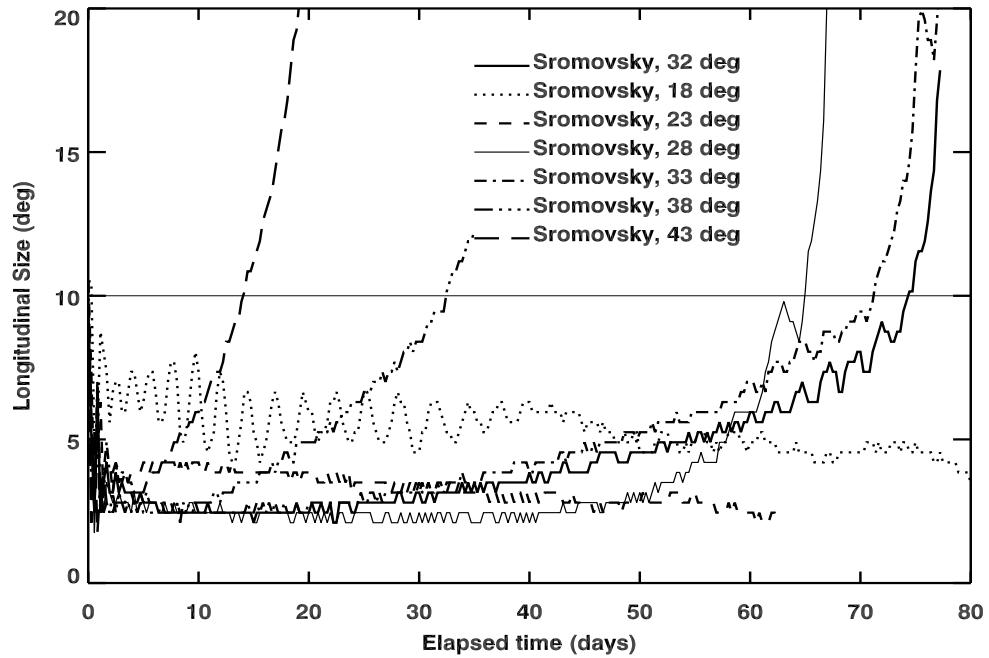


Figure 4.19: Change of longitudinal size vs. initial latitude of spot center. The zonal wind profile is Sromovsky and Fry 2005 and the maximum wind velocity is 70 m/s.

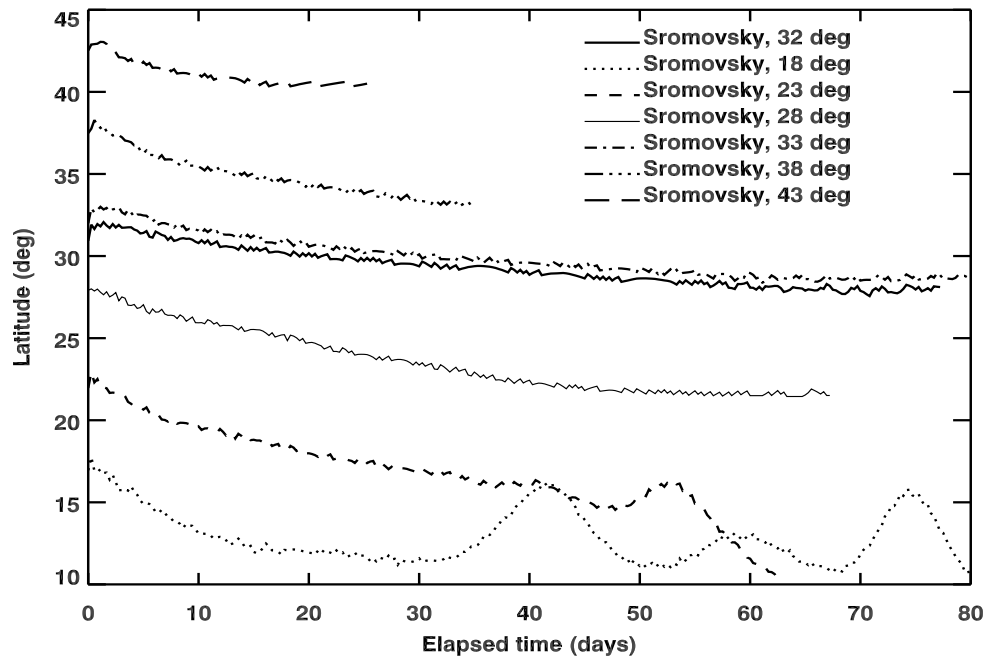


Figure 4.20: Drift of spot vs. initial latitude of spot center. The zonal wind profile is Sromovsky and Fry 2005 and the maximum wind velocity is 70 m/s.

Table 4.1: Uranus Vortex Simulations on the Coarse Grid

Profile	u_{max} (m/s)	λ_I ($^\circ$)	λ_F ($^\circ$)	Lifespan (days)	Comment
Smith	70	23	18.8	35	
Smith	70	28	24.8	23	
Smith	70	30.8	28.1	16	
Smith	70	30.9	28.5	16	
Smith	70	31	28.4	16	
Smith	70	38	36.7	9	
Karkoschka	70	23	19.0	32	
Karkoschka	70	28	24.6	25	
Karkoschka	70	31	28.0	19	
Karkoschka	70	38	36.3	11	
Sromovsky	30	28	27.0	14	
Sromovsky	50	28	26.3	20	
Sromovsky	70	28	25.4	23	
Sromovsky	90	28	24.6	27	
Sromovsky	110	28	24.4	27	
Sromovsky	130	28	24.3	28	
Sromovsky	70	13	9.1	8	
Sromovsky	70	18	13.4	>58	
Sromovsky	70	23	18.5	26	
Sromovsky	70	29.6	27.6	26	
Sromovsky	70	29.8	27.9	27	
Sromovsky	70	30	28.4	26	
Sromovsky	70	31	29.6	23	
Sromovsky	70	33	31.0	21	
Sromovsky	70	38	35.9	10	
$Q_y = 0$	30	28	28.5	23	shrink
$Q_y = 0$	50	28	28.3	29	shrink
$Q_y = 0$	70	28	28.0	31	shrink
$Q_y = 0$	90	28	27.7	32	shrink
$Q_y = 0$	110	28	25.7	33	shrink
$Q_y = 1/3$	70	28	26.6	29	shrink
$Q_y = 2/3$	70	28	25.5	27	shrink

1. Profile means the zonal wind profiles, including: fitting profiles from Sromovsky & Fry 2005[95], Smith et al. 1986 [86], and Karkoschka 1998 [42]; constructed profile identified by Q_y .
2. u_{max} is the initial maximum velocity.
3. λ_I is the initial vortex center latitude.
4. λ_F is the final vortex center latitude.

Table 4.2: Uranus Vortex Simulations on the Finer Grid

Profile	u_{max} (m/s)	$\lambda_I(^{\circ})$	$\lambda_F(^{\circ})$	Lifespan (days)	Comment
Smith	70	29	22.1	>80	
Smith	70	30	23.4	80	
Smith	70	30.9	24.4	63	
Smith	70	33	28.0	41	
Smith	70	35	31.1	32	
Karkoschka	70	31	24.1	75	
Karkoschka	70	33	27.1	51	
Karkoschka	70	33.6	28.1	46	
Karkoschka	70	35	30.4	37	
Sromovsky	30	29.8	28.3	29	
Sromovsky	50	29.8	26.9	54	
Sromovsky	70	29.8	24.7	74	
Sromovsky	90	29.8	22.3	81	
Sromovsky	110	29.8	20.7	79	
Sromovsky	70	18	5.5	>88	shrink
Sromovsky	70	23	11.0	>63	shrink
Sromovsky	70	28	21.5	65	
Sromovsky	70	32	27.9	74	
Sromovsky	70	33	28.6	71	
Sromovsky	70	34	29.0	69	
Sromovsky	70	38	33.4	33	
Sromovsky	70	43	40.8	14	
Sromovsky	70	48	46.6	13	
Sromovsky*	70	32	27.3	83	
$Q_y = 0$	70	28	23.6	48	
$Q_y = 0$	70	31	27.1	68	shrink

1. Parameters are same to the Table 4.1.
2. When calculating the lifespan, 10° is used as the critical value.
3. In the Sromovsky case marked with *, the spot is placed on 4000 mbar; in other cases, spots are placed on 1000 mbar.

Chapter 5 Radiation Model and Seasonal Change of Zonal Wind Profile on Uranus

Previously, EPIC did not have a radiation model. This made it impossible to simulate many important phenomena in planetary atmospheres. Solar radiation is a primary energy source for many planetary atmospheres. On the Earth, cloud formation, wind generation, and storm formation are all closely connected to the solar radiation. Although Uranus is much further than the Earth from the Sun, solar radiation is still the dominant energy source for Uranian atmosphere. Also, because of its unusual obliquity, Uranus has seasonal changes that are different from any other planet in the solar system. Possible seasonal change to the zonal wind profile has already been discussed in Chapter 1 and Chapter 4. Therefore, to simulate and better understand the seasonal changes and related dynamics phenomena on Uranus and other planets, a radiation model is needed.

In this chapter, the radiation model will first be presented. Then, this model is applied to the Uranian atmosphere by including a simple initial absorption coefficient. After that, a more elaborate absorption coefficient calculation model is included and additional results are presented.

5.1 Heat Term in EPIC Model

In EPIC, the heat into the system is related to the potential temperature

$$\frac{d\theta}{dt} \equiv \dot{\theta} = \frac{\dot{Q}}{\Pi}, \quad (5.1)$$

where $\Pi = C_p T / \theta$ is the Exner function. The hybrid vertical velocity is calculated by taking the full derivative of the hybrid coordinate (see equation 1.53) $\zeta = F(\theta, p, p_{bot})$

with respect to t [22],

$$\dot{\zeta} = \frac{\partial F}{\partial \theta} \dot{\theta} + \frac{\partial F}{\partial p} \dot{p} + \frac{\partial F}{\partial p_{bot}} \dot{p}_{bot}. \quad (5.2)$$

Including the related terms, this equation becomes

$$\dot{\zeta} = \tilde{g}(\sigma) \frac{\dot{Q}}{\Pi} + F_p \dot{p} + F_{p_{bot}} \dot{p}_{bot}, \quad (5.3)$$

where the subscripts on F denote partial differentiation. This equation forms the basis of a radiation-convection model in EPIC, in which the radiative heat flux in the system is analyzed and then linked to the heat Q in this equation.

5.2 Two-Flux Model

We will use an approach similar to the basic idea of the two-flux model in a planetary atmosphere presented in Raymond 1994[79]. It assumes that the energy transfer is one-dimensional and the intensity is isotropic for all radiation with components in the positive coordinate direction and also in the negative direction. In this model, on each layer, the heat flux is divided into two parts: one is upward and another is downward. Using I_+ to denote the upward flux into the layer and I_- to denote the downward flux into the layer, we can get the heat in a thin layer of thickness dz :

$$Q = \frac{d}{dz}(I_+ + I_-). \quad (5.4)$$

Note that the sign used here in our derivation is different from the original one in the equation in Raymond, where $Q = \frac{d}{dz}(I_+ - I_-)$, which derives the upward direction as positive such that I_- has the opposite sign. In our model, we regard the energy into the layer as positive. Therefore, $dI_- = I_-[i - 1] - I_-[i]$ has the same positive sign as $dI_+ = I_+[i] - I_+[i - 1]$ in this equation, although it is downward. Regarding the

planetary atmosphere as a grey body, then its radiation follows the equation:

$$Q_a = \rho\mu\sigma T^4, \quad (5.5)$$

where ρ is the density of the atmosphere, μ is the effective absorptivity and $\sigma = 5.6704 \times 10^{-8} \text{ Js}^{-1}\text{m}^{-2}\text{K}^{-4}$ is the Stefan-Boltzmann constant. Applying the two flux approximation, the change of the upward heat flux follows the equation:

$$\frac{dI_+}{dz} = \rho\mu(\sigma T^4 - I_+). \quad (5.6)$$

Similarly,

$$\frac{dI_-}{dz} = \rho\mu(\sigma T^4 - I_-). \quad (5.7)$$

Combining the above equations yields:

$$Q = \rho\mu(2\sigma T^4 - I_+ - I_-). \quad (5.8)$$

In our model, based on different wavebands, I_- is divided into two parts: solar radiation I_{-s} and infrared radiation I_{-i} :

$$I_- = I_{-s} + I_{-i}. \quad (5.9)$$

Figure 5.1 shows the scheme of the two-flux method used in this project. I_+ , I_{-s} and I_{-i} are all calculated on the boundaries of the layers. In the code, the heat $Q[i]$ in layer i is calculated as:

$$Q[i] = (I_+[i] - I_+[i-1]) + (I_{-s}[i-1] - I_{-s}[i]) + (I_{-i}[i-1] - I_{-i}[i]). \quad (5.10)$$

Obviously, the two-flux method can be generalized to higher order by breaking up

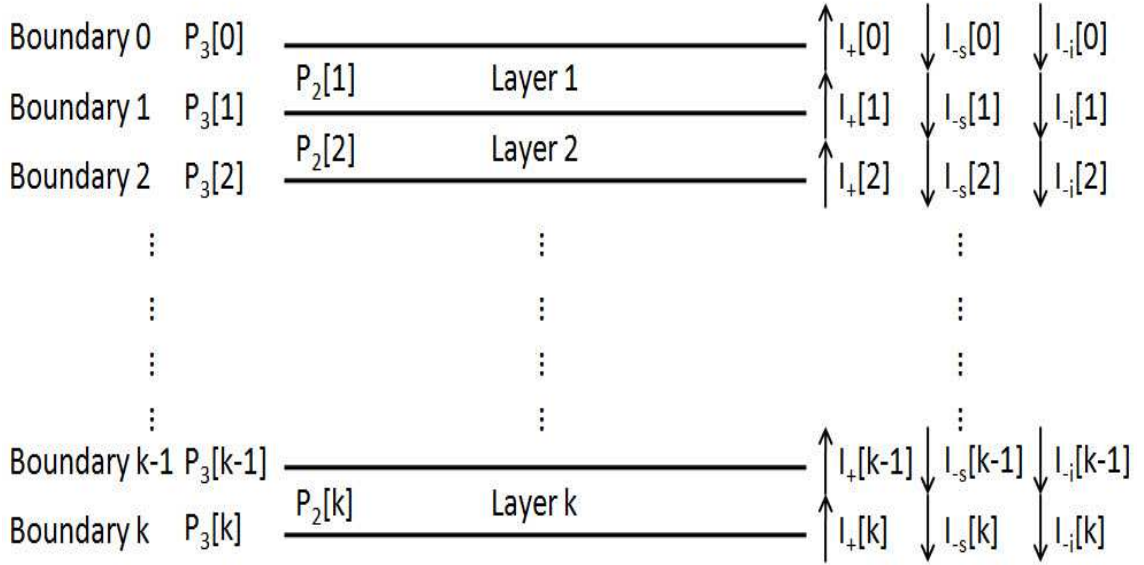


Figure 5.1: The scheme of the two-flux method used in this project.

the 4π solid angle into more than two directions. Chin and Churchill[7], and Shih and Chen[9] have used six-flux methods. Chan[10] has given a review of six-flux methods. In general, these methods are called discrete ordinate methods represented by S_N and a review of using this approach is given by Viskanta and Mengüç [102].

5.3 Basic Considerations

To use the two-flux method in EPIC, there are several basic considerations.

1. The heat source only includes solar insolation and the infrared radiation from the grey atmosphere. Other heat sources, like phase changes, are not included.
2. To simplify the geometry calculations, we assume the Uranian orbit around the Sun is a circle, ignoring the eccentricity (the eccentricity of the orbit is 0.044405586).
3. The lower boundary is regarded as a black body with constant temperature. Therefore, the radiation from the bottom is a constant σT_b^4 . The downward

flux into this lower boundary is totally absorbed.

4. In each layer, the atmosphere is regarded as isotropic and the pressure, temperature, density, potential temperature and velocities are same everywhere in this grid.
5. On the top of the first layer, input energy I_{-s} (all the wavebands of solar radiation are included in this variable) is calculated based on the insolation angle, the solar power and the distance from the Uranus to the Sun, and the albedo. Infrared flux I_{-i} into the atmosphere at the top boundary is 0. Upward flux at the top boundary is regarded as radiating to outer space.
6. Scattering of the solar radiation is simplified with the bond albedo. For Uranus, bond albedo is set at 0.3[105]. That means the incoming solar radiation I_{-s} is reduced by 30% only once at the top and there are no other scattering equations in the system. Therefore, we only consider emission and absorption in the layers.

5.4 Geometry

To simulate the evolution of the Uranian atmosphere, the main factor to represent is that Uranus has an unique obliquity in the solar system. The axial tilt angle is $\theta_{tilt} = 97.77^\circ$ relative to the vertical direction of the orbital plane. Other key parameters are orbital period ($T_o = 84.323326$ years), rotation period ($T_r = 0.71833$ day), equatorial radius ($r_e = 25560$ km), polar radius ($r_p = 24972$ km) and approximate distance to the sun ($L = 3.0 \times 10^{12}$ m, the aphelion of the Uranian orbit).

For the solar radiation, the total power emitted from the sun is $P_{solar} = 3.826 \times 10^{26}$ watt. Considering the distance of the Uranus to the Sun, the resulting power at the Uranus surface is

$$P_{sur} = \frac{P_{solar}}{4\pi L^2} = 3.383 \quad \text{watt.} \quad (5.11)$$

Including the bond albedo 0.3, the surface solar insolation power at the top of the atmosphere at normal incidence is 2.368 watt.

Starting the simulation from the solstice of the southern hemisphere (the most recent south solstice was in 1986, approximately the encounter with Voyager II, from which Smith *et al.* derived their symmetric Uranian zonal wind profile), at any time t , the angle between the pole and the Uranus-Sun center line γ is:

$$\gamma = \frac{\arccos(b^2 + 1 - c^2)}{2b}, \quad (5.12)$$

$$b = \cos(2\pi \frac{t}{T_o}) / \cos(\theta_{tilt}), \quad (5.13)$$

$$c = \sqrt{(b \sin(\theta_{tilt}))^2 + (\sin(2\pi \frac{t}{T_o}))^2}. \quad (5.14)$$

Regarding the Uranus as a perfect oblate ellipsoid, a nonnegative parameter μ can be used with $\tanh \mu = r_p/r_e$. Another nonnegative parameter a can also be used with $r_p = a \sinh \mu$, so that $r_e = a \cosh \mu$. Using the south pole (since the south solstice is the starting point $t = 0$) as the z direction, the center of Uranus is the origin (0,0,0), the y direction is perpendicular to the insolation-pole plate and the coordinates of each point can be written as:

$$x = a \cosh \mu \cos \theta \cos \phi, \quad (5.15)$$

$$y = a \cosh \mu \cos \theta \sin \phi, \quad (5.16)$$

$$z = a \sinh \mu \sin \theta, \quad (5.17)$$

where θ is latitude and ϕ is longitude. Notice the longitude used here should cancel the rotation effect by eliminating the rotated angle (Uranus rotates to the west by American Geophysical Union definition, different from other planets in the solar

system). In this way, the surface equation of this oblate ellipsoid is

$$\frac{x^2}{a^2 \cosh^2 \mu} + \frac{y^2}{a^2 \cosh^2 \mu} + \frac{z^2}{a^2 \sinh^2 \mu} = 1. \quad (5.18)$$

The normal direction at the surface is:

$$\nabla f = \left(\frac{2x}{a^2 \cosh^2 \mu}, \frac{2y}{a^2 \cosh^2 \mu}, \frac{2z}{a^2 \sinh^2 \mu} \right). \quad (5.19)$$

Considering the insolation direction $(\sin \gamma, 0, \cos \gamma)$, the insolation angle at each surface point can be calculated from the inner product:

$$\cos \beta = \frac{\frac{2x \sin \gamma}{a^2 \cosh^2 \mu} + \frac{2z \cos \gamma}{a^2 \sinh^2 \mu}}{\|\nabla f\|}. \quad (5.20)$$

5.5 Absorption Coefficient

One of the main parameters in the two-flux method is the absorption coefficient. The absorption coefficient changes with different components of the atmosphere, different temperatures and different pressures.

Wavebands

Since there are two wavebands in our simulations, we need to consider them separately. The effective temperature of the Sun is 5778K. For the Uranian atmosphere, the temperature of the part we consider is centered at about 80K. Wien's displacement law tells us that for a black body, the wavelength λ_{max} at which the intensity of the radiation it produces is at a maximum is:

$$\lambda_{max} = \frac{b}{T}, \quad (5.21)$$

where $b = 2.897768 \times 10^6$ nm·K is the Wien's displacement constant. From this, we can calculate that $\lambda_{max-solar} \approx 501.5\text{nm}$ and $\lambda_{max-uranus} \approx 36222\text{nm}$. The wavenumbers of these two wavelengths are 19940 cm^{-1} and 276 cm^{-1} , respectively. In the solar waveband, the absorption is mainly from the methane in the Uranian atmosphere. In the infrared waveband, the absorption is mainly from the H₂ dipoles induced by H₂-H₂, H₂-He and H₂-CH₄ collisions.

Experiment Results

The opacity contributed by the collisions of H₂-He, H₂-H₂ and H₂-CH₄ is reviewed by Weisstein in 1996[104]. Figure 5.2 shows the computed H₂-H₂ absorption from 0 to 2000 cm^{-1} . We can see that for the Uranian atmosphere the absorption coefficient from H₂-H₂ collisions should be around $0.2 - 0.4 \times 10^{-6} \text{ amagat}^{-2}\text{cm}^{-1}$ or $2 - 4 \times 10^{-5} \text{ amagat}^{-2}\text{m}^{-1}$. Figure 5.3 shows the H₂-He absorption from 0 to 2000 cm^{-1} . This figure places the absorption coefficient from H₂-He collisions be around $5 \times 10^{-7} \text{ amagat}^{-2}\text{cm}^{-1}$ or $5 \times 10^{-5} \text{ amagat}^{-2}\text{m}^{-1}$. Figure 5.4 shows the H₂-CH₄ absorption from 0 to 1000 cm^{-1} . The absorption coefficient from from H₂-CH₄ collisions should be around $3 \times 10^{-5} \text{ amagat}^{-2}\text{cm}^{-1}$ or $3 \times 10^{-3} \text{ amagat}^{-2}\text{m}^{-1}$.

As to the solar radiation, W. H. Smith *et al.* 1990[88] reported the absorption coefficients of methane. We know that methane is a strong greenhouse gas, stronger than CO₂ on a molecule-for-molecule basis. On Uranus, the main gas components in mole fraction are H₂ ($\sim 83\%$), He ($\sim 15\%$) and CH₄ ($\sim 2.3\%$)[58]. Both H₂ and He do not absorb much radiation in the solar waveband. Thus the absorption coefficient is mainly due to CH₄.

Figure 5.5 shows the absorption profile around 6190\AA at 290 and 100 K for methane. Figure 5.6 shows the table of absorption coefficients for CH₄ in this waveband. We can see that at low temperatures comparable to those on Uranus, the absorption coefficient is on the order of $0.1 \text{ km}^{-1}\text{am}^{-1}$ or $1 \times 10^{-4} \text{ m}^{-1}\text{am}^{-1}$.

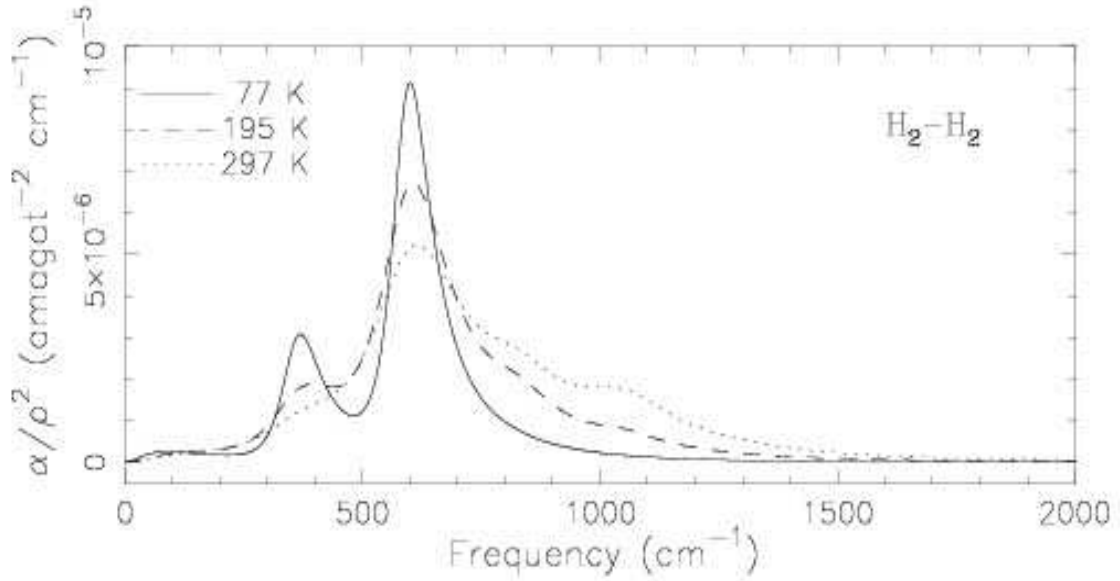


Figure 5.2: H₂-H₂ absorption calculated using the formalism of Bachet *et al.* 1983[4], from Weisstein 1996[104].

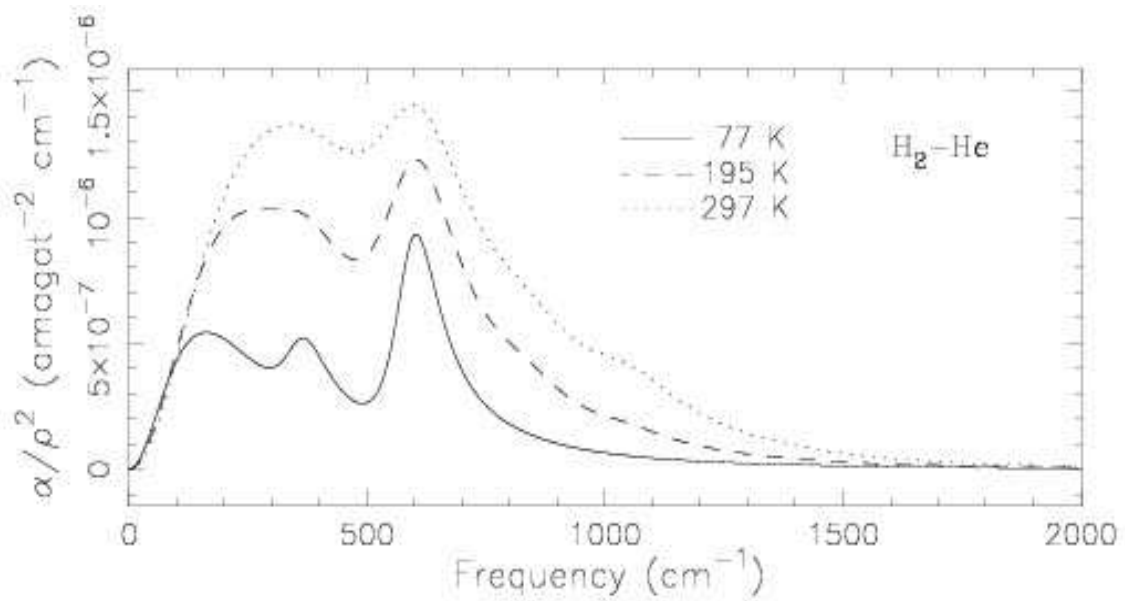


Figure 5.3: H₂-He absorption calculated using the formalism of Cohen *et al.* 1982[11], from Weisstein 1996[104].

Calculation of Absorption Coefficients

In our simplified model, we use two wavebands and in each waveband the absorption coefficient is set to one number - effective absorption coefficient. For the infrared

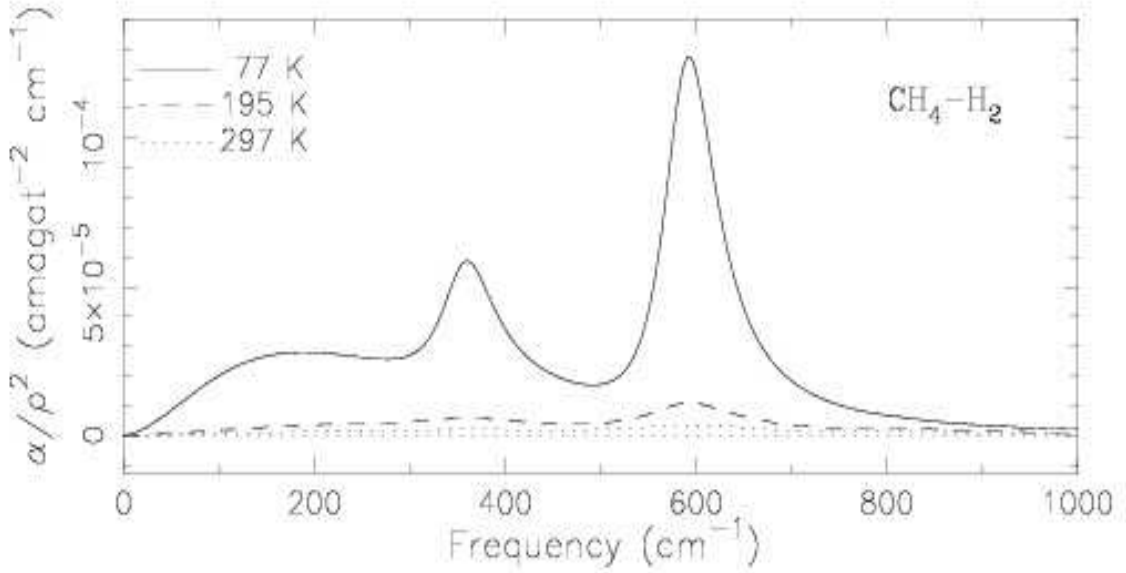


Figure 5.4: H₂-CH₄ absorption calculated using the formalism of Orton *et al.* 1983[73], from Weisstein 1996[104].

waveband, the absorption coefficient is calculated from the equation:

$$\alpha_i = (\alpha/\rho^2)_{H_2-H_2} * \rho_{H_2}^2 + (\alpha/\rho^2)_{H_2-He} * \rho_{H_2} * \rho_{He} + (\alpha/\rho^2)_{H_2-CH_4} * \rho_{H_2} * \rho_{CH_4}. \quad (5.22)$$

Here $(\alpha/\rho^2)_{H_2-H_2}$, $(\alpha/\rho^2)_{H_2-He}$ and $(\alpha/\rho^2)_{H_2-CH_4}$ are effective absorption coefficients estimated from Figure 5.2, Figure 5.3 and Figure 5.4. The variables ρ_{H_2} , ρ_{He} and ρ_{CH_4} are number density in unit amagat.

The amagat is a practical unit of number density, sometimes abbreviated as "am". This unit is defined as the number of ideal gas molecules per unit volume at a standard condition (pressure 1 atm = 101.325 kPa, temperature 0°C = 273.15 K). In our model, the atmosphere is regarded as ideal gas, and the number density of each component i in an amagat are calculated in the equation:

$$\eta_i = P_i \left(\frac{p}{p_0} \right) \left(\frac{T_0}{T} \right). \quad (5.23)$$

Here $T_0 = 273.15$ K, $P_0 = 101.325$ kPa, and P_i is the proportion of the component i .

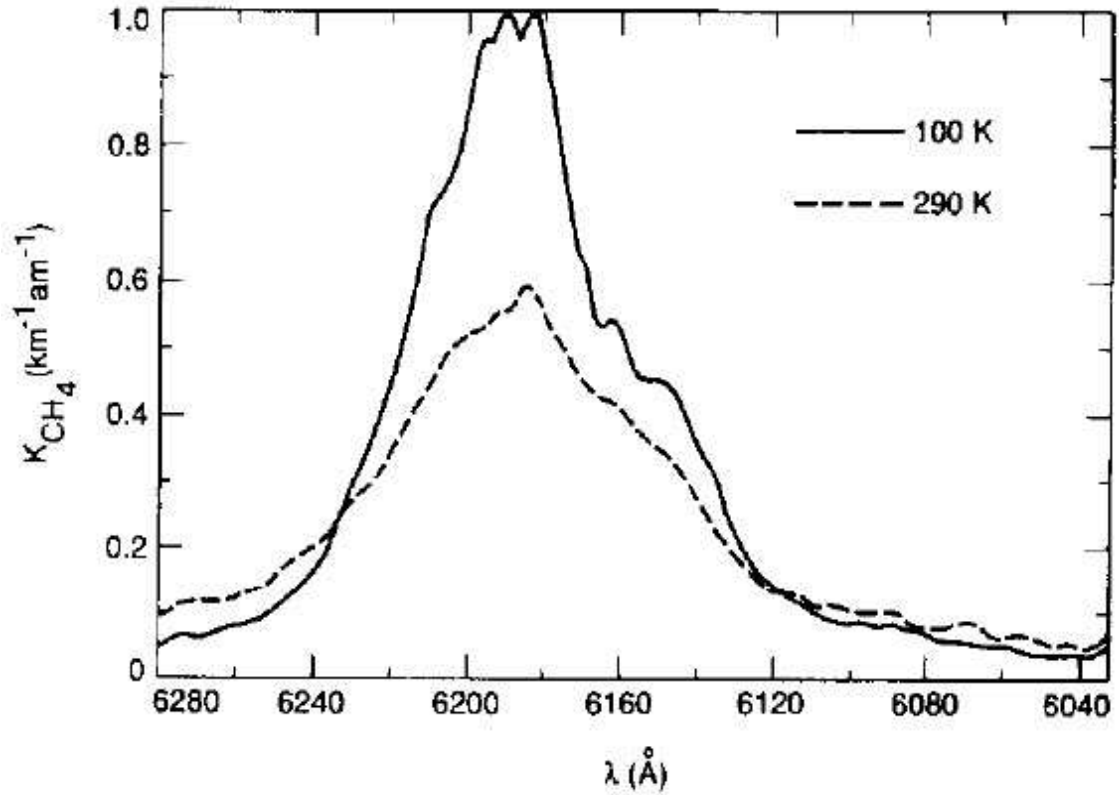


Figure 5.5: CH_4 absorption around 6190\AA at 290 and 100 K. This figure is from Lunine 1993[58].

The effective absorption coefficient in the solar waveband is estimated from Figure 5.5.

In the studied system, the proportions of components H_2 and He are regarded as constant and the proportion of CH_4 is calculated following the relative humidity. We know that when the temperature is low, the saturation proportion will be small. Here, we assume the relative humidity is a constant RH (for example, 0.8) and set an upper limit for the proportion of methane as 2.3%, which is the observed total methane proportion in the Uranian atmosphere. With these in mind, the molar fraction of methane is

$$P_{\text{CH}_4} = RH \frac{P_{\text{sat}}}{P}. \quad (5.24)$$

CH₄ ABSORPTION COEFFICIENTS AT 10-Å RESOLUTION

λ (Å)	K_{CH_4} (km ⁻¹ am ⁻¹)				
	100°K	125°K	150°K	200°K	290°K
6040	0.0359	0.0282	0.0455	0.0356	0.0498
6050	0.0382	0.0312	0.0494	0.0388	0.0588
6060	0.0485	0.0388	0.0604	0.0383	0.0666
6070	0.0574	0.0485	0.0680	0.0482	0.0863
6080	0.0690	0.0582	0.0803	0.0610	0.0860
6090	0.0830	0.0744	0.0967	0.0685	0.1016
6100	0.0891	0.0802	0.1047	0.0811	0.1068
6110	0.1092	0.1032	0.1235	0.1071	0.1194
6120	0.1470	0.1384	0.1653	0.1301	0.1405
6130	0.3083	0.2749	0.2996	0.2322	0.2268
6140	0.3723	0.3440	0.3720	0.2962	0.2808
6150	0.4528	0.4236	0.4617	0.3708	0.3699
6160	0.5183	0.4999	0.5418	0.4708	0.4068
6170	0.6309	0.5946	0.6376	0.5267	0.4594
6180	0.9318	0.8676	0.9048	0.7176	0.5567
6190	0.9787	0.9156	0.9468	0.7342	0.5391
6200	0.8552	0.8006	0.8550	0.6843	0.5134
6210	0.6738	0.6366	0.7023	0.5725	0.4345
6200	0.4397	0.4346	0.5049	0.4153	0.3371
6230	0.2726	0.2778	0.3510	0.2990	0.2621
6240	0.1574	0.1600	0.2268	0.2053	0.1987
6250	0.1013	0.1002	0.1573	0.1410	0.1500
6260	0.0775	0.0723	0.1152	0.1083	0.1272
6270	0.0644	0.0600	0.0990	0.0898	0.1157

Figure 5.6: Table of the absorption coefficients for CH₄ around 6190Å between 100 and 290K. This figure is from Lunine 1993[58].

Energy Balance

To get suitable estimates of the absorption coefficients, we need to consider the overall energy balance in the system. The absorption coefficients should be defined such that when the depth of the studied atmosphere is sufficient, the input solar radiation should equal or at least be close to the output infrared radiation. Otherwise, the atmosphere would eventually either cool or heat up over time.

To study the energy balance in the simulated Uranian atmosphere system, deep vertical layers from 7.4 mbars to 8.1 bars are included. Summing up and then comparing the total input $I_{-s}(0, J, I)$ and total output $I_{+}(0, J, I)$, we defined a group of consistent effective absorption coefficients: $(\alpha/\rho^2)_{H_2-H_2} = 4.0 \times 10^{-5} \text{m}^{-1} \text{am}^{-1}$, $(\alpha/\rho^2)_{H_2-He} = 5.0 \times 10^{-5} \text{m}^{-1} \text{am}^{-1}$ and $(\alpha/\rho^2)_{H_2-CH_4} = 3.0 \times 10^{-3} \text{m}^{-1} \text{am}^{-1}$.

5.6 Realizing the Radiation Model in the EPIC GCM

To realize this radiation model in the EPIC GCM, we need to locate the position of heat source in the code first. The heat source (subroutine `source_sink`, in the file `epic_funcs_diag.c`) in the EPIC GCM is calculated in each time step before the calculation of the hybrid vertical velocity (subroutine `calc_w`) and horizontal velocity tendencies (subroutine `uv_core`, `uv_drag` and `uv_horizontal_subgrid`). The solar insolation heat source (subroutine `solar_insolation`) is the first one calculated in the subroutine `source_sink`. Others include the ortho-para hydrogen conversion and the cloud microphysics.

Our work is on the subroutine `solar_insolation` and another subroutine used to calculate the absorption coefficients (subroutine `absorption_coefficient`). Both of them are in the file `epic_sensible_heating.c`. The subroutine `absorption_coefficient` uses the methods and parameters discussed above to calculate the molar fraction and density of hydrogen, helium and methane and then use these data to calculate the related absorption coefficients. The parameters pressure and temperature used here are all at the vertical layer centers. The subroutine `solar_insolation` is the main subroutine used to calculate the radiation heat source into each grid. Based on the methods and parameters discussed in previous sections, it calculates the solar insolation angle at each time step and each longitude and latitude grid. Then, after canceling the albedo, the solar insolation energy at the top boundary of each column can be calculated. With the two-flux method, the radiation heat flux I_{+} , I_{-s} and I_{-i} at each layer

interface can be calculated. Finally, the radiation heat into each grid can be decided with the equation 5.10 and stored in the array HEAT3. The parameters latitude and longitude used here and so the heat calculated here are all at the horizontal h grids, which are at the centers of the longitudinal u grids and latitudinal v grids.

5.7 Grid Setup and Time Step

As mentioned in Chapter 1, because we need to simulate the whole global seasonal changes in 21 years, we need to use a coarser grid setup and a longer time step in the simulations of this Uranian radiation model than in the previous dynamic simulations of GDS and UDS. Also, because our focus is on the whole global seasonal changes, not any small clouds or vortices in the atmosphere, increasing the grid spacing and the time step is also suitable. After balancing the accuracy and the simulation time, we use the horizontal grid spacing 2.8° and the time step 240 seconds. In the vertical direction, we still use 10 layer setup. With eight nodes on KFC5, we can simulate about one year in one real day. In this way, one simulation case can be finished in three weeks.

5.8 Simulation Results

In the simulations with this radiation model, we use 10 vertical layers, longitudinal grid number 128 from -180° to 180° (grid spacing of 1.4 degrees), latitudinal grid number 64 from -90° to 90° (grid spacing of 1.4 degrees). The time step is 240 seconds. With these parameters, the running time for one simulation year is about 1 real day. Normally, we run the cases about 21 simulation years from south solstice in 1986 to the equinox in 2007. With eight processors on the cluster KFC5, it will take more than half a month to run one case. Finally, we compare the simulation results with the observational results at different dates.

Initial Test Simulation

Table 5.1: The 10 layers setup on Uranus for the one-band test simulation case of the radiation model

Layer	ζ [K]	P [mbar]	T [K]	θ [K]	N^2 [1/s ⁻²]
1.0	672.8	3.26799e+00	68.0	672.8	0.000103
2.0	498.5	6.61541e+00	66.9	498.5	0.000137
3.0	349.4	1.33122e+01	62.0	349.4	0.000159
4.0	245.3	2.67270e+01	57.6	245.3	0.000159
5.0	176.9	5.38241e+01	54.9	176.9	0.000148
6.0	131.7	1.09093e+02	54.3	131.7	0.000136
7.0	101.6	2.20820e+02	55.5	101.6	0.000109
8.0	84.4	4.51908e+02	61.3	84.4	0.000055
9.0	76.2	9.21036e+02	74.4	77.1	0.000015
10.0	56.4	1.86293e+03	93.9	74.0	0.000011

1. ζ is the hybrid vertical coordinate.
2. θ is the potential temperature.
3. N^2 is the square of the Brunt-Väisälä frequency (buoyancy frequency).

The initial test simulation is somewhat different from the previously discussed standard method in terms of the absorption coefficient calculation. A uniform absorption coefficient $0.01 \text{ m}^{-1}(\text{kg}/\text{m}^3)^{-1}$ was used for all the wavebands without considering the components of the atmosphere. It was used to test the model and check the trend of the change of the Uranian zonal wind profile. The vertical layer setup for this case is in Table 5.1.

The results from this approach are shown in Figure 5.7. We can see the evolution of the zonal wind profile from this figure. The first several plots are in the adjustment time. Basically, we can see that the zonal wind speeds near the equator decreases when the solar radiation is incident near the south pole. Then when the solar radiation is closer to the equator, its amplitude increases again. In this process, kinks appears in the zonal wind profile.

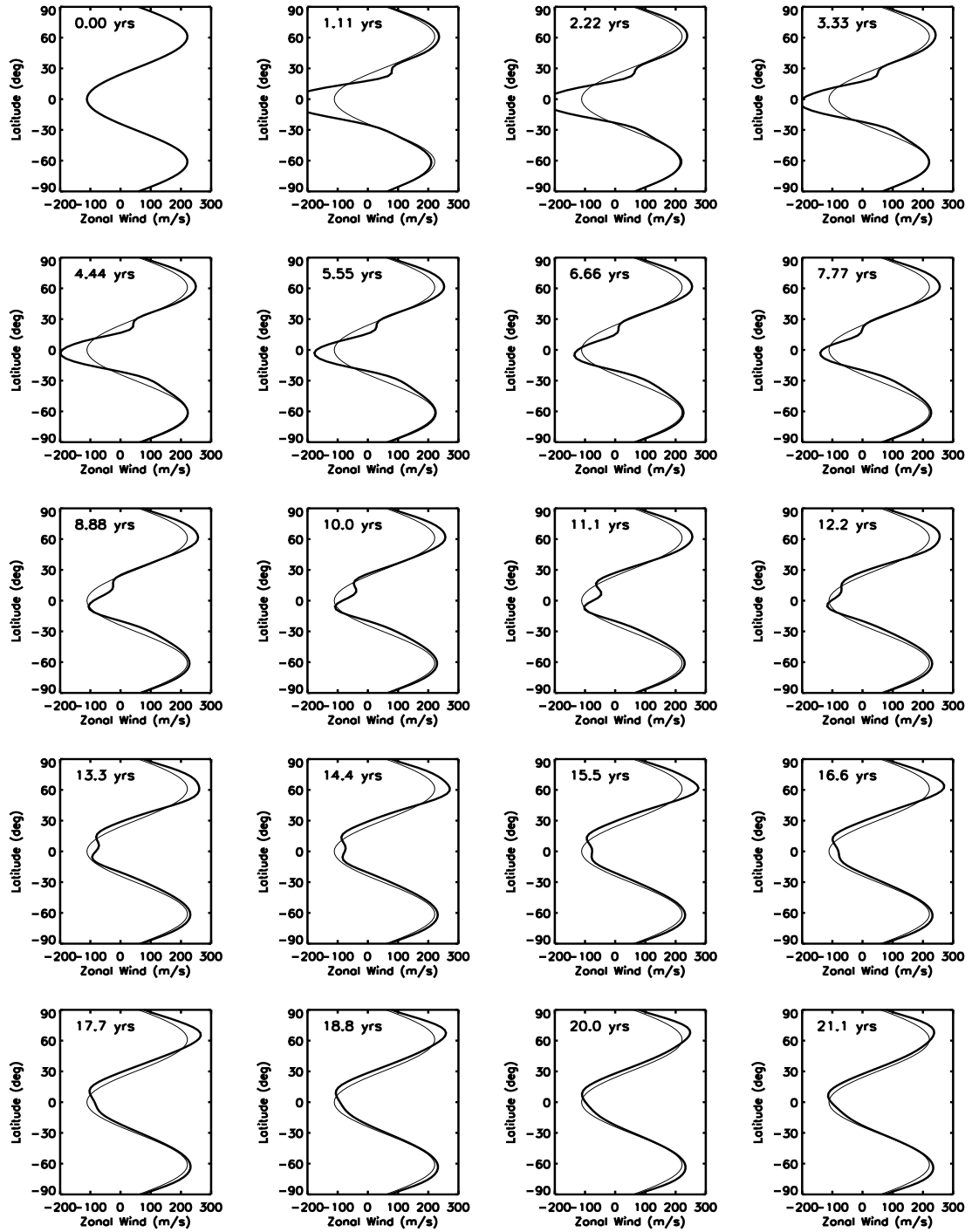


Figure 5.7: Evolution of the zonal wind profile starting from Smith 1986 symmetric fitting profile. This figure is about the one-band test case with absorption coefficient $0.01 \text{ m}^{-1}(\text{kg}/\text{m}^3)^{-1}$.

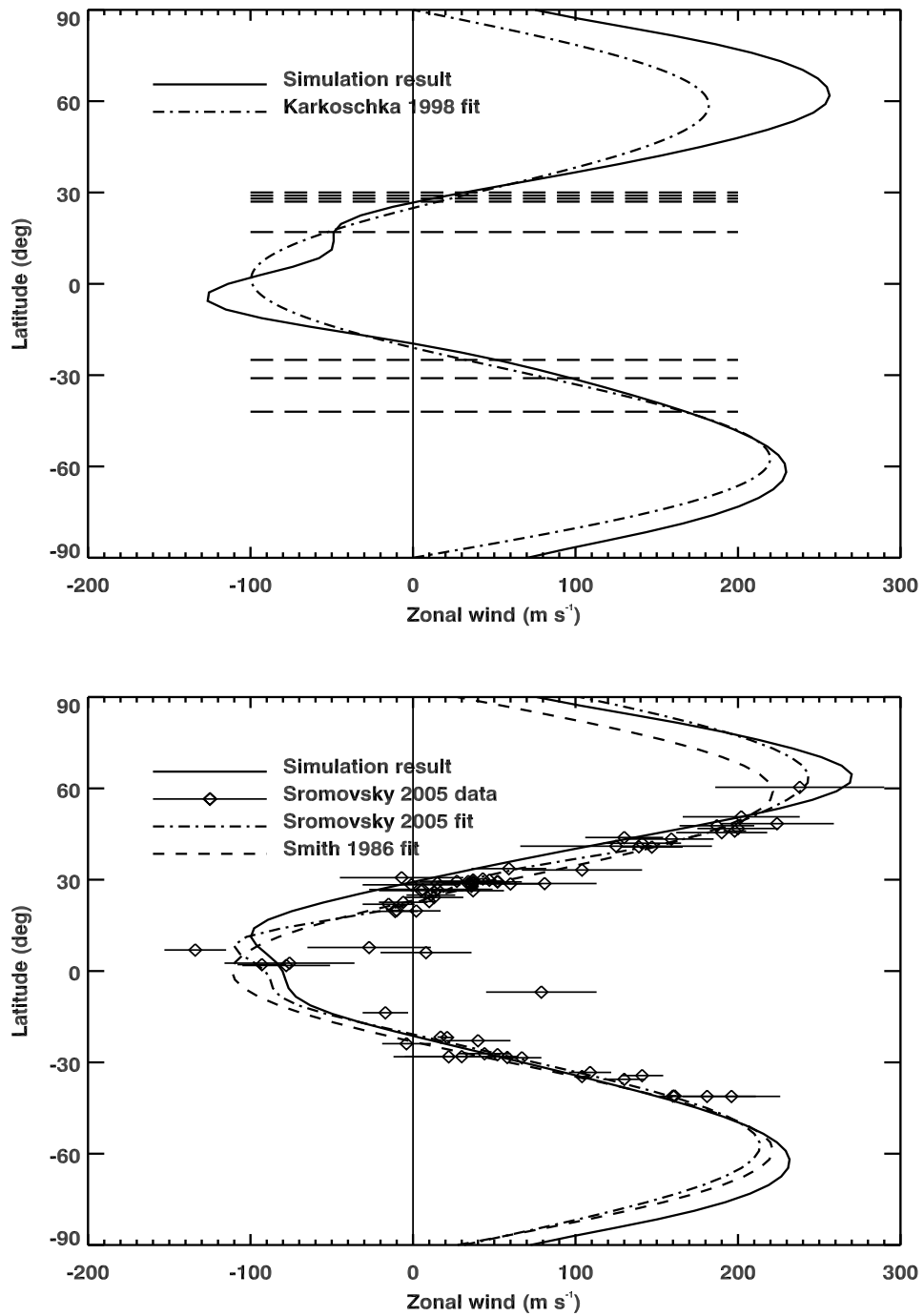


Figure 5.8: Comparison of simulation result with observational results. The upper panel compares the results to the Karkoschka observational result in 1997 and fitted curve in 1998[42]. The dashed straight lines are at the latitudes of observations. The lower panel compares the results to the observational (2003) points and fitted profile by Sromovsky and Fry in 2005[95].

The comparison between the observational results and the simulated results are shown in Figure 5.8. Horizontal dashed lines indicate latitudes at which Karkoschka tracked clouds for wind speed data. The upper panel in this figure shows that in 1997, our simulation curve fits the observational results well at the latitudes with dashed lines. The lower panel in Figure 5.8 shows that the simulation result in 2003 fit the trend of the observational results and fitted curve reasonably well. Since this is an initial test simulation, it is already very good to see that the basic trend of the change of the zonal wind profile can be simulated.

Recent Simulation Results

With the two-band radiation model, we run several simulations. Table 5.2 shows the vertical layer setup of some two-band cases. The deepest layer is at 7020 mbars. As discussed above, from energy balance, we get one set of consistent parameters for the absorption coefficient in the infrared waveband: $(\alpha/\rho^2)_{H_2-H_2} = 4.0 \times 10^{-5} \text{m}^{-1} \text{am}^{-1}$, $(\alpha/\rho^2)_{H_2-He} = 5.0 \times 10^{-5} \text{m}^{-1} \text{am}^{-1}$ and $(\alpha/\rho^2)_{H_2-CH_4} = 3.0 \times 10^{-3} \text{m}^{-1} \text{am}^{-1}$. We know the absorption coefficient of methane in the solar radiation waveband is on the order of $1.0 \times 10^{-4} \text{m}^{-1} \text{am}^{-1}$. The accurate number for the effective absorption coefficient in the solar radiation waveband is not well defined. We tried $(\alpha/\rho)_{CH_4} = 6.0 \times 10^{-4} \text{m}^{-1} \text{am}^{-1}$ and $(\alpha/\rho)_{CH_4} = 4.0 \times 10^{-4} \text{m}^{-1} \text{am}^{-1}$ for this parameter. Initial relative humidities 0.8 and 0.6 are used. With these parameters, some simulation results can be achieved. The following results all from layer 6 (2088 mbars), which is believed to be about the main cloud layer of Uranian atmosphere. Also, our results suggests that the center layers 5, 6 and 7 give similar zonal wind profiles at mid latitudes in the simulations. This is shown in Figure 5.9. The significant vertical shear near the equator in Figure 5.9 may be one reason that UDS cannot survive near the equator.

Figure 5.10 shows the evolution of a zonal wind profile, starting from the Smith

1986 fitted curve. This one has the parameter $(\alpha/\rho)_{CH_4} = 6.0 \times 10^{-4} \text{m}^{-1} \text{am}^{-1}$ and initial relative humidity 0.6. Although the curves in this figure look different from the curves in Figure 5.7, we can still see that the trend is similar. The zonal wind speeds near the equator decrease and then increase. Some kinks appear at some latitudes at different times. We notice that at the time of 18.8 years (corresponding to the year 2005), there is a kink near 28°N , which as discussed in Chapter 4 may be important for the sustainability of Uranian Dark Spot. The wind speeds change rapidly near the equator. That is consistent with the diverse velocities in the observational data points and another reason why no large vortices has been observed near the equator, although our simulations in Chapter 4 suggest that the latitudes closer to the equator may be able to sustain a great vortex.

Figure 5.11 compares this simulation case with the observational data in Karkoschka 1998 (observed in 1997) and Sromovsky and Fry 2005 (observed in 2003). The simulation results seem fit the observational data well.

Similar plots for initial relative humidity 0.8 are shown in Figure 5.12 and Figure 5.13. Changing $(\alpha/\rho)_{CH_4}$ to $4.0 \times 10^{-4} \text{m}^{-1} \text{am}^{-1}$ and using initial relative humidity 0.6 yields Figure 5.14 and Figure 5.15. In Figure 5.15, the simulated zonal wind profiles are somewhat far from the observed data points at some latitudes, although the basic trend of the zonal wind speeds near the equator shown in Figure 5.12 is similar to other simulations. This suggests that effective absorption coefficient $(\alpha/\rho)_{CH_4} = 6.0 \times 10^{-4} \text{m}^{-1} \text{am}^{-1}$ may be better than $(\alpha/\rho)_{CH_4} = 4.0 \times 10^{-4} \text{m}^{-1} \text{am}^{-1}$. Also, comparing the kink in the simulated zonal wind profiles near UDS time (2006), it seems initial relative humidity 0.6 might be closer to the real world than 0.8.

From Figure 5.10, we can see that in the southern hemisphere there is another kink near 30°S around 2003. It lasts longer than the northern kink, appearing many years earlier than the kink appears at the mid latitudes in the northern hemisphere. From this figure, this kind of kink near 30°S on the zonal wind profile exists from

1998 to 2006. After that it shifted and the profile becomes smooth near this latitude. Is it possible that another dark spot existed at this latitude on Uranus? Sromovsky and Fry 2005[95] tells us that there was a cloud feature near 34° in 2003 and this feature actually oscillated between 32°S and 36.5°S for about two decades (see Figure 5.16). In 2008, they reported that this feature at last drifted to the equator and disappeared[97]. They also suggested that there might be a deep vortex under the cloud governing these motions. Comparing with our simulation result, the kink in the zonal wind profile at the mid latitudes of the southern hemisphere exists for a long time and disappears near 2007. This gives a possible explanation to the sustainability of this possible long-lived deep vortex.

Heat Distribution

The heat at layer 6 (2088 mbar) is shown in Figure 5.17. From upper panel (5.56 days) to the bottom panel (2003), the heat center moves to the equator. This is related to the change of the solar insolation angle.

Temperature Distribution

In Figure 1.10, we can see that the south hemisphere is warmer than other regions. This figure was from the Voyager II data in 1986, when is the solstice in the southern hemisphere. Figure 5.18 shows the images of Uranus in 2003 to 2005 at different wavebands. The 2005 images show that the two regions near the poles still have highest temperature and near the equator there are also some higher temperature bands.

Figure 5.19 shows the temperature distribution of Uranian atmosphere at different date. Comparing with Figure 1.10 and Figure 5.18, we can see that our simulation achieves similar temperature distributions with the observed images. In the bottom

panel of Figure 5.19, the high latitude regions near the poles have higher temperatures. There is also one relatively higher temperature band near 30°S.

Convection

We notice that in 1997 the solar radiation to Uranus was basically on the southern hemisphere, but Figure 5.19 shows that the high latitudes of the northern hemisphere also show higher temperature. To explain this, we achieved the convection plot as shown in Figure 5.20. We can see that the atmospheric flow is from the southern hemisphere to the equator and the northern hemisphere.

Figure 5.21 shows the vertical velocities and convection mode in our simulations of Uranus with the radiation model in 2005. The basic convection is from the high latitudes in both hemispheres to the poles and the equator.

5.9 Discussion

In this chapter, we presented a two-flux radiation model in EPIC on Uranus. Our simulation results can capture the changes of the zonal wind profile on Uranus and fit the observational Karkoschka 1998 data and Sromovsky and Fry 2005 data relatively well. Also, our simulation results can give a kink in the profile near 28°N at UDS time, which may explain the long lifetime of UDS (see Chapter 4). Furthermore, in the southern hemisphere, our simulation results generate a long-lived oscillating kind profile near 30°S, which possibly can explain the S34 cloud feature reported by Sromovsky and Fry 2005[95] and Sromovsky et al. 2008[97]. Our simulation also generates temperature distributions similar to those observed on Uranus.

Future work on the radiation model can include more physics and energy processes, like the cloud model with latent heat and the ortho-para hydrogen conversion process. These can influence the energy generation and absorption in the atmosphere. Also,

together with these physics, more radiation-related phenomena can be simulated and explained, like the observed cloud band on Uranus.

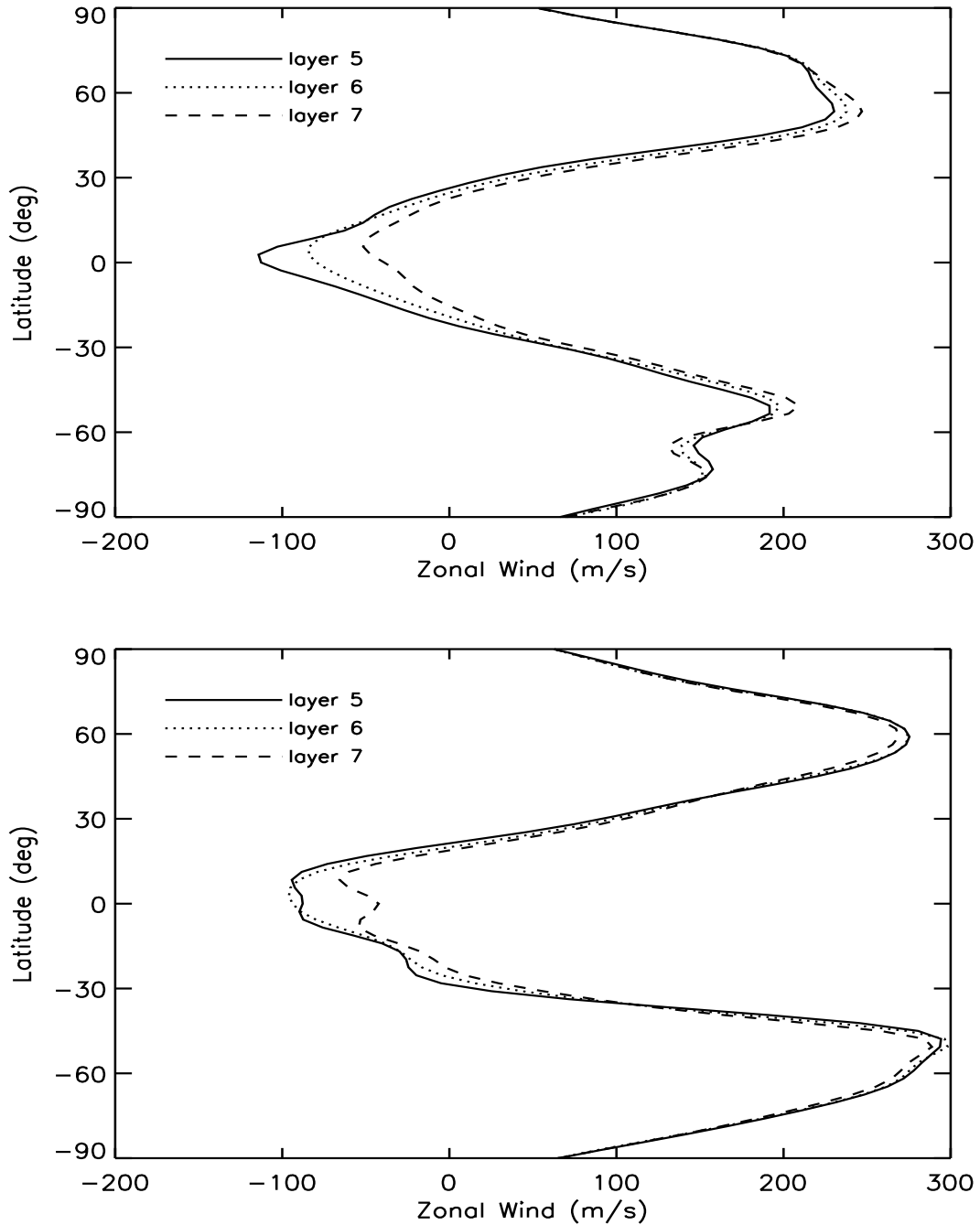


Figure 5.9: Comparison of the simulated zonal wind profiles in layer 5, layer 6 and layer 7 in 1997 (upper panel) and 2003 (lower panel). This figure is about the two-band simulation case with absorption coefficients in solar radiation waveband $(\alpha/\rho)_{CH_4} = 6.0 \times 10^{-4} \text{m}^{-1} \text{am}^{-1}$, and in infrared waveband $(\alpha/\rho^2)_{H_2-H_2} = 4.0 \times 10^{-5} \text{m}^{-1} \text{am}^{-1}$, $(\alpha/\rho^2)_{H_2-He} = 5.0 \times 10^{-5} \text{m}^{-1} \text{am}^{-1}$ and $(\alpha/\rho^2)_{H_2-CH_4} = 3.0 \times 10^{-3} \text{m}^{-1} \text{am}^{-1}$. The layer setup is the one in Table 5.2 and the initial methane relative humidity is 0.6.

Table 5.2: The 10 layers setup on Uranus for the two-band simulation cases of the radiation model

Layer	ζ [K]	P [mbar]	T [K]	θ [K]	N^2 [1/s ⁻²]
1.0	90.3	3.11254e+02	56.7	90.5	0.000088
2.0	80.1	5.15831e+02	62.3	81.3	0.000044
3.0	74.9	8.05401e+02	70.9	77.5	0.000035
4.0	70.9	1.13895e+03	79.7	76.0	0.000057
5.0	67.3	1.54219e+03	88.1	74.6	0.000004
6.0	63.8	2.08821e+03	97.3	73.4	0.000003
7.0	60.2	2.82755e+03	107.2	72.2	0.000002
8.0	56.7	3.82865e+03	118.0	71.0	0.000002
9.0	53.1	5.18420e+03	129.7	69.9	0.000001
10.0	49.6	7.01968e+03	142.2	68.8	0.000001

1. ζ is the hybrid vertical coordinate.
2. θ is the potential temperature.
3. N^2 is the square of the Brunt-Väisälä frequency (buoyancy frequency).

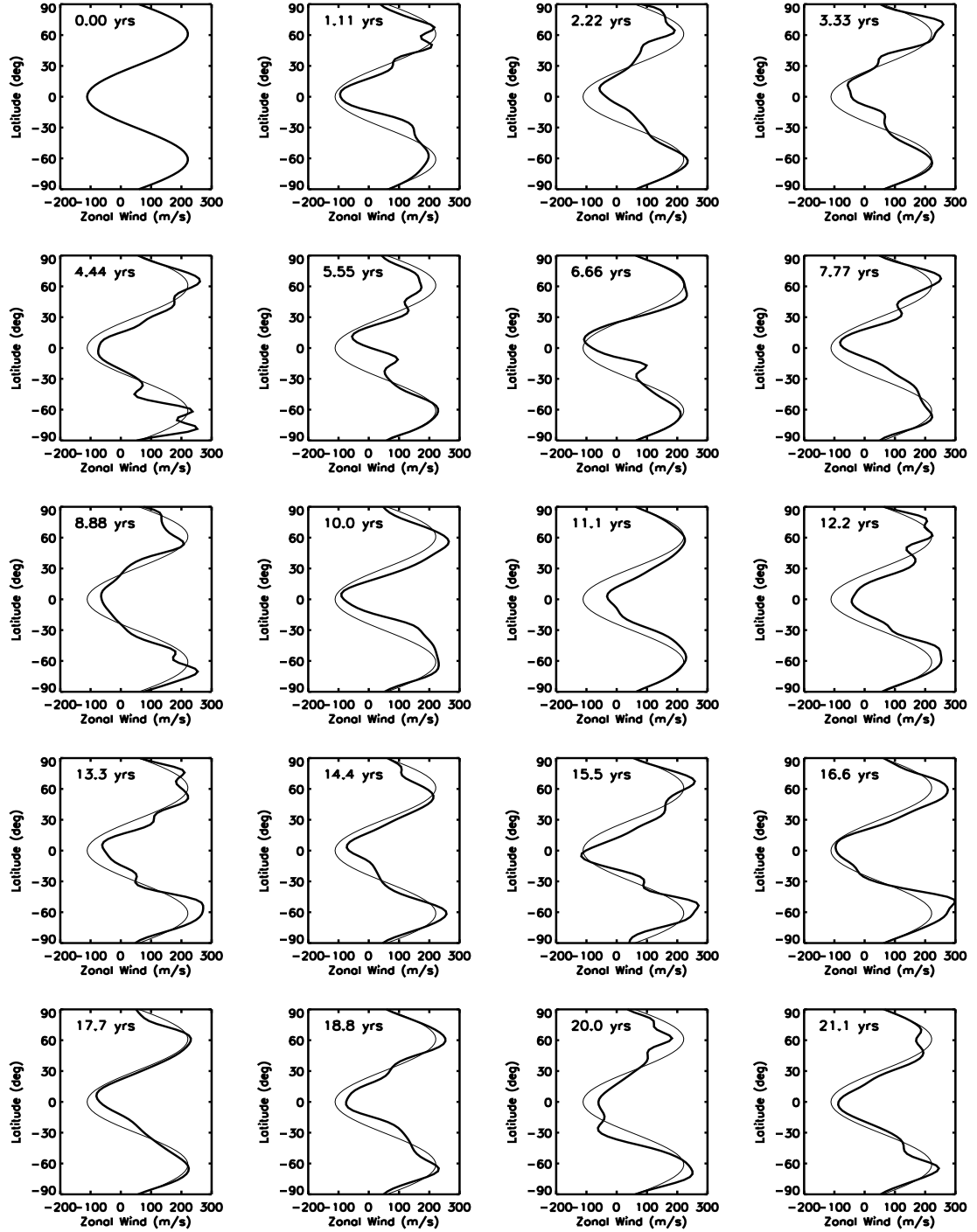


Figure 5.10: Evolution of the zonal wind profile starting from Smith 1986 symmetric fitted profile. This figure is about the two-band simulation case with absorption coefficients in solar radiation waveband $(\alpha/\rho)_{CH_4} = 6.0 \times 10^{-4} \text{m}^{-1} \text{am}^{-1}$, and in infrared waveband $(\alpha/\rho^2)_{H_2-H_2} = 4.0 \times 10^{-5} \text{m}^{-1} \text{am}^{-1}$, $(\alpha/\rho^2)_{H_2-He} = 5.0 \times 10^{-5} \text{m}^{-1} \text{am}^{-1}$ and $(\alpha/\rho^2)_{H_2-CH_4} = 3.0 \times 10^{-3} \text{m}^{-1} \text{am}^{-1}$. The layer setup is the one in Table 5.2 and the initial methane relative humidity is 0.6.

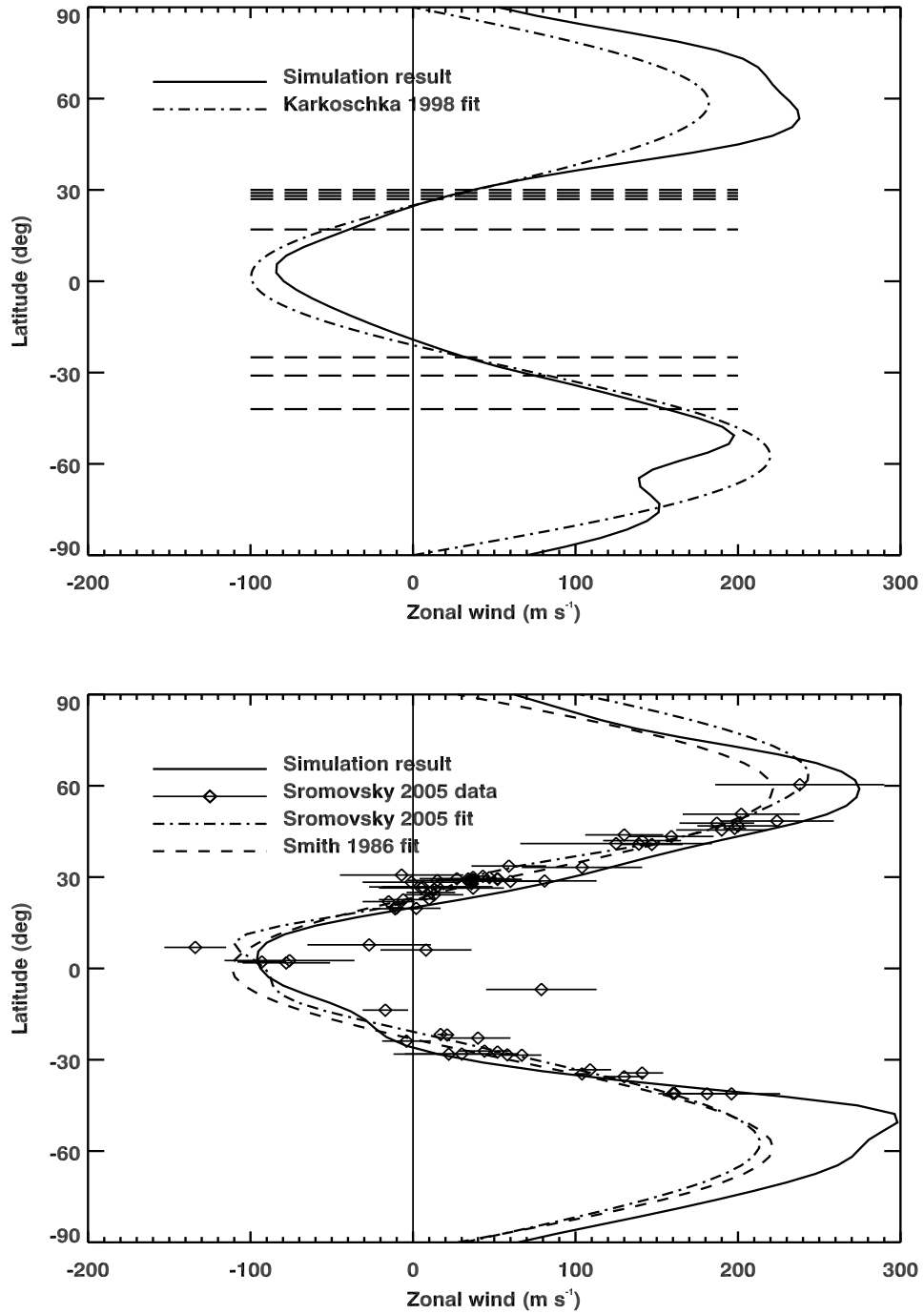


Figure 5.11: Comparison of simulation result with observational results. The upper panel compares the results to the Karkoschka observational result in 1997 and fitted curve in 1998[42]. The dashed straight lines are at the latitudes of observations. The lower panel compares the results to the observational (2003) points and fitted profile by Sromovsky and Fry in 2005[95]. This figure is about the same case as in Figure 5.10.

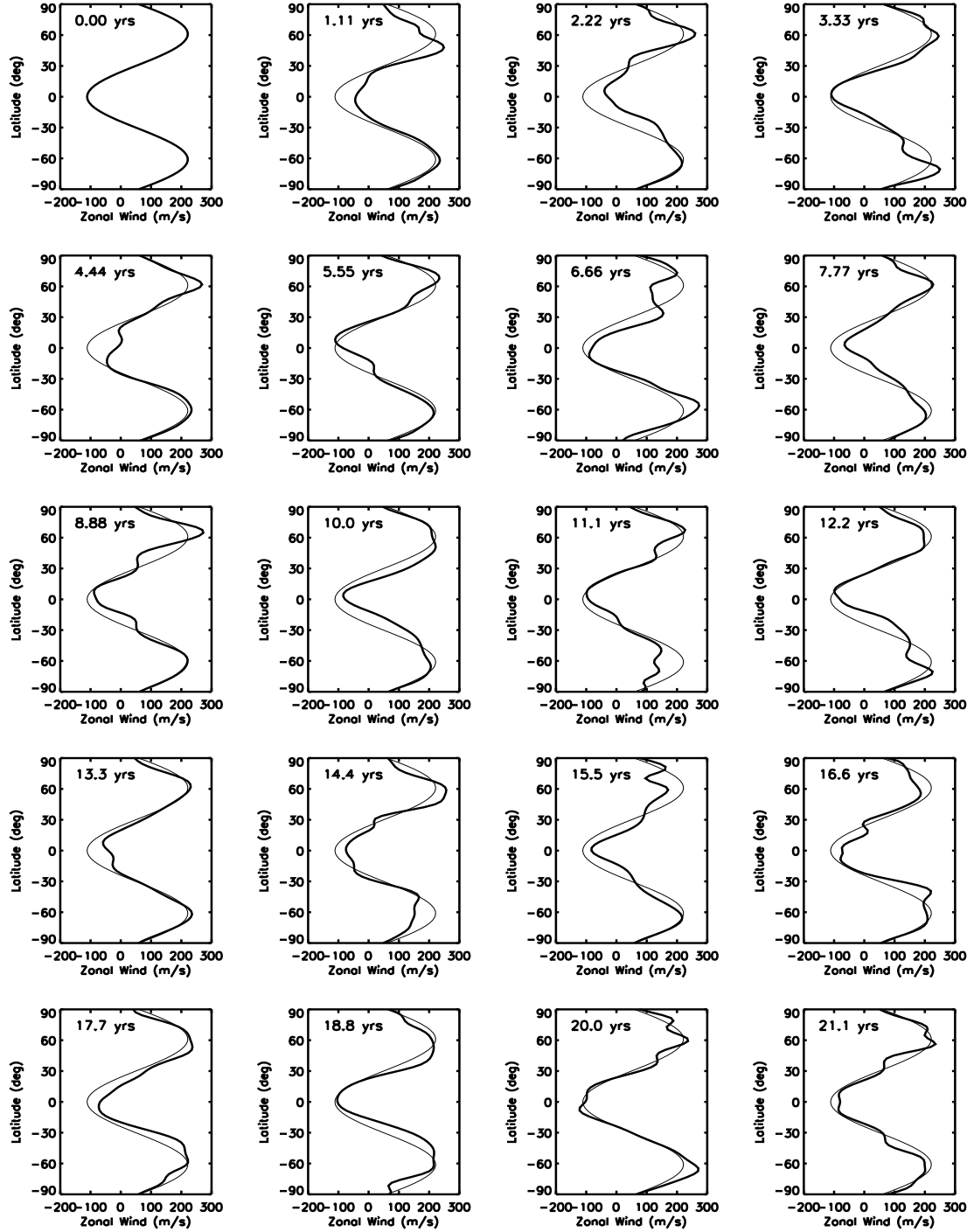


Figure 5.12: Evolution of the zonal wind profile starting from Smith 1986 symmetric fitted profile. This figure is about the two-band simulation case with absorption coefficients in solar radiation waveband $(\alpha/\rho)_{CH_4} = 6.0 \times 10^{-4} \text{m}^{-1} \text{am}^{-1}$, and in infrared waveband $(\alpha/\rho^2)_{H_2-H_2} = 4.0 \times 10^{-5} \text{m}^{-1} \text{am}^{-1}$, $(\alpha/\rho^2)_{H_2-He} = 5.0 \times 10^{-5} \text{m}^{-1} \text{am}^{-1}$ and $(\alpha/\rho^2)_{H_2-CH_4} = 3.0 \times 10^{-3} \text{m}^{-1} \text{am}^{-1}$. The layer setup is the one in Table 5.2 and the initial methane relative humidity is 0.8.

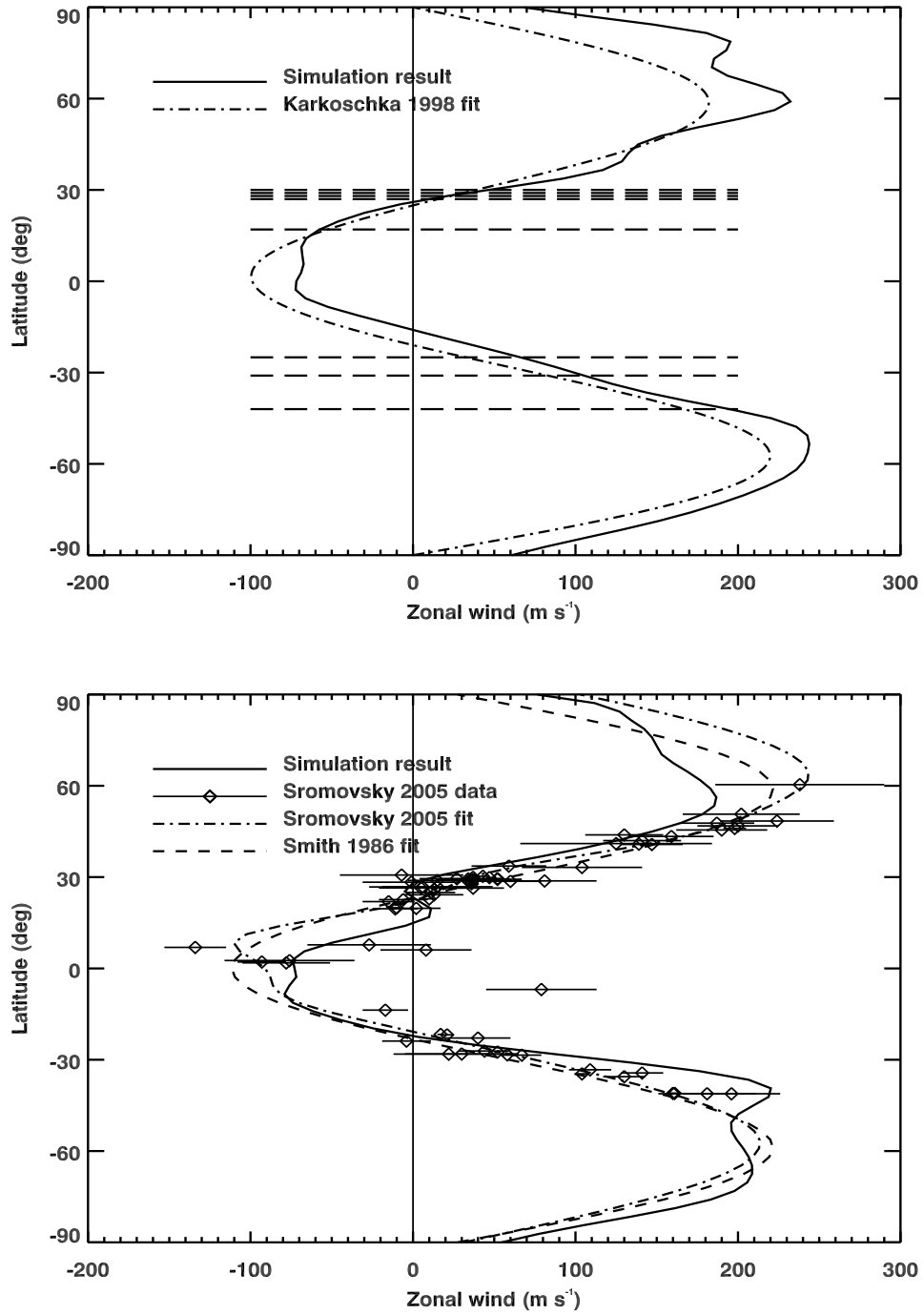


Figure 5.13: Comparison of simulation result with observational results. The upper panel compares the results to the Karkoschka observational result in 1997 and fitted curve in 1998[42]. The dashed straight lines are at the latitudes of observations. The lower panel compares the results to the observational (2003) points and fitted profile by Sromovsky and Fry in 2005[95]. This figure is about the same case as in Figure 5.12.

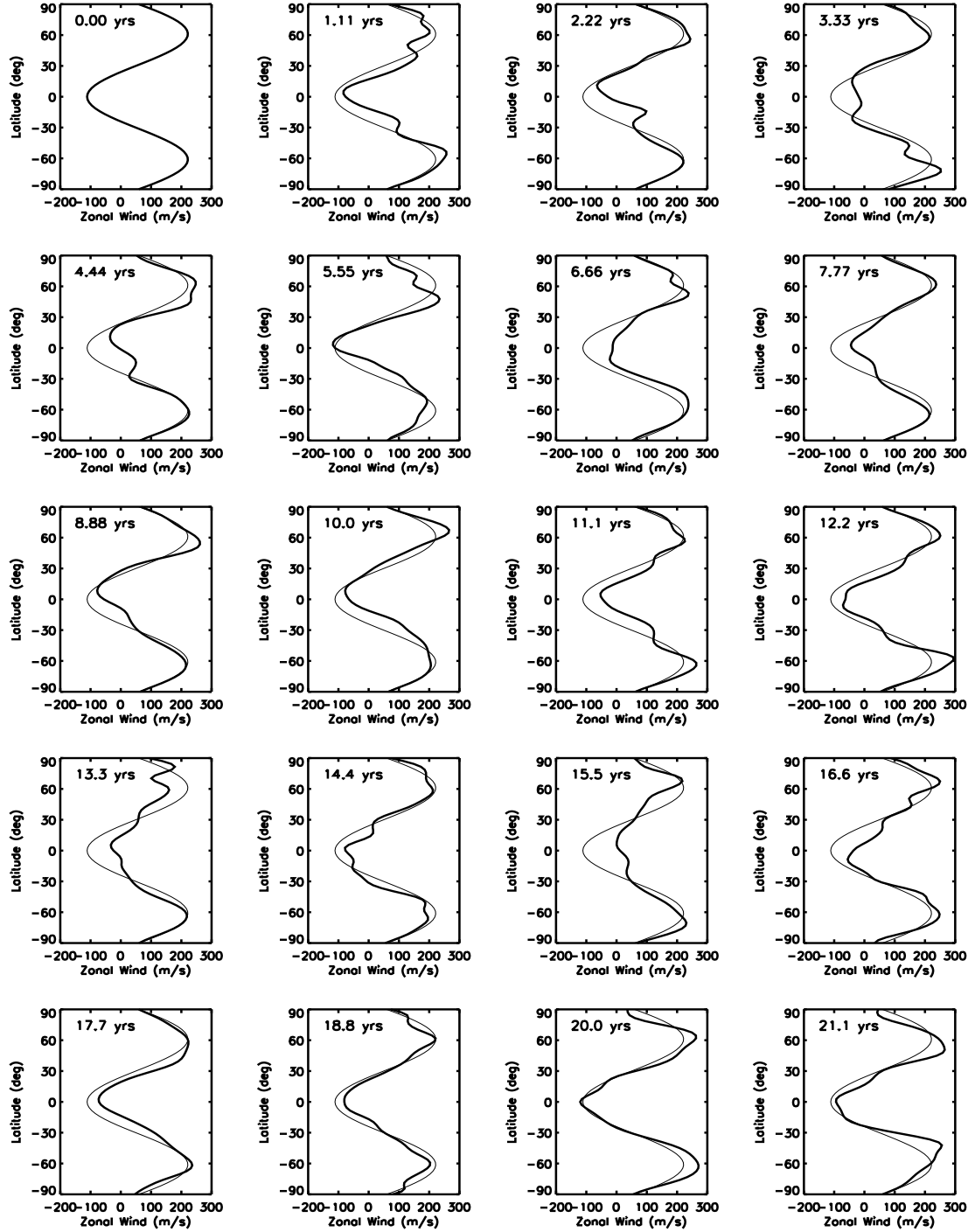


Figure 5.14: Evolution of the zonal wind profile starting from Smith 1986 symmetric fitted profile. This figure is about the two-band simulation case with absorption coefficients in solar radiation waveband $(\alpha/\rho)_{CH_4} = 4.0 \times 10^{-4} \text{m}^{-1} \text{am}^{-1}$, and in infrared waveband $(\alpha/\rho^2)_{H_2-H_2} = 4.0 \times 10^{-5} \text{m}^{-1} \text{am}^{-1}$, $(\alpha/\rho^2)_{H_2-He} = 5.0 \times 10^{-5} \text{m}^{-1} \text{am}^{-1}$ and $(\alpha/\rho^2)_{H_2-CH_4} = 3.0 \times 10^{-3} \text{m}^{-1} \text{am}^{-1}$. The layer setup is the one in Table 5.2 and the initial methane relative humidity is 0.6.

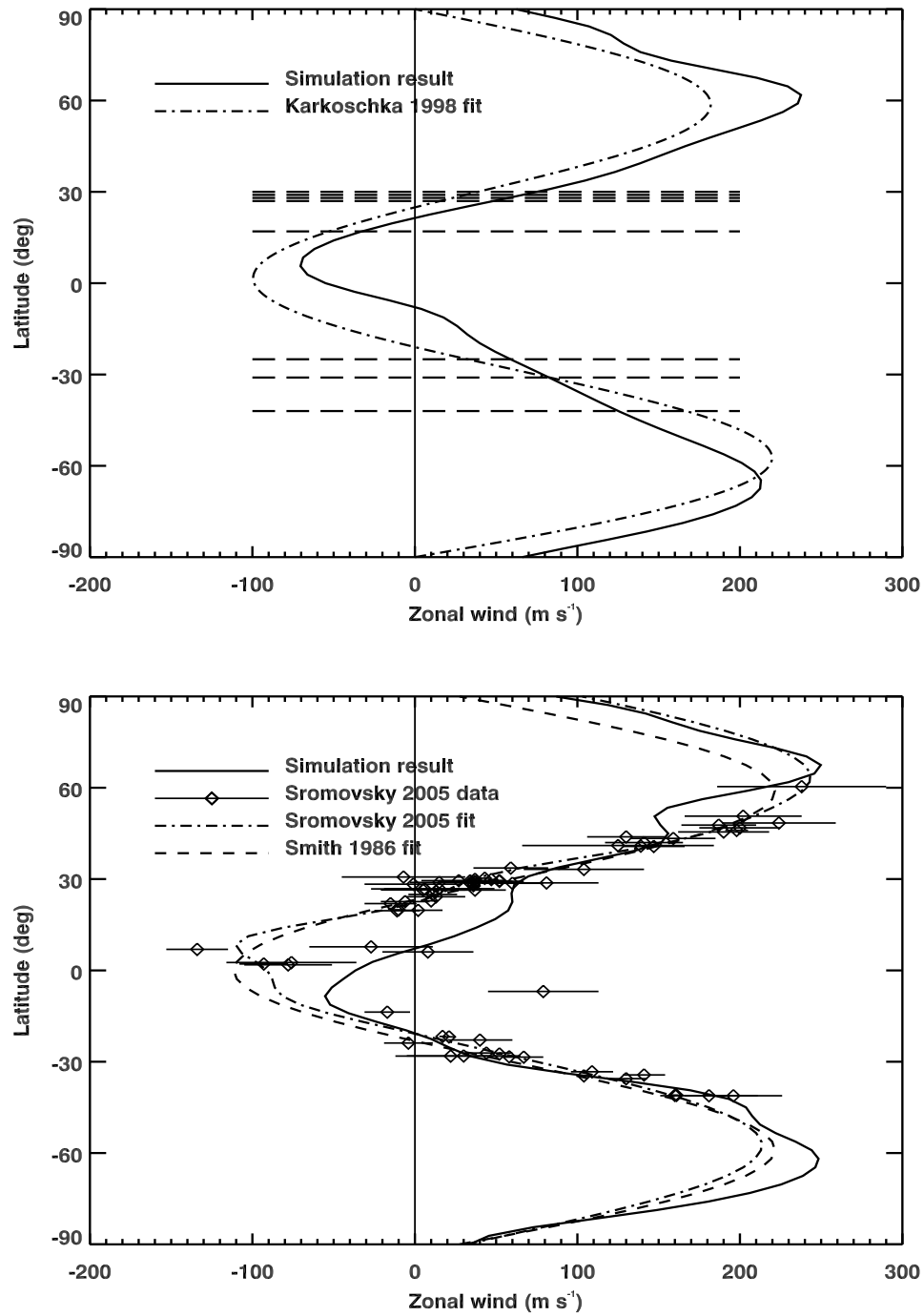


Figure 5.15: Comparison of simulation result with observational results. The upper panel compares the results to the Karkoschka observational result in 1997 and fitted curve in 1998[42]. The dashed straight lines are at the latitudes of observations. The lower panel compares the results to the observational (2003) points and fitted profile by Sromovsky and Fry in 2005[95]. This figure is about the same case as in Figure 5.14.

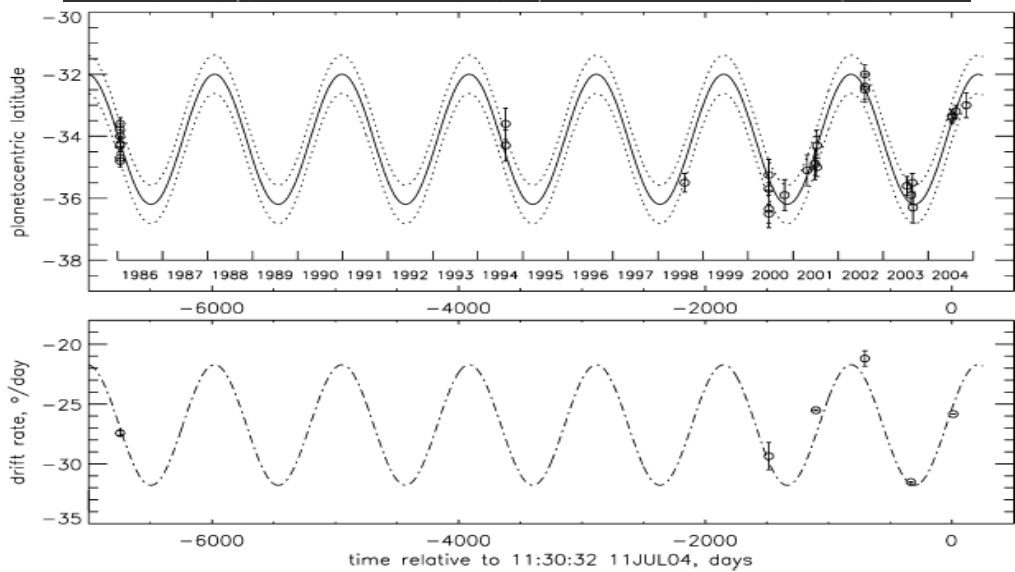
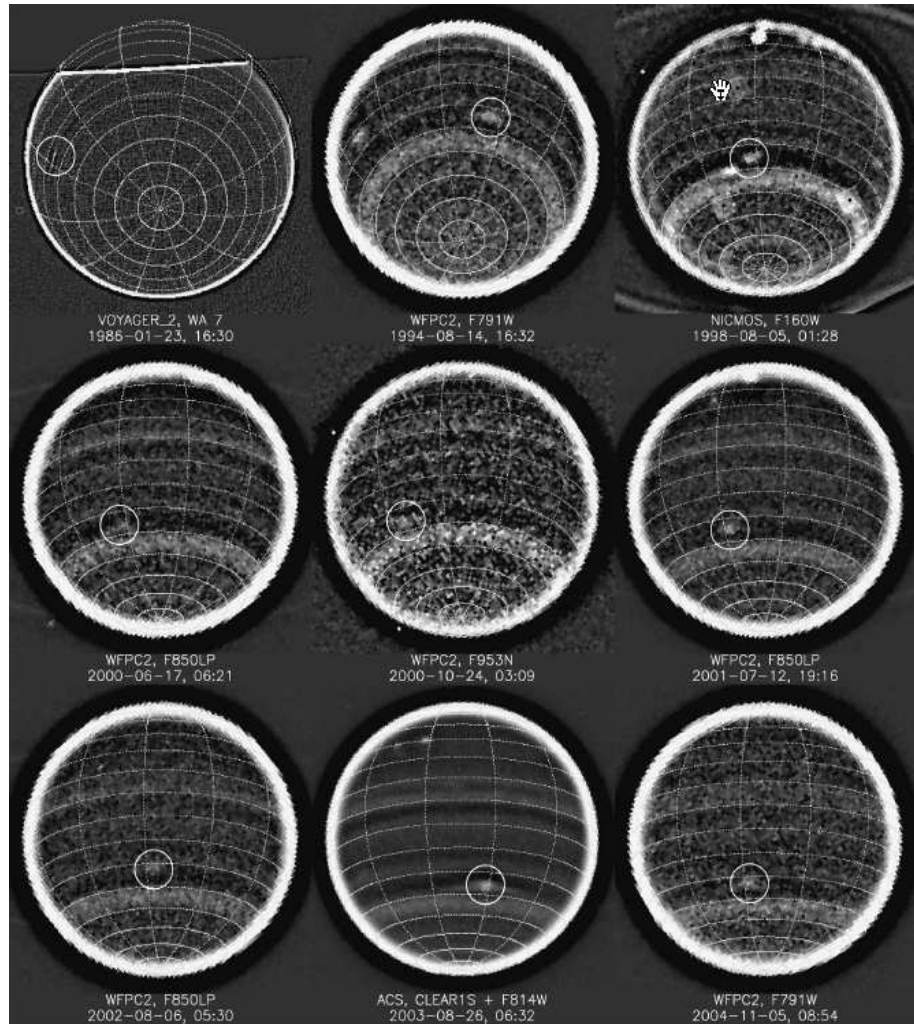


Figure 5.16: The S34 cloud feature (upper panel) and its oscillation (lower panel) plots from Sromovsky and Fry 2005[95].

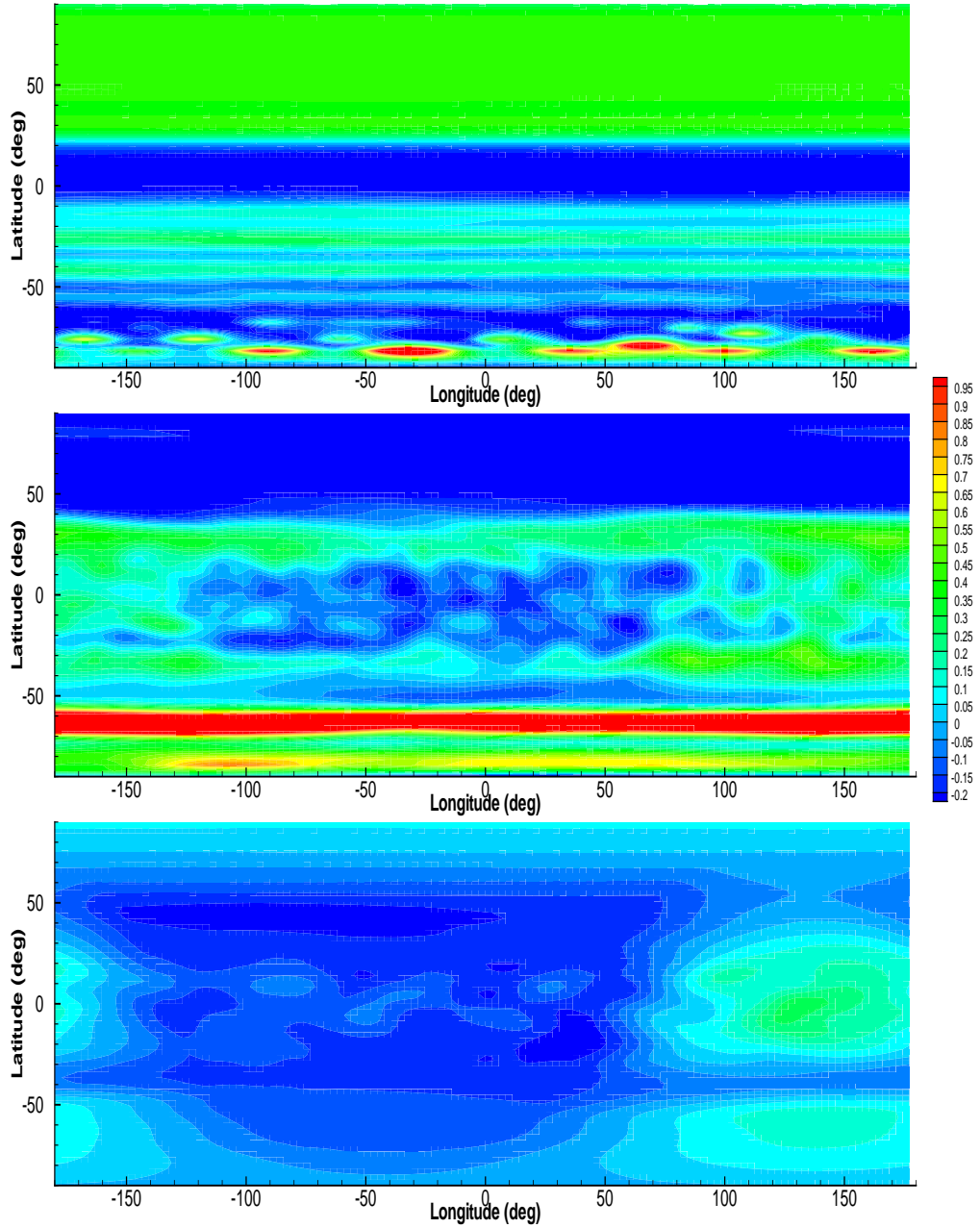


Figure 5.17: Heat distribution in the simulation with radiation model on Uranus. Upper panel is at 5.56 days (1986), middle panel is at 1997 and the bottom panel is at 2003. This figure is about the two-band simulation case with absorption coefficients in solar radiation waveband $(\alpha/\rho)_{CH_4} = 6.0 \times 10^{-4} \text{m}^{-1} \text{am}^{-1}$, and in infrared waveband $(\alpha/\rho^2)_{H_2-H_2} = 4.0 \times 10^{-5} \text{m}^{-1} \text{am}^{-1}$, $(\alpha/\rho^2)_{H_2-He} = 5.0 \times 10^{-5} \text{m}^{-1} \text{am}^{-1}$ and $(\alpha/\rho^2)_{H_2-CH_4} = 3.0 \times 10^{-3} \text{m}^{-1} \text{am}^{-1}$. The layer setup is the one in Table 5.2 and the initial methane relative humidity is 0.6.

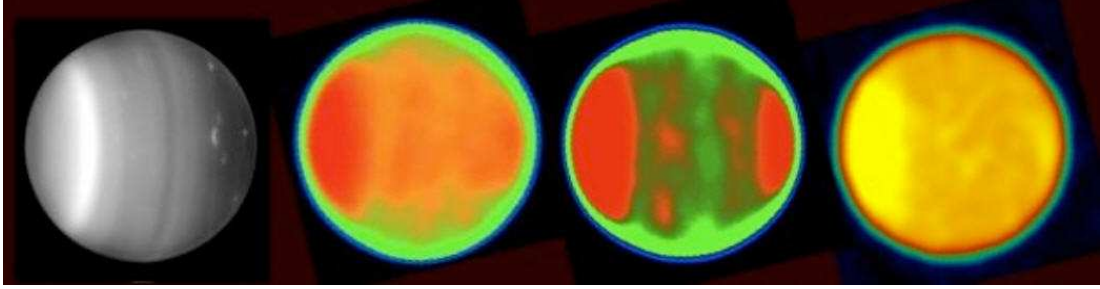


Figure 5.18: Uranus with Keck and VLA at different waveband and different time. The far left picture is taken in 2004 at H-band ($1.6\text{-}\mu\text{m}$); the other three are in 2005 at 0.7cm, 2005 at 1.3cm and 2003 at 2.0cm, respectively. This figure is from Hammel 2006[36].

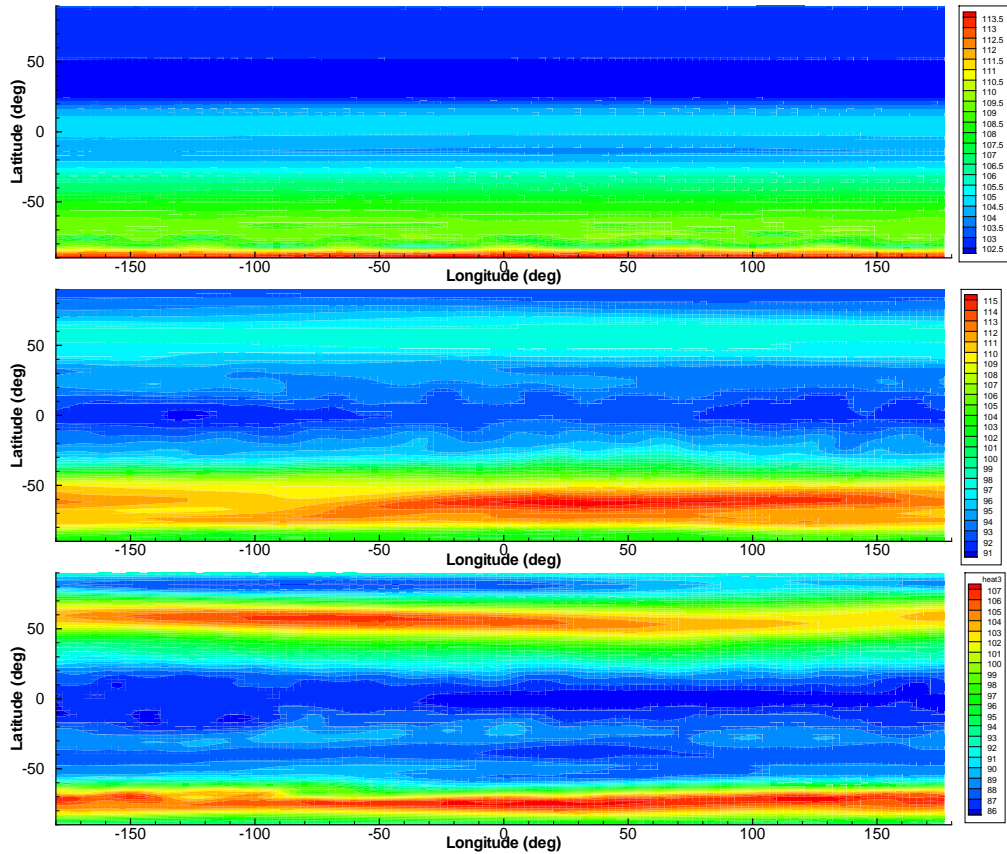


Figure 5.19: Temperature distribution of Uranian atmosphere at layer 6 (2088 mbars) from the simulation with radiation model. Upper panel is at 5.56 days (1986), middle panel is at 1997 and the bottom panel is at 2005. This figure is about the two-band simulation case with absorption coefficients in solar radiation waveband $(\alpha/\rho)_{CH_4} = 6.0 \times 10^{-4}\text{m}^{-1}\text{am}^{-1}$, and in infrared waveband $(\alpha/\rho^2)_{H_2-H_2} = 4.0 \times 10^{-5}\text{m}^{-1}\text{am}^{-1}$, $(\alpha/\rho^2)_{H_2-He} = 5.0 \times 10^{-5}\text{m}^{-1}\text{am}^{-1}$ and $(\alpha/\rho^2)_{H_2-CH_4} = 3.0 \times 10^{-3}\text{m}^{-1}\text{am}^{-1}$. The layer setup is the one in Table 5.2 and the initial methane relative humidity is 0.6.

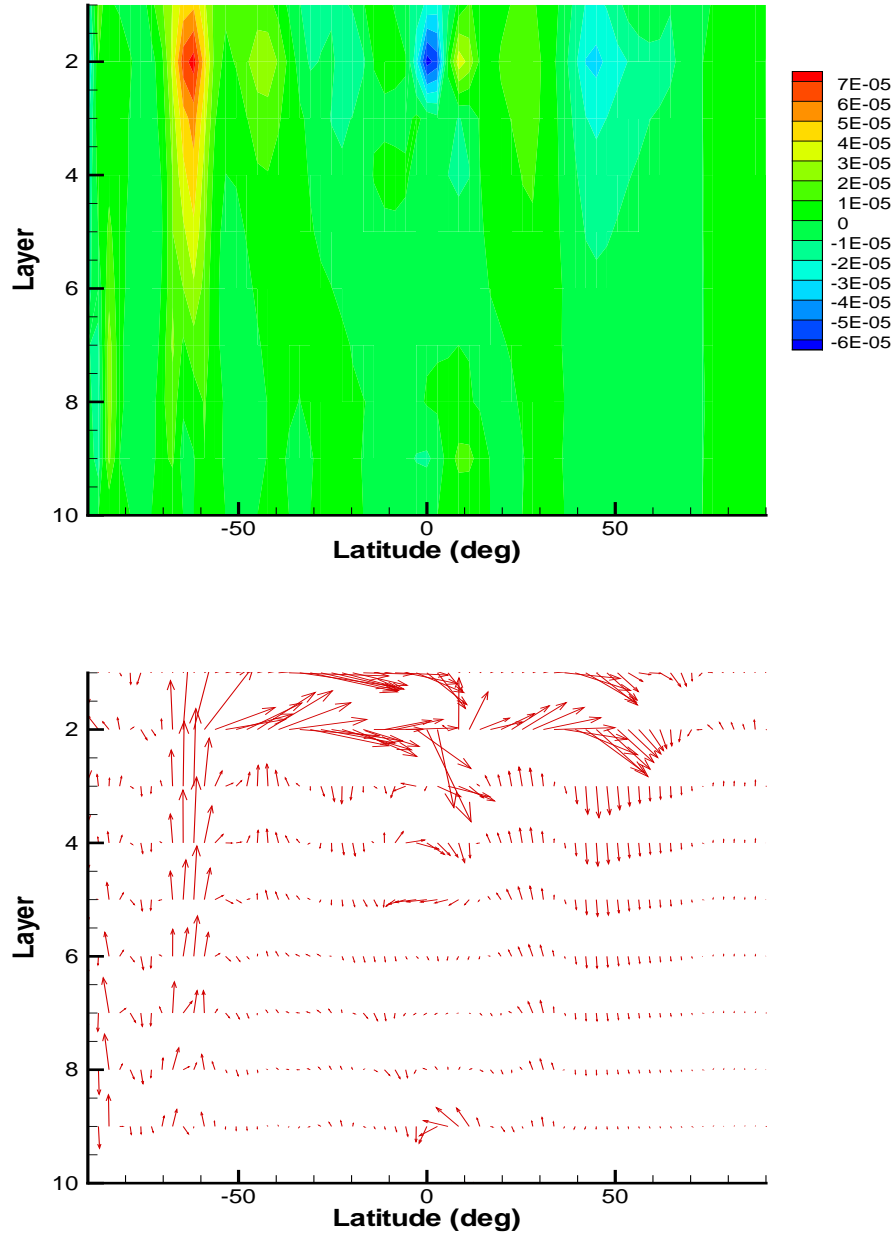


Figure 5.20: Convection in the simulation case with radiation model on Uranus in 1997. The upper panel shows the contour plot of vertical velocity in the unit K (potential temperature). The bottom panel shows the convection velocities. This figure is about the two-band simulation case with absorption coefficients in solar radiation waveband $(\alpha/\rho)_{CH_4} = 6.0 \times 10^{-4} \text{m}^{-1} \text{am}^{-1}$, and in infrared waveband $(\alpha/\rho^2)_{H_2-H_2} = 4.0 \times 10^{-5} \text{m}^{-1} \text{am}^{-1}$, $(\alpha/\rho^2)_{H_2-He} = 5.0 \times 10^{-5} \text{m}^{-1} \text{am}^{-1}$ and $(\alpha/\rho^2)_{H_2-CH_4} = 3.0 \times 10^{-3} \text{m}^{-1} \text{am}^{-1}$. The layer setup is the one in Table 5.2 and the initial methane relative humidity is 0.6.

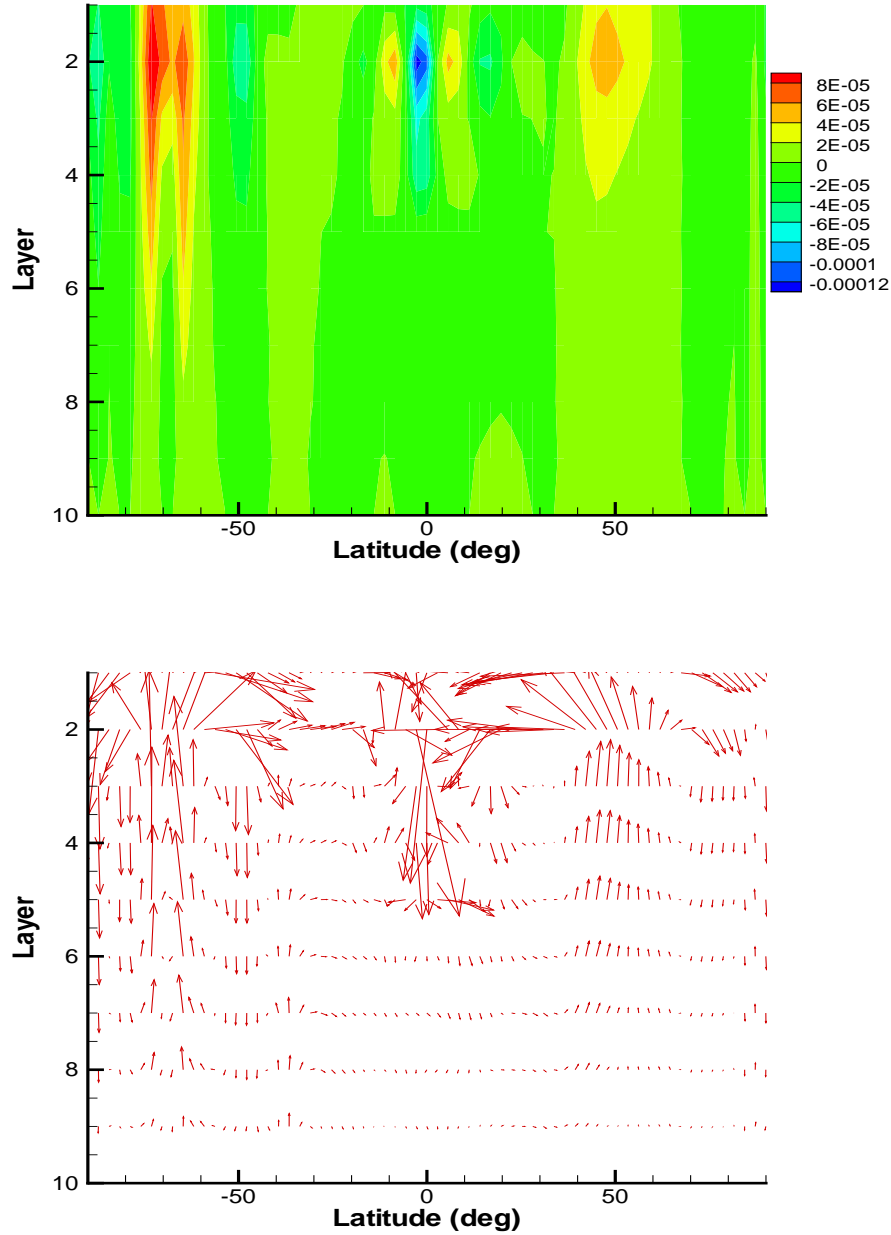


Figure 5.21: Convection in the simulation case with radiation model on Uranus in 2005. The upper panel shows the contour plot of vertical velocity in the unit K (potential temperature). The bottom panel shows the convection velocities. This figure is about the two-band simulation case with absorption coefficients in solar radiation waveband $(\alpha/\rho)_{CH_4} = 6.0 \times 10^{-4} \text{m}^{-1} \text{am}^{-1}$, and in infrared waveband $(\alpha/\rho^2)_{H_2-H_2} = 4.0 \times 10^{-5} \text{m}^{-1} \text{am}^{-1}$, $(\alpha/\rho^2)_{H_2-He} = 5.0 \times 10^{-5} \text{m}^{-1} \text{am}^{-1}$ and $(\alpha/\rho^2)_{H_2-CH_4} = 3.0 \times 10^{-3} \text{m}^{-1} \text{am}^{-1}$. The layer setup is the one in Table 5.2 and the initial methane relative humidity is 0.6.

Chapter 6 Cloud Model and Bright Companion

In planetary atmospheres, many weather phenomena are related to clouds. Cloud companions are frequently observed with Great Dark Spots, for example, GDS-89 and NGDS32, as seen in Chapter 1. Figure 6.1 is from Stratman et al. 2001[98]. It shows the bright companions of NGDS32 in 1994 and 1996. One inverted image of GDS-89 and its bright companion is also shown here in the rightmost panel. Obviously, GDS-89 and NGDS32 both had a poleward bright companion. From Figure 1.9, we can see that the Uranian Dark Spot also had a poleward bright companion, which was even observed earlier than UDS itself. Besides these, in the earth's atmosphere, clouds also accompany hurricanes. How is a cloud formed near a great vortex and if there is any interaction between the cloud and the vortex are two main questions about them. These are the main questions we want to answer with this cloud model.

Uranus and Neptune are gas-giant planets with methane in their atmospheres. Methane is the main component of the observed clouds on these two planets. Earth is a terrestrial planet. Water is the main component of the clouds on the Earth. As we know, the basic mechanism of cloud formation is the methane or water vapor shifting to a region of lower temperature so that the relative humidity increases and the vapor becomes saturated. We know that in the troposphere temperature decreases with altitude. When the atmosphere moved to a mountain and is forced up to higher altitude, the decrease of the temperature will lead to the formation of an orographic cloud. The basic idea is that when a great vortex moves in the atmosphere, similar mechanism will work and lead to the formation of clouds. At the same time, when the vapor becomes liquid, the density of the atmosphere will decrease and latent heat will be released. These could affect the dynamical behavior of the great vortex.

In this chapter, I first study the great dark spots and their companions in Nep-

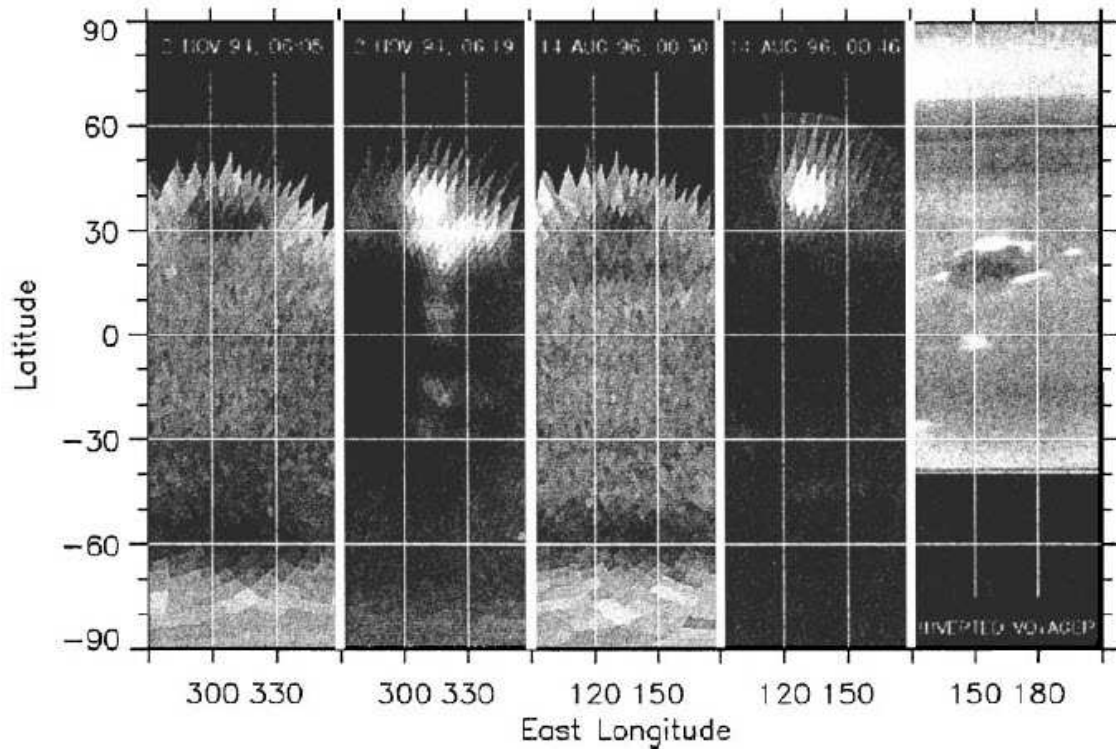


Figure 6.1: Observed bright companions to Neptune’s Great Dark Spots. The left four panels are NGDS32 and its bright companion in 1994 and 1996. The rightmost panel is about GDS-89 and its bright companion, inverted across the equator, for comparison. This figure is from Stratman et al. 2001[98].

tune’s atmosphere. A methane cloud model is imported to simulate the bright companions and study the interaction between the cloud and the great dark spot. GDS-89 and its bright companion are the two main simulated objects. After this, because of the similarity of the atmospheres of Neptune and Uranus, this cloud model is imported to simulate the UDS and its bright companion.

The first work with a cloud model in EPIC was presented in Stratman et al. 2001[98]. They included methane vapor in the planetary atmosphere, and used a Gaussian shape Montgomery potential (see Chapter 2) to generate a GDS-like vortex. Then they studied the saturation of methane around this great dark spot and used relative humidity 100% as the critical value. At last, they got orographic cloud formation in their simulations. In this simple model, they did not include phase

changes. They also did not study the evolution of the GDS and the dynamical interaction between the cloud and the GDS.

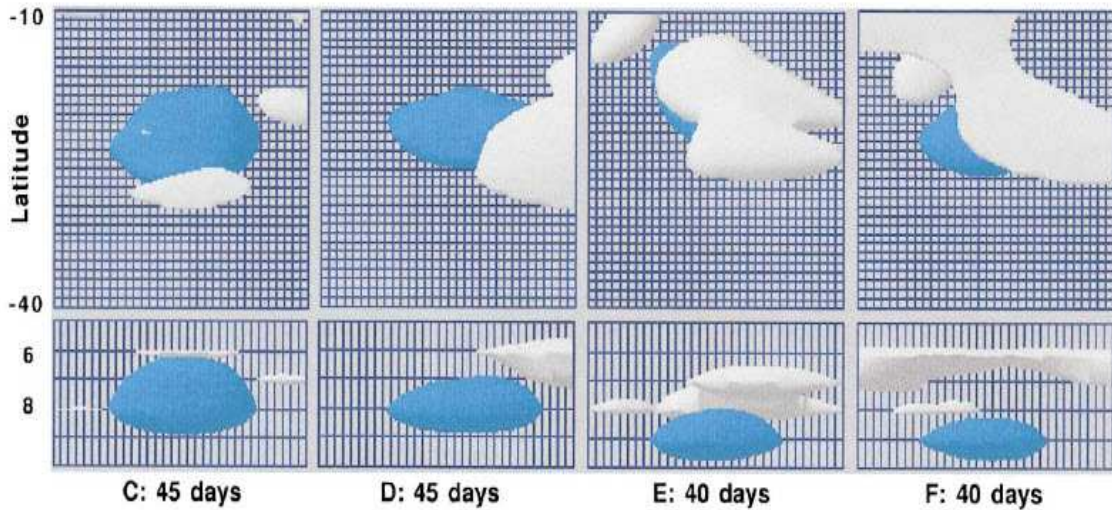


Figure 6.2: Stratman's simulated bright companions to great dark spots. C, D, E, F are cases with different vortex heights at different vortex center layers. This figure is from Stratman et al. 2001[98].

Figure 6.2 shows the simulation results of the simple methane cloud model in Stratman et al. 2001[98]. Great dark spots pushed the atmosphere to higher altitude (lower temperature, therefore lower saturation vapor pressure) so that the cloud was generated in the higher layers above the great dark spot. When the GDS is in a deeper layer, more clouds were generated.

In 2008, Palotai and Dowling imported an integrated cloud model in EPIC[75]. Figure 6.3 shows the scheme of the EPIC microphysics model from Palotai and Dowling 2008[75]. They applied their model to the water cloud and ammonia cloud on Jupiter.

The current work combines the methane methods from Stratman and the model from Palotai. We also adopt our previous simulation results about the GDS on Neptune. In this way, we can generate the methane cloud and study the interaction between the cloud and the GDS.

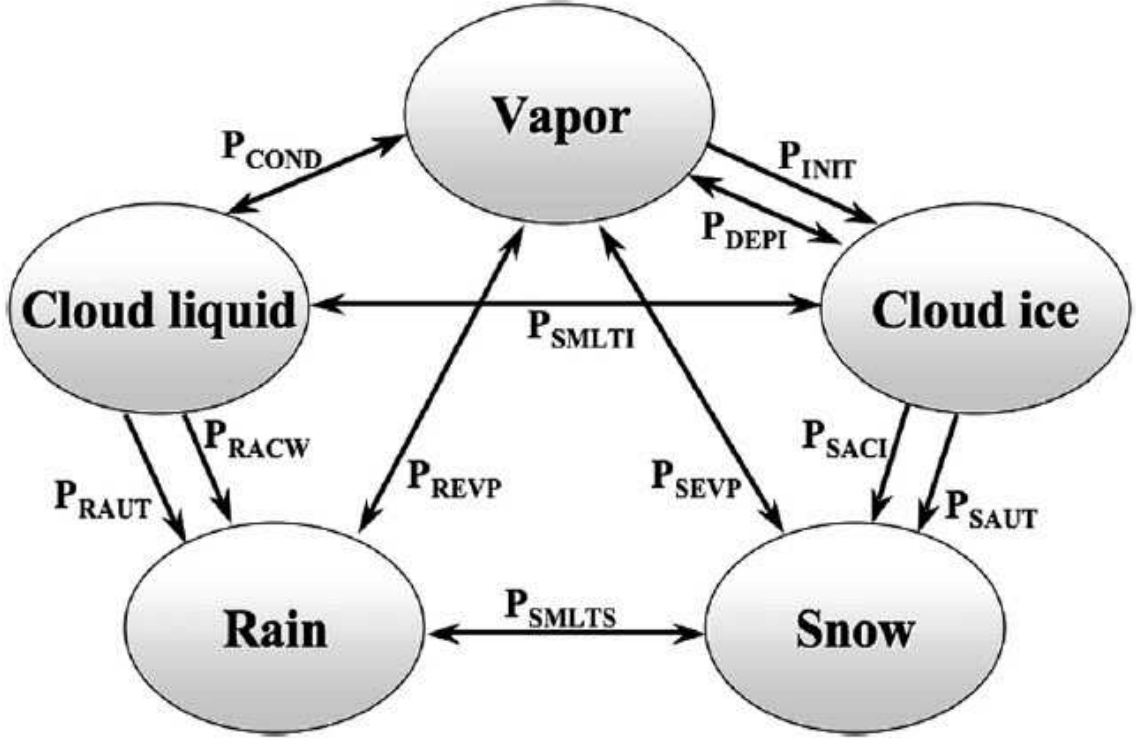


Figure 6.3: The scheme of the five phases and related eleven phase-change processes in the EPIC microphysics model. The processes are: P_{COND} : condensation of vapor to cloud liquid and evaporation of liquid cloud, P_{INIT} : initiation of ice crystals, P_{DEPI} : deposition of vapor onto ice crystals and sublimation of cloud ice to vapor, P_{SMLTI} : melting of cloud ice to form cloud liquid, P_{RACW} : collection of cloud liquid droplets by rain, P_{RAUT} : autoconversion of cloud liquid droplets to rain, P_{REVP} : evaporation of rain, P_{SEVP} : sublimation and depositional growth of snow, P_{SMLTS} : melting of snow to form rain, P_{SACI} : collection of cloud ice crystals by snow, and P_{SAUT} : autoconversion of cloud ice crystals to snow. This figure and its explanation are from Palotai and Dowling 2008[75].

6.1 Initial Methane Distribution

The initial methane distribution method is adapted from Stratman et al. 2001[98]. This work first adopts the solar C/H number fraction 0.000398 from Grevesse and Anders 1991[27]. On Neptune, they use H_2 number fraction 81% and He number fraction 19% so that $H_2 + He = H_2/0.81$. Also, because CH_4 is much less than H_2 , the number ratio $CH_4/H_2 \sim C/H_2$ and so $CH_4/H_2 \sim 2C/H$. Then the calculated solar

benchmark is[98]:

$$\frac{CH_4}{H_2 + He + CH_4} = \frac{1}{\frac{1}{0.81} \frac{1}{2C/H} + 1} = 0.00064, \quad (6.1)$$

which corresponds to a solar composite. Moreover, Baines et al. 1995[5] shows that the methane molar fraction range is between 0.016 and 0.027 in Neptune’s deep troposphere, which is 33 ± 9 times the above calculated solar benchmark methane molar fraction. So, we simply use a methane molar fraction of 33 times of the solar value when we initialize the methane component in EPIC in our simulations.

Another parameter is the initial relative humidity. We assume a initial background with constant relative humidity. In our simulations, we normally use the value 0.6 or 0.8 for the initial constant relative humidity.

With these parameters, at each grid point, the methane saturation vapor pressure is calculated with the parameters and equation from Lodders and Fegley 1998[57]:

$$\begin{aligned} P_{sat-vapor} &= 10^{a_s+b_s/T}, T < T_{triple}, \\ P_{sat-vapor} &= 10^{a_l+b_l/T}, T \geq T_{triple}. \end{aligned} \quad (6.2)$$

Here $a_s = 9.283$, $b_s = -475.6$, $a_l = 9.092$ and $b_l = -459.8$ for methane. The variable T_{triple} is the vapor-liquid-solid triple point temperature, which for methane is 88.7K. The variable T is the local temperature. Using this saturation vapor pressure and the initial relative humidity, local methane vapor pressure can be calculated and so that its fraction can be determined. As stated previously, 33 times the solar value is the upper limit of this initial methane molar fraction in our simulations. At higher altitude (lower pressure) in the troposphere, temperature is lower (look at the P-T profile), and the saturation vapor pressure is also lower so the methane molar fraction can also be lower.

6.2 Microphysics

In this work, we realized the P_{INIT} process in the scheme shown in Figure 6.3. When the local methane vapor is saturated (relative humidity > 1), the supersaturated part will be converted to the cloud ice phase. This is the main phase change when the Neptune’s atmosphere raises near the dark spots. Because of the low temperatures near the GDS at around $60K$ (see Table 6.1), no methane liquid can exist in this region. Currently, latent heat effects are not included.

6.3 Realizing the Cloud Model in the EPIC GCM

The main subroutine used to calculate the microphysics of cloud in the EPIC GCM is `cloud_microphysics`, which is in the file `epic_microphysics.c`, called by the subroutine `source_sink`. This is controlled by the parameter `grid.microphysics_on`. When this parameter is turned on (with value 1), the subroutine `cloud_microphysics` will be calculated.

Our work is based on the previous work of Stratman et al. in 2001[98]. The arrays for methane vapor, methane liquid and methane ice have already been included in the EPIC GCM. The initialization of methane based on the discussion above is in the subroutine `init_species`, which is in the file `epic_init_funcs.c`. The calculation of the relative humidity (subroutine `relative_humidity`) at the bottom of each layer for different species is calculated based on the saturation pressure at the local temperature. These are controlled by the species parameter `CH_4_INDEX`.

In the subroutine `cloud_microphysics`, the relative humidity of the local grid (call the subroutine `relative_humidity`) is calculated first. With this result, the supersaturation of methane can be calculated. Considering the phase change of methane under the condition of supersaturation, the humidity quantity (HQ) can be calculated by subtracting the supersaturation part. Finally, in the subroutine `timestep.c`, before

the end of each time step, the subroutine `relative_humidity` is called again to retrieve the data to the array `RI2`, which will be stored in the extract files when it is turned on. Currently, the latent heat and more phase changes have not been realized. These will be done in the future.

6.4 Zonal Wind Profile

We apply the simulation results from Chapter 3. From those simulations, we know that to maintain a stable great dark spot, the local absolute vorticity should be near constant. We also want to simulate the cloud formation near a oscillating great vortex and check the effects of the cloud to the vortex. Therefore, we choose the zonal wind profile with $Q_y = 1/12$ between 28°S and 38°S, reference latitude 24°S, and transiting smoothly to both ends, as the dash dotted curve shown in Figure 6.4.

6.5 Other Parameters

The vertical P-T profile used here is the $N^2 = 0.64 \times 10^{-4} s^{-2}$ profile shown in Figure 2.5. To generate the great dark spot in the atmosphere, we still use the method described in Chapter 3 of perturbing the Montgomery potential. The parameters used for the initial spot generation are: relative size 0.8, relative strength 0.6, initial aspect ratio 1.5 and starting latitude 29°S.

The simulation domain is the whole globe. The horizontal grids are 512×256 (Longitude×Latitude) with grid spacing of 0.7°. There are ten vertical layers with an upper boundary at 2.3mbar and a lower boundary at 7435 mbars. The ten layers at latitude -89.2° and longitude -179.6° are shown in Table 6.1. The time step used is 60 seconds. With these parameters and 8 nodes/16 cores of KFC6I, we can simulate about one month in three real days.

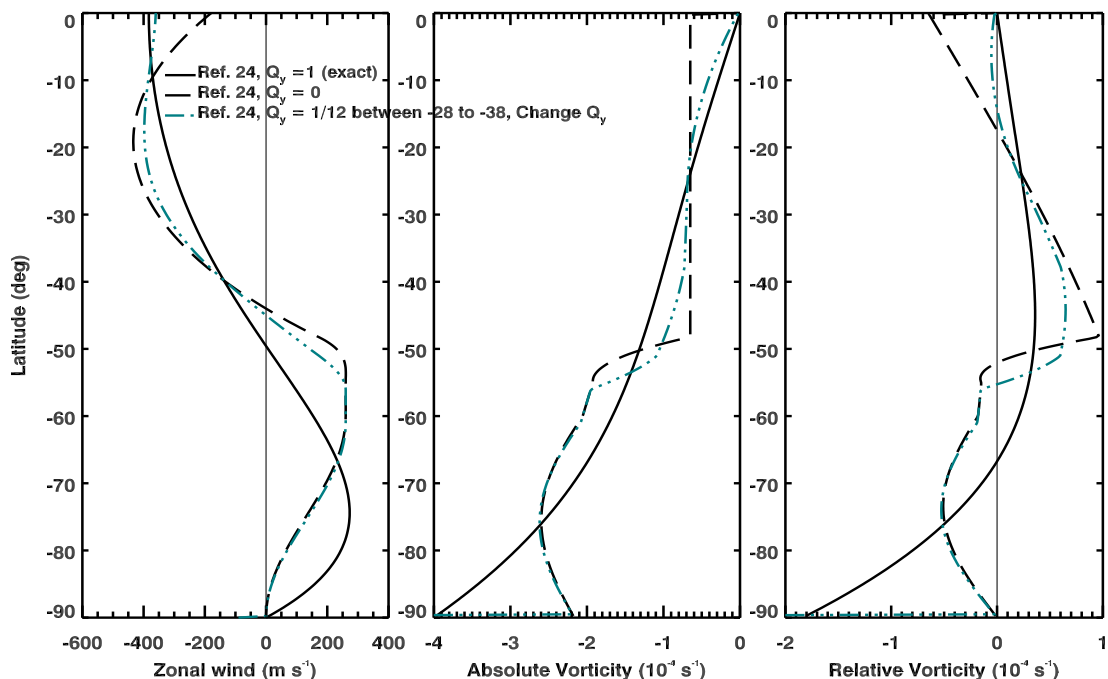


Figure 6.4: Three zonal wind profiles on Neptune. The left panel shows the zonal wind profile; the middle panel shows the related absolute vorticity, and the right one shows the relative vorticity. The solid curve is the fitted zonal wind profile from Sromovsky et al. 1993[91]. The dashed curve is the artificial $Q_y = 0$ case, which has a constant absolute vorticity from 0° to 48°S in the middle panel. The dash dotted curve is the artificial zonal wind profile used in this work. It has near constant absolute vorticity $Q_y = 1/12$ from 28°S to 38°S , with reference latitude 24°S . At the southern end, it merges smoothly to the $Q_y = 0$ case; at the northern end, it merges smoothly to the equator. The zonal wind profile has zero potential vorticity at the equator and the poles.

6.6 Simulation Results

Generated Cloud on Neptune

With initial relative humidity 80% and centers the vortex at layer 7 (~ 868 mbar, see Table 6.1), some cloud features are generated in layer 5 (~ 266 mbar). Figure 6.5 shows the result of this simulation. The main cloud is on the south of the great dark spot and some small features are around it.

Decreasing the initial relative humidity to 60%, in Figure 6.6, the cloud feature

Table 6.1: The 10 layers setup on Neptune in the cloud model simulations

Layer	ζ [K]	P [mbar]	T [K]	θ [K]	N^2 [1/s ⁻²]
1.0	926.8	4.86523e+00	108.0	926.8	0.000411
2.0	345.6	1.76663e+01	68.7	345.6	0.000378
3.0	176.4	5.73250e+01	56.2	176.4	0.000388
4.0	115.6	1.50029e+02	54.1	115.6	0.000173
5.0	95.9	2.65714e+02	56.4	95.9	0.000261
6.0	85.1	4.53318e+02	61.9	85.1	0.000075
7.0	77.3	8.67576e+02	74.1	78.7	0.000063
8.0	64.1	1.63586e+03	87.0	71.9	0.000061
9.0	57.9	3.04325e+03	100.2	65.1	0.000056
10.0	51.6	5.66144e+03	113.7	58.2	0.000058

1. ζ is the hybrid vertical coordinate.
2. θ is the potential temperature.
3. N^2 is the square of the Brunt-Väisälä frequency (buoyancy frequency).

is more distinct. A single well-defined poleward cloud is above the great dark spot. We can see some other small cloud features around the great vortex, especially in the initial relative humidity 80% case. This is because the simulated great vortex generates waves in the whole globe. The main stable cloud feature is that one above the south of the dark spot.

Keeping the initial relative humidity 60% and placing the dark spot at a deeper layer (layer 8, ~ 1636 mbar, see Table 6.1) yields the result shown in Figure 6.7. In this case, we can still see a well-defined cloud above the south of the dark spot. This cloud is larger than that one in the upper layer case (Figure 6.6). In addition, there are more small cloud features around the Great Dark Spot.

These results suggest that a moderate background relative humidity may reflect the real world in the Neptune's atmosphere. Also, a vortex centered more deeply in the atmosphere will generate more clouds than a higher one, which agrees with the results in the Stratman et al. 2001[98].

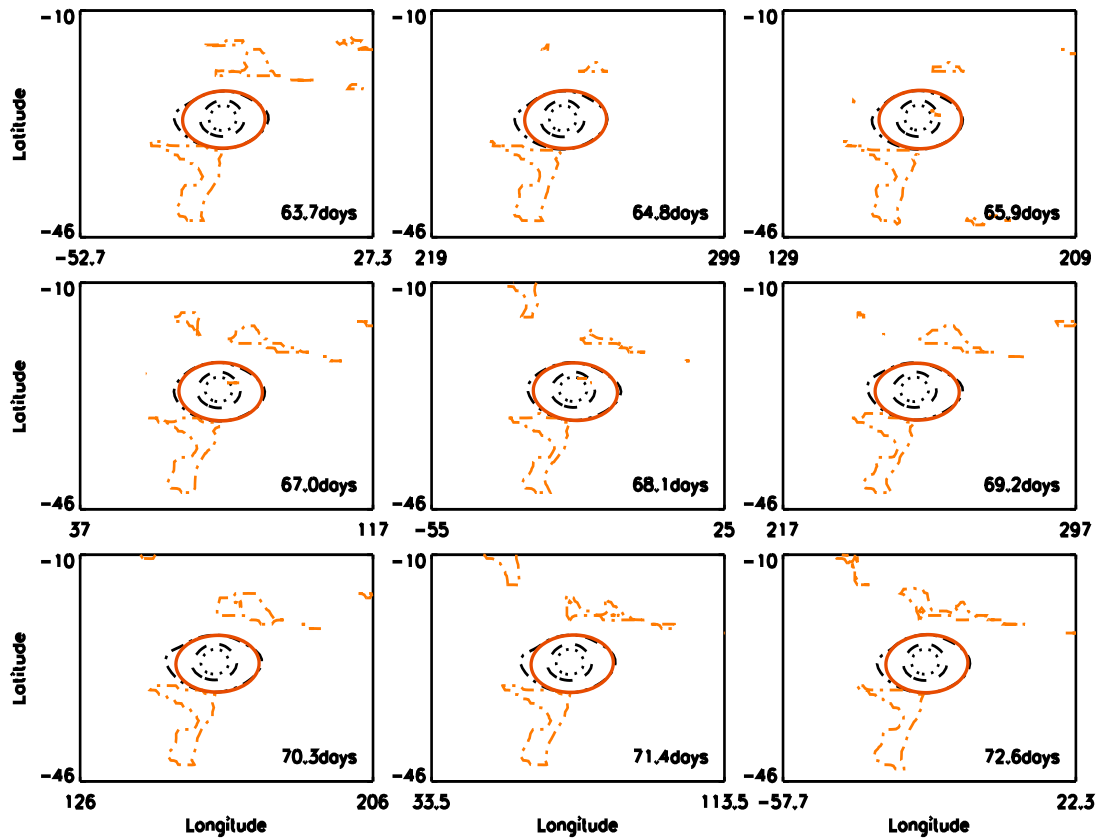


Figure 6.5: Simulated great dark spot and the cloud features around it, with initial relative humidity 80%. Spot is at layer 7 and the cloud is at layer 5. The dotted, dashed and dash-dotted curves near the center are the contour plots of the potential vorticity. The solid ellipse curve is the fitting ellipse to the contour shape, which is used to calculate the aspect ratio and the orientation angle. The orange dash-dotted curves around are the methane relative humidity contour at saturation level - 1.0.

Figure 6.8 shows the evolution of the cloud features near a GDS. We can see that after 29.44 days, a stable cloud is formed above the southern portion of the GDS.

Effect of the Cloud to the GDS

As mentioned before, Stratman et al. 2001[98] shows orographic cloud formation above a GDS. But they did not study the effects of the cloud model on the GDS motions. In our work, through studying the drift rates and the oscillations of the Great Dark Spots, we found that not only the GDSs have effect on the clouds generation,

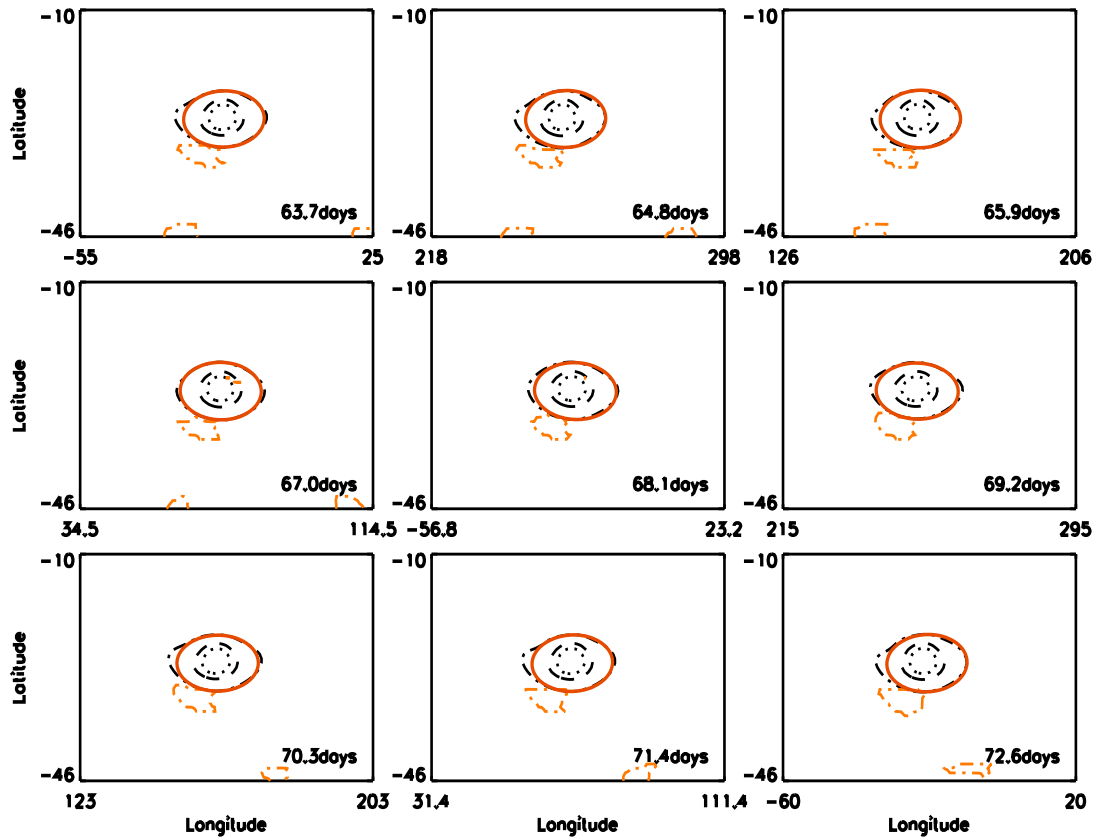


Figure 6.6: Simulated great dark spot and the cloud features around it, with initial relative humidity 60%. Spot is at layer 7 and the cloud is at layer 5. The meaning of the curves is same as that in Figure 6.5.

the clouds also have their effect on the evolution of the great dark spots.

Figure 6.9 shows the drift rates of five cases. The deeper spot without cloud case (solid) shows strong instability after 50 days. Including clouds (dashed, dash-dot) result in more stable behavior without changing the drift rate. The dotted line is about the spot in upper layer without clouds. Obviously, upper layer leads to better stability and smaller oscillations. Including the cloud model (dash-dot-dot-dot) still does not change the drift rate.

Figure 6.10 shows the effect of the cloud on the oscillation of the great dark spot in deeper layers. In this case, without clouds, the GDS oscillate unsteadily and the amplitude becomes erratic and irregular after two months. Also, the inverse aspect

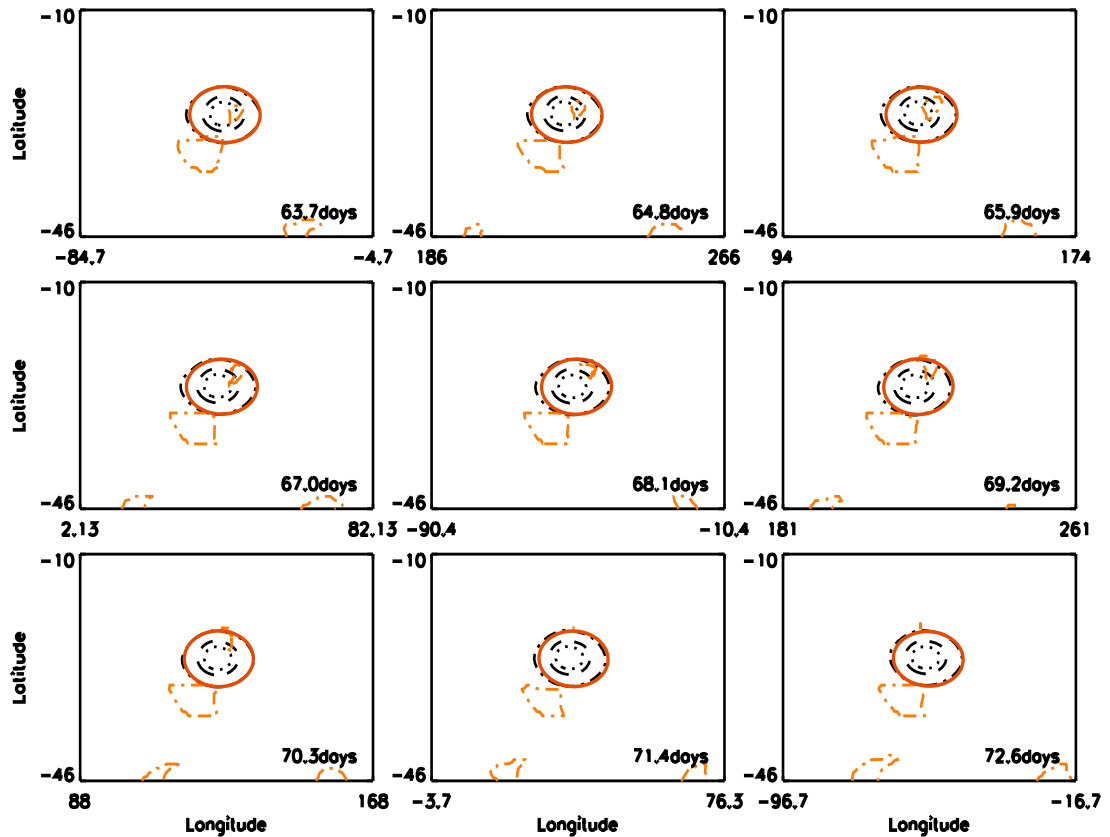


Figure 6.7: Simulated great dark spot and the cloud features around it, with initial relative humidity 60%. Spot is at layer 8 and the cloud is at layer 5. The meaning of the curves is same as that in Figure 6.5.

ratio decreases with time. After including the cloud model, the oscillation becomes much more steady. After an initial adjustment, the inverse aspect ratio increases with time. This is an important result. The Voyager II observation showed that when the GDS-89 drifted to the equator, its shape became rounder, which means that the inverse aspect ratio of the fitting ellipse of GDS-89 was larger over time. The 80% case and 60% case are similar in this plot, suggesting that after a certain amount of methane is included, the effect of adding further methane on the Great Dark Spot will be limited.

Figure 6.11 shows the effect of the cloud on the oscillation in the Great Dark Spot centering at layer 7. Similar results can be concluded. We can still get increasing

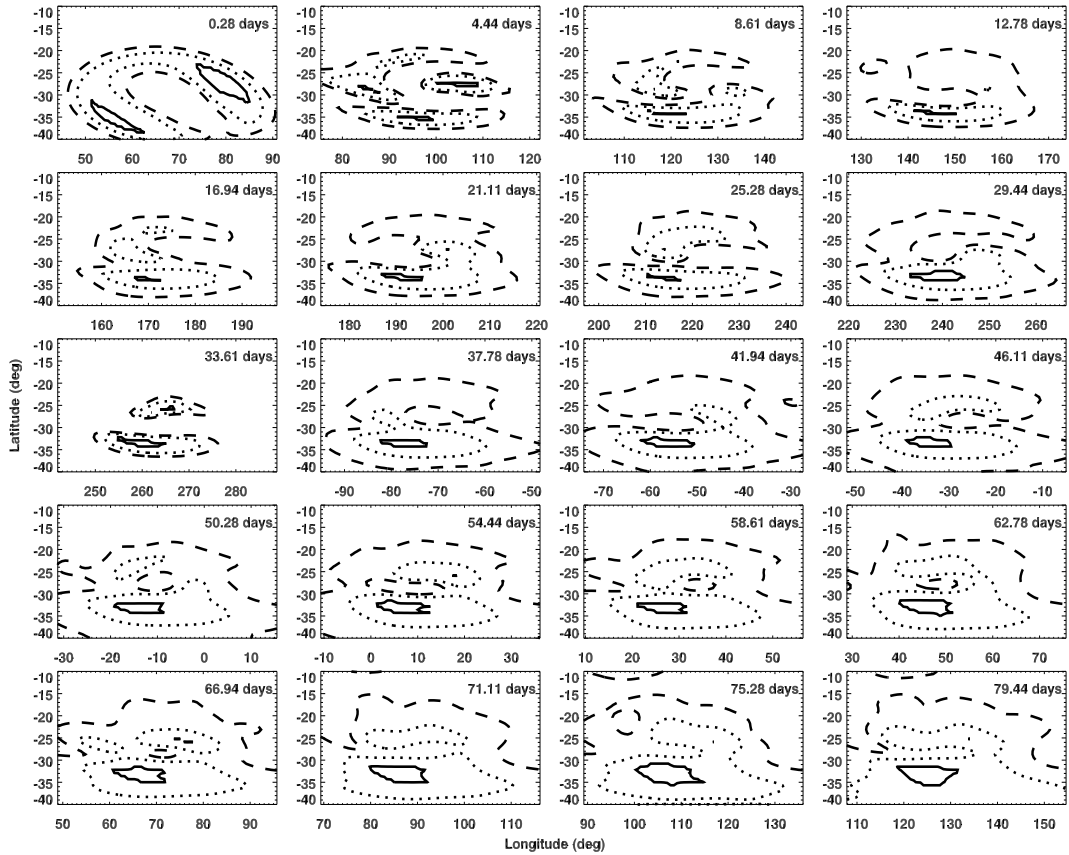


Figure 6.8: Evolution of the methane cloud near a great vortex. This plot shows the contour of the relative humidity. The solid curve is the cloud boundary - relative humidity ≥ 1 . After initial adjustment, a stable cloud is formed on the south top of the great dark spot. This plot is from 0.28 days to 79.44 days.

inverse aspect ratio in the cloud cases.

The parameters and results of these cases with and without clouds are shown in Table 6.2.

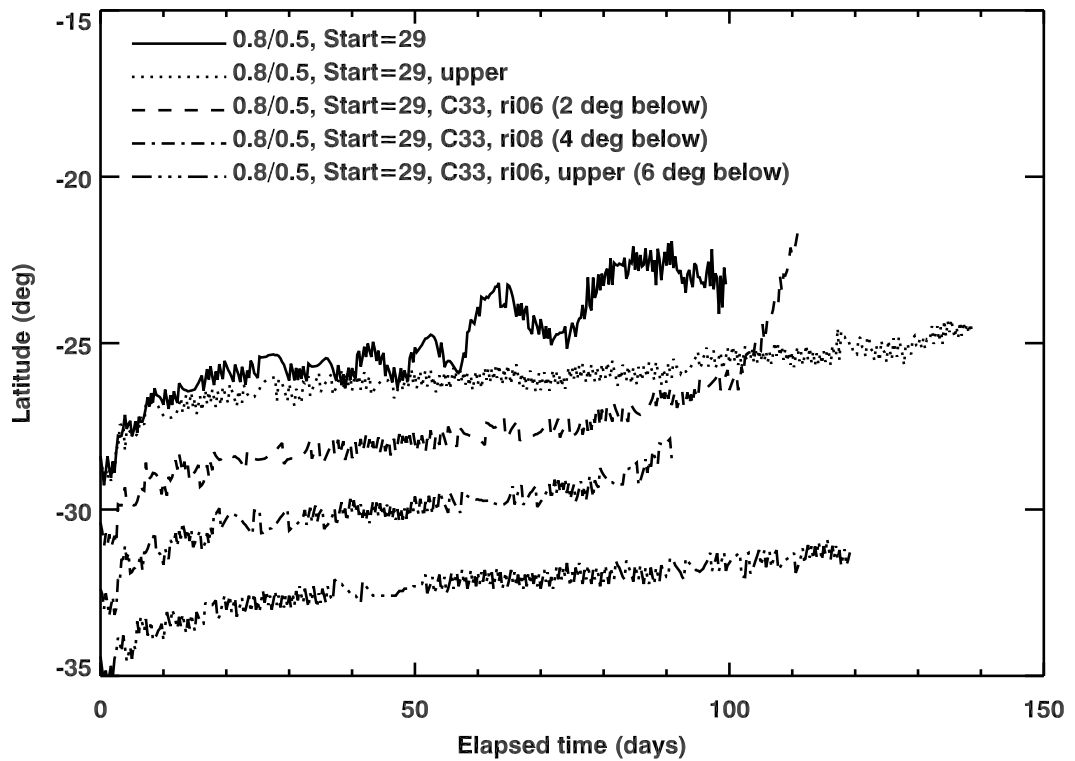


Figure 6.9: Drifts of great dark spots with time. To compare more clearly, the dashed line is shifted 2° downwards; the dash-dot line is shifted 4° downwards; the dash-dot-dot line is shifted 6° downwards.

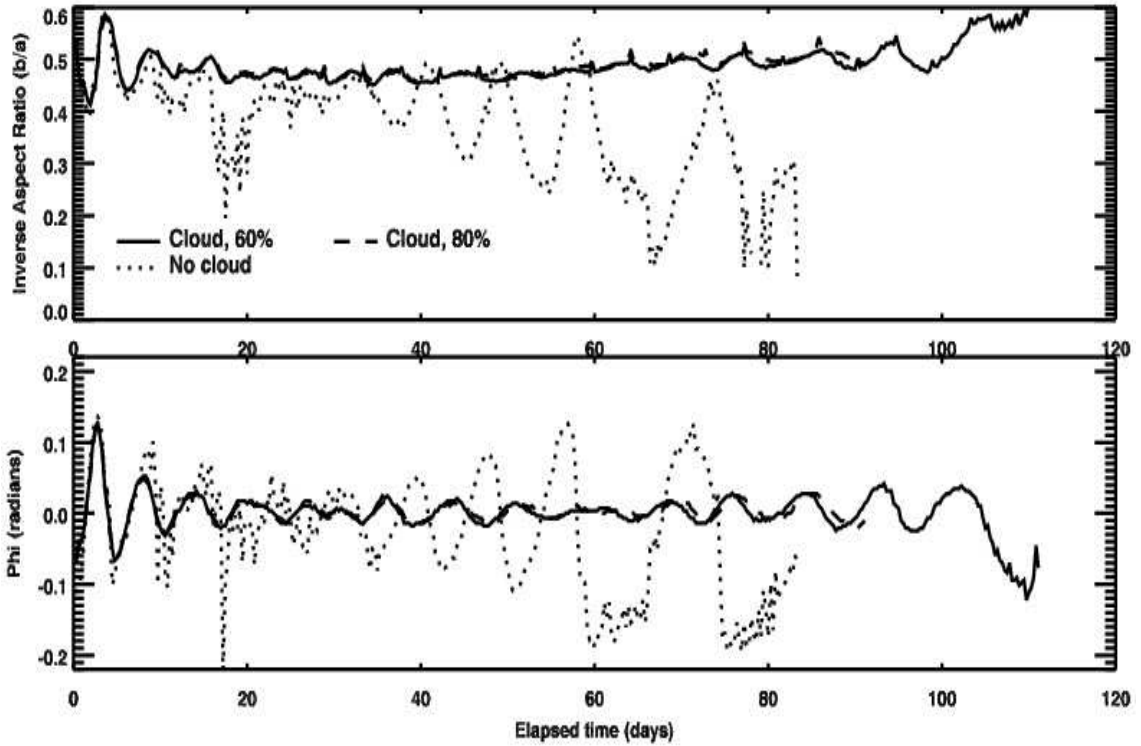


Figure 6.10: Oscillation of inverse aspect ratio (upper panel) and orientation angle (lower panel) of the fitting ellipse to the great dark spot, with or without cloud model, in the deeper layer - layer 8.

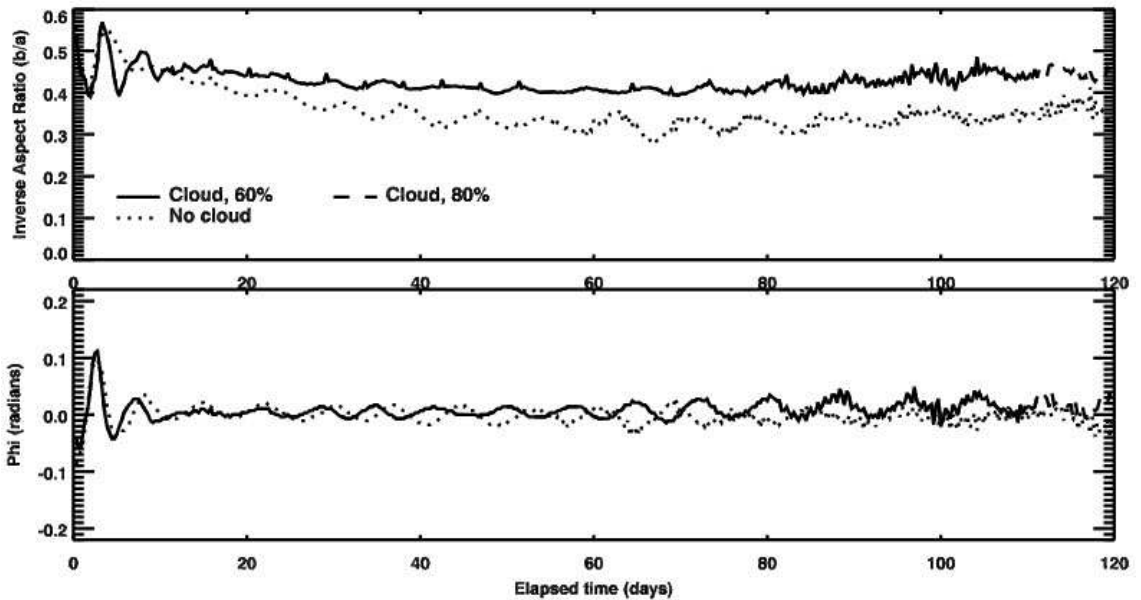


Figure 6.11: Oscillation of inverse aspect ratio (upper panel) and orientation angle (lower panel) of the fitting ellipse to the great dark spot, with or without cloud model, in the upper layer - layer 7.

Table 6.2: Comparison between the simulation cases with cloud model and without cloud model.

Q_y	λ_0	Str./Size/AR	Drift	Periods	Inverse AR	ϕ (rad)	Others
1/12	29°S	0.8/0.5/1.5	0.4	N/A/8.0	0.32±0.02	0.00±0.01	main layer 7
1/12	29°S	0.8/0.5/1.5	1.6	N/A/14.3	0.39±0.09	-0.01±0.10	main layer 8
1/12	29°S	0.8/0.5/1.5	0.4	N/A/7.7	0.41±0.01	0.00±0.02	main layer 7, RH 0.6
1/12	29°S	0.8/0.5/1.5	0.4	N/A/7.7	0.41±0.02	0.01±0.02	main layer 7, RH 0.8
1/12	29°S	0.8/0.5/1.5	0.6	N/A/8.1	0.50±0.02	0.01±0.02	main layer 8, RH 0.6
1/12	29°S	0.8/0.5/1.5	0.6	N/A/8.3	0.51±0.02	0.00±0.02	main layer 8, RH 0.8

1. All the simulation cases in this table have reference latitude 24°S, constant Q_y between 28°S and 38°S and smooth transition on both ends.
2. The mark "RH" means initial relative humidity.
3. Other parameters used here are same as those in Table 3.3.

To find the reason of the influence of the cloud, a plot about the pressure change was generated. Figure 6.12 shows the changes of the pressures in different layers in the cases with or without the cloud model. This plot is about the deeper vortex cases. Since GDS-89 was an anticyclone, pressure decreases around the great dark spot region. In each layer (layer 5: upper, layer 6: middle, layer 7: lower), the cloud case shows more pressure decrease than the case without cloud. Obviously, the cloud formation process decreases the local pressure. This helps a Great Dark Spot to keep its size and shape so that the oscillation of the spot is more stable.

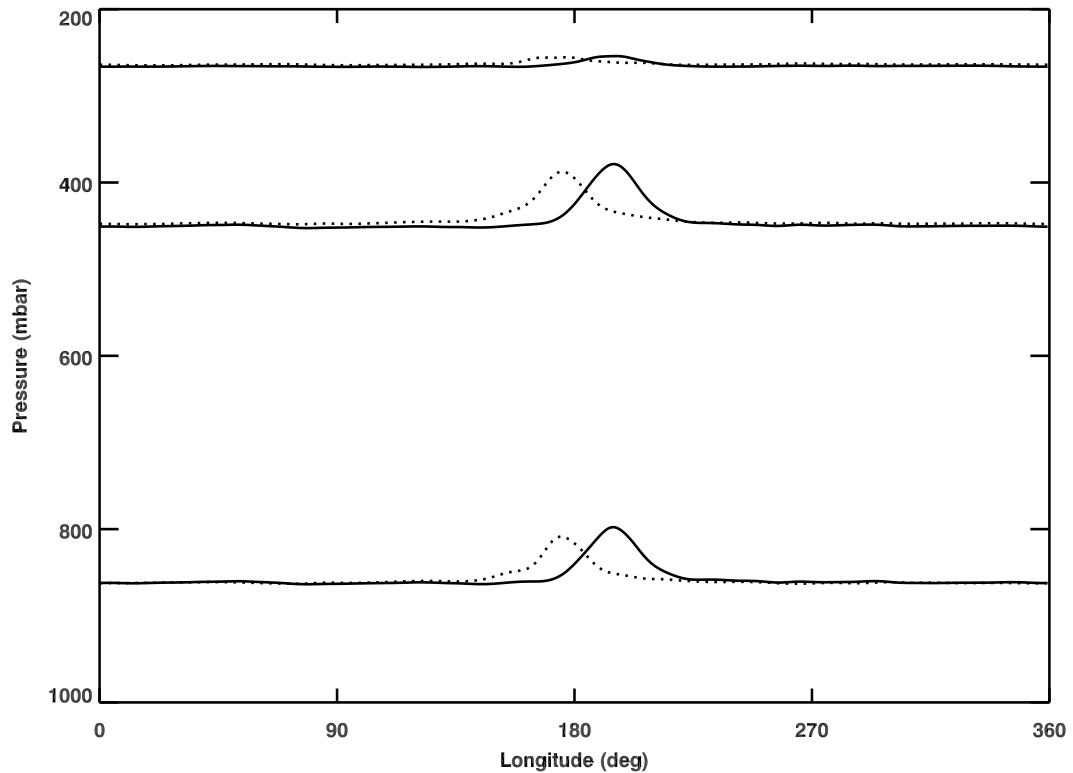


Figure 6.12: Comparison of the pressure changes. The two cases included here are the deeper spot cases with or without cloud. This comparison is at the time 48 days and 14.7 hours. These curves show the pressures at the latitude of the centers of the great dark spots. The solid curves are about the cases with the cloud model; the dotted curves are about the cases without the cloud model. Pressures in layer 5 (upper), layer 6 (middle) and layer 7 (lower) are shown here.

The above cases show that the observed long period oscillations were generated

in our simulations. After initial adjustment, the deeper case has a $0.75^\circ/\text{month}$ drift rate; the upper case has a $0.42^\circ/\text{month}$ drift rate.

We also checked the conservation of potential vorticity of the great dark spot. After canceling the background potential vorticity and using a critical value to define the vortex area, we can calculate the averaged potential vorticity in the vortex area. Figure 6.13 shows the area-weighted averaged potential vorticity profiles of the two deep layer cases. The case without clouds shows a bad conservation profile. The potential vorticity decreases with time. The case with clouds shows a near constant potential vorticity profile after 10 days. This tells us that the cloud physics can help the great dark spot achieve a better conservation of potential vorticity. This is also why the performance of the cloud case is much better than that of the no-cloud case.

Figure 6.14 shows the similar cases in a upper layer. From Chapter 3, we know that the upper layer case in this zonal wind profile has more stable drift and oscillations. Therefore, we expect the upper layer case will show a better potential vorticity profile than the deeper layer case. Comparing these figure with Figure 6.13, we can see that the upper layer no-cloud case does exhibit a better conservation of potential vorticity, after an initial adjustment. But still, the case with clouds shows a better potential vorticity profile than the one without clouds.

Cloud Model on Uranus

Similar to the bright companion of Neptune's GDS-89, there are also poleward clouds above the Uranian Dark Spot. The bright companion clouds can be seen in Figure 1.8.

We apply this methane cloud model to the simulation of bright companion clouds on Uranus. We want to generate the poleward cloud and test the effect of this cloud to the dynamic evolution of the UDS. Similar to above discussion, we use methane molar fraction of 33 times of the solar value and relative humidity 0.6 for the initial

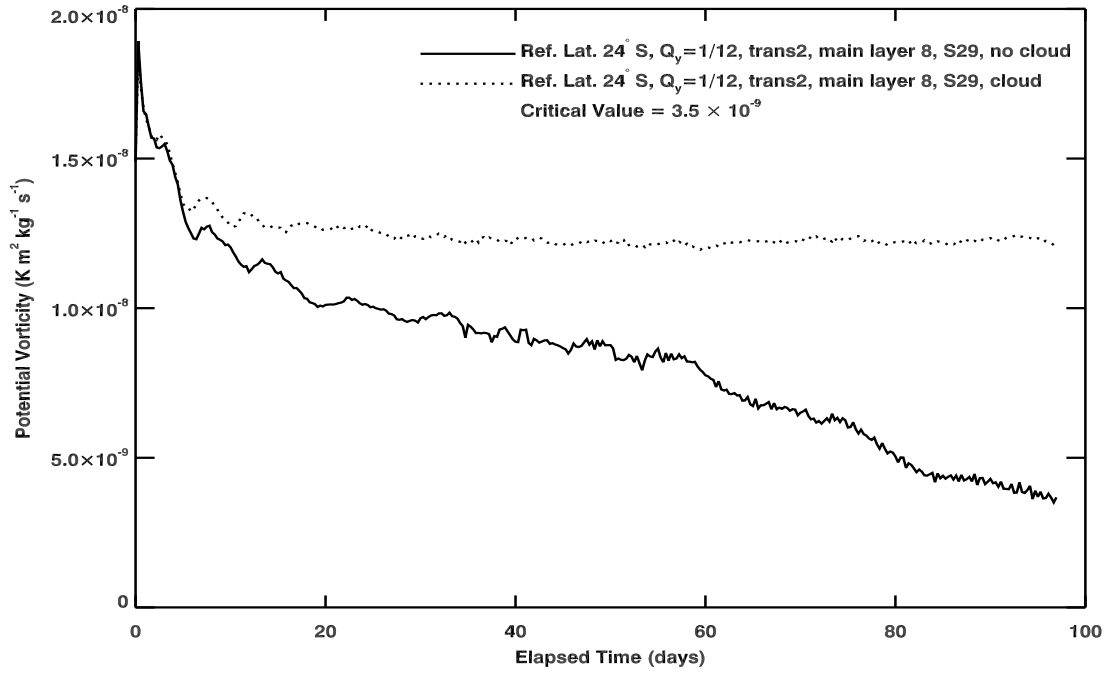


Figure 6.13: Comparison of the conservation of potential vorticity. The two cases included here are the deeper spot cases with or without cloud.

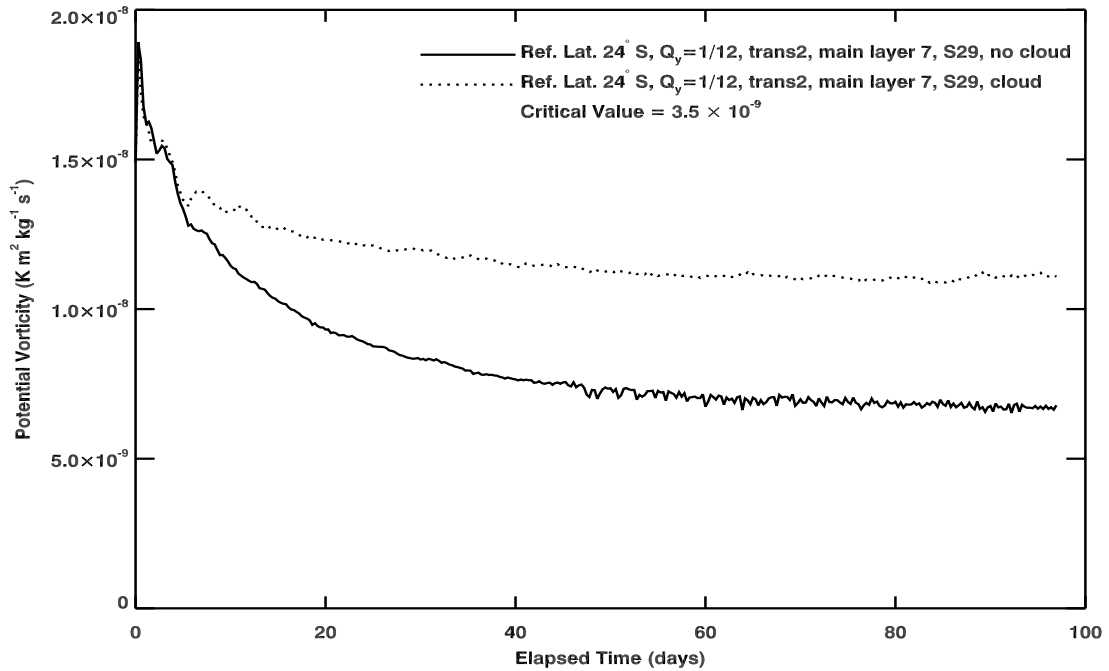


Figure 6.14: Comparison of the conservation of potential vorticity. The two cases included here are the upper spot cases with or without cloud.

condition. Same as those fine grid cases in Chapter 4, the grid spacing used here is 0.35° and the time step is 30 seconds. With these parameters, using 8 nodes/16 cores of KFC6I, we can simulate one month in about three weeks.

The methane cloud formation plot is shown in Figure 6.15. We can see the formation and evolution of the poleward cloud above the simulated UDS.

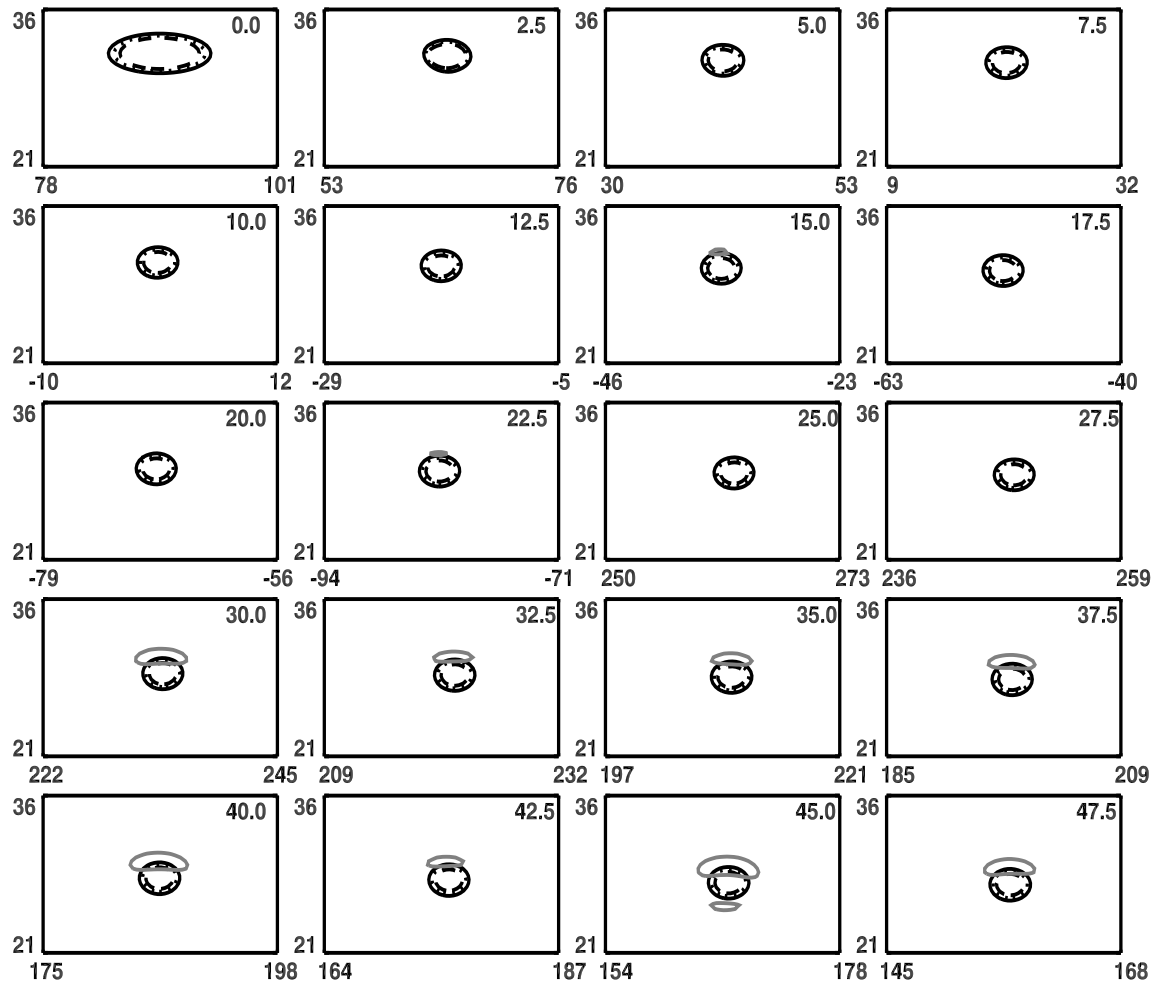


Figure 6.15: Formation of cloud above the simulated UDS. The dark curves are the contours of potential vorticity of the simulated UDS at layer 7 (868 mbar). The grey solid curves are the contours of methane relative humidity at layer 5 (247 mbar). The horizontal axis is longitude (deg) and the vertical axis is latitude (deg). The numbers in each subplot is the time in unit days.

Similar to Neptune's cases, the cloud model also has its effects on the dynamics of the simulated UDS. Figure 6.16 shows the size change of the spots starting from

32°N in Sromovsky and Fry 2005 fit profile. The adjustment time of the case with the cloud model is short and after that the spot keeps its size near constant for a long time. This is very different from the case without the cloud model, which decreases at the beginning to a small size and then increases its size steadily. Obviously, the inclusion of this cloud model extends the viability of a simulated vortex on Uranus and helps maintain a constant size for a longer time. This is similar to the Neptune's simulation cases.

Different from the Neptune's cases, with cloud model, the simulated UDS drifts faster than that without cloud model. This is shown in Figure 6.17.

The comparison contour plots of these two cases are shown in Figure 6.18.

6.7 Discussion

From the above analysis, we can make several possible conclusions. First, a poleward cloud can be generated around a great dark spot on Neptune and on Uranus simply by adding a cloud model and letting the model run. Second, a lower vortex can generate more clouds, a result that agrees with the result in Stratman et al. 2001. Furthermore, cloud formation causes the GDS to be more stable, both in drifting and in oscillation. It does not change the drift rate when the GDS is stable without clouds. This may allow the GDS to drift closer to the equator in the EPIC simulations. On Uranus, the cloud physics also helps the dark spot to keep its compact size at a constant level. But different from the simulations on Neptune, the vortex on Uranus drifts faster with the cloud model. Finally, when clouds are included, the GDS shows increasing inverse aspect ratio with time. This is consistent with the Voyager II observational result.

Our current simulations are all in the southern hemisphere. Just as was showed in Chapter 2, we expect that the northern hemisphere will be the mirror hemisphere to the southern one if we use a symmetric zonal wind profile. Therefore, these simulation

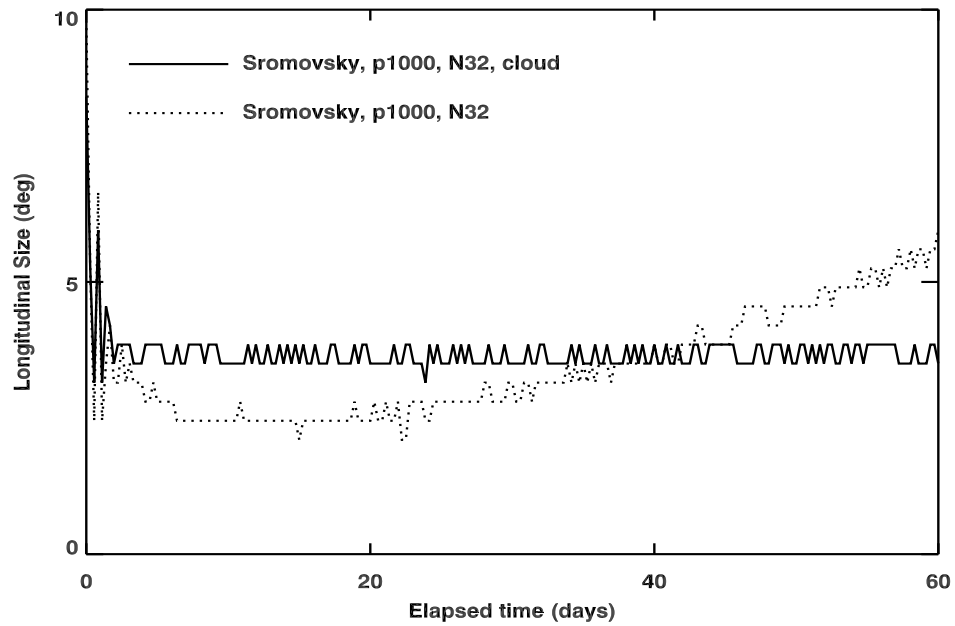


Figure 6.16: Comparison of longitudinal size change of spots in finer grid with and without cloud. These two cases are all in Sromovsky and Fry 2005 fit zonal wind profile and start from 32°N. Other parameters are same as those standard parameters of finer grid simulation cases in Chapter 4.

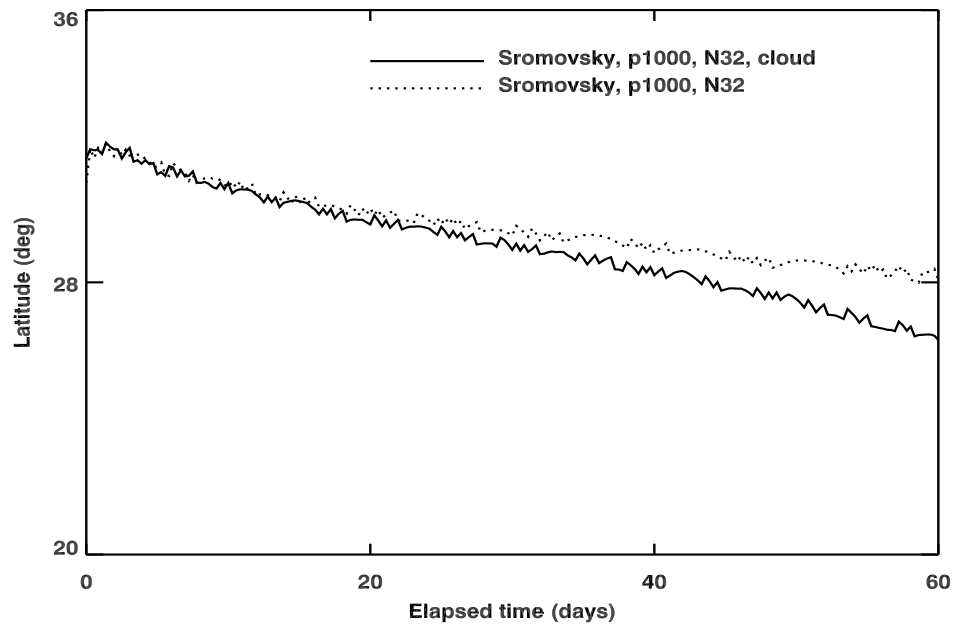


Figure 6.17: Comparison of drift rate in finer grid with and without cloud. These two cases are same as those in Figure 6.16.

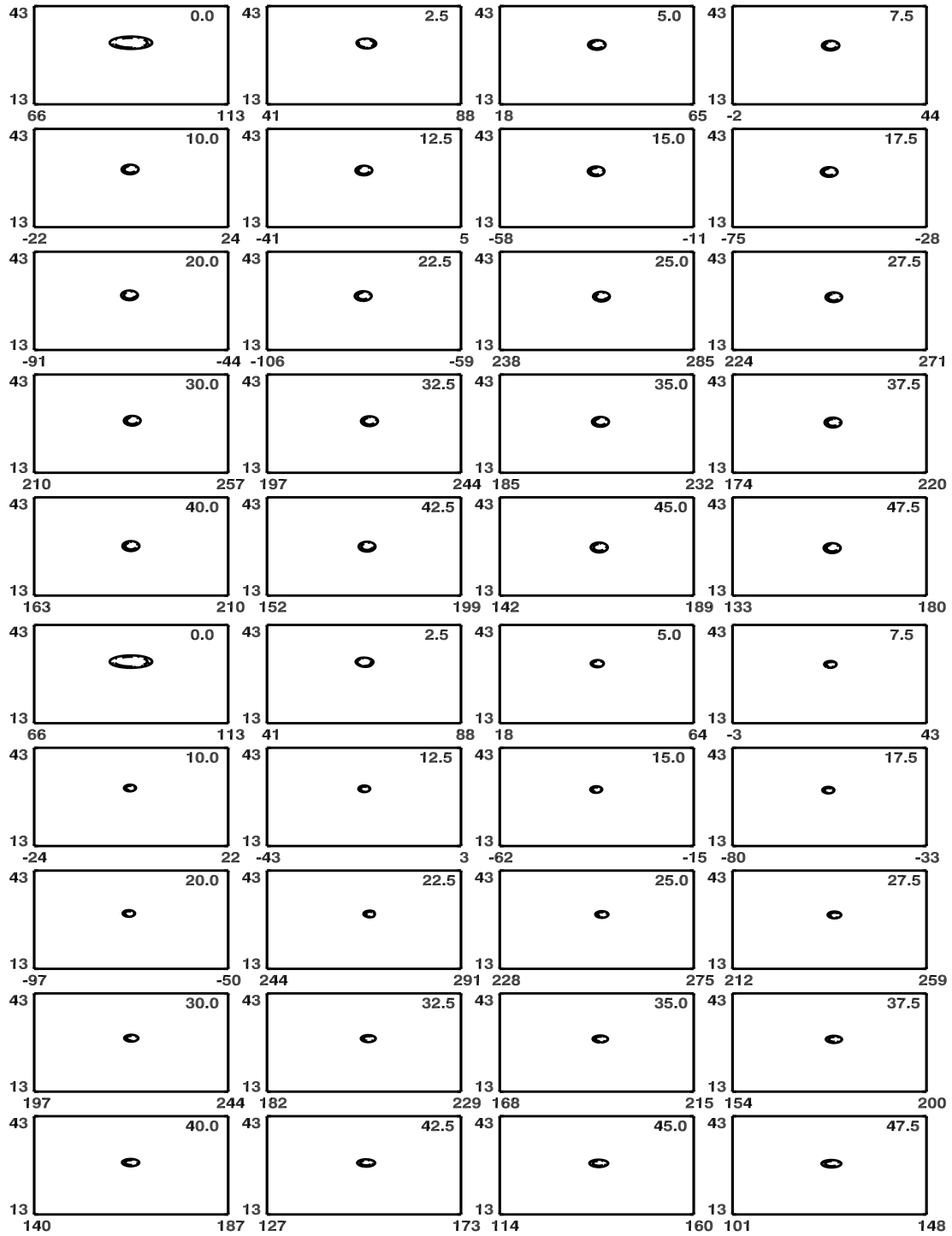


Figure 6.18: Contour plot of the simulated UDS on Sromovsky and Fry 2005 fit zonal wind profile with (upper panel) and without (lower panel) cloud model. These two cases are same as those in Figure 6.16. The numbers in the subplots are the times of the simulations, in unit days.

results also potentially stand for NGDSs.

In the future work, latent heat can be included in this cloud model to make the model be able to study more cloud phenomena. More microphysics can be included, like the ice to vapor process. In previous observations, a cloud ring was observed at high latitudes in the southern hemisphere of Uranian. With the cloud model including more cloud physics, we may be able to explain this phenomenon.

Chapter 7 Discussion

In this work, we discussed several applications of the CFD simulations on planetary atmospheres, including the dynamic simulations of Great Dark Spots on Neptune, the sustainability study of Uranian Dark Spot, the implementation of a two-flux radiation model to the seasonal changes of Uranian atmosphere and the implementation of a methane cloud model to the formation of bright companions and their interaction with dark spots. The equations and methods used in these simulations are discussed. The simulation results are investigated.

The dynamic simulations to Neptune's Great Dark Spot is the beginning of this work. The main original idea is that we wanted to explain the characteristics of the observed GDS-89 by Voyager II. One reason is that it is one of the most dynamic vortex ever observed. Studying this will be helpful for us to understand the vortex phenomena. Another reason is that due to the pass by of Voyager II, we have more information about this great vortex than any other vortex on Uranus or Neptune, although it is very far away from the Earth. Furthermore, through the simulations of GDS-89, we can study the background environment of the Neptune's atmosphere. With these in mind, we constructed different zonal wind profiles and vertical P-T profiles based on the observational data. We then generated different vortices in the simulated atmosphere and let them run in the system.

The results suggest that with suitable parameters we can simulate the basic characters of the GDS-89. The most important parameter is the background absolute vorticity. A parameter Q_y is used to indicate the local gradient of the absolute vorticity. When $Q_y \sim 0$, which means the local background absolute vorticity is near constant, the great vortex behaves the best with small drift and consistent oscillations. Simulation results indicate that the behavior of the great vortex is sensitive

to Q_y . Because the GDS-89 drifted in a wide latitudinal area from 27° to 18°S , constructing the zonal wind profile with a small Q_y in this wide area while achieving a good match to the observational data becomes difficult. This leads to different modifications to the basic Q_y methods, including changing the reference latitude, modifying the near-equator profile and changing Q_y in a wider area with smooth transitions. The behavior of the great vortex seems not sensitive to the vertical P-T profile, which means we cannot get more information about the P-T profile from these simulations.

As to the vortex itself, we tested different initial conditions, including size, strength and aspect ratio. We also generated vortices at different latitudes and different vertical layers. Smaller size will increase the drift rate and yield a rounder shape; smaller strength will decrease the drift rate and yield a smaller inverse aspect ratio; initial aspect ratio will influence the final aspect ratio. In some profiles, locating at different vertical layers does not influence the behavior of the simulated vortex much. However, in the changing Q_y with smooth transition profile, we saw that in the deep layer the great vortex drifted more wildly. The starting latitude does not change the drift rate much when the latitude is far away enough from the equator. After adjustment, the vortices from different latitudes will have similar drift rates. This result works when the constant Q_y area is wide and cover the whole studying latitudes.

Since the used Neptune's zonal wind profile is symmetric, the vortex in the northern hemisphere can be studied symmetrically in the southern hemisphere. Therefore, we do not have special consideration for the NGDSs.

When we were still working on the dynamic simulations of Neptune's GDS, we got the information that the first Uranian Dark Spot was defined. This leads to a question about the sustainability of great vortices in the Uranian atmosphere. Because of the limitation of the observations, we can only know the basic latitude, size, shape and lifetime of the UDS. We applied the basic methods of the Neptune GDS project to the study of the UDS. We investigated the effects of different zonal wind profiles, different

latitudes and different strengths of the vortex. Because of the relatively small size of UDS, a finer grid with a smaller time step is used. The results answered the question of suitable zonal wind background and suitable latitude. Through the simulations, it seems that ordinarily the Uranian zonal wind environment is not suitable for a great vortex to survive, which may explain why it is hard to observe a dark spot on Uranus. But because of the seasonal change of the zonal wind profile, near 2006, a kink near 28°N appeared in the zonal wind profile, which led to a small gradient of absolute vorticity near this latitude and provide a suitable area for the survival of the UDS. As to the strength of the spot, it only in a range influence the behavior of the UDS and does not change the above basic trend.

In the study of the UDS, we noticed that the seasonal change of the Uranian atmosphere is strong and different from other gas giant planets. The zonal wind profile is the key profile for the survival of UDS, which also change with the season of Uranus. This encouraged us to construct a radiation model to study the seasonal changes on Uranus. The simulation results of the radiation model can explain the change of the zonal wind profile, the kink appearing at the UDS latitude and the possible vortex at $\sim 34^{\circ}\text{S}$. It also gives the explanation of the observed temperature distribution. A global convection is formed to transfer energy from the radiation area to the poles.

The dynamic simulations on Neptune and Uranus do not explain the poleward bright companion clouds above the great vortices. How did they form above the vortices and what are the effects of these clouds to the vortices? With these in mind, we started from the basic methane cloud model presented by Stratman et al. 2001[98] and the cloud physics scheme by Palotai and Dowling in 2008[75] to study the interaction between the cloud and the vortices. Poleward orographic clouds are simulated above the Neptune's GDS-89 and the UDS. The cloud model also helps the great vortices to conserve their potential vorticity and therefore keep their size

and produce stable oscillations. This helps to better answer the previous questions about Neptune's GDS-89 and UDS. We can say that the cloud formation is also an important aspect of the long-lived GDSs and UDS.

Because of the significant effects of the cloud model on the dynamics of the Neptune's GDS, for the next step, we will investigate more parameters in the simulations of the Neptune's GDS with cloud model. Hopefully, with the cloud model, the simulation results can fit the observational data better. Also, current cloud model just includes the phase change of vapor to ice and does not include latent heat physics. A more complete cloud model needs to be developed in the future. With more cloud physics, combining with the radiation model, more cloud phenomena can be simulated, including the observed cloud band on Uranus. Furthermore, there are more heat sources in the atmospheres of Neptune and Uranus. The ortho-para hydrogen conversion process has been realized in EPIC but not been turned on in our simulations. The effects of this process need to be investigated. We know that for Neptune, the internal heat is stronger than the solar heat into the atmosphere. To better study the dynamics of a planetary atmosphere, we may need to include the internal heat, especially for Neptune. These require more work and more observational data in the future.

Through these CFD simulations on gas-giant planets Neptune and Uranus, we have achieved a better understanding about the vortex physics and the background atmospheric environments on these planets. In the future, these can be applied to the vortex simulations on terrestrial planets, including the Earth. Currently, the EPIC GCM is still being developed to meet the requirements of studying terrestrial planets, especially for the Earth, which includes atmosphere, ocean and land. Considering the effects of the solid ground, we can also develop the radiation model for terrestrial planets, including the absorption, reflection and radiation of the ground. To study the movement of the atmosphere near the solid ground and the formation and the effects

of the Planetary Boundary Layer (PBL), turbulence models are needed. Currently, the EPIC GCM has a SA Detached Eddy Simulation (DES) model, which needs to be tested and applied in the study of some phenomena near the ground. Also, a Large Eddy Simulation (LES) turbulence model is more popular in the simulations of planetary atmospheres, which will also be developed in the future. In the future, when people plan a mission to Neptune or Uranus, these simulation methods and the related results can be used to decide the orbit, the equipments and the entry point to their atmospheres.

Bibliography

- [1] Adcroft, A., J-M Campin, C. Hill and J. Marshall, Implementation of an atmosphere-ocean general circulation model on the expanded spherical cube, *Mon. Wea. Rev.*, 132 (12), 2845-2863, 2004.
- [2] Allison, M., R. F. Beebe, B. J. Conrath, D. P. Hinson, A. P. Ingersoll, Uranus atmospheric dynamics and circulation, In: Bergstralh, J. T., E. D. Miner, M. S. Matthews (Eds.) *Uranus Univ. of Arizona Press, Tucson*, pp. 253-295, 1991.
- [3] ATOC Consortium, Ocean Climate Change: Comparison of Acoustic Tomography, Satellite Altimetry, and Modeling, *Science* 281, 1327A, 1998.
- [4] Bachet, G., E. R. Cohen, P. Dore, and G. Birnbaum, The Translational-Rotational Absorption Spectrum of Hydrogen, *Can. J. Phys.* 61, 591-603, 1983.
- [5] Baines, K. H., M. E. Mickelson, L. E. Larson, and D. W. Ferguson, The abundances of methane and ortho/para hydrogen in Uranus and Neptune: Implications of new laboratory 4-0 H-2 quadrupole line parameters. *Icarus* 114, 328C340, 1995.
- [6] Choi, David S., A.P. Showman, T.E. Dowling, C.J. Palotai, Numerical Simulations Of Jupiter's 5-micron Hot Spots, 39th Annual Meeting of the Division for Planetary Sciences, Orlando, FL, October 7-12, 2007.
- [7] Chin, J. H., and S. W. Churchill, Anisotropic, Multiply Scattered Radiation from an Arbitrary, Cyclindrical Source in an Infinite Slab, *ASME Journal of Heat Transfer*, Vol. 87, pp. 167-172, 1965.
- [8] Colon, E., and T. E. Dowling, EPIC Simulations of Topographic Effects on the General Circulation of Venus, 32th Annual Meeting of the Division for Planetary Sciences, 2000.
- [9] Shih, T. M. and Y. N. Chen, A Discretized-Intensity Method Proposed for Two-

- Dimensional Systems Enclosing Radiative and Conductive Media, Numerical Heat Transfer, Vol. 6, pp. 117-134, 1983.
- [10] Chan, S. H., Numerical Methods for Multidimensional Radiative Transfer Analysis in Participating Media, Annual Review of Numerical Fluid Dynamics and Heat Transfer, Vol. 1, Hemisphere, New York, pp. 305-350, 1987.
- [11] Cohen, E. R., L. Frommhold, and G. Birnbaum, Analysis of the far infrared H₂-He Spectrum. J. Chem. Phys. 77, 4933-4941, 1982.
- [12] Conrath, B. J., P. J. Gierasch, S. S. Leroy, Temperature and circulation in the stratosphere of the outer planets, Icarus 83, 255-281, 1990.
- [13] Conrath, B. J., F. M. Flasar, and P. J. Gierasch, Thermal structure and dynamics of Neptune's atmosphere from Voyager measurements, J. Geophys. Res. 96, 18931-18939, 1991.
- [14] Conrath B. J., P. P. J. Gierasch, and E. A. Ustinov, Thermal Structure and Para Hydrogen Fraction on the Outer Planets from Voyager IRIS Measurements, Icarus 135, pp. 501-517, 1998.
- [15] Deng, X., R.P. LeBeau. Parametric Simulations of the Great Dark Spots of Neptune. 38th Annual DPS meeting, Pasadena, CA, October 8-13, 2006
- [16] Deng, X., R.P. LeBeau, Comparative CFD Simulations of the Dark Spots of Uranus and Neptune, AIAA-2007-4119, 37th AIAA Fluid Dynamics Conference and Exhibit, Miami, FL, June 25-28, 2007.
- [17] Deng, X., and R.P. LeBeau, Dynamic Simulations of Potential Dark Spots in the Atmosphere of Uranus, 39th Annual Meeting of the Division for Planetary Sciences, Orlando, FL, October 7-12, 2007.
- [18] Deng, X., and R.P. LeBeau, Comparative Dynamical Simulations of the Atmospheres of Neptune and Uranus, 40th Annual Meeting of the Division for Planetary Sciences, Ithaca, NY, October 10-15, 2008.
- [19] Dowling, T. E., et al., The Explicit Planetary Isentropic-Coordinate (EPIC)

- Atmospheric Model, ICARUS, 132, 221-238, 1998.
- [20] Dowling, T. E., P. W. Stratman, A. P. Showman, L. A. Sromovsky, EPIC Simulations of Condensables Interacting with Anticyclones on Neptune and Jupiter, 32nd Annual DPS meeting, 2000.
- [21] Dowling, T. E., and A. Herrnstein, Venus EPIC Model Spinup Results, 38th Annual DPS meeting, Pasadena, CA, October 8-13, 2006.
- [22] Dowling, T. E., M. E. Bradley, E. Colon, J. Kramer, R.P. LeBeau, G.C.H. Lee, T.I. Mattox, R. Morales-Juberias, C.J. Palotai, V.K. Parimi, and A.P. Showman, The EPIC Atmospheric Model with an Isentropic/Terrain-Following Hybrid Vertical Coordinate, *Icarus* 182, pp. 259-273, 2006.
- [23] Dowling, T. E., A. Herrnstein, and K.M. Sayanagi, Clearing two atmospheric modeling hurdles: Full-globe balanced initialization and an accurate steep-terrain pressure-gradient-force scheme for the EPIC model, *Bulletin of the American Astronomical Society* 39, 527, 2007.
- [24] Friedson, J. & A.P. Ingersoll. Seasonal Meridional Energy Balance and Thermal Structure of the Atmosphere of Uranus: A Radiative-Convective-Dynamical Model. *Icarus* 69, pp. 139-156, 1987.
- [25] García-Melendo, E., A. Sánchez-Lavega, R. Hueso, Numerical models of Saturn's long-lived anticyclones, *Icarus* 191, 665-677, 2007.
- [26] Greathouse, T. K., S. B. Strong, J. I. Moses, and T. E. Dowling, A Radiative Seasonal Climate Model Applied to Saturn, 40th Annual Meeting of the Division for Planetary Sciences, Ithaca, NY, October 10-15, 2008.
- [27] Grevesse, N., and E. Anders, Appendix A: Solar Element Abundances, Table 1. In *Solar Interior and Atmosphere* (A. N. Cox, W. C. Livingston, and M. S. Matthews, Eds.), Univ. of Arizona Press, Tucson, pp. 1229C1230, 1991.
- [28] Gross, R. S., I. Fukumori and D. Menemenlis, Atmospheric and oceanic excitation of the Earth's wobbles during 1980-2000, *Journal of Geophysical Research-*

Solid Earth, vol.108, 2003.

- [29] Hammel, H. B., R. F. Beebe, E. M. de Jong, C. J. Hansen, C. D. Howell, A. P. Ingersoll, T. V. Johnson, S. S. Limaye, J. A. Magalhaes, J. B. Pollack, L. A. Sromovsky, V. E. Suomi, C. E. Swift, Neptune's wind speeds obtained by tracking clouds in Voyager images, *Science* 245, p. 1367-1369, 1989.
- [30] Hammel, H. B., Discrete cloud structure on Neptune, *Icarus* 80, p. 14-22, 1989.
- [31] Hammel, H. B., Neptune cloud structure at visible wavelengths, *Science* 244, p. 1165-1167, 1989.
- [32] Hammel, H.B., G.W. Lockwood, J.R. Mills, and C.D. Barnet. Hubble Space Telescope Imaging of Neptune's Cloud Structure in 1994. *Science* 268, pp. 1740-1742, 1995.
- [33] Hammel, H.B. and G.W. Lockwood. Atmospheric Structure of Neptune in 1994, 1995, and 1996. *Icarus* 129, pp. 466-481, 1997.
- [34] Hammel, H.B., K. Rages, G. W. Lockwood, E. Karkoschka, and I. de Pater, I., New measurements of the winds of Uranus. *Icarus* 153, 229C235, 2001.
- [35] Hammel, H.B., I. de Pater, S. Gibbard, G.W. Lockwood, and K. Rages, Uranus in 2003: Zonal winds, banded structure, and discrete features. *Icarus*, 175, 534-545, 2005.
- [36] Hammel, H.B. Uranus nears Equinox: A report from the 2006 Pasadena Workshop. 5 September 2006
- [37] Hammel, H.B., G.W. Lockwood, Long-term atmospheric variability on Uranus and Neptune, *Icarus* 186, pp. 291-301, 2007.
- [38] Hammel, H. B. , L. A. Sromovsky, P. M. Fry, K. Ragesc, M. Showalter, I. de Pater, M. A. van Dam, R. P. LeBeau, and X. Deng, The Dark Spot in the Atmosphere of Uranus in 2006: Discovery, Description, and Dynamical Simulations, accepted by *Icarus*, 2009.
- [39] Holton, J. R., *An Introduction to Dynamic Meteorology*, 3rd ed. Academic Press,

1992.

- [40] Ingersoll, A. P. Solar Heating and Internal Heat Flow on Jupiter. *Icarus*, 35, pp. 27-43, 1978.
- [41] Ingersoll, A.P., C.D. Barnet, R.F. Beebe, F.M. Flasar, D.P. Hinson, S.S. Limaye, L.A. Sromovsky, and V.E. Suomi. Dynamic Meteorology of Neptune. In *Neptune and Triton*, ed. D.P. Cruikshank, University of Arizona Press, pp. 613-684, 1995.
- [42] Karkoschka, E. Clouds of High Contrast on Uranus. *Science*, 280, p. 570, 1998.
- [43] Kida, S., Motion of an elliptic vortex in a uniform shear flow. *J. in each layer. Phys. Soc. Jpn.* 50, 3517C3520, 1981.
- [44] LeBeau, R. P., Simulations of Time-Dependent Three-Dimensional Vortices with Application to Neptune's Great Dark Spot, Ph. D. Dissertation, June 1997.
- [45] LeBeau, R. P. and T. E. Dowling. EPIC Simulations of Time-Dependent, Three-Dimensional Vortices with Application to Neptune's Great Dark Spot. *Icarus* 132, 239-265, 1998.
- [46] LeBeau, R. P. and X. Deng. CFD Simulation of the Great Dark Spots of Neptune. AIAA-2006-3727, 36th AIAA Fluid Dynamics Conference and Exhibit, San Francisco, CA, June 5-8, 2006.
- [47] LeBeau, R. P. and X. Deng, Toward Capturing the Many Motions of Neptune's Original Great Dark Spot. 39th Annual Meeting of the Division for Planetary Sciences, Orlando, FL, October 7-12, 2007.
- [48] LeBeau, R.P., X. Deng, and C. Palotai, Dynamic Simulation of Neptune's 1989 Great Dark Spot and its Bright Companion, 40th Annual Meeting of the Division for Planetary Sciences, Ithaca, NY, October 10-15, 2008.
- [49] Lee, G. C., and T. E. Dowling, Application of the Isentropic/Terrain-Following Hybrid EPIC GCM to Venus with Topography, American Geophysical Union, Spring Meeting 2004.
- [50] Legarreta, J. and A. Sanchez-Lavega, Vertical structure of Jupiter's troposphere

- from nonlinear simulations of long-lived vortices, *Icarus* 196, 184-201, 2008.
- [51] Lian Y., and A. P. Showman, Deep jets on gas-giant planets, *Icarus*, Volume 194, Issue 2, p. 597-615, 2008.
- [52] Lian Y., and A. P. Showman, Formation of zonal jets by moist convection on gas-giant planets, 40th Annual Meeting of the Division for Planetary Sciences, Ithaca, NY, October 10-15, 2008.
- [53] Limaye, S. S., and L. A. Sromovsky, Winds of Neptune: Voyager observations of cloud motions, *J. Geophys. Res.* 96, 18941-18960, 1991.
- [54] Lindal, G. F., J. R. Lyons, D. N. Sweetnam, V. R. Eshleman, and D. P. Hinson, The atmosphere of Uranus - Results of radio occultation measurements with Voyager 2, *Journal of Geophysical Research* 92, 14987-15001, 1987.
- [55] Lindal, G. F., J. R. Lyons, D. N. Sweetnam, V. R. Eshleman, D. P. Hinson, and G. L. Tyler, The atmosphere of Neptune: Results of the radio occultation measurements with the Voyager 2 spacecraft, *Geophys. Res. Letters* 17, 1733-1736, 1990.
- [56] Lindal, G. F., The atmosphere of Neptune: An analysis of radio occultation data acquired with Voyager 2, *Astron. J.* 103, 967-982.
- [57] Lodders and Fegley, *The Planetary Scientist's Companion*, Oxford University Press, 1998.
- [58] Lunine, J. I., The Atmospheres of Uranus and Neptune, *Annual Review of Astronomy and Astrophysics* 31, 217-263, 1993.
- [59] Marotzke, J., R., Giering, K. Q. Zhang, D. Stammer, C. Hill, T. Lee, Construction of the adjoint MIT ocean general circulation model and application to Atlantic heat transport sensitivity, *JGR, Journal of Geophysical Research*, Volume 104, Issue C12, p. 29529-29548, 1999.
- [60] Marten A., H. E. Matthews, T. Owen, R. Moreno, T. Hidayat, and Y. Biraud, Improved constraints on Neptune's atmosphere from submillimetre-wavelength

- observations, *A&A* 429, 1097-1105, 2005.
- [61] Marshall, J., A. Adcroft, C. Hill, L. Perelman, and C. Heisey: A finite volume, incompressible navier-stokes model for studies of the ocean on parallel computers. *J. Geophys. Res.*, 102, 5753C5766, 1997a.
- [62] Marshall, J., C. Hill, L. Perelman, and A. Adcroft: Hydrostatic, quasi-hydrostatic, and nonhydrostatic ocean modeling. *J. Geophys. Res.*, 102, 5733C 5752, 1997b.
- [63] McKinley, G.A., M.J. Follows, J. Marshall, and S.M. Fan, Interannual variability of air-sea O₂ fluxes and the determination of CO₂ sinks using atmospheric O₂/N₂, *Geophysical Research Letters*, vol.30, 2003.
- [64] Meacham, S. P., G. R. Flierl, and U. Send, Vortices in shear. *Dyn. Atmos. Oceans* 14, 333-386, 1989.
- [65] Meacham, S. P., K. K. Pankratov, A. F. Shchepetkin, and V. V. Zhmur, The interaction of ellipsoidal vortices with background shear flows in a stratified fluid, *Dyn. Atmos. Oceans* 21, 167-212, 1994.
- [66] Moore, D. W., and P. G. Saffman 1971. Structure of a line vortex in an imposed strain.
- [67] Morales-Juberias, R., A. Sanchez-Lavega, and T. E. Dowling, EPIC simulations of the merger of Jupiter's White Ovals BE and FA: altitude-dependent behavior, *Icarus*, Volume 166, Issue 1, p. 63-74, 2003.
- [68] Morales-Juberias, R. and T. E. Dowling, Simulations of high-latitude spots on Jupiter: Constraints on vortex strength and the deep wind, *Planetary and Space Science* 53, 12, 1221-1233, 2005.
- [69] Morales-Juberias, R., M. Liang, T.E. Dowling, Jupiter Stratospheric Jet Simulations, American Geophysical Union, P51A-0203, 2007.
- [70] Morales-Juberias R., K. M. Sayanagi, and T. E. Dowling, Numerical Simulations of Saturn's North Polar Hexagon and Jupiter's Great Red Spot, 40th Meeting

- of the Division for Planetary Sciences, 2008.
- [71] http://www.nasa.gov/vision/earth/lookingatearth/h2005_katrina.html.
- [72] [http://www.nytimes.com/2006/05/05/science/space/05jupiter.html?
_r=1&ex=1177819200&en=e3c0e43d660623d4&ei=5070](http://www.nytimes.com/2006/05/05/science/space/05jupiter.html?_r=1&ex=1177819200&en=e3c0e43d660623d4&ei=5070).
- [73] Orton, G. S., A. T. Tokunaga, and J. Caldwell, Observational Constraints on the Atmospheres of Uranus and Neptune from New Measurements near 10 μm . *Icarus* 56, 147-164, 1983.
- [74] Orton, G. S., D. K. Aitken, C. Smith, P. F. Roche, J. Cadwell, and R. Synder, The spectra of Uranus and Neptune at 8-14 and 17-23 μm , *Icarus* 70, 1-12.
- [75] Palotai, C., T. E. Dowling, Addition of water and ammonia cloud microphysics to the EPIC model, *Icarus* 194, 303-326, 2008.
- [76] Polvani, L. M., J. Wisdom, E. DeJong, and A. P. Ingersoll. Simple dynamical models of Neptunes Great Dark Spot. *Science* 249, pp. 1393C1398, 1990.
- [77] Ponte, R. M., D. Stammer, and J. Marshall, Oceanic signals in observed motions of the Earth's pole of rotation, *Nature* 391, 476P, 1998.
- [78] Press, W. H., S. A. Teukolsky, W. T. Vetterling, and B. P. Flannery, *Numerical Recipes in C*, second edition, Cambridge University Press, 1992.
- [79] Raymond, David J., Convective processes and tropical atmospheric circulations, *Quarterly Journal of the Royal Meteorological Society*, 120, 520, 1994.
- [80] Sanchez-Lavega, A., J. Legarreta, E. Garcia-Melendo, J. M. Gomez, S. Perez-Hoyos, R. Hueso, G. S. Orton, IOPW (International Outer Planet Watch) Team, Observations and Models of the Interaction of a Large Red Oval with the Great Red Spot in June-July 2008, *DPS* 40, 5001S, 2008.
- [81] Sayanagi, K. M., A. P. Showman, Effects of a large convective storm on Saturn's equatorial jet, *Icarus* 187, pp. 520-539, 2006.
- [82] Sayanagi, K. M., T. E. Dowling, A. P. Showman, Stability of Shallow Jovian Atmospheric Zonal Jets, *DPS* 39, 0101S, 2007.

- [83] Sayanagi, K. M., N. Ghurtskaia, T.E. Dowling, Venus Wind Spin-up Experiments with Topography; Sensitivity to Model Resolution, American Geophysical Union, P33B-1294, 2007.
- [84] Sayanagi, K. M., R. Morales-Juberias, and T. E. Dowling, Numerical Simulations of Saturn's Northern Hemisphere Ribbon Wave, 40th Meeting of the Division for Planetary Sciences, 2008.
- [85] Showman, A. P., and T. E. Dowling, EPIC Simulations of Jovian Equatorial Dynamics: Implications for Jupiter's Dry Downdrafts, 31st Annual Meeting of the Division for Planetary Sciences, 1999.
- [86] Smith, B. A., L. A. Soderblom, R.F. Beebe, et al., Voyager 2 in the Uranian system: Imaging science results, *Science* 233, pp. 43-64, 1986.
- [87] Smith, B. A., L. A. Soderblom, D. Banfield, et al., Voyager 2 at Neptune: Imaging science results, *Science* 246, 1422, 1989.
- [88] Smith, W. H., C. P. Conner, and K. H. Baines, Absorption Coefficients for the 6190-Å CH₄ Band between 290 and 100°K with Application to Uranus' Atmosphere, *Icarus* 85, 58-64, 1990.
- [89] Spall, M.A., and R.S. Pickart, Wind-driven recirculations and exchange in the Labrador and Irminger Seas. *Journal of Physical Oceanography*, vol.33, pp.1829-1845, 2003.
- [90] Sromovsky, L. A., Latitudinal and longitudinal oscillations of cloud features on Neptune, *Science* 254, 684-686, 1991.
- [91] Sromovsky, L. A., S. S. Limaye, and P. M. Frye. Dynamics of Neptune's major cloud features. *Icarus* 105, pp. 110-141, 1993.
- [92] Sromovsky, L. A., S. S. Limaye, and P. M. Frye. Clouds and circulation on Neptune: Implications of 1991 HST observations. *Icarus* 118, pp. 25-38, 1995.
- [93] Sromovsky, L. A., P. M. Fry, T. E. Dowling, K. H. Baines, and S. S. Limaye. Coordinated 1996 HST and IRTF Imaging of Neptune and Triton: III. Neptune's

- Atmospheric Circulation and Cloud Structure. *Icarus* 149, pp. 459-488, 2001.
- [94] Sromovsky, L. A., P. M. Fry, and K. H. Baines. The Unusual Dynamics of Northern Dark Spots on Neptune. *Icarus* 156, pp. 16-36, 2002.
- [95] Sromovsky, L. A., P. M. Fry, Dynamics of cloud features on Uranus. *Icarus* 179, pp.459-484, 2005.
- [96] Sromovsky, L.A. <http://hubblesite.org/newscenter/archive/releases/2006/47>
- [97] Sromovsky, L. A., P. M. Fry, W. M. Ahue, H. B. Hammel, I. de Pater, K. A. Rages, M. R. Showalter, M. A. van Dam, Uranus at Equinox: Cloud Morphology and Dynamics, DPS 40.5007S, 2008.
- [98] Stratman, P. W., A. P. Showman, T. E. Dowling, and L. A.Sromovsky. EPIC Simulations of Bright Companions to Neptune's Great Dark Spots. *Icarus* 151, pp. 275-285, 2001.
- [99] Strang, G., Introduction to Applied Mathematics, Wellesley-Cambridge Press, 1986.
- [100] Sussman, M., and T. E. Dowling, EPIC Modeling of Seasonal Thermal Forcing on Uranus, 40th Annual Meeting of the Division for Planetary Sciences, Ithaca, NY, October 10-15, 2008.
- [101] Tyler G. L., D. N. Sweetnam, J. D. Anderson, S. E. Borutzki, J. K. Campbell, V. R. Eshleman, D. L. Gresh, E. M. Gurrola, D. P. Hinson, N. Kawashima, E. R. Kursinski, G. S. Levy, G. F. Lindal, J. R. Lyons, E. A. Marouf, P. A. Rosen, R. A. Simpson, G. E. Wood, Voyager radio science observations of Neptune and Triton, *Science* 246, 1466-1473, 1989.
- [102] Viskanta, R. and M. P. Mengüç, Radiative Heat Transfer in Combustion Systems, *Progress in Energy and Combustion Sciences*, Vol. 13, pp. 97-160, 1987.
- [103] Warwick, James W., David R. Evans, Gerard R. Peltzer, Robert G. Peltzer, Joseph H. Romig, Constance B. Sawyer, Anthony C. Riddle, Andrea E. Schweitzer, Michael D. Desch, Michael L. Kaiser, Voyager planetary radio as-

- tronomy at Neptune, *Science* 246, p. 1498-1501, 1989.
- [104] Weisstein, E. W., Millimeter/Submillimeter Fourier Transform Spectroscopy of Jovian Planet Atmospheres, Ph. D. Dissertation, 1996.
- [105] Williams, D. R., Uranus Fact Sheet, <http://nssdc.gsfc.nasa.gov/planetary/factsheet/uranusfact.html>, January 31, 2005.
- [106] Williams, D. R., Sun Fact Sheet, <http://nssdc.gsfc.nasa.gov/planetary/factsheet/sunfact.html>, September 1, 2004.

Vita

Xiaolong Deng

Date of Birth: 05/05/1981

Birthplace: Linchuan, Jiangxi Province, P. R. China

Education

- 2009 Ph.D. in Mechanical Engineering
 University of Kentucky
- 2005 Ph.D. in Astrophysics
 University of Science and Technology of China
- 2000 B.E. in Computer Science and Engineering
 University of Science and Technology of China

Scholastic and professional honors

- 2009 Univ. of Kentucky Outstanding Mechanical Engineering Graduate Student
- 2007 American Astronomical Society Division for Planetary Sciences Travel Award
- 1997 Beijing Lenovo Scholarship for Outstanding Students
- 1996 Univ. of Science and Technology of China Outstanding Student Scholarship

Professional Positions

- 2005-present Research Assistant, University of Kentucky
- 2005-2008 Teaching Assistant, University of Kentucky
- 2001-2005 Research Assistant, University of Science and Technology of China
- 2000-2001 Teaching Assistant, University of Science and Technology of China

Professional Publications

Deng, X., R. P. LeBeau, A Radiation Model in EPIC and Seasonal Changes on Uranus, in preparation

Deng, X., R. P. LeBeau, A Cloud Model in EPIC and the Effects of Cloud on the Dynamics of dark spots on Neptune and Uranus, in preparation

Deng, X., R. P. LeBeau, CFD investigations on Great Dark Spot and Background Environment on Neptune, in preparation.

Deng, X., R. P. LeBeau, and C. Palotai, Numerical Investigation of Orographic Cloud and Vortex Dynamics on Ice Giant Planets, accepted by 1st AIAA Atmospheric and Space Environments Conference, San Antonio, Texas, June 22-25, 2009.

Hammel H. B., L. A. Sromovsky, P. M. Fry, K. A. Rages, M. Showalter, I. de Pater, M. A. van Dam, R. P. LeBeau, and X. Deng, The Dark Spot in the Atmosphere of Uranus in 2006: Discovery, Description, and Dynamical Simulations, accepted by Icarus.

Deng, X., and R. P. LeBeau, Comparative CFD Simulations of the Dark Spots of Uranus and Neptune, AIAA-2007-4119, 37th AIAA Fluid Dynamics Conference and Exhibit, Miami, FL, June 25-28, 2007.

LeBeau, R. P. and X. Deng, CFD Simulation of the Great Dark Spots of Neptune, AIAA-2006-3727, 36th AIAA Fluid Dynamics Conference and Exhibit, San Francisco, CA, June 5-8, 2006.

Deng X., J. Liu, and J. M. Yang, A New Explanation for GRB Transient Spectra, Journal of University of Science and Technology of China, 8, 2, 2008.

J. Liu, Y. F. Yuan, and X. L. Deng, Radiation Mechanism and Maser Emission for Relativistic Electrons Spiralling and Drifting in Curved Magnetic Fields, Chinese Journal of Astronomy and Astrophysics, 7, 304, 2007.

J. Liu, Y. F. Yuan, and X. L. Deng, Characteristics of the synchrotron radiation from relativistic electrons in plasma, Acta Physica Sinica (Chinese), 56, 1214, 2007.

Deng, X., T. S. Xia, and J. Liu, Gamma-Ray Bursts' Spectra and Synchro-Curvature Mechanism, Astronomy & Astrophysics, 443, 747D, 2005.

Professional Presentations and Posters

Deng, X., R.P. LeBeau, and C. Palotai, Numerical Simulations of Great Dark Spots and Their Bright Companions. 34th Annual Dayton-Cincinnati Aerospace

Science Symposium, Dayton, OH, March 3, 2009.

Deng, X., and R. P. LeBeau, Comparative Dynamical Simulations of the Atmospheres of Neptune and Uranus, 40th Annual Meeting of the Division for Planetary Sciences, Ithaca, NY, October 10-15, 2008.

LeBeau, R. P., X. Deng, and C. Palotai, Dynamic Simulation of Neptune's 1989 Great Dark Spot and its Bright Companion, 40th Annual Meeting of the Division for Planetary Sciences, Ithaca, NY, October 10-15, 2008.

Hammel H. B., L. A. Sromovsky, P. M. Fry, K. A. Rages, M. Showalter, I. de Pater, M. A. van Dam, R. P. LeBeau, and X. Deng, The Dark Spot in the Atmosphere of Uranus in 2006: Discovery, Description, and Dynamical Simulations, 40th Annual Meeting of the Division for Planetary Sciences, Ithaca, NY, October 10-15, 2008.

Deng, X. and R.P. LeBeau, Making Meteorology Better on Uranus and Neptune. 14th Annual Kentucky EPSCoR Conference, Louisville, Kentucky, October 3, 2008.

Deng, X., R.P. LeBeau, Numerical Investigation of the First Uranian Dark Spot, 33rd Annual Dayton-Cincinnati Aerospace Science Symposium, Dayton, OH, March 4, 2008.

Deng, X., and R.P. LeBeau, Dynamic Simulations of Potential Dark Spots in the Atmosphere of Uranus, 39th Annual Meeting of the Division for Planetary Sciences, Orlando, FL, October 7-12, 2007.

LeBeau, R.P., and X. Deng, Toward Capturing the Many Motions of Neptune's Original Great Dark Spot. 39th Annual Meeting of the Division for Planetary Sciences, Orlando, FL, October 7-12, 2007.

Deng, X., R.P. LeBeau, Simulations of the Great Dark Spots of Neptune and Uranus, 32nd Annual Dayton-Cincinnati Aerospace Science Symposium, Dayton, OH, March 6, 2007.

LeBeau, R.P., D.A. Reasor, X. Deng, S. Panguluri, N. Beliganur and T. Hauser,

Performance Assessment of Fluid Dynamics codes on Different Computer Architectures, 32nd Annual Dayton-Cincinnati Aerospace Science Symposium, Dayton, OH, March 6, 2007.

Deng, X., and R. P. LeBeau, Parametric Simulations of the Great Dark Spots of Neptune, 38th Annual Meeting of the Division for Planetary Sciences, Pasadena, CA, October 8-13, 2006.

LeBeau, R.P. and X. Deng, CFD Simulation of the Great Dark Spots of Neptune, International Conference of Computational Fluid Dynamics 4, Ghent, Belgium, July 10-14, 2006.

Deng, X. and R.P. LeBeau, CFD Simulation of the Great Dark Spots of Neptune, 31st Annual Dayton-Cincinnati Aerospace Science Symposium, Dayton, OH, March 7, 2006.

Xiaolong Deng